neuroprotective role.[65]. Further, controlled synthesis and purification of (pNAG-b-A) hydrogel with different molecular weights can provide the clear insight about the neurogenesis and neuroprotection efficacy of the hydrogel.

3.2.5 SUMMARY and CONCLUSIONS

In this work, we have successfully synthesized porous, cross-linked p(NAG-b-A) hydrogel with high swelling behaviour. The p(NAG-b-A) shows shear thing behavior and injectable in nature. p(NAG-b-A) can promote the axon growth in primary neuron and can improve the microtubule integrity. However, its exact mechanism is yet to be found out. *In silico* study reveals that the p(NAG-b-A) hydrogel could be involved in the GSK3β inhibition and promotes neuronal growth via modulating the GSK pathway. Presence of various functional groups such as –COOH and amide group in p(NAG-b-A) hydrogel scavenge the free radicals via oxidation reaction and protect neuronal damage from the oxidative stress conditions. It is found that the viscoelastic nature of p(NAG-b-A) hydrogel favor astrocyte differentiation and consequently neuroprotection. Finally, it can be concluded that the p(NAG-b-A) hydrogel is a potential candidate to induce neuronal regeneration and can be used in other regenerative purposes. Furthermore, (pNAG-b-A) hydrogel can provide a huge scope to analyze the mechanistic activities for the various leading neurodegenerative diseases which could be the future direction of this work.

3.2.6. REFERENCES

(1) Serger, E.; Luengo-Gutierrez, L.; Chadwick, J. S.; Kong, G.; Zhou, L.; Crawford, G.; Danzi, M. C.; Myridakis, A.; Brandis, A.; Bello, A. T.; Müller, F.; Sanchez-Vassopoulos, A.; De Virgiliis, F.; Liddell, P.; Dumas, M. E.; Strid, J.; Mani, S.; Dodd, D.; Di Giovanni, S. The gut metabolite indole-3 propionate promotes nerve regeneration and repair. *Nature* **2022**, *607* (7919), 585-592. DOI: 10.1038/s41586-022-04884-x.

(2) Liu, Y.; Hsu, S. H. Biomaterials and neural regeneration. *Neural regeneration research* **2020**, *15* (7), 1243-1244. DOI: 10.4103/1673-5374.272573 From NLM.

(3) Scheib, J.; Höke, A. Advances in peripheral nerve regeneration. *Nature Reviews Neurology* **2013**, *9* (12), 668-676. DOI: 10.1038/nrneurol.2013.227.

(4) Ruediger, T.; Bolz, J. Neurotransmitters and the development of neuronal circuits. *Axon growth and guidance* **2007**, 104-114. DOI: DOI: 10.1007/978-0-387-76715-4_8.

(5) Hansen, J. Y.; Shafiei, G.; Markello, R. D.; Smart, K.; Cox, S. M. L.; Nørgaard, M.; Beliveau, V.; Wu, Y.; Gallezot, J.-D.; Aumont, É.; Servaes, S.; Scala, S. G.; DuBois, J. M.; Wainstein, G.; Bezgin, G.; Funck, T.; Schmitz, T. W.; Spreng, R. N.; Galovic, M.; Koepp, M. J.; Duncan, J. S.; Coles, J. P.; Fryer, T. D.; Aigbirhio, F. I.; McGinnity, C. J.; Hammers, A.; Soucy, J.-P.; Baillet, S.; Guimond, S.; Hietala, J.; Bedard, M.-A.; Leyton, M.; Kobayashi, E.; Rosa-Neto, P.; Ganz, M.; Knudsen, G. M.; Palomero-Gallagher, N.; Shine, J. M.; Carson, R. E.; Tuominen, L.; Dagher, A.; Misic, B. Mapping neurotransmitter systems to the structural and functional organization of the human neocortex. *Nature Neuroscience* **2022**, *25* (11), 1569-1581. DOI: 10.1038/s41593-022-01186-3.

(6) Bekri, A.; Drapeau, P. Glycine promotes the survival of a subpopulation of neural stem cells. *Frontiers in Cell and Developmental Biology* **2018**, *6*, 68. DOI: 10.3389/fcell.2018.00068.

(7) Eric Samarut1, A. B. a. P. D. Transcriptomic Analysis of Purified Embryonic Neural Stem Cells from Zebrafish Embryos Reveals Signaling Pathways Involved in Glycine-Dependent Neurogenesis. *Frontiers in Molecular Neuroscience* **2016**, *9* (22). DOI: 10.3389/fnmol.2016.00022.

(8) Edna Brustein, S. b. C., Julien Ghislain, Pierre Drapeau. Spontaneous Glycine-Induced Calcium Transients in Spinal Cord Progenitors Promote Neurogenesis. *Calcium Transients in Neurogenesis* **2012**. DOI: 10.1002/dneu.22050.

(9) Yang, L.; Wang, H.; Liu, L.; Xie, A. The Role of Insulin/IGF-1/PI3K/Akt/GSK3beta Signaling in Parkinson's Disease Dementia. *Front Neurosci* **2018**, *12*, 73. DOI: 10.3389/fnins.2018.00073.

(10) van Niekerk, E. A.; Tuszynski, M. H.; Lu, P.; Dulin, J. N. Molecular and cellular mechanisms of axonal regeneration after spinal cord injury. *Molecular & Cellular Proteomics* **2016**, *15* (2), 394-408. DOI: 10.1074/mcp.R115.053751.

(11) Daggupati, T.; Pamanji, R.; Yeguvapalli, S. In silico screening and identification of potential GSK3beta inhibitors. *J Recept Signal Transduct Res* **2018**, *38* (4), 279-289. DOI: 10.1080/10799893.2018.1478854.

(12) J. Guana, G. B. T., H. Lin b, S. Mathaib, D.C. Bachelor b, S. Georgea,; Gluckmana, P. D. Neuroprotective effects of the N-terminal tripeptide of insulin-like growth factor-1, glycine-proline-glutamate (GPE) following intravenous infusion in hypoxic–ischemic adult rats. *Neuropharmacology* **2004**, *47*, 892–903. DOI: 10.1016/j.neuropharm.2004.07.002.

(13) Zhang, Q.; Deng, Y.-X.; Luo, H.-X.; Shi, C.-Y.; Geise, G. M.; Feringa, B. L.; Tian, H.; Qu, D.-H. Assembling a Natural Small Molecule into a Supramolecular Network with High Structural Order and Dynamic Functions. *Journal of the American Chemical Society* **2019**, *141* (32), 12804-12814. DOI: 10.1021/jacs.9b05740.

(14) Peressotti, S.; Koehl, G. E.; Goding, J. A.; Green, R. A. Self-Assembling Hydrogel Structures for Neural Tissue Repair. *ACS Biomater Sci Eng* **2021**, *7* (9), 4136-4163. DOI: 10.1021/acsbiomaterials.1c00030.

(15) Cheng, Q.; Yu, X.; Xiong, Z.; Wan, Z.; Li, Y.; Ma, W.; Tan, W.; Liu, M.; Shea, K. J. Abiotic Synthetic Antibodies to Target a Specific Protein Domain and Inhibit Its Function. *ACS Applied Materials & Interfaces* **2022**, *14* (17), 19178-19191. DOI: 10.1021/acsami.2c02287.

(16) Bentolila, A.; Vlodavsky, I.; Ishai-Michaeli, R.; Kovalchuk, O.; Haloun, C.; Domb, A. J. Poly (N-acryl amino acids): a new class of biologically active polyanions. *Journal of medicinal chemistry* **2000**, *43* (13), 2591-2600. DOI: 10.1021/jm000089j.

(17) Seuring, J.; Agarwal, S. Polymers with Upper Critical Solution Temperature in Aqueous Solution: Unexpected Properties from Known Building Blocks. *ACS Macro Letters* **2013**, *2* (7), 597-600. DOI: 10.1021/mz400227y.

(18) Cui, C.; Wu, T.; Gao, F.; Fan, C.; Xu, Z.; Wang, H.; Liu, B.; Liu, W. An Autolytic High Strength Instant Adhesive Hydrogel for Emergency Self-Rescue. *Advanced Functional Materials* **2018**, *28* (42), 1804925. DOI: 10.1002/adfm.201804925.

(19) Gao, F.; Xu, Z.; Liang, Q.; Li, H.; Peng, L.; Wu, M.; Zhao, X.; Cui, X.; Ruan, C.; Liu, W. Osteochondral regeneration with 3D-printed biodegradable high-strength supramolecular polymer reinforced-gelatin hydrogel scaffolds. *Advanced Science* **2019**, *6* (15), 1900867. DOI: 10.1002/advs.201900867.

(20) Deepuppha, N.; Khadsai, S.; Rutnakornpituk, B.; Wichai, U.; Rutnakornpituk, M. Multiresponsive Poly(N-Acryloyl glycine)-Based Nanocomposite and Its Drug Release Characteristics. *Journal of Nanomaterials* **2019**, *2019*, 1-12. DOI: 10.1155/2019/8252036.

(21) Liumin He, Q. X., Yuyuan Zhao, Jun Li, Sathish Reddy, Xueshuang Shi, Xin Su, Kin Chiu,; Ramakrishna, a. S. Engineering an Injectable Electroactive Nanohybrid Hydrogel for Boosting Peripheral Nerve Growth and Myelination in Combination with Electrical Stimulation. *ACS Appl. Mater. Interfaces* **2020**, *12*, 53150−53163. DOI: 10.1021/acsami.0c16885.

(22) Hsieh, F.-Y.; Tseng, T.-C.; Hsu, S.-h. Self-healing hydrogel for tissue repair in the central nervous system. *Neural regeneration research* **2015**, *10* (12), 1922. DOI: 10.4103/1673-5374.169624.

(23) Nagappan, P. G.; Chen, H.; Wang, D.-Y. Neuroregeneration and plasticity: a review of the physiological mechanisms for achieving functional recovery postinjury. *Military Medical Research* **2020**, *7* (1), 30-30. DOI: 10.1186/s40779-020-00259-3 PubMed.

(24) Zamproni, L. N.; Mundim, M. T.; Porcionatto, M. A. Neurorepair and regeneration of the brain: a decade of bioscaffolds and engineered microtissue. *Frontiers in cell and developmental biology* **2021**, *9*, 649891. DOI: 10.3389/fcell.2021.649891.

(25) Zewen Liu, 2 Tingyang Zhou,1,3 Alexander C. Ziegler,4 Peter Dimitrion,4 and Li Zuo1,3. Oxidative Stress in Neurodegenerative Diseases: From Molecular Mechanisms to Clinical Applications. *Oxidative Medicine and Cellular Longevity* **2017**, 11. DOI: 10.1155/2017/2525967.

(26) Lv, Z.-F.; Xu, B.; Wang, J.-T. N-Acryloylglycine. *Acta Crystallographica Section E Structure Reports Online* **2006**, *62* (8), o3344-o3345. DOI: 10.1107/s1600536806026201.

(27) Schindelin, J.; Arganda-Carreras, I.; Frise, E.; Kaynig, V.; Longair, M.; Pietzsch, T.; Preibisch, S.; Rueden, C.; Saalfeld, S.; Schmid, B.; Tinevez, J.-Y.; White, D. J.; Hartenstein, V.; Eliceiri, K.; Tomancak, P.; Cardona, A. Fiji: an open-source platform for biological-image analysis. *Nature Methods* **2012**, *9* (7), 676-682. DOI: 10.1038/nmeth.2019.

(28) Yamala, A. K.; Nadella, V.; Mastai, Y.; Prakash, H.; Paik, P. Poly-N-acryloyl-(L-phenylalanine methyl ester) hollow core nanocapsules facilitate sustained delivery of immunomodulatory drugs and exhibit adjuvant properties. *Nanoscale* **2017**, *9* (37), 14006-14014. DOI: 10.1039/c7nr03724d.

(29) Brady, J.; Dürig, T.; Lee, P.; Li, J.-X. Polymer properties and characterization. *Developing solid oral dosage forms* **2017**, 181-223. DOI: https://doi.org/10.1016/B978-0-12-802447-8.00007-8.

(30) Ringeard, J. M.; Griesmar, P.; Caplain, E.; Michiel, M.; Serfaty, S.; Huerou, J. Y. L.; Marinkova, D.; Yotova, L. Design of poly (N-acryloylglycine) materials for incorporation of microorganisms. *Journal of Applied Polymer Science* **2013**, *130* (2), 835-841. DOI: 10.1002/app.39242.

(31) Shim, S. E.; Yang, S.; Jung, H.; Choe, S. Thermally robust highly crosslinked poly (methyl methacrylate-co-divinyl benzene) microspheres by precipitation polymerization. *Macromolecular research* **2004**, *12* (2), 233-239. DOI: 10.1007/BF03218393.

(32) Vlad, C. D.; Dinu, M. V.; Dragan, S. Thermogravimetric analysis of some crosslinked acrylamide copolymers and ion exchangers. *Polymer degradation and stability* **2003**, *79* (1), 153-159. DOI: 10.1016/S0141-3910(02)00268-9.

(33) Van Dyke, J. D.; Kasperski, K. L. Thermogravimetric study of polyacrylamide with evolved gas analysis. *Journal of Polymer Science Part A: Polymer Chemistry* **1993**, *31* (7), 1807-1823. DOI: https://doi.org/10.1002/pola.1993.080310720.

(34) Dassanayake, N. L.; Phillips, R. W. Determination of the composition of acrylamide/acrylate copolymers using thermogravimetric analysis. *Analytical Chemistry* **1984**, *56* (9), 1753-1755. DOI: https://doi.org/10.1021/ac00273a056.

(35) Kornev, V. A.; Grebenik, E. A.; Solovieva, A. B.; Dmitriev, R. I.; Timashev, P. S. Hydrogel-assisted neuroregeneration approaches towards brain injury therapy: A state-of-the-art review. *Comput Struct Biotechnol J* **2018**, *16*, 488-502. DOI: 10.1016/j.csbj.2018.10.011.

(36) Madhusudanan, P.; Raju, G.; Shankarappa, S. Hydrogel systems and their role in neural tissue engineering. *Journal of the Royal Society Interface* **2020**, *17* (162), 20190505. DOI: https://doi.org/10.1098/rsif.2019.0505.

(37) Shah, R.; Saha, N.; Kitano, T.; Saha, P. Influence of Strain on Dynamic Viscoelastic Properties of Swelled (H2o) And Biomineralized (Caco3) Pvp-Cmc Hydrogels. *Applied Rheology* **2015**, *25* (3), 13-22. DOI: 10.3933/applrheol-25-33979 (acccessed 2023-02-06).

(38) Donato, M. T.; Tolosa, L.; Gómez-Lechón, M. J. Culture and functional characterization of human hepatoma HepG2 cells. In *Protocols in In Vitro Hepatocyte Research*, Springer, 2015; pp 77-93.

(39) Lee, I. B.; Son, H. H.; Um, C. M. Rheologic properties of flowable, conventional hybrid, and condensable composite resins. *Dental materials : official publication of the Academy of Dental Materials* **2003**, *19* (4), 298-307. DOI: 10.1016/s0109-5641(02)00058-1.

(40) Wiatrak, B.; Kubis-Kubiak, A.; Piwowar, A.; Barg, E. PC12 cell line: cell types, coating of culture vessels, differentiation and other culture conditions. *Cells* **2020**, *9* (4), 958. DOI: 10.3390/cells9040958.

(41) Wang, J.; Tian, L.; Chen, N.; Ramakrishna, S.; Mo, X. The cellular response of nerve cells on poly-l-lysine coated PLGA-MWCNTs aligned nanofibers under electrical stimulation. *Materials Science and Engineering: C* **2018**, *91*, 715-726. DOI: DOI: 10.1016/j.msec.2018.06.025.

(42) Xu, G.; Pierson, C. R.; Murakawa, Y.; Sima, A. A. Altered tubulin and neurofilament expression and impaired axonal growth in diabetic nerve regeneration. *Journal of Neuropathology & Experimental Neurology* **2002**, *61* (2), 164-175. DOI: https://doi.org/10.1093/jnen/61.2.164.

(43) Latremoliere, A.; Cheng, L.; DeLisle, M.; Wu, C.; Chew, S.; Hutchinson, E. B.; Sheridan, A.; Alexandre, C.; Latremoliere, F.; Sheu, S. H.; Golidy, S.; Omura, T.; Huebner, E. A.; Fan, Y.; Whitman, M. C.; Nguyen, E.; Hermawan, C.; Pierpaoli, C.; Tischfield, M. A.; Woolf, C. J.; Engle, E. C. Neuronal-Specific TUBB3 Is Not Required for Normal Neuronal Function but Is Essential for Timely Axon Regeneration. *Cell Rep* **2018**, *24* (7), 1865-1879 e1869. DOI: 10.1016/j.celrep.2018.07.029.

(44) Dráberová, E.; Del Valle, L.; Gordon, J.; Marková, V.; Šmejkalová, B.; Bertrand, L.; de Chadarévian, J.-P.; Agamanolis, D. P.; Legido, A.; Khalili, K. Class III β-tubulin is constitutively coexpressed with glial fibrillary acidic protein and nestin in midgestational human fetal astrocytes: implications for phenotypic identity. *Journal of Neuropathology & Experimental Neurology* **2008**, *67* (4), 341-354. DOI: 10.1097/NEN.0b013e31816a686d.

(45) Silva, T. P.; Bekman, E. P.; Fernandes, T. G.; Vaz, S. H.; Rodrigues, C. A. V.; Diogo, M. M.; Cabral, J. M. S.; Carmo-Fonseca, M. Maturation of Human Pluripotent Stem Cell-Derived Cerebellar Neurons in the Absence of Co-culture. *Front Bioeng Biotechnol* **2020**, *8*, 70. DOI: 10.3389/fbioe.2020.00070.

(46) Clark, B. A.; Monsivais, P.; Branco, T.; London, M.; Häusser, M. The site of action potential initiation in cerebellar Purkinje neurons. *Nature neuroscience* **2005**, *8* (2), 137-139. DOI: 10.1038/nn1390.

(47) Masoli, S.; Solinas, S.; D'Angelo, E. Action potential processing in a detailed Purkinje cell model reveals a critical role for axonal compartmentalization. *Frontiers in Cellular Neuroscience* **2015**, *9*, 47. DOI: 10.3389/fncel.2015.00047.

(48) Bhat, R.; Xue, Y.; Berg, S.; Hellberg, S.; Ormo, M.; Nilsson, Y.; Radesater, A. C.; Jerning, E.; Markgren, P. O.; Borgegard, T.; Nylof, M.; Gimenez-Cassina, A.; Hernandez, F.; Lucas, J. J.; Diaz-Nido, J.; Avila, J. Structural insights and biological effects of glycogen synthase kinase 3-specific inhibitor AR-A014418. *The Journal of biological chemistry* **2003**, *278* (46), 45937-45945. DOI: 10.1074/jbc.M306268200.

(49) de la Torre, A. V.; Junyent, F.; Folch, J.; Pelegrí, C.; Vilaplana, J.; Auladell, C.; Beas-Zarate, C.; Pallàs, M.; Verdaguer, E.; Camins, A. GSK3β inhibition is involved in the neuroprotective effects of cyclin-dependent kinase inhibitors in neurons. *Pharmacological research* **2012**, *65* (1), 66-73. DOI: 10.1016/j.phrs.2011.08.006.

(50) Lee, Y.; Yoon, S. B.; Hong, H.; Kim, H. Y.; Jung, D.; Moon, B. S.; Park, W. K.; Lee, S.; Kwon, H.; Park, J.; Cho, H. Discovery of GSK3beta Inhibitors through In Silico Prediction-and-Experiment Cycling Strategy, and Biological Evaluation. *Molecules* **2022**, *27* (12). DOI: 10.3390/molecules27123825.

(51) Riley, L.; Schirmer, L.; Segura, T. Granular hydrogels: emergent properties of jammed hydrogel microparticles and their applications in tissue repair and regeneration. *Curr Opin Biotechnol* **2019**, *60*, 1-8. DOI: 10.1016/j.copbio.2018.11.001.

(52) Clausen, T.; Khaldi, A.; Zauner, A.; Reinert, M.; Doppenberg, E.; Menzel, M.; Soukup, J.; Alves, O. L.; Bullock, M. R. Cerebral acid—base homeostasis after severe traumatic brain injury. *Journal of neurosurgery* **2005**, *103* (4), 597-607. DOI: 10.3171/jns.2005.103.4.0597.

(53) Chaumeil, M. M.; Valette, J.; Baligand, C.; Brouillet, E.; Hantraye, P.; Bloch, G.; Gaura, V.; Rialland, A.; Krystkowiak, P.; Verny, C.; Damier, P.; Remy, P.; Bachoud-Levi, A.

C.; Carlier, P.; Lebon, V. pH as a biomarker of neurodegeneration in Huntington's disease: a translational rodent-human MRS study. *Journal of cerebral blood flow and metabolism : official journal of the International Society of Cerebral Blood Flow and Metabolism* **2012**, *32* (5), 771-779. DOI: 10.1038/jcbfm.2012.15.

(54) Anderson, R. L.; Merkler, D. J. N-FATTY ACYLGLYCINES: UNDERAPPRECIATED ENDOCANNABINOID-LIKE FATTY ACID AMIDES? *J Biol Nat* **2017**, *8* (4), 156-165. From NLM.

(55) Guvendiren, M.; Lu, H. D.; Burdick, J. A. Shear-thinning hydrogels for biomedical applications. *Soft Matter* **2012**, *8* (2), 260-272. DOI: 10.1039/c1sm06513k.

(56) Grevesse, T.; Dabiri, B. E.; Parker, K. K.; Gabriele, S. Opposite rheological properties of neuronal microcompartments predict axonal vulnerability in brain injury. *Sci Rep* **2015**, *5*, 9475. DOI: 10.1038/srep09475.

(57) Leipzig, N. D.; Shoichet, M. S. The effect of substrate stiffness on adult neural stem cell behavior. *Biomaterials* **2009**, *30* (36), 6867-6878. DOI: 10.1016/j.biomaterials.2009.09.002.

(58) Ali, S.; Wall, I. B.; Mason, C.; Pelling, A. E.; Veraitch, F. S. The effect of Young's modulus on the neuronal differentiation of mouse embryonic stem cells. *Acta Biomater* **2015**, *25*, 253-267. DOI: 10.1016/j.actbio.2015.07.008.

(59) Lamprecht, R. Actin Cytoskeleton Role in the Maintenance of Neuronal Morphology and Long-Term Memory. *Cells* **2021**, *10* (7). DOI: 10.3390/cells10071795.

(60) Liz, M. A.; Mar, F. M.; Santos, T. E.; Pimentel, H. I.; Marques, A. M.; Morgado, M. M.; Vieira, S.; Sousa, V. F.; Pemble, H.; Wittmann, T.; Sutherland, C.; Woodgett, J. R.; Sousa, M. M. Neuronal deletion of GSK3β increases microtubule speed in the growth cone and enhances axon regeneration via CRMP-2 and independently of MAP1B and CLASP2. *BMC Biology* **2014**, *12* (1), 47. DOI: 10.1186/1741-7007-12-47.

(61) Cuesto, G.; Jordan-Alvarez, S.; Enriquez-Barreto, L.; Ferrus, A.; Morales, M.; Acebes, A. GSK3beta inhibition promotes synaptogenesis in Drosophila and mammalian neurons. *PLoS One* **2015**, *10* (3), e0118475. DOI: 10.1371/journal.pone.0118475.

(62) Reddy, P. H. Amyloid beta-induced glycogen synthase kinase 3beta phosphorylated VDAC1 in Alzheimer's disease: implications for synaptic dysfunction and neuronal damage. *chim Biophys Acta* **2013**, *1832* (12), 1913-1921. DOI: 10.1016/j.bbadis.2013.06.012.

(63) Khatri, N.; Thakur, M.; Pareek, V.; Kumar, S.; Sharma, S.; Datusalia, A. K. Oxidative stress: major threat in traumatic brain injury. *CNS & Neurological Disorders-Drug Targets (Formerly Current Drug Targets-CNS & Neurological Disorders)* **2018**, *17* (9), 689-695. DOI: https://doi.org/10.2174/1871527317666180627120501.

(64) Musgrove, R. E.; Helwig, M.; Bae, E.-J.; Aboutalebi, H.; Lee, S.-J.; Ulusoy, A.; Di Monte, D. A. Oxidative stress in vagal neurons promotes parkinsonian pathology and intercellular α-synuclein transfer. *The Journal of Clinical Investigation* **2019**, *129* (9), 3738-3753. DOI: 10.1172/JCI127330.

(65) Smethurst, P.; Risse, E.; Tyzack, G. E.; Mitchell, J. S.; Taha, D. M.; Chen, Y.-R.; Newcombe, J.; Collinge, J.; Sidle, K.; Patani, R. Distinct responses of neurons and astrocytes to TDP-43 proteinopathy in amyotrophic lateral sclerosis. *Brain* **2020**, *143* (2), 430-440. DOI: 10.1093/brain/awz419.

LIST OF PUBLICATIONS

Journals:

1. **Wasnik, K**., et al. Neurogenic and Angiogenic poly(N-Acryloylglycine)-co-(acrylamide)-co-(N-acryloyl-glutamate) Hydrogel: Preconditioning Effect Under Oxidative Stress and use in neuroregeneration. Journal of Materials Chemistry B, 2024.
2. **Wasnik, K**., et al., Poly (N-acryloylglycine-acrylamide) Hydrogel Mimics the Cellular Microenvironment and Promotes Neurite Growth with Protection from Oxidative Stress.ACS Applied Bio Materials, 2023. 6(12): p. 5644-5661.
3. Gupta, P.S.#, **Wasnik, K**.#, et al., Nitric oxide releasing novel amino acid-derived polymeric nanotherapeutic with anti-inflammatory properties for rapid wound tissue regeneration.Nanoscale, 2024. 16(4): p. 1770-1791.
4. Gupta, P.S., **Wasnik, K**., et al., In vivo potential of polymeric N-acryloyl-glycine nanoparticles with anti-inflammatory activities for wound healing. Materials Advances,2023. 4(20): p. 4718-4731.
5. Maity, S., **Wasnik, K**., et al., Facile cost-effective green synthesis of carbon dots: selective detection of biologically relevant metal ions and synergetic efficiency for treatment of cancer. Biomedical Materials, 2024.
6. **Wasnik K**, Mittal P, Ghope P, Sonkar SC, Arora G, Saluja D. Multiple sexually transmitted co-infections are associated with adverse reproductive outcomes in asymptomatic adolescent pregnant women; A Prospective cohort study. Frontiers in Medicine. 2022;9. (IF:5.091)
7. Amgoth, C.; Patra, S.; **Wasnik, K**.; Maity, P.; Paik, P., Controlled synthesis of thermosensitive tunable porous film of (pNIPAM)-b-(PCL) copolymer for sustain drug delivery. Journal of Applied Polymer Science, e53854.(IF 3.125)

8. Pandey M, **Wasnik K**, Gupta S, Singh M, Patra S, Gupta P, et al. Targeted specific inhibition of bacterial and Candida species by mesoporous Ag/Sn–SnO 2 composite nanoparticles: in silico and in vitro investigation. RSC advances. 2022;12(2):1105-20.(IF:4.036)
9. Panigrahi G, Medhi H, **Wasnik K**, Patra S, Gupta P, Pareek D, et al. Hollow mesoporous SiO2–ZnO nanocapsules and effective in vitro delivery of anticancer drugs against different cancers with low doses of drugs. Materials Chemistry and Physics. 2022;287:126287.(IF:4.094)
10. Maity S, Tomar MS, **Wasnik K**, Patra S, Modak MD, Gupta PS, et al. Azadirachta indica Seed Derived Carbon Nanocapsules: Cell Imaging, Depolarization of Mitochondrial Membrane Potential, and Dose-Dependent Control Death of Breast Cancer. ACS Biomaterials Science & Engineering. 2022.(IF:4.749)
11. Sonkar SC, Arora G, **Wasnik K**, Ali M, Mittal P, Saluja D. Improved management can be achieved by introducing additional parameters in the syndromic diagnosis of nonviral sexually transmitted infections at low-resource settings. AJOG Global Reports.2022;2(1):100037.
12. Patra S, Singh M, **Wasnik K**, Pareek D, Gupta PS, Mukherjee S, et al. Polymeric nanoparticle based diagnosis and nanomedicine for treatment and development of vaccines for cerebral malaria: a review on recent advancement. ACS Applied Bio Materials.2021;4(10):7342-65.(IF:3.25)
13. Pandey M, Singh M, **Wasnik K**, Gupta S, Patra S, Gupta PS, et al. Targeted and enhanced antimicrobial inhibition of mesoporous ZnO–Ag2O/Ag, ZnO–CuO, and ZnO–SnO2 composite nanoparticles. ACS omega. 2021;6(47):31615-31.(IF: 4.132)

14. Amgoth C, Dharmapuri G, Patra S, **Wasnik K**, Gupta P, Kalle AM, et al. 'Plate-like-coral ‘ polymer particles with dendritic structure and porous channels: Effective delivery of anti-cancer drugs. Journal of Applied Polymer Science. 2021;138(19):50386. (IF: 3.057)
15. **Wasnik K**#, Sachdev D#, Patel AL, Sonkar SC, Desai P, Mania-Pramanik J, et al. Multi-centric validation of an in-house-developed beacon-based PCR diagnostic assay kit for Chlamydia and Neisseria and portable fluorescence detector. Journal of medical microbiology. 2018;67(9):1287-93.(IF: 3.196)
16. Sonkar SC, **Wasnik K**, Kumar A, Sharma V, Mittal P, Mishra PK, et al. Evaluating the utility of syndromic case management for three sexually transmitted infections in women visiting hospitals in Delhi, India. Scientific Reports. 2017;7(1):1-9.(IF: 4.996)
17. Sonkar SC, **Wasnik K**, Kumar A, Mittal P, Saluja D. Comparative analysis of syndromic and PCR-based diagnostic assay reveals misdiagnosis/overtreatment for trichomoniasis based on subjective judgment in symptomatic patients. Infectious diseases of poverty.2016;5(03):48-57.(IF:10.485)
18. Purkait B, Singh R, **Wasnik K**, Das S, Kumar A, Paine M, et al. Up-regulation of silent information regulator 2 (Sir2) is associated with amphotericin B resistance in clinical isolates of Leishmania donovani. Journal of Antimicrobial Chemotherapy. 2015;70(5):1343-56.(IF:5.758)

Manuscripts under communication/communicated:

1. **Wasnik** and Paik et al. Chemically Modified RNAs for Regenerative Medicines (review Article), (to be communicated),
2. **Wasnik** and Paik et al. siRNA loaded p(NAPA-co-LME) nanocapsule for the treatment of triple-negative breast cancer, (to be communicated)

Patent Applications:

1. Pradip Paik, Prem Shankar Gupta and **Kirti Wasnik**, A nano-formulation and a method of preparation thereof, **Patent Application No.: 02311051276**, date of filing: 31-07-2023.
2. Pradip Paik, Prem Shankar Gupta, **Kirti Wasnik**, Sukanya Patra, Divya Pareek, A Polymeric Nanoparticle Formulation And A Method Of Preparation Thereof, **Patent Application No.: 202311041625**, June 19, 2023
3. Pradip Paik, **Kirti Wasnik**, Prem Shankar Gupta, Sukanya Patra, Divya Pareek, Gurmeet Singh, A polymeric nano-hydrogel composition and a method of preparation thereof **Patent Application No.: 202311038604**, Date of filing: June 5th, 2023
4. Paik et al. Preparation of carbon nanocapsules from Azadirachta indica seed for the treatment of breast cancer, **Application No.: 202111060434**, dated: December 12, 2022" (Indian)
5. Paik et al. A mesoporous anti-microbial nanocomposite and a method of preparation thereof, **Application No.:202011031802**, dated: July 24, 2020" (Indian)

6. Paik et al. A method of synthesizing carbon dots and a product thereof**, Application No.: 202011018557**, Dated: 30th April 2020 (Indian)

Conference proceedings published:

1. Sonkar SC, Bharti R, **Wasnik K**, Kumar A, Mittal P, et al. P1. 17 Effectiveness of syndormic case managements (SCM) in control of sexually transmitted infection and antibiotic resistance. BMJ Publishing Group Ltd; 2017. DOI:10.1136/sextrans-2017-053264.125
2. Sonkar S, **Wasnik K**, Kumar A, Mittal P, Saluja D. O10. 3 Low effectiveness of syndromic diseases management in women infected with chlamydia trachomatis, trichomonas vaginalis and neisseria gonorrhoeae leads in delhi india. BMJ Publishing Group Ltd; 2015.DOI:10.1136/sextrans-2015-052270.134
3. Sonkar S, **Wasnik K**, Mishra P, Mittal P, Kumar A, Suri J, et al. Prevalence and co-infection study of Chlamydia trachomatis, Neisseria gonorrhoeae, and Trichomonas vaginalis among symptomatic women using PCR assay. BMC Infectious Diseases.2014;14(3):1-. DOI: 10.1186/1471-2334-14-S3-P5
4. Ghope P, Sonkar SC, **Wasnik K**, Mittal P, Saluja D. Prevalence of Chlamydia trachomatis, Neisseria gonorrhoeae and Trichomonas vaginalis infection in pregnant adolescent women and its association with pregnancy outcomes. BMC Infectious Diseases. 2014;14(3):1-.DOI:10.1186/1471-2334-14-S3-E33

Book chapters:

1. Sukanya Patra#, Monika Singh#, Divya Pareek, **Kirti Wasnik**, Prem Shankar Gupta, Pradip Paik*, 2022, *Advances in the Development of Biodegradable Polymeric Materials for Biomedical Applications*. In: Hashmi, M.S.J. (ed.)

Encyclopedia of Materials: Plastics and Polymers, vol. 4, pp. 532–566. Oxford: Elsevier.

2. Prem Shankar Gupta#, **Kirti Wasnik**#, Sukanya Patra, Divya Pareek, Monika Singh,Somedutta Maity, Monica Pandey, Pradip Paik*, 2022, *A Review on Biodegradable Polymeric Materials for Bone Tissue Engineering (BTE) Applications*. In: Hashmi, M.S.J.(ed.) Encyclopedia of Materials: Plastics and Polymers, vol. 4, pp. 498–531. Oxford: Elsevier.
3. Singh M, Patra S, Pareek D, **Wasnik K**, Gupta PS, Maity S, et al. *Polymer Nanoparticles and their Biomedical applications. Springer Nature*. (Submitted after review, Dec. 2022).

Poster presented and conference proceedings:

1. ICONC 2022. Oral presentation: Novel Nanopolymer: Synthesis Characterization And Application For Cancer Treatment Without Conventional Drugs Jamia Millia Islamia, Date:28-30th Nov 2022
2. ICONC 2022. Poster: Delivery of nitric oxide through polymer nanoparticles for chronic wound healing, Jamia Millia Islamia, Date: 28-30th Nov 2022
3. ICDD 2022. Novel Nanopolymer for poor prognosis cancer treatment without Conventional Drugs in heparanase driven malignancies, BITS Pilani, K. K. Birla Goa Campus and 6 Schrodinger, 10-11th November 2022
4. MACRO-SPSI 2022. Poster: Anti-tumorigenic characteristics of poly (N-Acryloyl-glycine-acrylamide) co-polymeric hydrogel NCL-Pune, 2-4th November 2022.
5. MACRO-SPSI 2022: Poster: Nitric oxide realising polymer for wound healing, NCL-Pune, 2-4th November 2022.

6. Advanced functional materials; future perspectives 2022. Gas therapy for chronic wound healing, Dr. B. R. Ambedkar, National Institute of Technology Jalandhar. 6-8th August, 2022(Awarded Best poster).

Appendix-1:

Supporting Information

CHAPTER 3: Results and Discussion (Part-I)

Poly(N-acryloylglycine-acrylamide) hydrogel mimics the cellular microenvironment and promotes neurite growth with protection from oxidative stress

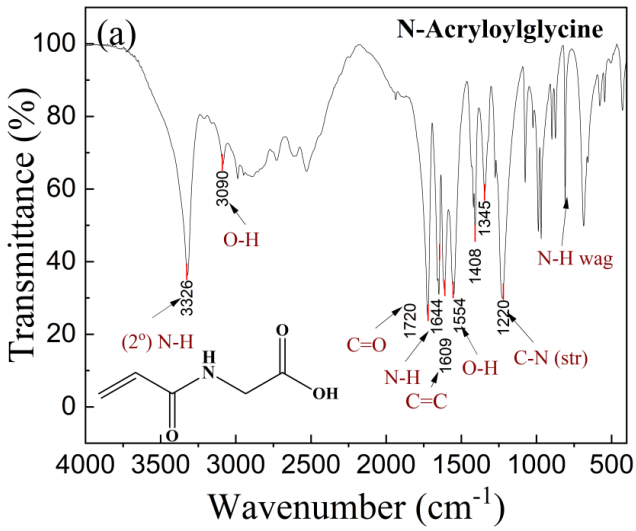

S3.1. 1 FTIR Spectrum of N-acryloylglycine (NAG) monomer.

FTIR spectrum for NAG is shown in Fig.S1 (a) and confirmed for the presence of amine -N-H (stretching) at 3319 cm^{-1} with additional bands appeared at 3083 cm^{-1}, 1720 cm^{-1}, 1706 cm^{-1}, 1658 cm^{-1}, 1616 cm^{-1} and 1213 cm^{-1} are due to the -O-H stretching of carboxylic acid group, C=O (carbonyl) stretching of C=O of carboxylic acid, a 1st overtone of ─NH, C=C associated of α, β-unsaturated ketone, and due to the presence of -C-N stretching.

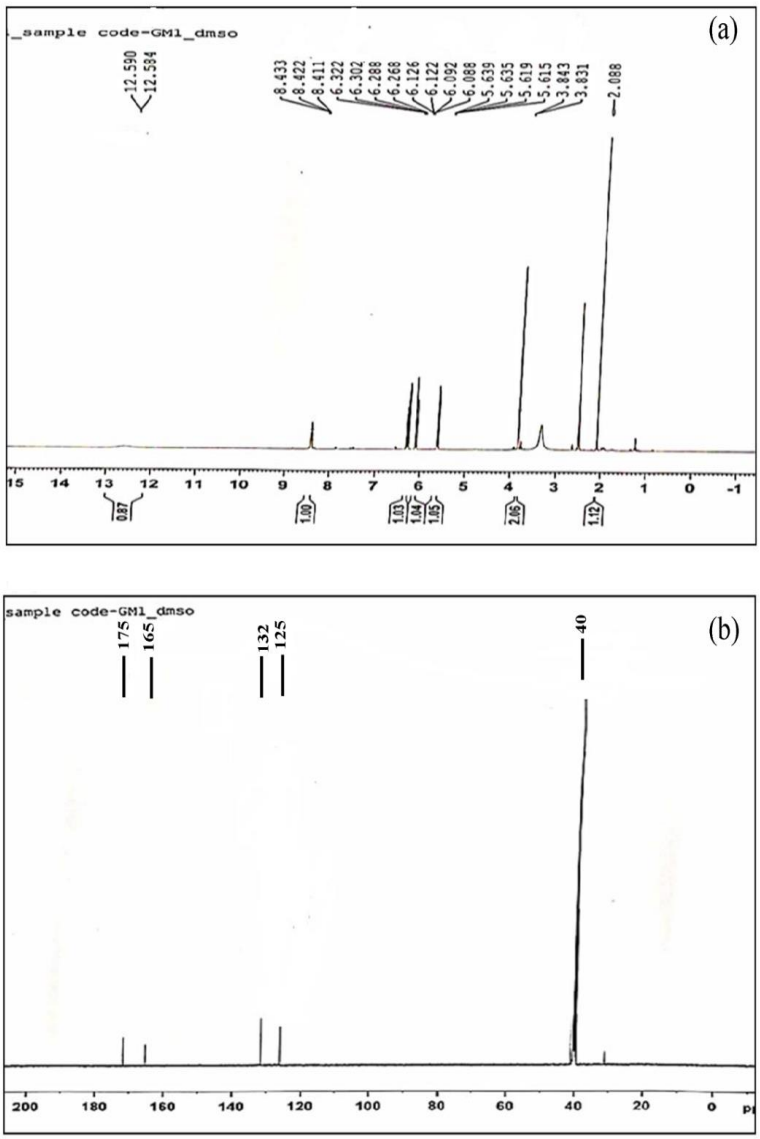

*S3.1. 2 [1]H NMR and [13]C NMR (a) [1]H NMR of N-acryloylglycine monomer and(b) [13]C NMR of N-acryloylglycine monomer. Fig. S2(a) shows the H[1] NMR (DMSO-d6) spectrum of NAG with the corresponding chemical shifts (δ in ppm): 12.5 (O─H of carboxylic acid), 8.4 (N─H of 2° amine), 6.1(═C─H_2), 6.3 (cis) and 5.6 (trans) of (H_2C═CH_2), 3.4 for H_2O and 2.5 for DMSO-d_6. [13]C-NMR (Fig. S**3.1.**2(b)) spectrum confirmed the presence of 5 carbon moiety with the corresponding chemical shift at 175 ppm (─COOH), 165 ppm (O═C─NH-R), 125 ppm (─HC-NH), 132 ppm (C═C) and 40 ppm band of DMSO-d_6.*

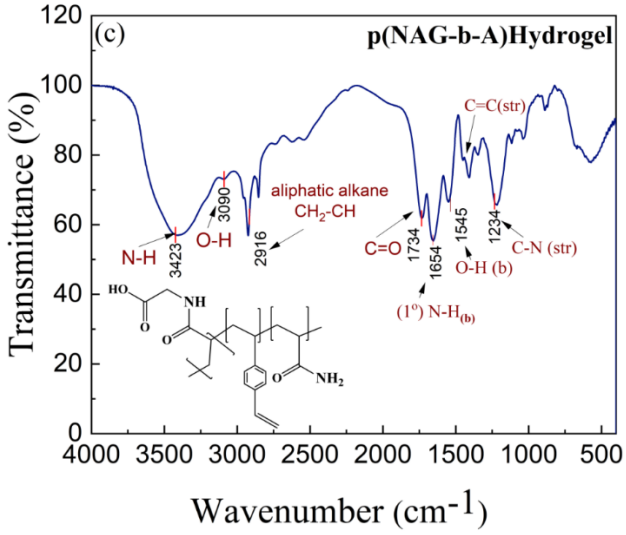

S3.1. 3**.** FTIR Spectrum of poly(N-acryloylglycine-acrylamide) co-polymeric hydrogel.

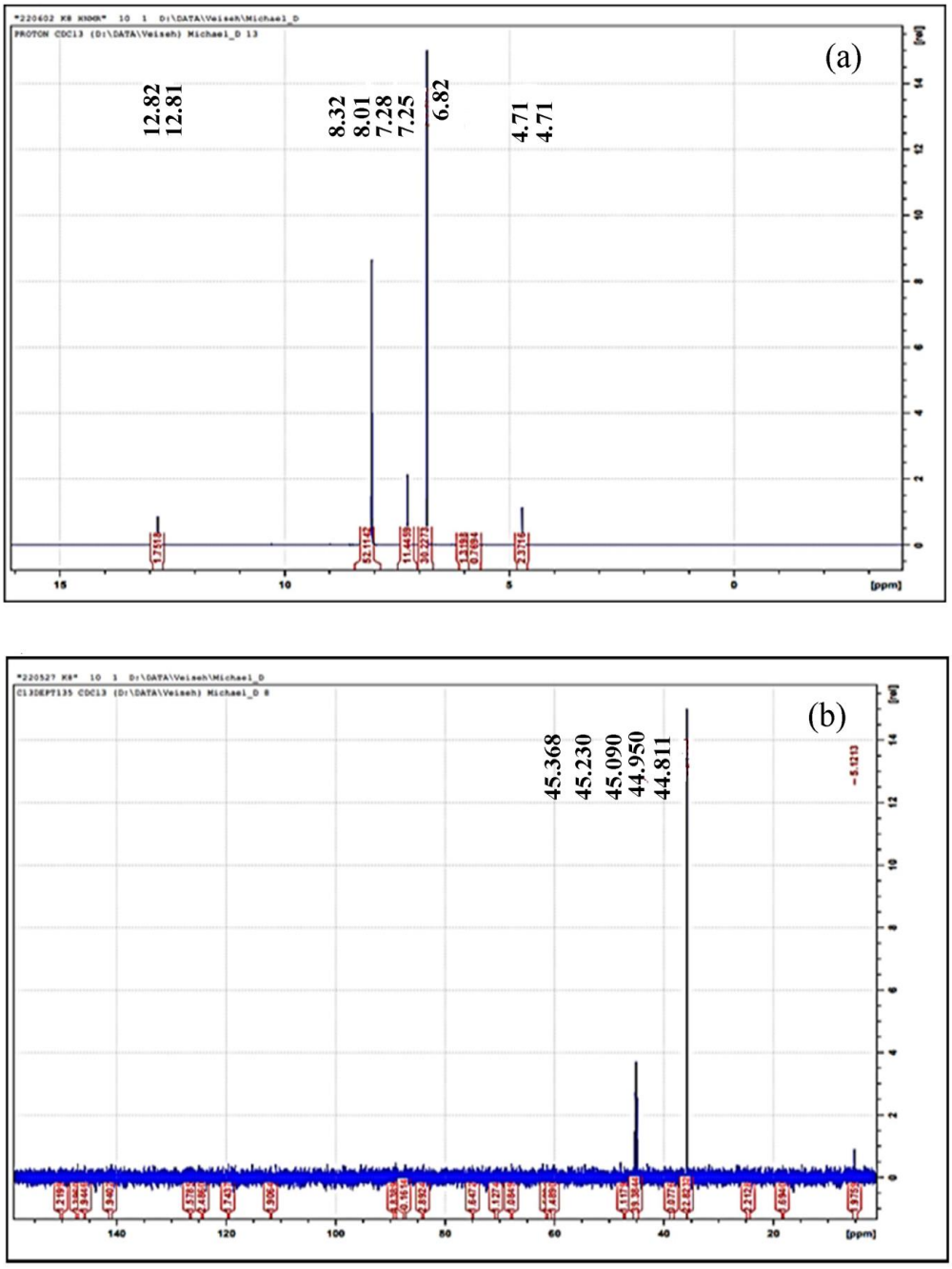

S3.1. 4. (a) H1 NMR of p(NAG-b-A) hydrogel and (b) C13 NMR of p(NAG-b-A)nanohydrogel.

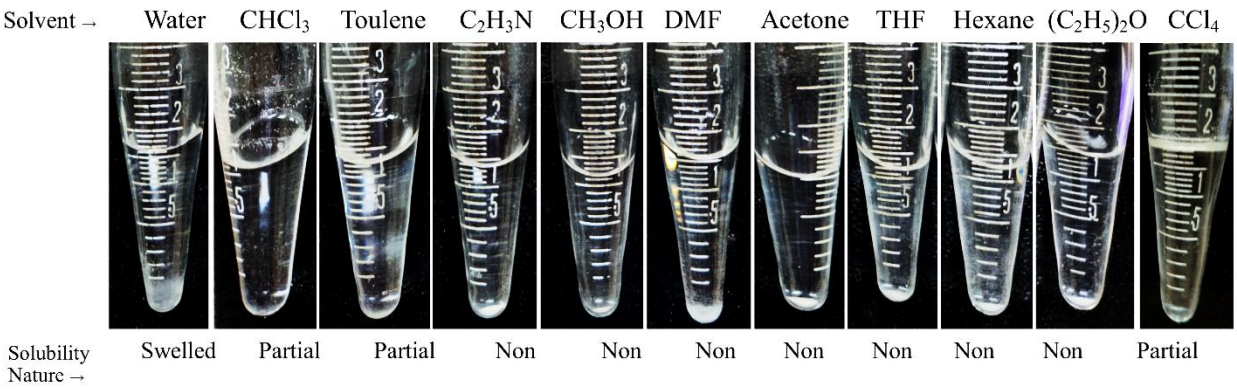

S3.1. 5(a). Solubility test of the p(NAG-b-A) hydrogel in different solvents at room temperature.

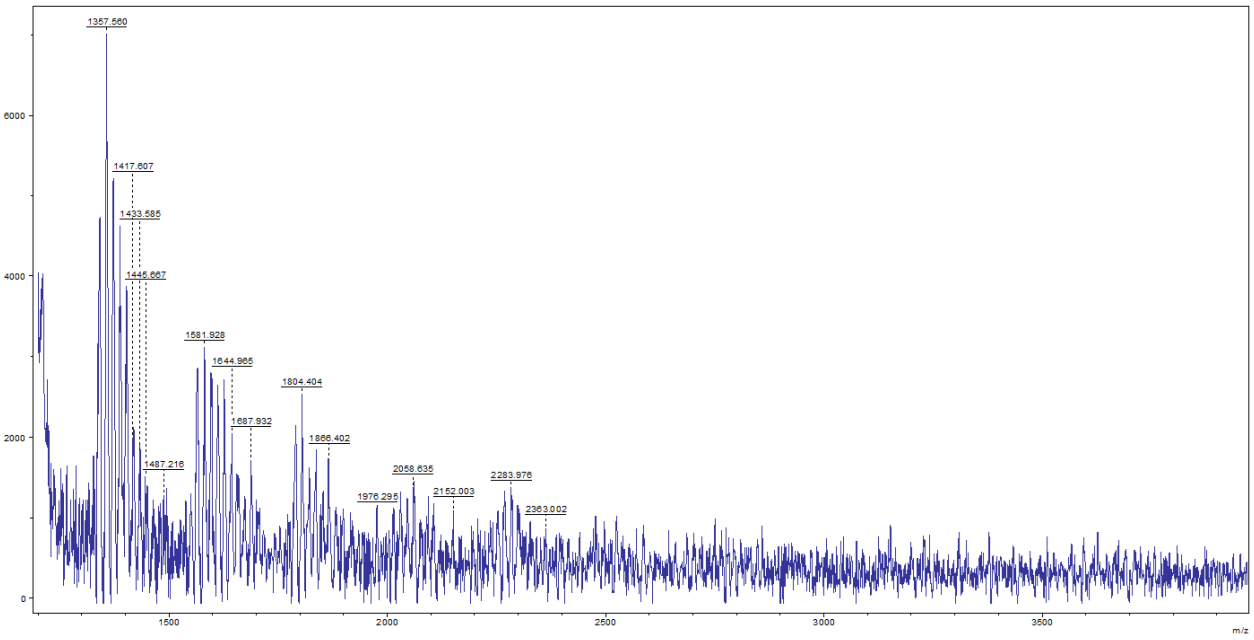

*S3.1. 5(a)**. Shows the molecular weight (MW) distribution of p(NAG-b-A) hydrogel determined by MALDI-ToF spectra (for batch-1)*

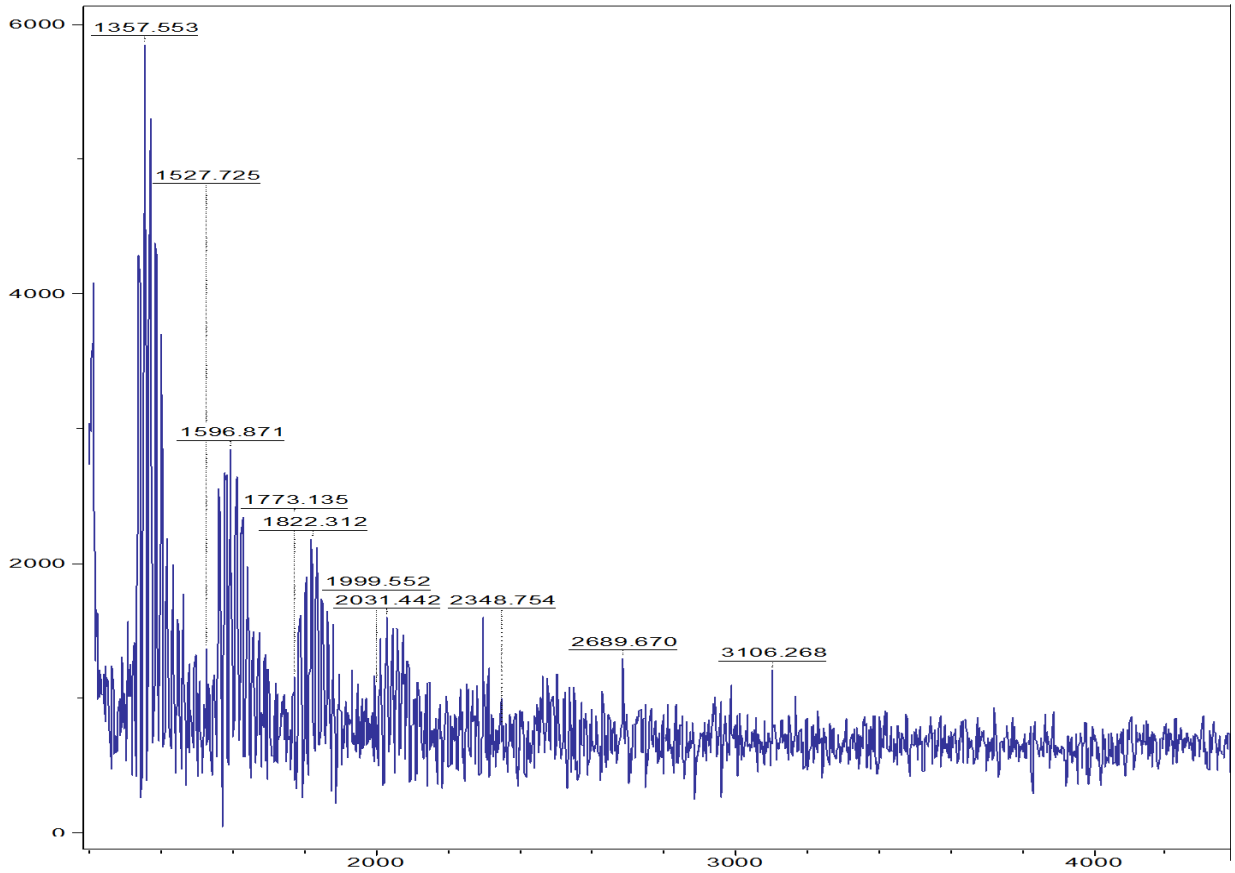

Figure S3.1.5(c). Shows the molecular weight (MW) distribution of p(NAG-b-A) hydrogel determined by MALDI-ToF spectra (for batch-2)

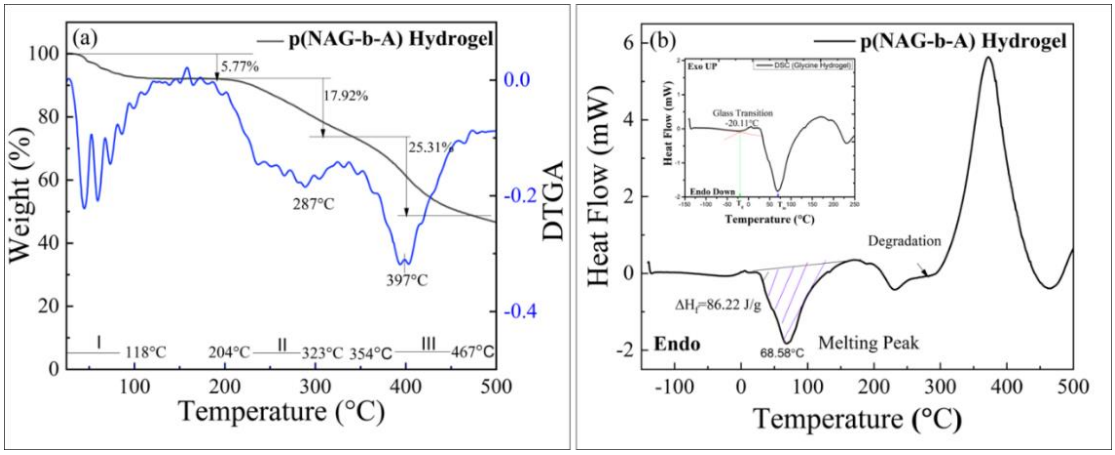

S3.1. 6. Thermal stability and heat flow shown in Fig.(a) represents TGA of p(NAG-b-A) co-polymeric hydrogel and Fig. (b) represents DSC plot of p(NAG-b-A) hydrogel.

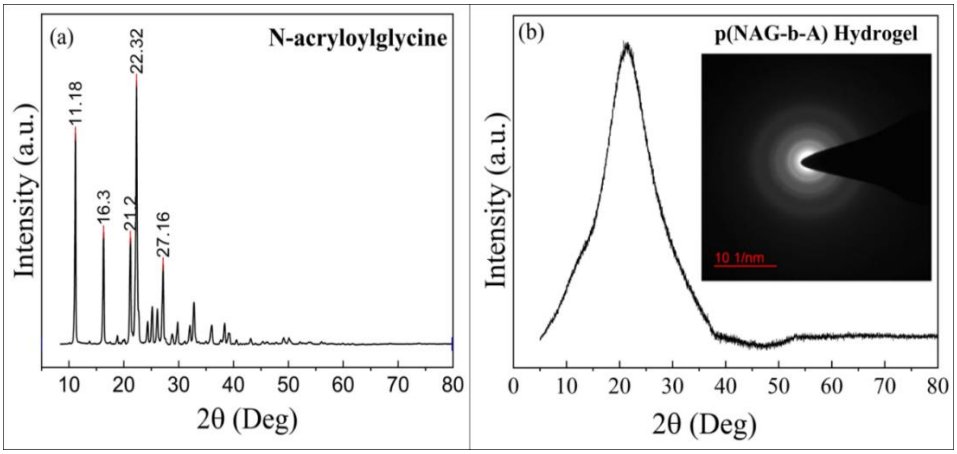

S3.1. 7. (a) XRD pattern of NAG and (b) XRD pattern of p(NAG-b-A).

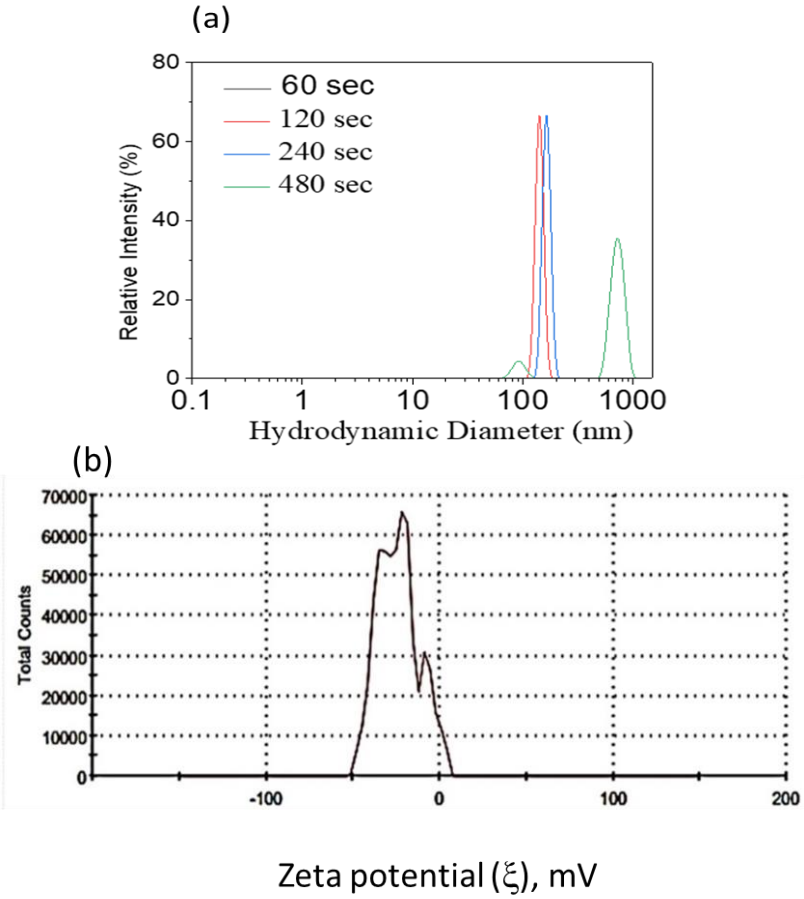

S3.1. 8. (a) Size distribution of p(NAG-b-A) hydrogel NPs and (b) zeta potential (ζ) of p(NAG-b-A) hydrogel in water measured through DLS at room temperature.

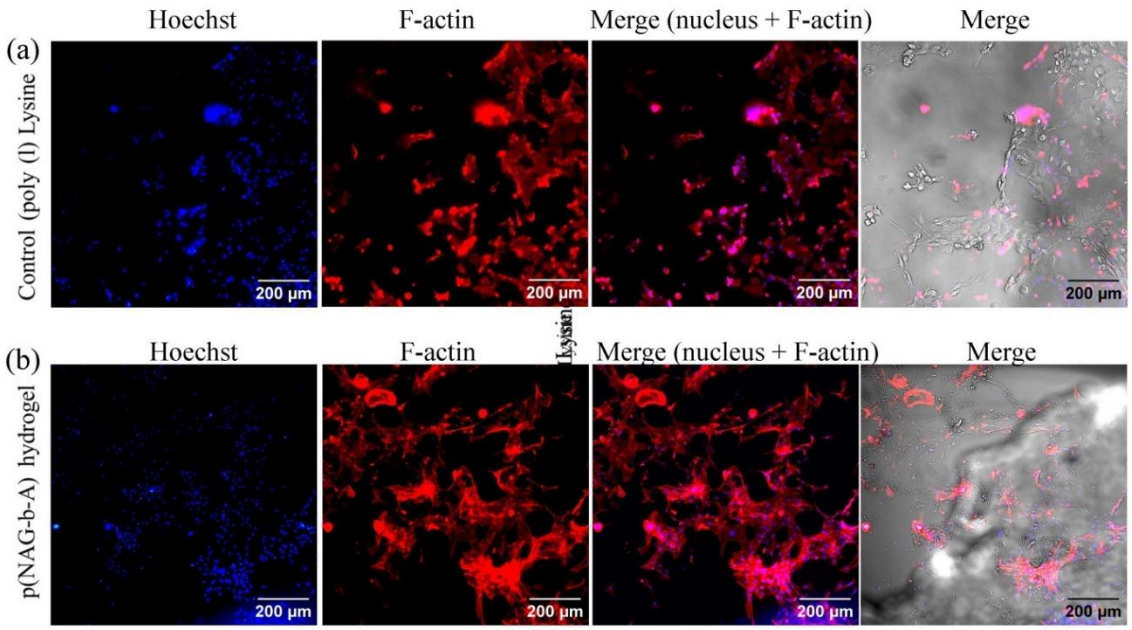

S3.1. 9. Show the actin filament stabilization in primary neuron cultured on Fig. (a) poly (l) lysine coated slide (control) and on Fig. (b) p(NAG-b-A) hydrogel. All fluorescent microscopy images were acquired at 10X and cells were stained with the Hoechst 33258 and immunolabeled with Phalloidin. Images show the merged (Hoechst 33258 + F-actin) and bright field (merged) images.

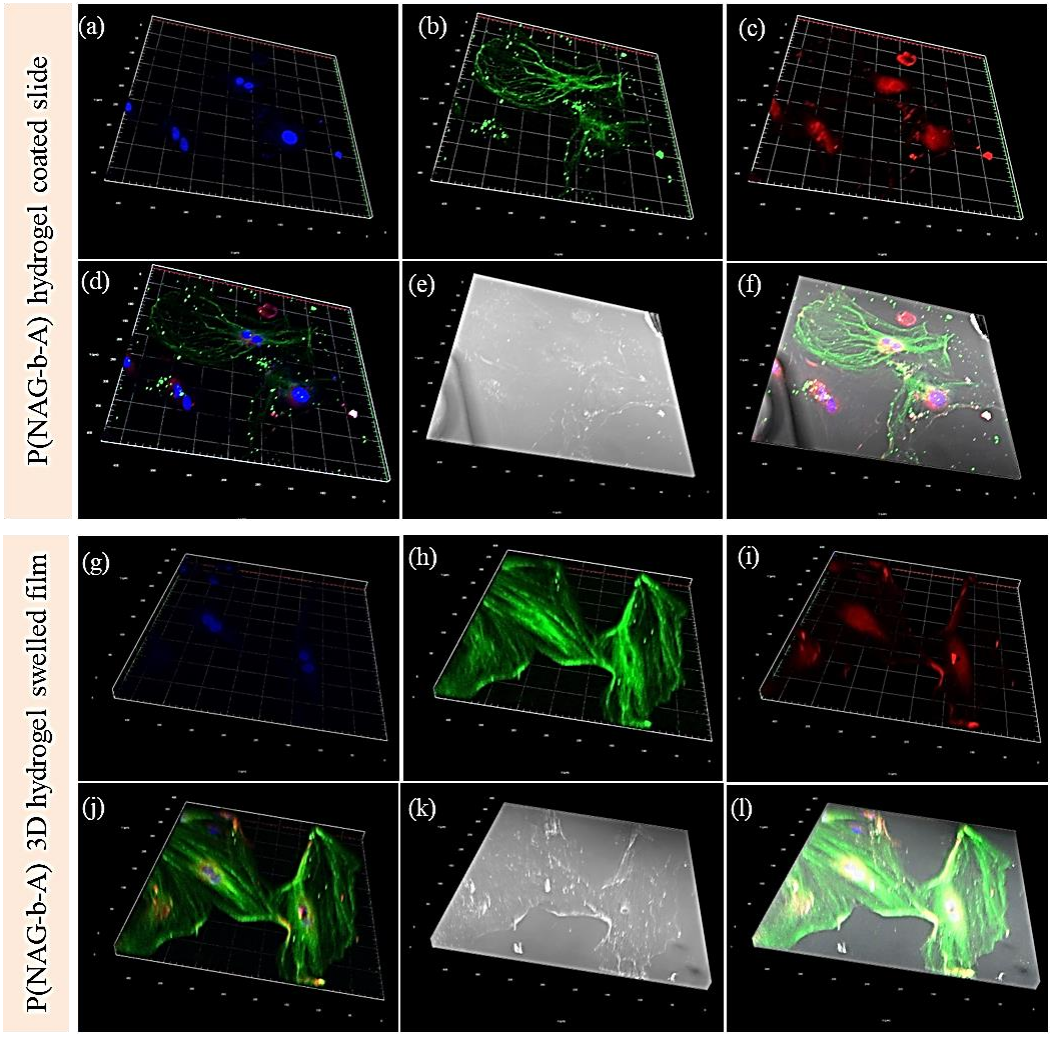

S3.1. 10. Figure shows the 3D orientation of the longer neurite growth on the 2D substrate (Figs. a-f) (for A-group). Figs (g-l) show the neurite growth in longer and deep penetration depth of p(NAG-b-A) hydrogel on 14th Day of culture (B-group sample). Figs. (a) and (g) are for Hoechst 33258 staining of nucleus of neurons, Figs. (b) and (h) for the beta tubulin III immunolabeled hippocampal neurons, Fig. (c) and (i) Phalloidin (red) immunolabeled hippocampal neuron; Figs. (d) and (j) represent the merged images of immunolabeled hippocampal neurons; Figs. (e) and (k) show the bright field images of hippocampal neurons and Figs. (f) and (l) show the merged 3D images of bright field and immunolabeled stained neurons, respectively.

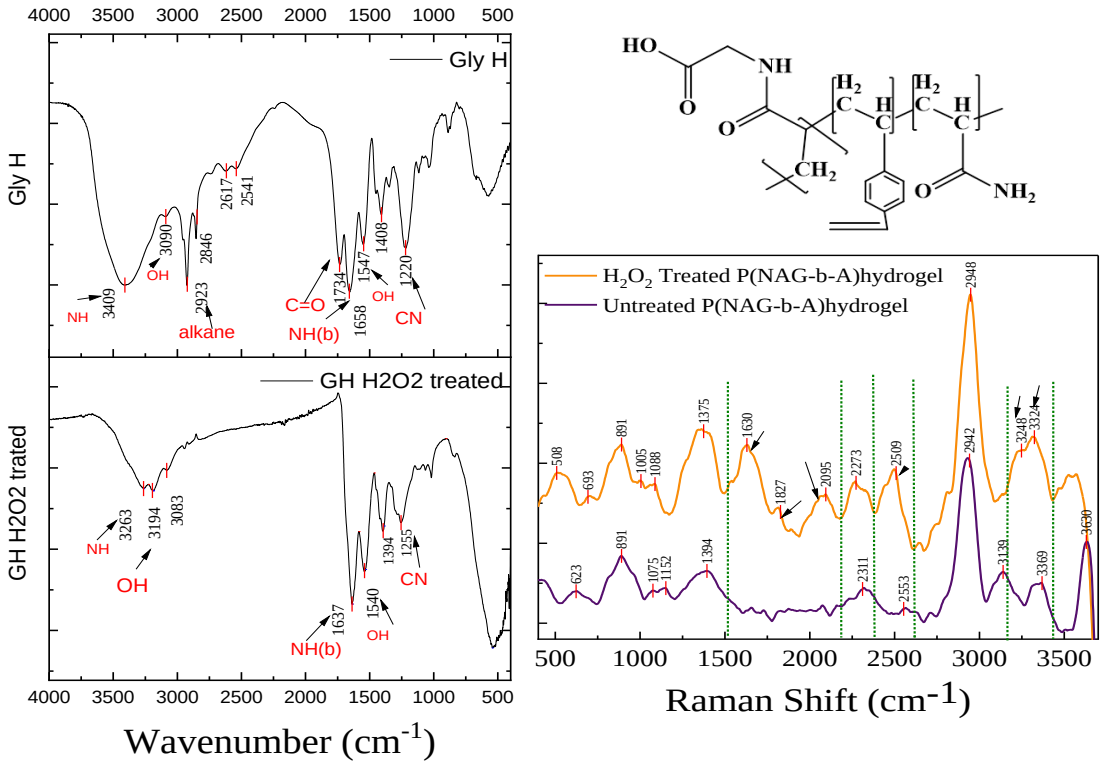

S3.1. 11 FTIR and Raman shift of untreated and H_2O_2 treated p(NAG-b-A) hydrogel

Table S3.1. 1 Molecular interaction between GSK3β and reference inhibitor

S. No.	Ligands	Lowest Binding Energy (kcal.mol^{-1})	Estimated inhibition constant, Ki	Interacting residues
1	TMU	-7.2	5.29μM	VAL135, ARG141(1H) ARG144(2H), GLN185(2H), THR138 (1H), AlA83, TYR134, ASP133, ILE62,
2	SB415286 (C1)	-8.00	1.37 μM	ASP58(1H), THR59(1H), THR57, THR38(1H), TYR56, LYS86(1H), LYS36(1H)
3	SB415286 (C2)	-6.9	7.48 μM	VAL135(1H), ASP133(1H), GLN185(1H), ASN64,GLY63, ASN186, THR138, LEU188, TYR134, ALA83, ASP200, ILE62, LYS85VAL70

4	SB216763	-7.6	5.09μM	ARG96(2H), GLY202(1H), GLN89, PHE93, ASN95, LYS94, LEU88, GLU97

TMU: N-(4-Methoxybenzyl)-N'-(5-nitro-1,3-thiazol-2-yl)urea

SB415286: 3-(3-chloro-4-hydroxyphenylamino)-4-(2-nitrophenyl)-1H-pyrrole-2,5-dione,

SB216763: 3-(2,4-Dichlorophenyl)-4-(1-methyl-1H-indol-3-yl)-1H-pyrrole-2,5-dione).

Table S3.1. 2 Molecular interaction of GSK3β (Glycogen synthase kinase-3) with polymeric units

S.No.	Ligands	Lowest Binding Energy (kcal.mol^{-1})	Estimated inhibition constant, Ki	Interacting residues
1.	Glycine	-3.62	2.22 mM	Lys205, Val214
2.	N-Acryloylglycine (G)	-4.77	318.04 uM	Arg96(1H), Gly202, Ser203, Arg180(1H), Asn213, Val214(1H), Lys205(1H)
3.	N-Acryloylglycine-Acrylamide (GA)	-8.38	715.40 nM	Asp105, His106(1H), Leu104, Val110, Ile109, Met101, Gln46, Leu112, Arg111
4.	Dipeptide (G-G)	-11.26	5.58 nM	Gln46(1H), Leu112, Asp105, His106(1H), Leu104, Ile109, Val110, Arg111, Met101
5.	Acrylamide- Acrylamide (A-A)			Ala83, Asp133, Leu188, Val135, Tyr134
6.	Tripeptide (G-G-G)	-12.67	512.32 pM	Ala83, Lue132, Cys199, Tyr134, Ile62, Leu188, Val135, Asp133, Val110
7.	Tripeptide (A-A-G)	-7.48	3.26 uM	Tyr134, Asp133, Ile62, Pro136, Glu137, Leu188, Thr138, Val135, Ala83
8.	Tripeptide (A-G-G)	-9.31	148.61 nM	Arg111, Gln46(1H), Asp105, His106, Ile109, Val110, Leu104, Met101, Leu112(1H)
9.	Tripeptide (G-A-G)	-10.99	8.73 nM	Met101, Leu112, Gln46, Arg111, His106(1H), Asp105, Ile109, Val110, Leu104

(G: N-Acryloyl glycine, A: Acrylamide)

Appendix-2

Supporting information

Modulation Of P(NAG-b-Ac) Bio-Polymer By Glutamate To Synthesize For Poly (N-Acryloyl Glycine)-Co-(Acrylamide)-(N-Acryloyl Glutamate) For Angiogenesis And Neuroregeneration.

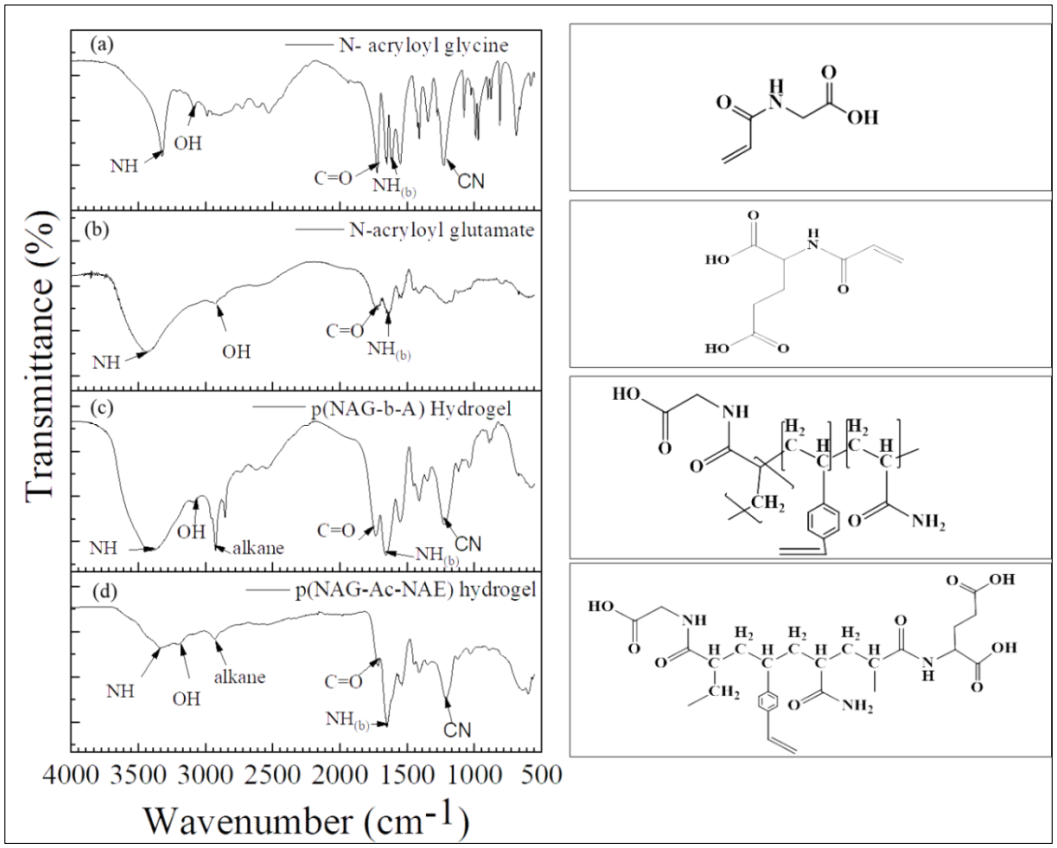

S3.2 1. (a) FTIR spectra of N-acryloylglycine, (b) N-acryloylglutamic acid, (c) poly [(N-acryloylglycine)-b-(acrylamide)] (d) poly(N-acryloylglycine)-co-(acrylamide)-co-(N-acryloylglutamate) co-polymeric hydrogel.

For N- acryloylglycine**,** FTIR performed with KBr (Figure S**3.2.**1(a)): 3323 cm^{-1} (N-H (stretching), 3092 cm^{-1} (-O-H stretching), 1716 cm^{-1} (C=O (carbonyl) stretching), 1549 cm^{-1} (-

O-H overtone), 1653 cm^{-1} (1^{st} overtone of ─NH), 1613 cm^{-1} (C=C α,β-unsaturated ketone and due to the presence of of amine).

Fig. S**3.2.**1(b): N- acryloylglutamaic FTIR performed in KBr: 3413 cm^{-1} (N-H (stretching)), 2912 cm^{-1} and 1408 cm^{-1} (─O─H stretching(hump); bending carboxylic acid), 1716 cm^{-1} (C=O (carbonyl) stretching), 1549 cm^{-1} (-O-H overtone), 1626 cm^{-1} (─NH_2), 1613 cm^{-1} (C=C α, β-unsaturated ketone, and due to the presence of amine).

Fig. S**3.2.**1(c): poly [(N-acryloyl glycine)-co-(acrylamide)-co-(N-acryloylglutamate)] nanohydrogel (p(NAG-Ac-NAE)) functional group analysis was performed through the ATR method: 3336 cm^{-1} (N─H (stretching)), 3182 cm^{-1} (─O─H stretching; strong broad carboxylic acid), 2912 (C─H stretching, conform the formation of polymer chain chain) 1716 cm^{-1} (–C═O (carbonyl) stretching), 1549 cm^{-1} (─O─H overtone), 1653 cm^{-1} (1^{st} overtone of ─NH).

FTIR results of poly(N-Acryloylglycine)-co-(acrylamide)-co-(N-acryloylglutamate) hydrogel has been discussed in the main texts of the manuscript

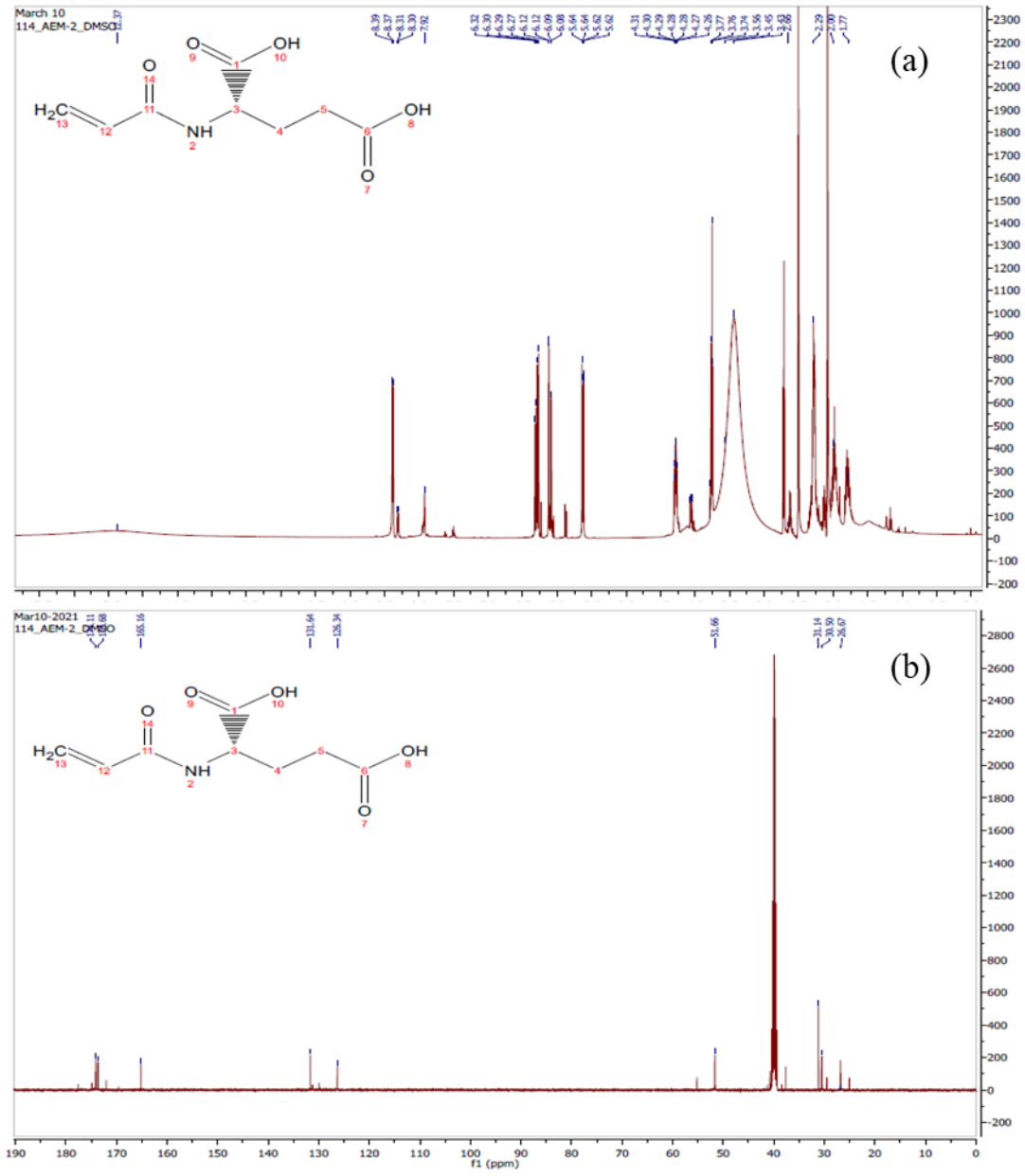

S3.2 2. (A) [1]H NMR of N-acryloylglutamate monomer and (B) [13]C NMR of N-acryloylglycine monomer

[1]H NMR spectrum chemical shifts (in ppm) (Fig. S**3.2.**2(a)): 12.5 δ (O─H of carboxylic acid (8[th] and 12[th] position)), 8.37 δ (N─H of 2° amines (2)), 6.13 δ (═C─H_2(13)), 6.13 δ (cis) and 5.64 δ (trans) of (H_2C═CH_2 (13 and 12)), 6.17 (─CH (12)), 4.29 δ (─CH (3)), 1.99 δ (─C─H_2 (4a and 4b)), 2.20 δ (─C─H_2 (5a and 5b)) 3.4 δ for H_2O and 2.5 for DMSO-d_6.

[13]C NMR (500MHz, DMSO-d_6) (Figure S**3.2.**2 (b)): 174 and 173 ppm (─COOH (1 and 6)), 165 ppm (O═C─NH-R (11)), 126 ppm and 132ppm (C═C (13 and 12)) and 51.66 ppm (─CH (3)), 26.67 ppm 31.14 ppm (─CH_2─CH_2 (4 and 5)) 40 ppm band of DMSO-d_6

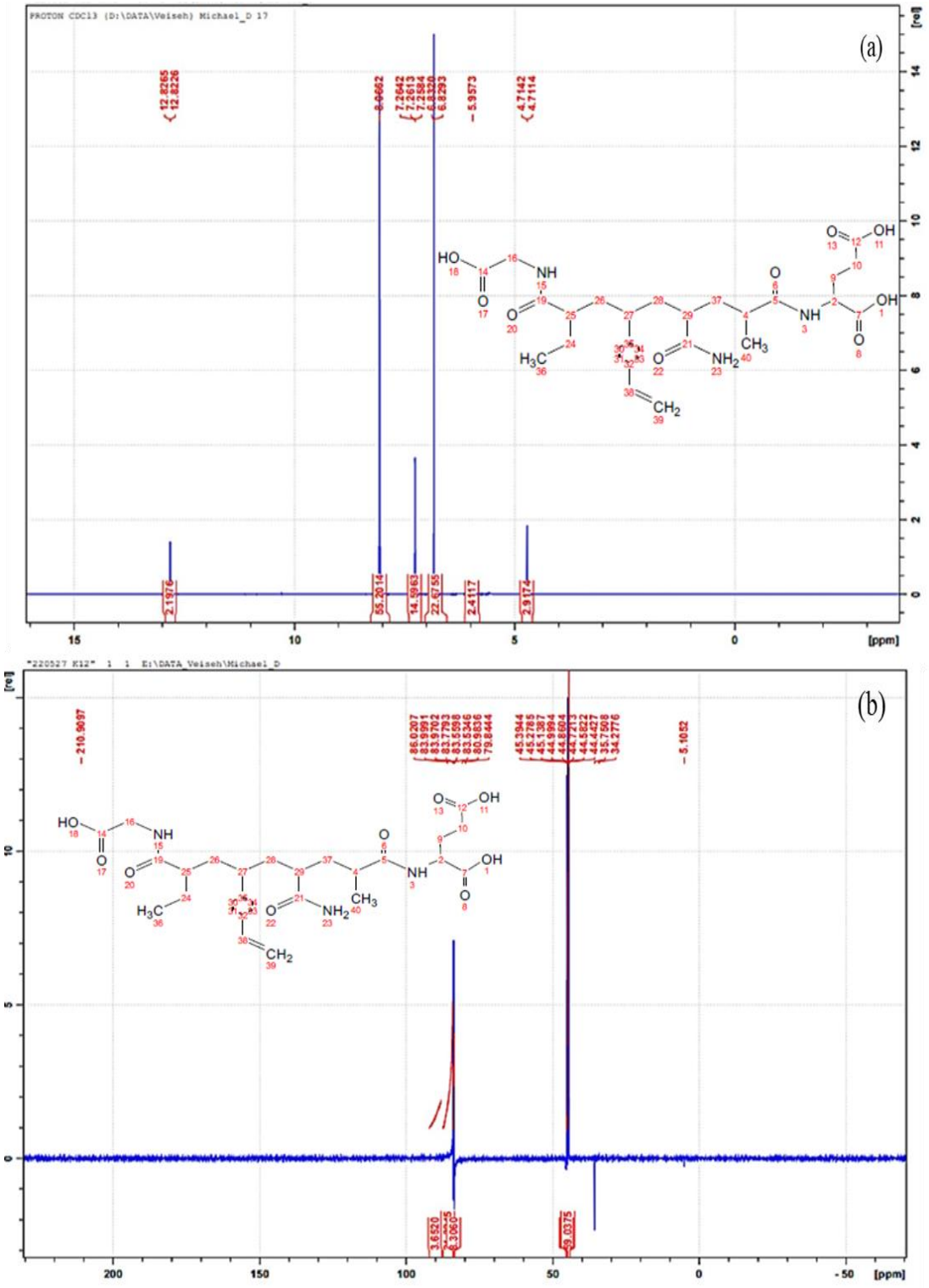

S3.2 3. (A) ^{1}H NMR of p(NAG-Ac-NAE) nanohydrogel and (B) ^{13}C NMR of p(NAG-Ac-NAE)) nanohydrogel.

Disappearance and shifting of peak observed in ^{1}H NMR and ^{13}C NMR. For ^{1}H NMR spectrum chemical shifts (in ppm; $CDCl_3$ and DMSO-d_6) (Figure S**3.2.**3(a)): 12.5 δ (O─H of carboxylic acid, 8.9 δ (N─H of 2° amine), 7.26 δ (benzene), compound, 6.8 δ (H_2C ═ CH_2), 6.17 (─CH (12))

^{13}C NMR (500 MHz in ppm; $CDCl_3$ and DMSO-d_6)) (Figure S**3.2.**3(b)): 44 and 34 ppm (8+2 splinted peak of 2° alkane) and 86-79 ppm (carboxylic ─OH and ester)

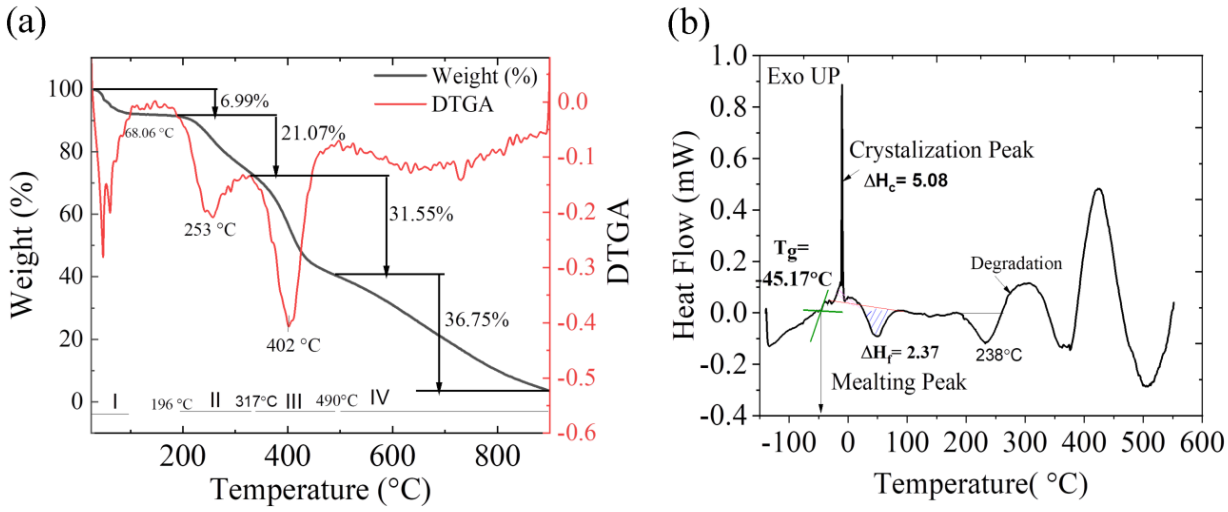

S3.2 4. (a) TGA and (b) DSC of the poly(N-acryloylglycine)-co-(acrylamide)-co-(N-acryloylglutamate) hydrogel.

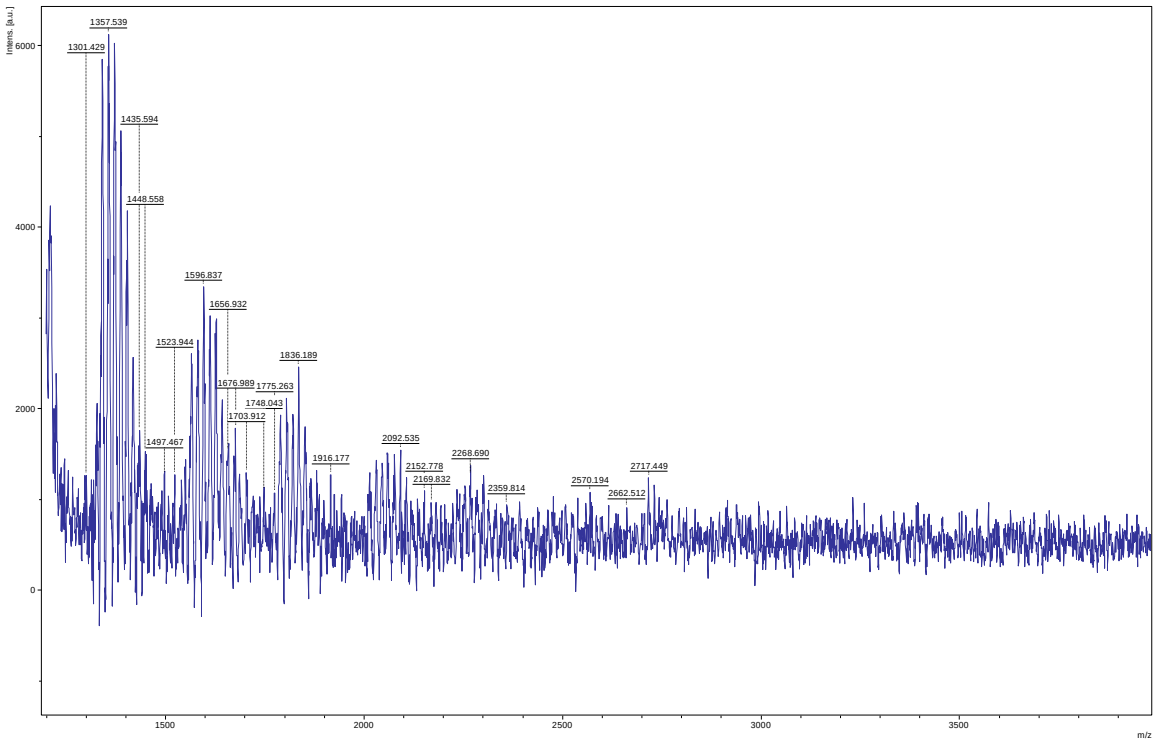

S3.2 5. Shows the MALDI-TOF spectrum of p(NAG-Ac-NAE) hydrogel

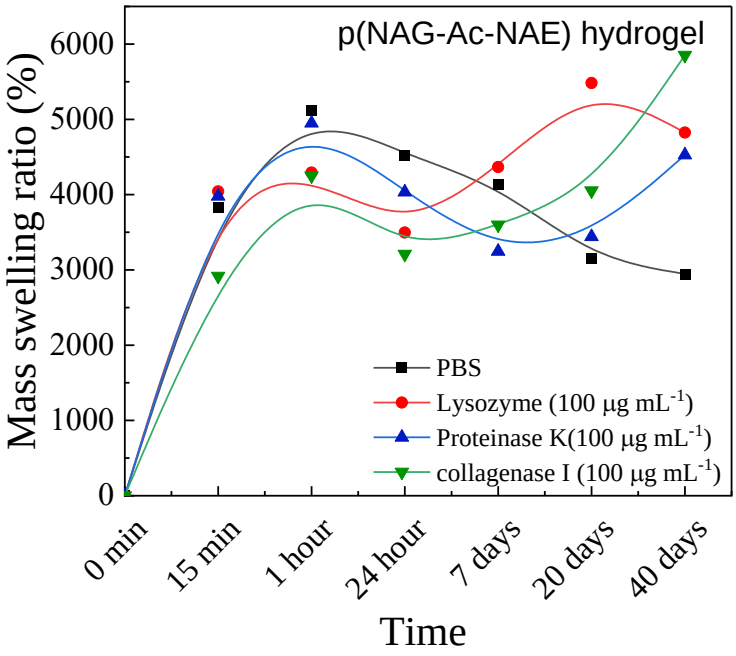

S3.2 6. Biodegradation behavior of [p(NAG-Ac-NAE)] without replacing media, studied in PBS (pH 7.4) and in presence of different enzymes.

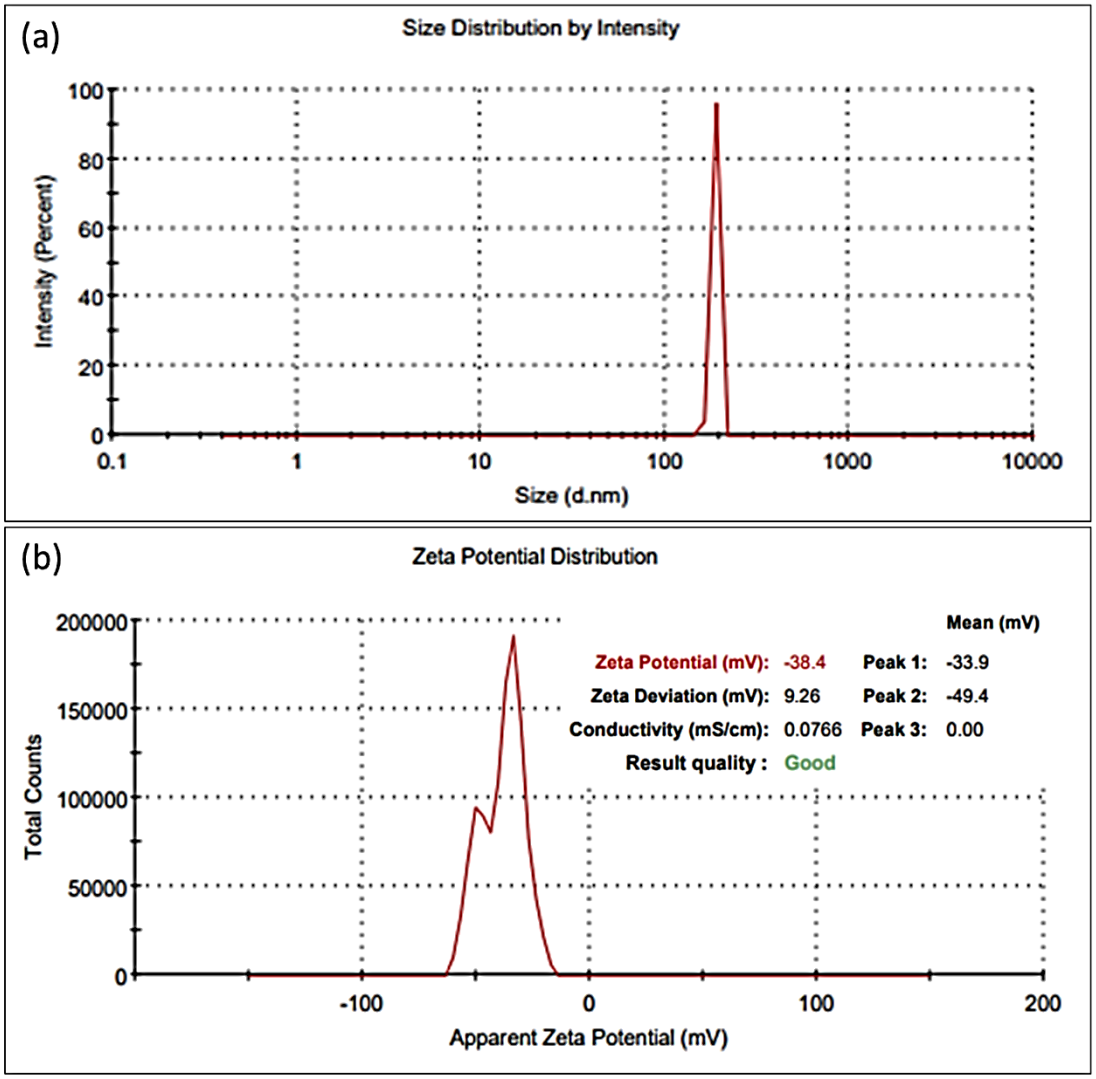

S3.2 7. (a) Size distribution and (b) zeta potential of p(NAG-Ac-NAE) hydrogel, studied in PBS (pH 7.4)

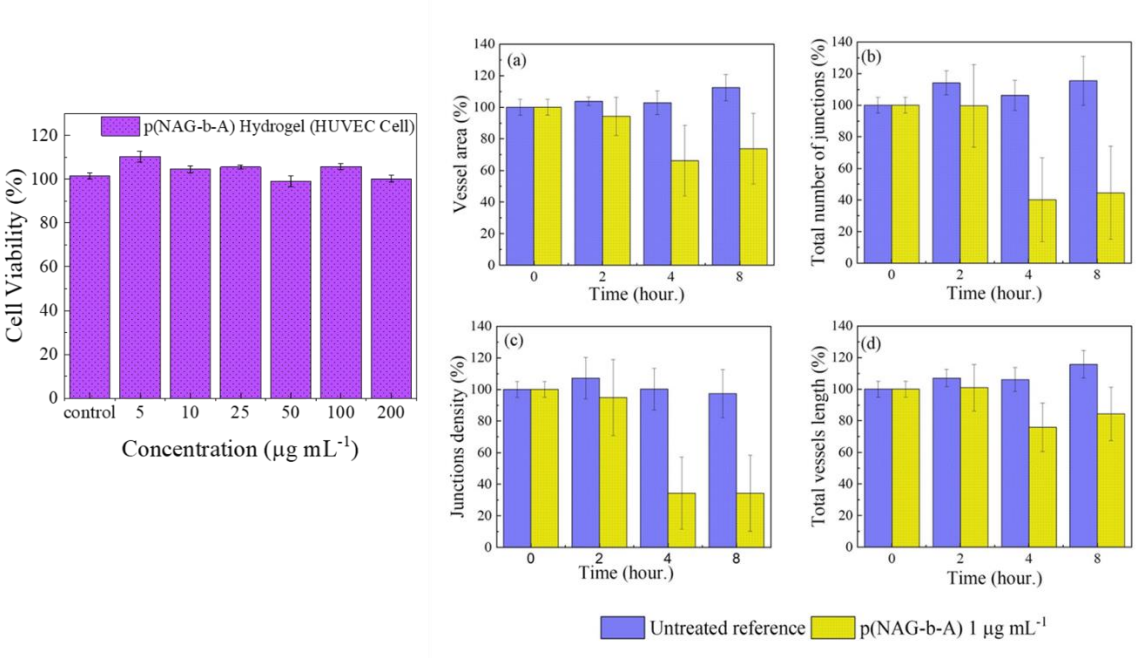

S3.2 8. (a) Cell viability of HUVEC cells in treatment of p(NAG-b-A) hydrogel, (b-e) Anti-angiogenic property of p(NAG-b-A) hydrogel. (a) Vessel area (%) vs Time, (b) Total number of junctions (%) vs Time, (c) Junction density (%) vs time and (d) Total Vessel length (%) vs time.

Table S3.2.1. Bioactivity of random structure of p(NAG-Ac-NAE) obtained through Molinspiration software

Sr.No	p(NAG-Ac-NAE) random series	Protease inhibitor	GPCR ligand	Ion channel modulator	Kinase inhibitor	Nuclear receptor ligand	Enzyme inhibitor
1	N-acryloyl glycine (G)	-1.97	-2.23	-1.72	-2.82	-2.34	-1.62
2	N-acryloyl glutamate €	-0.16	-0.26	-0.06	-0.93	-0.47	0.08
3	G-A-E	0.64	0.26	-0.05	-0.4	-0.09	0.21
4	G-A-E-G	0.48	0.2	-0.1	-0.3	-0.06	0.16
5	G-A-E-E	0.42	0.12	-0.42	-0.42	-0.25	-0.03
6	G-G-E-E	0.24	-0.12	-0.85	-0.77	-0.57	-0.36

Appendix-3

Supporting Document

CHAPTER 3: Results and Discussion (Part-III)

Comparative assessment of glycine, n-acryloyl glycine and glycine based Anti-cancer poly(N-acryloyl glycine-b-acrylamide) hydrogel for its geometric properties and induce cell killing in poor prognosis heparanase driven malignancies through in silico and in vitro approach.

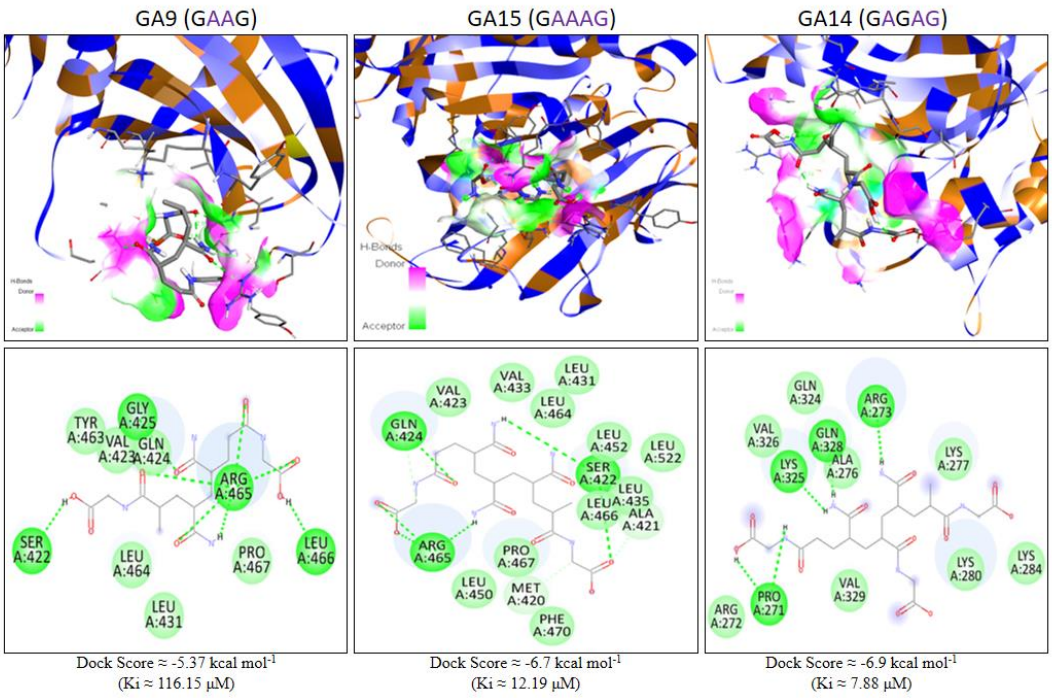

S3.3. 1. Docking poses for complex of GA9, GA15 and GA14

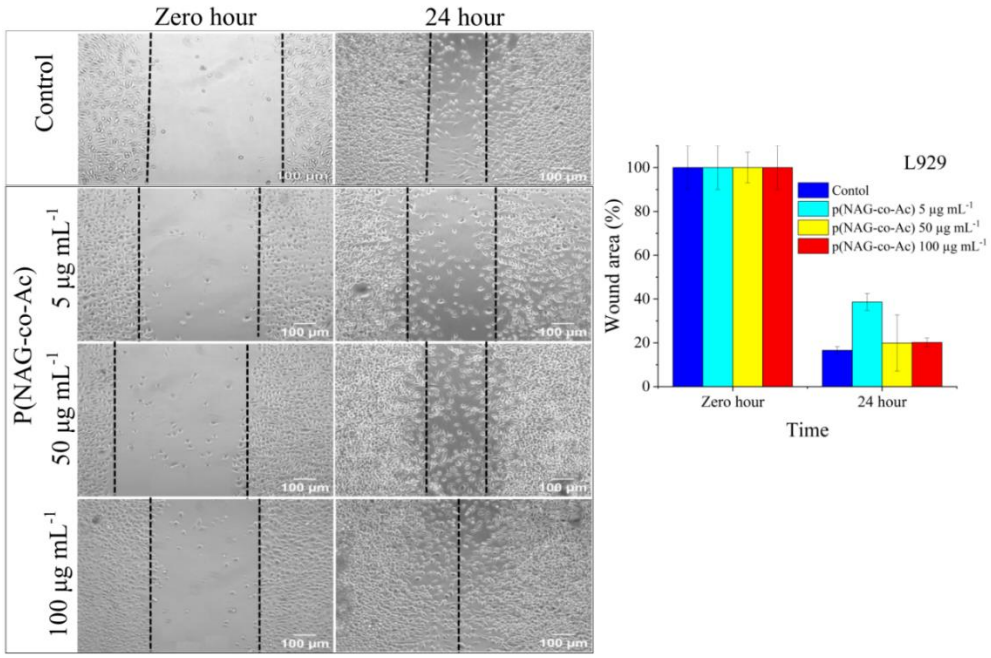

S3.3. 2. wound scratch assay on L929 cell line after treatment with p(Nag-co-Ac) hydrogel

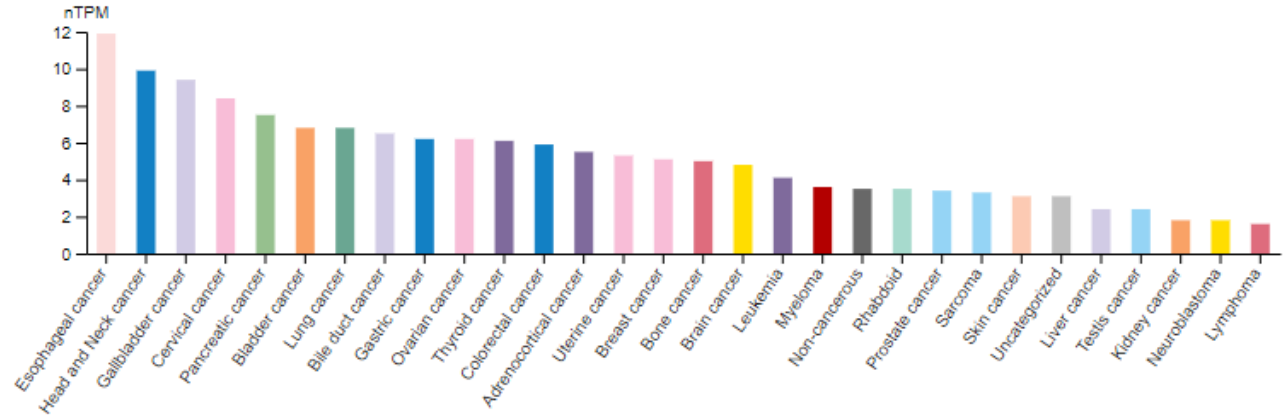

S3.3. 3. Heparanase gene expression in cancer obtained from Human Protein Atlas

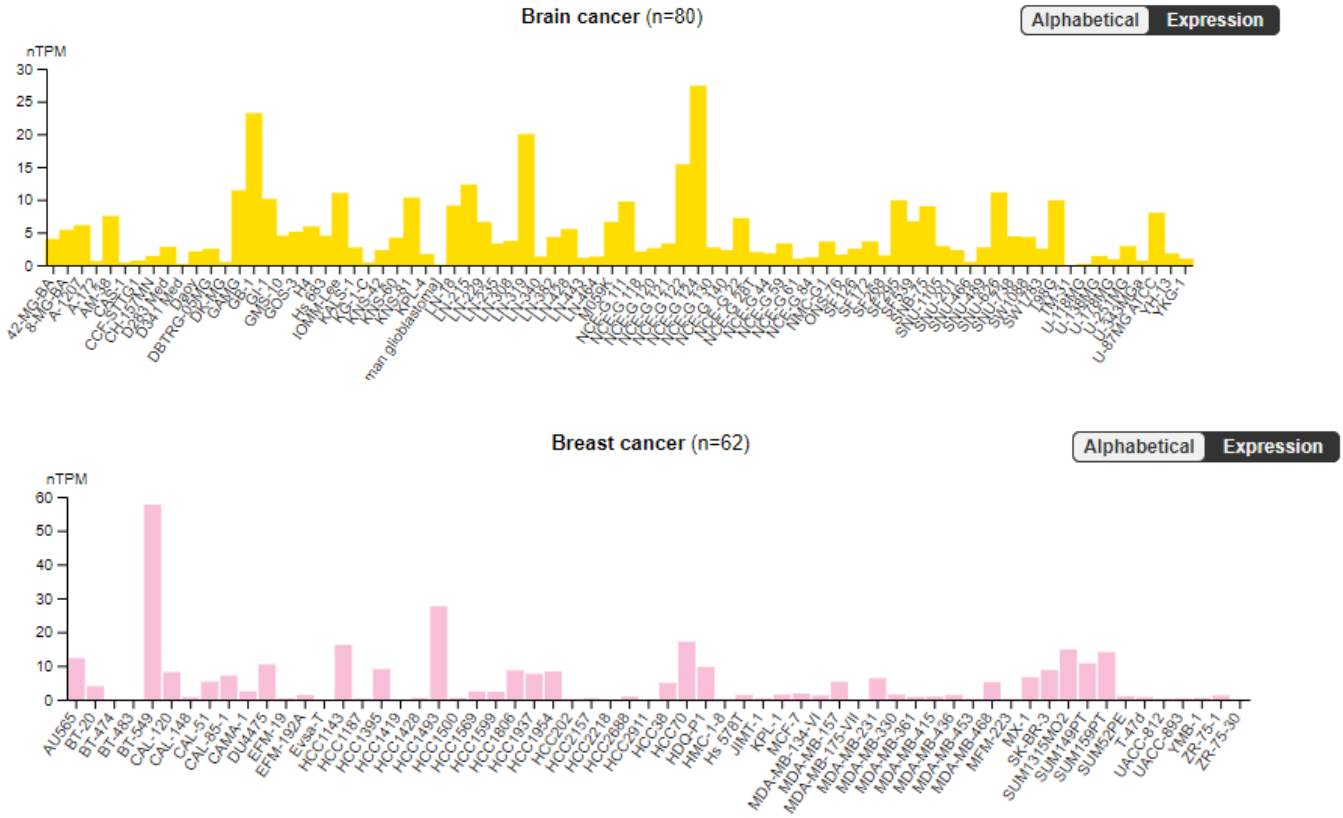

S3.3. 4. Heparanase gene expression in brain cancer and in breast cancer obtained from Human Protein Atlas

Table S3.3. 1. Bioactivity score of (a) homopolymer of n-acryloyl glycine (b) Linear hetro-polymer of n-acryloyl glycine and acrylamide and (c) cross-linked homopolymer and (d) cross-linked hetropolymer represent p(NAG-co-Ac) polymer.

Sr.No	p(NAG-co-Ac) random series	Protease inhibitor	GPCR ligand	Ion channel modulator	Kinase inhibitor	Nuclear receptor ligand	Enzyme inhibitor
1	G1	-1.97	-2.23	-1.72	-2.82	-2.34	-1.62
2	G2	0.26	-0.06	-0.1	-0.74	-0.36	0.06
3	G3	0.41	0.1	-0.1	-0.39	-0.1	0.39
4	G4	0.29	0.07	-11	-0.29	-0.07	0.04
5	G5	0.17	-0.14	-0.76	-0.63	-0.48	-0.36
6	G6	-0.61	-1.17	-2.29	-1.97	-1.91	-1.6
7	G7	-2.21	-2.94	-3.58	-3.55	-3.53	-3.26
8	G8	-3.52	-3.66	-3.78	-3.79	-3.77	-3.52
9	G9	-3.78	-3.9	-3.94	-3.96	-3.85	-3.91
10	G10	-3.85	-3.96	-3.99	-4	-4	-3.97
11	G11	-3.92	-3.83	-3.83	-3.66	-3.87	-3.67
12	A1	-3.74	-3.83	-3.83	-3.66	-3.87	-3.67
13	A2	-0.64	-1.02	-0.71	-1.48	-1.46	-0.65
14	A3	-0.12	-0.4	-0.34	-0.74	-0.68	-0.22
15	GA1	0.16	-0.45	-0.33	-1.19	-0.97	-0.15
16	GA4.1	0.38	0.02	-0.17	-0.57	-0.27	0.09
17	GA2	0.54	0.14	-0.11	-0.33	-0.07	0.1
18	GA3	0.5	0.13	-0.15	-0.41	-0.14	0.08
19	GA4	0.5	0.13	-0.15	-0.41	-0.14	0.08
20	GA5	0.41	0.1	-0.08	-0.24	-0.04	0.07
21	GA6	0.38	0.1	-0.11	-0.29	-0.1	0.06
22	GA7	0.45	0.11	-0.13	-0.27	-0.05	0.07
23	GA8	0.45	0.11	-0.13	-0.27	-0.05	0.07
24	GA9	0.44	0.11	-0.13	-0.33	-0.11	0.07
25	GA10	0.32	0.06	-0.36	-0.28	-0.15	-0.06
26	GA11	0.3	0.06	-0.38	-0.33	-0.19	-0.07
27	GA12	0.3	0.06	-0.38	-0.33	-0.19	-0.07
28	GA13	0.33	0.09	-0.16	-0.25	-0.09	0.05
29	GA14	0.33	0.09	-0.16	-0.25	-0.09	0.05
30	GA15	0.37	0.1	-0.11	-0.28	-0.09	0.06
31	GA16	0.44	0.1	-0.13	-0.27	-0.05	0.06
32	GA17	0.32	0.08	-0.2	-0.25	-0.09	0.04
33	D1	0.28	0.06	0.05	-0.58	-0.03	0.2

34	D2	0.42	0.18	-0.03	-0.28	0.04	0.13
35	D3	0.32	0.14	0.01	-0.31	-0.06	0.1
36	D4	0.17	0	-0.39	-0.38	-0.23	-0.14
37	D5	-0.24	-0.62	-1.5	-1.31	-1.22	-1
38	D6	-1.28	-1.93	-3.07	-2.89	-2.85	-1.28
39	D7	-2.83	-3.37	-3.66	-3.67	-3.65	-3.55
40	D8	-3.59	-3.71	-3.81	-3.82	-3.81	-3.75
41	D9	-3.76	-3.83	-3.89	-3.9	-3.9	-3.85
42	D10	-3.85	-3.9	-3.95	-3.96	-3.96	-3.92
43	D11	-3.81	-3.87	-3.92	-3.93	-3.93	-3.88
44	D12	-3.75	-3.83	-3.89	-3.9	-3.9	-3.85
45	D13	-3.68	-3.77	-3.86	-3.86	-3.87	-3.81
46	D14	-3.58	-3.7	-3.81	-3.81	-3.82	-3.75
47	D15	-2.79	-3.37	-3.67	-3.66	-3.67	-3.55
48	D16	-1.96	-2.77	-3.56	-3.51	-3.51	-3.16
49	D17	-1.19	-1.91	-3.14	-2.88	-2.9	-2.45
50	D18	-0.11	-0.59	-1.54	-1.22	-1.23	-0.94
51	D19	0.35	0.04	-0.46	-0.38	-0.27	-0.12
52	D20	0.2	-0.18	-0.9	-0.72	-0.64	-0.44
53	D21	0.45	0.15	-0.16	-0.27	-0.07	0.05
54	D22	0.5	0.17	-0.06	-0.29	-0.07	0.07
55	D23	0.44	0.13	-0.06	-0.33	-0.12	0.01
56	D24	0.45	0.19	-0.09	-0.43	-0.09	0.08
57	D25	0.41	0.17	-0.07	-0.32	-0.18	0.07
58	D26	0.26	0.07	-0.16	-0.25	-0.09	0.01

Table S3.3. 2. DFT calculation for (a) homopolymer of n-acryloyl glycine (b) Linear hetro-polymer of n-acryloyl glycine and acrylamide and (c) cross-linked homopolymer and (d) cross-linked hetropolymer represent p(NAG-co-Ac) polymer, changes in dipole moment and Intramolecular hydrogen bonding in different solvent

			Molecular weight (g/ mol)	hERG beta (ADMET)	Free energy in Vaccume (Fc)(Eh)	Dipole moment in gas (μ'c) (Debye)	Free energy in gas (Fw)(Eh)	Dipole moment in gas (μ'w) (Debye)	Free energy in ethanol (Fe)(Eh)	Dipole moment in ethanol (μ'e) (Debye)	Intramolcular hydrogen bonding in water (Kcal /mol)	Intermolecular hydrogen bonding energy in ethanol (Kcal /mol)	Intramolcular hydrogen bonding in CHCl3(Kcal /mol)	Intramolcular hydrogen bonding in Hexane (Kcal/mol) /mol)
1		Glycine			-284.073	5.59	-284.091	7.27	-284.090	7.21	11.25	10.84	8.66	4.79
2	G1	N-Acryloyl glycine (G)			-475.029	1.93	-475.053	1.95	-475.052	1.95	14.98	14.45	11.56	6.39
3	G2	GG			-951.319	3.00	-951.366	3.34	-951.365	3.33	29.84	28.80	23.13	12.87
4	G3	GGG			-1424.991	2.95	-1425.057	6.68	-1425.055	6.51	41.58	40.10	32.13	18.00
5	G4	GGGG			-1899.644	5.45	-1899.711	8.67	-1899.708	8.50	41.81	40.23	31.81	17.35
6	G5	GGGGG			-2374.251	7.74	-2374.332	13.92			50.42	48.53	38.81	18.73
7	G6	GGGGGG			-2848.880	3.83	-2848.962	4.77	-2848.959	4.82	51.69	49.79	39.65	21.83

8	GA1	GA	202.21	3.78(safe)	-722.795	4.53	-722.830	5.47	-722.829	5.44	21.98	21.21	16.99	9.42
10	GA4.1	AAG	273.29	3.88(safe)	-969.822	5.50	-969.864	7.55	-969.863	7.46	26.79	25.84	20.66	11.44
11	GA2	GGA	331.33	4.24(safe)	-1197.432	3.85	-1197.479	11.04	-1197.477	10.86	29.59	28.47	22.47	11.39
12	GA3	AGG	331.33	4.25(safe)	-1197.431	8.49	-1197.487	8.66	-1197.486	8.59	35.10	34.25	20.32	0.00
13	GA4	GAG	331.33	4.25(safe)	-1197.410	4.77	-1197.457	7.12	-1197.456	6.99	30.02	28.92	22.97	12.66
14	GA5	GGGA			-1672.050	5.32	-1672.108	9.62	-1672.106	9.43	36.44	35.02	27.56	14.93
15	GA6	GGAG	460.44	4.42(safe)	-1672.059	12.59	-1672.111	24.98	-1672.109	24.44	32.82	31.45	24.04	12.79
16	GA7	GGAA	402.40	4.31(safe)	-1444.450	6.66	-1444.494	10.51	-1444.492	10.31	27.34	26.37	21.15	11.79
17	GA8	GAGA			-1444.421	6.04	-1444.486	9.39	-1444.483	8.70	40.77	39.19	30.81	16.37
18	GA9	GAAG			-1444.429	15.96	-1444.492	22.31	-1444.490	22.04	40.04	38.54	30.52	16.66
19	GA10	GGGGA			-2146.682	6.28	-2146.735	10.70	-2146.733	10.44	33.37	32.08	25.61	14.08

20	GA11	GGGAG	589.56	4.51(safe)	-2146.657	14.84	-2146.741	24.30	-2146.738	23.72	52.65	50.54	39.55	21.23
21	GA12	GGAGG	589.56		-2146.640	13.87	-2146.719	20.97	-2146.716	20.52	49.35	47.45	37.47	20.35
22	GA13	GGAAG	531.52	4.47(safe)	-1919.048	3.36	-1919.118	7.81	-1919.115	7.67	43.70	42.11	32.45	18.04
23	GA14	GAGAG	531.52	4.47(safe)	-1919.042	9.71	-1919.115	14.15	-1919.113	14.01	45.95	44.23	35.00	19.01
24	GA15	GAAAG	473.48	4.41(safe)	-1691.419	8.99	R				44.80	43.07	34.50	19.09
25	GA16	GGGGGA	718.67	4.64(safe)	-2621.240	6.97	-2621.333	9.69	-2621.329	9.51	58.02	55.77	43.94	23.91
26	GA17	GGGAGG	718.67	4.64(safe)	-2595.339	3.25	-2595.390	3.96	-2595.391	4.75	32.07	32.39	0.00	0.00
27	GA18	GAGGAG	660.63	4.54(safe)	-2368.721	4.41					41.16	0.00	0.00	0.00
25	D1	D-G	247.29		-823.083	1.92	-823.108	2.83	-823.107	2.79	15.87	15.30	12.25	6.77
26	D2	G-D-G	364.40		-1260.846	2.45	-1260.897	2.17			32.18	31.04	24.88	13.80
27	D3	GG-D-G	479.49		-1694.985	2.24	-1695.049	3.88	-1695.047	3.76	40.20	38.78	31.09	17.23

28	D4	GGDGG	594.57		-2130.338	9.55	-2130.417	12.93	-2130.414	12.79	49.53	47.66	37.81	20.68
29	D5	GGGDGG	709.66	4.73(safe)	-2565.674	6.22					54.63	52.62	41.82	22.88
30	D6	GGGDGGG	824.75	4.86 (safe)	-3000.995	6.03					0.00	0.00	53.10	28.86
	D7	GAGDGAG	764.79	4.75 safe	-2702.911	17.27	-2703.007	22.41	-2703.003	21.76	60.18	57.85	45.79	25.04
31	D18	GAGDGGA									55.51	53.41	42.26	23.23
32	D19	GAGDGA	610.62	4.82 (safe)	-2170.756	6.01	-2170.831	9.13			46.65	44.92	35.94	19.88
33	D20	GAGDGG	651.63	4.77(safe)	-2338.114	6.42	-2338.190	10.97	-2338.187	10.79	47.43	45.63	35.81	19.62
34	D21	GADGG	536.54	4.77 (safe)	-1902.748	4.89	-1902.816	8.21	-1902.814	8.04	42.92	41.34	32.87	17.96
35	D22	GADGA	478.50	4.7 (safe)	-1675.144	8.72	-1675.213	10.89	-1675.210	10.77	43.13	41.55	33.10	18.20
36	D24	ADG	306.36	4.1 (safe)	-1032.056	5.99	-1032.092	7.95	-1032.091	7.82	22.68	21.96	18.08	11.23
37	D25	GADG	407.42	4.68 (safe)	-1428.145	5.41	-1428.198	6.63	-1428.196	6.57	33.08	31.89	25.43	14.01

38	D26	GGADG	537.52	4.74(safe)	-1922.568	7.87	-1922.644	11.92	-1922.641	11.82	47.45	45.62	34.63	18.47

Table S3.3. 3 HOMO LUMO energy difference with increase in size of monomer to polymer and in presence of cross linker

	HOMO (eV)	LUMO (eV)	Band gap (eV)	Chemical hardness (η)	Chemical softness (σ)	Electronegativity (χ)	Electrophilicity (ω)
D1	-6.097	-1.079	5.018	2.509	0.398565165	3.588	2.565513
D2	-6.5	-0.379	6.121	3.0605	0.326743996	3.4395	1.932717
D3	-6.53	-0.414	6.116	3.058	0.327011118	3.472	1.971024
D4	-6.473	-0.657	5.816	2.908	0.343878955	3.565	2.185218
D5			0	0		0	
D6				0		0	
D7	-6.398	-0.302	6.096	3.048	0.32808399	3.35	1.840961
D18			0	0	#DIV/0!	0	
D19	-6.356	-0.527	5.829	2.9145	0.343112026	3.4415	2.031896
D20	-6.473	-0.46	6.013	3.0065	0.332612673	3.4665	1.99844
D21	-6.424	-0.378	6.046	3.023	0.330797221	3.401	1.913133
D22	-6.428	-0.357	6.071	3.0355	0.329435019	3.3925	1.895743
D24	-6.448	-0.314	6.134	3.067	0.326051516	3.381	1.863574
D25	-6.496	-0.567	5.929	2.9645	0.337325013	3.5315	2.103473
D26	-6.58	-0.716	5.864	2.932	0.34106412	3.648	2.269424
Glycine	-6.881	0.535	7.416	3.708	0.269687163	3.173	1.357596
G1	-7.143	-1.137	6.006	3.003	0.333000333	4.14	2.853746
G2	-7.018	-0.106	6.912	3.456	0.289351852	3.562	1.835626
G3	-6.919	0.017	6.936	3.468	0.288350634	3.451	1.717042
G4	-6.98	-0.546	6.434	3.217	0.310848617	3.763	2.200834
G5	-6.988	-0.418	6.57	3.285	0.304414003	3.703	2.087094
G6	-6.867	-0.48	6.387	3.1935	0.313136058	3.6735	2.112823
GA1	-6.881	0.074	6.955	3.4775	0.287562904	3.4035	1.665537
GA2	-6.888	-0.148	6.74	3.37	0.296735905	3.518	1.83625
GA3	-7.018	-0.031	6.987	3.4935	0.286245885	3.5245	1.777888
GA4	-6.829	-0.219	6.61	3.305	0.302571861	3.524	1.878756
GA4.1	-6.793	-0.042	6.751	3.3755	0.296252407	3.4175	1.730011
GA5	-6.92	-0.543	6.377	3.1885	0.313627097	3.7315	2.183486
GA6	-6.966	-0.228	6.738	3.369	0.296823983	3.597	1.920215
GA7	-6.766	-0.196	6.57	3.285	0.304414003	3.481	1.844347

GA8	-6.783	0.013	6.796	3.398	0.294290759	3.385	1.686025
GA9	-6.883	-0.016	6.867	3.4335	0.291247998	3.4495	1.732787
GA10	-6.89	-0.414	6.476	3.238	0.308832613	3.652	2.059466
GA11	-6.949	-0.115	6.834	3.417	0.292654375	3.532	1.825435
GA12	-6.881	-0.56	6.321	3.1605	0.316405632	3.7205	2.189862
GA13	-6.787	-0.098	6.689	3.3445	0.298998356	3.4425	1.771686
GA14	-6.74	0.002	6.742	3.371	0.296647879	3.369	1.683501
GA15	-6.738	0.048	6.786	3.393	0.294724433	3.345	1.64884
GA16	-6.712	-0.592	6.12	3.06	0.326797386	3.652	2.179265
GA17	-7.475	-3.996	3.479	1.7395	0.574877838	5.7355	9.455579

Table S3.3.4: protein ligand interaction with heparanase PDBID-7PRT

S.No.		Ligands	Lowest binding energy (kcal mol-1)	Estimated inhibition constant (Ki)	H-bond	Interacting Residue (non hydrogen bond)
Reference Molecules						
1		*Cyclophellitol*	-4.65	829.53 uM	SER422 (2.036,1.901), GLN424(1.828), ARG465(2.135,1.928)	
2		*Roneparstat*	-1.36	100.76mM	ASP183(2.204), ARG382(1.989)	ILE185,PHE385.LEU408,TYR404,SER407,TRP365,LYS411,LEU398,LEU182
Ligands						
1		*Glycine*	-4.09	1.00 mM	**H(1)** Lys232(1.79),	GLU225, Ser228
2	G1	*N-Acryloylglycine (G)*	-5.16	166.36uM	**H(3)** LYS538(1.851), LYS473(1.849,1.699)	PRO469,ALA537
3	G2	*GG*	-4.53	479.91 uM	**H(3) LYS280**(1.916), LYS284(1.725), LYS277(1.812)	
4	G3	*GGG*	-4.52	487.79uM	H(6) LYS232(1.703), **ARG272**(1.915), THR275(2.129,1.828, 1.946), LYS274(2.236)	ASN227,GLN276,ARG273
5	G4	*GGGG*	-5.46	99.29 uM	H (7) LYS277(2.073),LYS284(1.865),ARG273(2.059,1.852,1.819)**, LYS280**(2.054)	

6	G5	*GGGGG*	-7.76	2.05uM	LYS325(2.169,2.134, 1.836), **ARG272**(2.063), **LYS280**(1.928,1.926), **ARG273**(2.207)	ALA276
7	G6	*GGGGGG*	-7.62	2.62 uM	AG273(2.159,2.094,1.895), LYS325(2.22), **LYS280**(2.079,1.995), LYS284(1.996), LYS277(1.863)	
8	GA1	*G-A*	-4.73	339.9uM	**H (4)** VAL433(2.183,1.925), VAL423(2.019), ARG374(2.215)	MET420,ALA421,SER422,LEU371,TYR434,LEU431
9	GA4.1	*A-A-G*	-5.18	159.74uM	**H(4)** ARG465(2.208, 2.121, 2.063, 2.002), **GLN424(**2.003)	LEU452,LEU466,PRO467
10	GA2	G-G-A	-5.57	81.94 uM	MET512(2.114), ASN496(2.149), LYS514(1.858,1.791)	LEU498,LEU495
11	GA3	*A-G-G*				
12	GA4	*G-A-G*	-4.4	597.59uM	LYS411(1.885),VAL380(2.086),ARH382(2.115,1.747),PHE385(1.889),PHE386(2.042)	VAL384
13	GA5	*G-G-G-A*	-5.05	199.39uM	SER422(2.007,1.693), GLN424(2.235,2.013)	LEU452,LEU464,ARG465,VAL433,VAL423
14	GA6	*G-G-A-G*	-5.11	178.43 uM	SER422(2.206),ARG465(2.001,1.693),GLN424(2.19,1.825)	VAL423,LEU466,LEU452,PRO467,LEU450,PHE470,ILE534
15	GA7	*G-G-A-A*		689.02uM	**LYS280**(1.977,1.952), LYS325(2.153),GLN328(1.971),VAL329,ALA276,ARG273,SER332	HIS458,PHE527

16	GA8	*G-A-G-A*	-4.56	451.4uM	LYS412(1.78),VAL380(1.752),LYS411(2.0,1.861,2.14)	VAL414,PHE410,ASN439,VAL379
17	GA9	*G-A-A-G*	-5.37	116.15uM	GLN424(2.062),GLY425(2.144),ARG465(2.092,2.08,2.024)	SER422,VAL423,LE464,LEU466,TYR463
18	GA10	GGGGA	-6	39.88 uM	LYS352(2.215),LYS284(1.869),**LYS280(2.082,1.759),**GLN328(2.145)	VAL329,LYS277,ARG283,LYS325,ALA276
19	GA11	GGGAG	-4.52	489.68 uM	ARG481(2.127),LYS514(1.79),THR461(2.04,2.0),ALA526(1.966),LYS477(2.115)	PRO525,LEU479,ASN496
20	GA12	GGAGG	-5.93	44.91uM	ARG273(2.134,1.811),LYS277(1.87,1.682),LYS280(1.983),LYS284(1.866)	LYS274
21	GA13	GGAAG	-6.26	25.68uM	ARG465(2.079,1.89,1.877),TYR463(2.199),SER422(2.093),LYS462(2.029)	LEU464,PRO467,GLN424,ALA421,VAL423
22	GA14	GAGAG	-6.96	7.88 uM	GLN328(1.891),LYS325(1.91),LYS284(1.892),**LYS280**(2.053),ARG273(2.149)	PRO271,VAL329,ALA276,LYS277
23	GA15	GAAAG	-6.7	12.19uM	ARG465(2.028,2.004,1.93),**SER422**(2.149,1.992),GLN424(2.129)	VAL423,VAL433,MET420,PRO467,LEU452,LEU466,LEU435,ALA421
24	GA16	GGGGGA	-3.31	3.75mM	ARG273, ARG 273, **LYS 280**	
25	GA17	GGGAGG	-6.46	18.25uM	ARG273(2.218,1.929,1.873),**LYS280**(1.766),LYS284(1.918),LYS277(1.975,1.844)	SER281
26	*D1*	D-G	-6.83	9.8 uM	GLN424(2.131),ARG465(2.074,1.982)	LEU464,LEU452
27	*D2*	G-D-G	-7.59	274.09 nM	Lys 280 () Lys 325	ARG273, PRO271, LYS325, ARG272, Lys284, ALA276

28	*D3*	GG-D-G	-9.04	235nM	LYS274(2.199,1.826), LYS231(2.107,1.957), **ARG272** (1.802),LYS277(1.849)	SER228,LEU230,PHE236,ASN227,ARG273
29	*D4*	GGDGG	-11.08	7.53 nM	**LYS231(2.217,2.083), LYS232**(1.913),LEU230(2.076),**ARG272**(1.946,1.939),LYS274(1.758)	VAL329, ALA276, PRO 271,ARG272
30	*D5*	GGGDGG	-10.72	13.87nm	**ARG272**(2.063),ARG273(2.207),LYS325(2.169,2.134,1.836), lys277, lys280' lys280	SER332,VAL329, PRO271,
31	*D6*	GGGDGGG	-8.39	705.85 nM	**LYS231**(1.798,1.763), ASN227(1.826),LYS274(1.941,1.799),**ARG272**(2.182,1.973)	ARG273,SER228,LEU230
32	*D7*	GAGDGAG	-5.67	69.31µM	**ARG273**(2.063,1.724),**LYS325**(1.882),**LYS280**(1.981),**GLN328**(2.229)	VAL329,ALA276,ARG272,PRO271
33	*D18*	GAGDGGA	-7.66	2.43 µM	**ARG273**(1.895),**LYS325**(2.058),**LYS280(**2.224, 2.18), LYS277 (2.175)	SER332, GLN 328, PRO271
34	*D20*	GAGDGG	-7.6	2.7uM	LYS277(2.122), **LYS280(**2.045, 2.232), LYS 325 (2.17)	GLN328, PRO 271
35	*D21*	GADGG	-8.22	940.4 nM	LYS277(1.916),LYS325(1.979),LYS284(2.177),PRO271(2.132)**,LYS280**(1.933)	SER281,SER332,VAL329,ALA276,**ARG273**
36	*D22*	GADGA	-6.68	12.66 uM	ARG374(2.182,2.031, 1.919),ALA421(2.175),VAL433(1.9421.839)	MET420,MET375,ALA421,VAL433,LEU371, ARG432,LEU431
37	*D24*	ADG	-5.8	55.81 µM	SER422, TYR463	ALA421, VAL423, TYR463, LYS462, PRO467
38	*D25*	GADG	-6.68	12.7 µM	GLN424(1.951),**SER422**(2.127),ARG465(1.909,1.631)	ALA421,VAL423,VAL433,LEU452,LEU466,PRO467

Journal of Materials Chemistry B

ROYAL SOCIETY OF CHEMISTRY

PAPER

View Article Online
View Journal

Cite this: DOI: 10.1039/d4tb00243a

Neurogenic and angiogenic poly(*N*-acryloylglycine)-*co*-(acrylamide)-*co*-(*N*-acryloyl-glutamate) hydrogel: preconditioning effect under oxidative stress and use in neuroregeneration†

Kirti Wasnik,[a] Prem Shankar Gupta,[a] Gurmeet Singh,[a] Somedutta Maity,[b] Sukanya Patra,[a] Divya Pareek,[a] Sandeep Kumar,[c] Vipin Rai,‡[d] Ravi Prakash,[e] Arbind Acharya,[c] Pralay Maiti,[e] Sudip Mukherjee,[a] Yitzhak Mastai[f] and Pradip Paik*[a]

Received 5th February 2024,
Accepted 22nd May 2024

DOI: 10.1039/d4tb00243a

rsc.li/materials-b

Traumatic injuries, neurodegenerative diseases and oxidative stress serve as the early biomarkers for neuronal damage and impede angiogenesis and subsequently neuronal growth. Considering this, the present work aimed to develop a poly(*N*-acryloylglycine)-*co*-(acrylamide)-*co*-(*N*-acryloylglutamate) hydrogel [p(NAG-Ac-NAE)] with angiogenesis/neurogenesis properties. As constituents of this polymer modulate their vital role in biological functions, inhibitory neurotransmitter glycine regulates neuronal homeostasis, and glutamatergic signalling regulates angiogenesis. The p(NAG-Ac-NAE) hydrogel is a highly branched, biodegradable and pH-responsive polymer with a very high swelling behavior of 6188%. The mechanical stability (*G*′, 2.3–2.7 kPa) of this polymeric hydrogel is commendable in the differentiation of mature neurons. This hydrogel is biocompatible (as tested in HUVEC cells) and helps to proliferate PC12 cells (152.7 ± 13.7%), whereas it is cytotoxic towards aggressive cancers such as glioblastoma (LN229 cells) and triple negative breast cancer (TNBC; MDA-MB-231 cells) and helps to maintain the healthy cytoskeleton framework structure of primary cortical neurons by facilitating the elongation of the axonal pathway. Furthermore, FACS results revealed that the synthesized hydrogel potentiates neurogenesis by inducing the cell cycle (G0/G1) and arresting the sub-G1 phase by limiting apoptosis. Additionally, RT-PCR results revealed that this hydrogel induced an increased level of HIF-1α expression, providing preconditioning effects towards neuronal cells under oxidative stress by scavenging ROS and initiating neurogenic and angiogenic signalling. This hydrogel further exhibits more pro-angiogenic activities by increasing the expression of VEGF isoforms compared to previously reported hydrogels. In conclusion, the newly synthesized p(NAG-Ac-NAE) hydrogel can be one of the potential neuroregenerative materials for vasculogenesis-assisted neurogenic applications and paramount for the management of neurodegenerative diseases.

New concepts

In this work, we pioneer the synthesis of a new copolymer hydrogel [p(NAG-Ac-NAE)] consisting of *N*-acryloylglycine, *N*-acryloylglutamate and acrylamide to facilitate the treatment of traumatic injuries and other neurodegenerative diseases under oxidative stress conditions. The uniqueness of this polymer hydrogel is that it mimics the inhibitory neurotransmitter glycine, which regulates neuronal homeostasis, and glutamatergic signalling, which regulates angiogenesis. This hydrogel promotes neurogenesis by inducing the cell cycle and arresting the sub-G1 phase, followed by restricting apoptosis. This hydrogel induces HIF-1α expression, thus providing preconditioning effects towards neuronal cells under oxidative stress conditions. Through HIF-1α/VEGF signalling, this hydrogel promotes angiogenesis and neurogenesis. In summary, the p(NAG-Ac-NAE) hydrogel is one of the potential neuroregenerative materials useful for the treatment of neurodegenerative diseases.

[a] *School of Biomedical Engineering, Indian Institute of Technology, Banaras Hindu University (BHU), Varanasi, Uttar Pradesh 221 005, India. E-mail: paik.bme@iitbhu.ac.in, pradip.paik@gmail.com*
[b] *School of Engineering Sciences and Technology, University of Hyderabad, Telangana State 500 046, India*
[c] *Department of Zoology, Banaras Hindu University (BHU), Varanasi, Uttar Pradesh 221005, India*
[d] *Department of Biochemistry, Institute of Sciences, Banaras Hindu University (BHU), Varanasi, Uttar Pradesh 221005, India*
[e] *School of Material Science, Indian Institute of Technology, Banaras Hindu University (BHU), Varanasi, Uttar Pradesh 221 005, India*
[f] *Department of Chemistry and the Institute of Nanotechnology, Bar-Ilan University, Ramat-Gan, 52900, Israel*
† Electronic supplementary information (ESI) available. See DOI: https://doi.org/10.1039/d4tb00243a
‡ Department of Anesthesiology, Rutgers New Jersey Medical School, Newark 7103, USA

1. Introduction

The lack of regenerative properties of the nervous system (CNS/PNS); inadequate knowledge of CNS development, pathophysiology, and disease progression mechanisms; diminished therapeutic effect of active ingredients due to the blood–brain barrier (BBB) and the lack of multifunctional responses of biomaterials limit the development of clinically effective neuroregenerative properties,[1] resulting in a limited therapeutic success rate.[1,2] Injury and aging-associated neurological disorders are continuously increasing and are the second leading cause of death worldwide.[3,4] Among the neurological disorders, stroke, migraine, and Alzheimer dementias (AD) are the major contributors of traumatic brain injury (TBI).[4,5] Vascular damage, increased inflammation, oxidative stress and insufficient blood supply are the leading causes of death and neurological disability by stroke/TBI and failure in recovery with the existing treatment options.[6,7] Hence, angiogenic therapeutic material could promote the de nevo tissue formation along with the increase in developed blood vessels and axonal network.[8] Polymeric materials exhibit fascinating advantages in medical biotechnology due to their biocompatibility, possibility of multiple interactions with proteins and excellent *in vivo* stability.[9] Chitosan, albumin, polylactic acid (PLA) and poly(ethylenimine) are the few polymers that are used to develop 3D scaffolds and hydrogels[10] for nerve repair. Unfortunately, available synthetic polymeric hydrogels have numerous limitations; for example, most of them are poor in cell adhesion, produce toxic degradation products, and photo-responsive hydrogels show potential toxicity owing to the presence of functional groups and poor reproducibility of the structure.[1] For example, alginate hydrogel limits its applications due to the requirement of the multistep purification process. The use of various polymers, such as polylactic glycolic acid (PLA), is limited due to the lack of functional groups and low electric conduction. Polycaprolactone (PCL) limits their uses due to the high crystallinity and use of protein/peptide that have failed to get FDA approval due to unsatisfactory pharmacokinetics and missing the targets.[11]

The incorporation of amino acids into synthetic polymer forms the ordered hierarchical structures and favors the exceptional chemical, physical and stimuli-responsive properties along with excellent biocompatibility and degradability.[12] Reported glutamate-based poly(γ-glutamic acid) (PLGA) is a promising polymer for biomedical applications due to its biocompatible and non-immunogenic nature.[13] PLGA in conjugation with different organic moieties exhibits pH responsiveness[14] and shows excellent adhesive strength in visceral tissues.[15] PLGA composites inherit good mechanical strength with self-healing ability beneficial in chondrogenic differentiation and accelerate the cutaneous wound healing efficiency.[16] Recently, we showed the neurogenic potential of p(NAG-*b*-A) hydrogel.[17] However, previous studies were limited to neurogenic potential, but it was not explored owing to its angiogenic properties. Similarly, none of these studies have supported the development of glutamate- and glycine-based co-polymeric hydrogels for their dual angiogenic and neurogenic potential.

Glutamate and glycine are crucial components in neuronal homeostasis, learning and memory, and cell–cell communication and play ubiquitous roles in neuroprotective action, neural stem cell survival and neurogenic programming. The accumulated form of glycine and glutamate in synaptic vesicles is involved in synaptic plasticity. Aging is associated with disturbed protein synthesis kinetics due to decreasing levels of transmitters.[18,19] Anatomically, neurons and vasculature undergo parallel development; hence, the material should deliver the neurotrophic factors in a specific concentration or should have angiogenic and neurogenic properties. A few nanomaterials are known for both neurogenic and angiogenic properties,[20,21] but not known for hydrogel or hydrogel encapsulated with neurotrophic factors.[22] Therefore, in the present work, a novel polymeric hydrogel was applied to develop a neurogenic and angiogenic dual property-bearing hydrogel for effective neurogenesis. Hence, in the present work, the synthesis of angiogenic and neurogenic biological cues containing non-tumorigenic p(NAG-Ac-NAE) hydrogel was carried out. After performing physical characterization and analysing the rheological properties, biocompatibility was assessed in HUVEC and normal healthy cell lines. It is known that the angiogenic potential of the material could have a positive impact on recovery from nerve injury. In the present work, the angiogenic behaviour of p(NAG-Ac-NAE) is also evaluated *in ovo* system and compared with the inhibitory glycine-containing p(NAG-*b*-A) hydrogel. Through the *in vitro* study, the neurogenic potential and protective role in oxidative stress are investigated. Finally, based on the experimental evidence, the p(NAG-Ac-NAE) hydrogel is used in this work, which plays a potential role in promoting neurite growth along with the pro-angiogenic properties, and is paramount for the management of neurodegenerative diseases.

2. Experimental

Materials and methods

Materials. Materials used in this work are glycine (Qualigens), L-glutamic acid (Sigma-Aldrich), sodium hydroxide (Sigma-Aldrich), acryloyl chloride, diethyl ether, ethyl acetate, magnesium sulphate, neuronal growth factor (Gibco), neurobasal medium (ThermoFisher), supplement-B27 (ThermoFisher), fetal bovine serum (Gibco), DMEM media, rhodamine phalloidin (400X) (ThermoFisher), β tubulin antibody, acridine orange, Hoechst 33258, methyl thiazoltetrazolium (Himedia), hexadecane anhydrous (99%, Sigma-Aldrich), divinyl-benzene divinylbenzene (Alfa aesar), 1, 4-dioxan (99%, Merck), 2,2-azobis isobutyronitrile (AIBN, 98% SRL), SDS (90%, Merck), HBSS 1X (Himedia), streptomycin–penicillin 100U (Himedia), gentamycin (Sigma-Aldrich), gentamicin and poly(L-lysine) (Sigma-Aldrich).

Synthesis of N-acryloylglycine and N-acryloylglutamate monomers. N-Acryloylglycine (patent no.: 419638, granted on. 30-01-2023) and *N*-acryloylglutamic acid[23] were prepared using a similar method. In brief, 0.1 mol of amino acid was dissolved

in chilled NaOH solution, and 1 equivalent of acryloyl chloride was dissolved in 1,4-dioxane with continuous stirring separately. Dissolved acryloyl chloride was then added to a mixture of acids under a chilled condition with vigorous stirring for 30 min and gentle stirring overnight at room temperature (25 °C). Furthermore, the reaction mixture was extracted using diethyl ether, and the aqueous layer was acidified using HCl maintaining pH = 2, followed by over-saturation with NaCl at 25 °C. Finally, the monomer was extracted using warm ethyl acetate (dried over $MgSO_4$), and the solvent was removed by rotary evaporation. Both monomers were characterized and used for polymer synthesis.

Synthesis of p(NAG-Ac-NAE) hydrogel. A free radical, mini-emulsification polymerization technique was used for the synthesis of p(NAG-Ac-NAE) hydrogel. Briefly, 400 mg of *N*-acryloylglycine and 400 mg of *N*-acryloylglutamate were dispersed in 1,4-dioxane (8 mL for 20 min), followed by the addition of completely dissolved 200 mg of acrylamide in cold water. Further, the reaction mixture stabilized with the addition of hexadecane (40 mg), cross-linker DVB (40 mg) and free radical initiator AIBN (20 mg) was added sequentially. After 10 min of stirring, the reaction mixture was sonicated for 5 minutes in a water bath sonicator. Then, 44 mg of sodium dodecyl sulphate (SDS) in 300 μL water was added to the reaction mixture and stirred for another 20 minutes. Further, the suspended mixture was sonicated for 7 minutes with a 45 : 15 on–off cycle at 30% amplitude. Then, the emulsion was transferred to a 50 mL round bottom flask and stirred for 12 hours at 70 °C till the precipitate was formed. The polymerized product was washed with a 70 : 30 ethanol–water mixture, followed by 50 : 50 (ethanol : water) 8 times with proper sonication to remove the unreacted monomer and SDS. Then, the swelled hydrogel was freeze-dried to obtain a nanohydrogel. Further, the chemical functionality was confirmed through FTIR, ^{1}H NMR and ^{13}C NMR. To measure the molecular weight, MALDI-TOF experiments were performed for p(NAG-Ac-NAE) using $CDCl_3$ and DMSO-d_6 solvent (1 : 1) and using the dithranol matrix. The molecular weight (MW) and polydispersity index (PDI) were calculated using eqn (1)–(3):

$$M_n = \frac{\sum M_i N_i}{\sum N_i}, \quad (1)$$

$$M_w = \frac{\sum M_i^2 N_i}{\sum M_i N_i}, \quad (2)$$

$$PDI = \frac{M_w}{M_n}, \quad (3)$$

where M_n is the number of average molecular weight, M_w is the weight average molecular weight, M_i is the mass of the '*i*' oligomer and N_i is the number of the *i*th oligomer.[24] Detailed synthesis method of this hydrogel was filed for an Indian Patent (ref. 202311038604, dated: June 5th, 2023).

Physical and morphological evaluation of p(NAG-NAE-A) hydrogel. For functional group analysis of monomer and polymer, FTIR spectrum was obtained using Thermo electron scientific instrument LLC/model NicoletiS5. The KBr pelleting method was used for monomer, while the ATR method was used for polymer. 10 mg of monomer/polymer was dissolved in solvent (DMSO-d_6 and $CDCl_3$), and ^{1}H NMR and ^{13}C NMR spectra were acquired using an AVH D 500 AVANCE III HD 500 MHz spectrometer. Thermal stability was studied using TGA-50, and phase transition was studied using DSC60 with 10 °C min^{-1} in a nitrogen environment. X-ray diffraction (XRD) patterns for samples were recorded from 2θ = 5 to 90° using HR-XRD (Rigaku SmartLab 9 kW; without χ cradle). Further, structural and surface morphologies were elucidated with an accelerating voltage of 15 kV using a field-emission scanning electron microscope (FESEM; Nova Nano SEM 450) and a high-resolution transmission electron microscope (HRTEM; Tecnai G2 20 TWIN). FESEM images were acquired using a sample coated with Au–Pd for 30 s, while HRTEM images were acquired by dispersing the p(NAG-Ac-NAE) hydrogel in dried isopropanol, negatively stained with 2% uranyl acetate (UA) and drop cast on the 200 mesh-sized C-coated Cu grid.

Mass swelling index (MSI) measurement. Dynamic swelling behaviour was obtained by immersing hydrogel in PBS buffer (1X, pH 7.2) of different pH levels (3, 5, 6, 7.4 and 8). After the specified time interval, the excess buffer was removed, and the molecular mass was measured. Then, the mass swelling indexes (MSI) were calculated by applying eqn (4):

$$MSI = \frac{(W_s - W_d)}{W_i} \times 100, \quad (4)$$

where W_s is the weight of the swelled hydrogel and W_d is the weight of the dried hydrogel.

Furthermore, the hydrodynamic diameter was calculated using a zeta sizer by dispersing the polymeric hydrogel particles in water, and the results were compared with those obtained from HRTEM.

Biodegradation study. Bio-degradation studies were performed by immersing 4 mg of p(NAG-Ac-NAE) hydrogel in 1 mL of PBS (pH 7.2) containing 100 μg mL^{-1} proteinase K in PBS, 100 μg mL^{-1} Collagenase in PBS and 100 μg mL^{-1} lysozyme in PBS solution separately and were incubated for 1, 7, 15, 21 and 30 days. After each incubation period, MSI was calculated.

Study of rheological parameters. Swelled p(NAG-Ac-NAE) hydrogel was placed between preheated and cooled rheometer parallel plates (30 mm in dia.) with 0.5 mm gap height and allowed to equilibrate at ambient room temperature (25 °C) for 2 min in each run. The rheological data were obtained using an Anton Paar MCR 102 Rheometer. The shear tests were performed in the range from 10^{-6} to 10^2 s^{-1} at 34 °C, 37 °C, 40 °C and 43 °C. Frequency sweep tests were conducted in the range of ω = 0.1–100 rad s^{-1} with an oscillation strain of 5%. To determine the relationship between loss modulus (G''), storage modulus (G'), viscoelastic modulus and complex viscosity (η^*),

the experiment was conducted as a function of angular frequency (ω) at various temperatures.

Cell viability assay. Cell lines were collected from a repository of NCCS-Pune, India and maintained in 10% FBS-supplemented DMEM with 100 U of streptomycin–penicillin antibiotic. Cellular viability was assessed in the presence of p(NAG-Ac-NAE) hydrogel by performing an MTT assay using different cell lines (PC12, HUVEC, MDA-MB-231, MCF7 and LN229 cells). In brief, 1×10^4 cells per well were cultured for 24 h in FBS-supplemented DMEM, followed by treatment with varied concentrations of p(NAG-Ac-NAE) hydrogel for more than 24 h. Afterwards, complete treatment was performed with 5 μg mL^{-1} MTT reagent for 4 h. Furthermore, the MTT regent was replaced with DMSO to dissolve formazone, and the intensity of the absorbance was recorded at 570 nm using a Bioteck microplate reader to calculate the cell viability.

Cell cycle and cell proliferation assay. 1×10^5 per well PC12 cells were cultured overnight (12 h), and 250 μg mL^{-1} p(NAG-Ac-NAE) hydrogel and p(NAG-*b*-A) hydrogel were added separately in the presence/absence of 40 μM H_2O_2 and incubated for 24 hours. Afterward, the cells were stained with propidium iodide (PI), and the cell cycle stages were identified by flow cytometry.

Animal ethical approval. Animal ethical approval was considered (IIT(BHU)/IAEC/2022/079), and all the experiments were carried out as per the CPCSEA guideline of the Institution Animal Ethical Committee (IAEC) of IIT (BHU), Varanasi, Uttar Pradesh, India (regd. no. 2123/GO/Re/S/21/CPCSEA).

Hemocompatibility of hydrogel. Whole blood samples were obtained from the animal, and RBCs were separated. Then, 5×10^{10} were suspended in a 5% dextrose solution (pH 7.4). Treatment with 5% dextrose solution was considered a negative control, while treatment with 0.1–1% Triton-X was considered a positive control. RBCs were incubated for 12 and 24 h at 37 °C/100 RPM with varied concentrations from 62.5 to 1000 μg mL^{-1} of p(NAG-Ac-NAE) hydrogel, and generated haemolysis was estimated by recording the absorbance at 540 nm.

Primary neuron culture and immunolabeling. Wistar rats E18 were taken, and pups were sacrificed to obtain their brains. The cerebellum was collected in serum free neurobasal media. Brain tissue was triturated and aspirated using a 20 mL syringe, followed by 10 mL, 5 mL and 2 mL syringes. Next, trypsinization was conducted using 0.25% trypsin for 10 min at 37 °C. Treated mucus was removed, and cells were collected using a 70 μM strainer, followed by centrifugation at 1600 RPM for 10 min at RT to collect the cell palette. Then, the cell palette was dispersed in 1 mL of complete media. Subsequently, 3×10^6 cells were loaded on a positive control coated with poly(L-lysine) and on a hydrogel-coated slide (250 μg mL^{-1} hydrogel suspended in 1× HBSS solution and coated for 18 mm coverslip) and on ~1 mm thin film slice (air dried hydrogel), in 6-well plates with 1X B27, 50 ng NGF supplemented. 10% FBS contained complete neurobasal media with continuous changes at 4-day intervals. After specified time intervals, the media were removed, and the cell fixation was conducted using 4% paraformaldehyde (20 min) and chilled methanol (5 min), followed by permeabilization with 0.1% PBST (15 min). 2% BSA was used to block the cells for 1 h at RT, followed by incubation with primary antibody β-tubulin III (1:500 dilutions in 0.1% BSA) at RT for 1 h, followed by adding the secondary antibody (1:1000 dilution in 01% BSA), rhodamine phalloidin and Hoechst 33258 overnight at 4 °C. It is noteworthy that in each step, the proper washing was conducted for 3 cycles using 1X PBS. Afterward, the confocal microscopic images were acquired using an LSM780 Carl Zeiss confocal microscope. Then, the image was reconstructed using Fiji image j software.[25]

In vitro neuroprotection study in oxidative stress. To evaluate the material's response under stress conditions, 1×10^4 cells per well were cultured for 24 h and pre-treated with 10–160 μM varied concentration of H_2O_2 for 12 h to induce oxidative stress on cells, followed by the replacement of stress media with fresh complete DMEM and treated with 250 μg mL^{-1} of hydrogel. A further 24 h of treatment recovery status was assessed using an MTT assay. For the neuroprotection study, 60% confluent cells were exposed to 10–160 μM concentration of H_2O_2 along with 250 μg mL^{-1} of hydrogel for 24 h; then, an MTT assay was performed for each concentration. Further, for macroscopic analysis, a glass coverslip was coated with 250 μg mL^{-1} of hydrogel for 1 h before performing the experiment. Next, 1×10^5 cells per well were seeded for 12 h to obtain the cells to adhere, followed by the induction of stress *via* 40 μM of H_2O_2 for 24 h. Then, AO/EtBr staining was performed for 30 min, and images were acquired and analysed. Similar experiments were performed on differentiated neurons. To analyse the protective role of hydrogel on differentiated neurons, 1×10^5 cells were cultured and differentiated in the presence of 250 μg mL^{-1} p(NAG-Ac-NAE) hydrogel using 50 ng NGF-supplemented DMEM. Next, the differentiated neurons were exposed to 40 μM H_2O_2-induced oxidative stress (OS) for 24 h. After all the treatment procedures, the cells were immunolabeled, as mentioned in the previous section, and confocal macroscopic images were acquired and evaluated for morphology. Furthermore, the hydrogel was centrifuged and lyophilized. Finally, Raman and FTIR spectroscopy analyses were performed, and the results were compared with the untreated hydrogel to determine whether there was any change in the hydrogel structure.

Determination of intracellular ROS and mitochondrial membrane potential. PC12 cells were cultured for 24 h in 6-well plates. Then, the cells were exposed to 20 μM and 40 μM of H_2O_2 along with 250 μg mL^{-1} of p(NAG-Ac-NAE) hydrogel and p(NAG-*b*-A) hydrogel separately for 24 h. Only 20 μM and 40 μM of H_2O_2-treated cells were considered the positive control, and samples without treatment were considered the negative control. Similarly, PC12 cells were also treated with 250 μg mL^{-1} of p(NAG-Ac-NAE) hydrogel and p(NAG-*b*-A) hydrogel separately without exposure to H_2O_2. After 24 h of incubation with H_2O_2,

p(NAG-Ac-NAE) hydrogel and p(NAG-*b*-A) hydrogel, the cells were harvested by treating the cells with 1 mM of EDTA for 20 min and washed with ice-cold PBS by centrifuging at 1000 × *g* for 5 min. The pellet was resuspended in 500 μL of PBS and 50 μM solution of 2′,7′-dichlorofluorescin diacetate DCFDA added and incubated in a 5% CO_2 incubator at 37 °C for 30 min. The ability of intracellular ROS production was measured using a flow cytometer (Beckman Coulter). Similarly, to determine the effect on mitochondrial potential, 1×10^4 PC12 cells were seeded in each well of 48-well plates, and the cells were exposed to 20 μM and 40 μM of H_2O_2, with/without 250 μg mL^{-1} of p(NAG-Ac-NAE) hydrogel and p(NAG-*b*-A) hydrogel separately. After 24 h of treatment, the treated media were replaced with 5 μM rhodamine 123 and 1 μg mL^{-1} of propidium iodide containing serum-free media. Then, it was incubated for 15 min at a 5% CO_2 incubator at 37 °C; then, fluorescent intensity was measured at an excitation of 488 nm to an emission of 520 nm and excitation of 550 nm to an emission of 610 nm.

Egg yolk angiogenesis assay. The investigation of vascular sprouting CEA assay was performed using fertilized chicken eggs purchased from certified poultry, Varanasi, Uttar Pradesh, India. Eggs were incubated in a humidified 37 °C incubator for 4 days. After that, a small window was created and suspended particles of different concentrations (1 μg mL^{-1}, 25 μg mL^{-1} and 100 μg mL^{-1}) of hydrogel. Further images were acquired at different time intervals (0, 2, 4 and 8 h) by fixing the Magnus Mag Cam DC-10-megapixel camera to the stereo zoom microscope. Images were then analysed using Angiotool Fiji image J software.

Semi-quantitative reverse transcription and polymerase chain reaction (sqRT-PCR). In brief, 1×10^5 PC12 cells and Raw264.7 cells were cultured in 6-well plates, followed by treatment with p(NAG-Ac-NAE) and p(NAG-*b*-A) for 24 h in the presence of H_2O_2 as per the experimental design. Afterwards, the cells were collected and homogenized in 500 μL TRIZOL reagent, and RNA was isolated using the phenol:chloroform extraction method. Then, RNA was precipitated from the collected aqueous layer using 1 mL of isopropanol, pelleted by centrifugation at 12 000*g* for 15 min at 4 °C and washed using 70% ethanol. Then, the pallet was suspended in 50 μL of DEPC-treated water and quantified using a nanodrop. Then, cDNA was synthesized using 1 μg of RNA with oligo dT primer and reverse transcriptase as per the manufacturer's protocol. Afterward, using kicqkstart forward and reverse primers for biomarker target gene VEGFa, Kdr, HIF-1α, TNFα, IL1β and housekeeping gene GAPDH, a polymerase chain reaction was performed using Takara Taq polymer kit R001A, with repetitive cycle number 35, steps of denaturation at 95 °C for 30 s, and annealed at 59 °C for 35 s and extension at 72 °C for 40 s, followed by final extension for 7 min at 72 °C temperature. Then, the amplified products were run on 2% agarose gel, and densitometry calculations were performed.

Statistical analysis. All the data were expressed as the mean of at least three means of separate experiments with (±) standard deviation. The statistical significance ($p < 0.05$) level was calculated by applying the one-way ANOVA test software.

3. Results

Physical properties of p(NAG-Ac-NAE) hydrogel

The p(NAG-Ac-NAE) hydrogel was synthesized through a free radical/cross-linking polymerization approach, as shown in Scheme 1. *N*-Acryloylglycine, *N*-acrylamide and *N*-acryloylglutamate were taken in a 2 : 1 : 2 ratio. Sonication was applied to obtain spherical hydrogel, and polymerization was initiated by AIBN at 70 °C. Cross-linking agent DVB was used to obtain spherical, pH-sensitive, highly branched and high wettability containing co-polymeric hydrogel nanoparticles. Chemical functionality for monomers and polymers was confirmed through FTIR (Fig. S1(a)–(d), ESI†), ^{1}H NMR and ^{13}C NMR (Fig. S2 and S3, ESI†). From FTIR, the characteristic bands are detected at 3336 cm^{-1} (N–H (stretching), 3182 cm^{-1} (–O–H stretching), 2912 cm^{-1} (–CH stretching, confirming the formation of a polymer chain), 1716 cm^{-1} (–C═O, carbonyl stretching), 1549 cm^{-1} (–O–H, overtone), and 1653 cm^{-1} (1st overtone of –NH) functional groups. From ^{1}H NMR ($CDCl_3$), the chemical shifts of 12.5 δ (O–H of carboxylic acid), 8.9 δ (N–H of 2° amine), 7.26 δ (benzene), compound, 6.8 δ (H_2C═CH_2), 6.17 (–CH (12)) in ^{1}H NMR spectrum, and 44 and 34 ppm (8 + 2 splinted peak of 2° alkane) were identified, and 86–79 ppm (carboxylic –OH and ester) in ^{13}C NMR spectrum confirmed the synthesis of p(NAG-Ac-NAE) polymers. To determine the average molecular weight, the MALDI-ToF spectrum was obtained

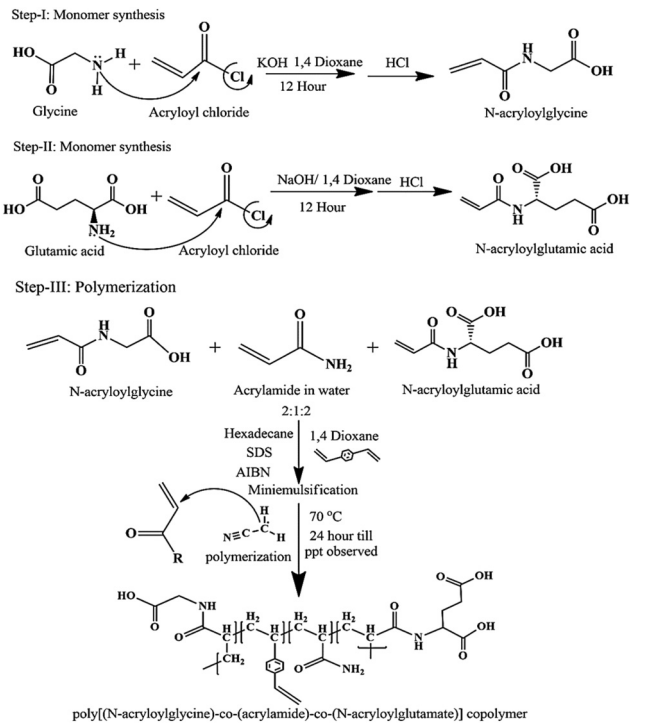

Scheme 1 Representative steps for the synthesis of the poly[(*N*-acryloylglycine)-*co*-(acrylamide)-*co*-(*N*-acryloylglutamate)] hydrogel.

(Fig. S6, ESI†), and the results showed that the repeating units varied from 194 to 224. The M_n and M_w are calculated to be 1690 Da and 1773 Da, respectively, with a polydispersity index (PDI) of 1.04.

The particle size of the polymeric particles was confirmed through FESEM (Fig. 1(a)) and HRTEM (Fig. 1(b) and (c)), and they are amorphous/semi crystalline (Fig. 1(d)). The HRTEM macrograph (Fig. S4a, ESI†) shows the darker block patches inside the orientation, and light block patches in the outer side orientation show the random co-polymer formation. The particle size was calculated to be 20–50 nm in diameter (Fig. 1(e) and (f)), while the hydrodynamic diameter was obtained to be 189 ± 5.16 nm (Fig. S8, ESI†). This increase in the diameter is observed due to the swelling of the hydrogel. Polymer particles developed here are highly branched, co-connected (HRTEM micrographs, Fig. 1(b)) and porous (pore dia. ~1.2 to 2.6 nm) (Fig. 1(c)–(g)). From the HRTEM macrograph, it is also confirmed that there are short-range crystalline fringes (~0.25 nm) (Fig. 1(c) and Xb) present in the polymeric particles, which are responsible for the semi-crystalline nature of the hydrogel particles (Fig. 1(d), SAED obtained from HRTEM). The crystalline nature is further confirmed through the XRD (Fig. 1(h)). These particles are semi-crystalline due to the formation of an ordered network structure by a cross-linking agent (DVB) and acryloylglycine. This semi-crystalline nature of this hydrogel enhances the thermal stability confirmed through the TGA (Fig. S5a, ESI†) and DSC analysis (Fig. S5b, ESI†). From the TGA, four stages of mass loss are observed. For example, in stage 1, a 6.99% mass loss at ~100 °C occurs due to the presence of free moisture. In stages 2, 3, and 4, 21.07%, 31.55% and 36.75% mass losses, respectively, were observed (Fig. S5a, ESI†), which occurred due to the degradation of the polymeric chains. To evaluate the thermal phase transition, DSC was recorded from −140 °C to 550 °C (Fig. S5b, ESI†). The glass transition (T_g) for p(NAG-Ac-NAE) hydrogel is observed to be −45.17 °C, and the first exothermic transition of p(NAG-Ac-NAE) hydrogel observed at −10.48 °C (ΔH_c = 5.08 J g^{-1}) revealed that at a lower temperature, hydrogel recrystallized to form a secondary phase(s). An endothermic transition is observed at 31–69 °C with a peak position of 48.22 °C (ΔH_f = 2.37 J g^{-1}) due to the formation of a tertiary phase.

The third endothermic transition is observed at 238 °C, which correlates with the stage-2 mass loss of DSC and corresponds to the loss of low molecular weight components. The transition phase started at 210 °C due to the evolution of NH-containing components.[26] Another exothermic transition that appeared at 305 °C can be correlated with the DSC plot of hydrogel, which occurred due to the degradation of the alkene and carboxylate groups.[26,27]

Swelling behaviour of p(NAG-Ac-NAE) hydrogel

The incorporation of a cross-linking agent (DVB) created the porous structure of the hydrogel particles, as shown in HRTEM (Fig. 1(c)). These hydrogel particles swelled as they came in contact with water (Fig. 2(a)). Furthermore, the swelling behaviour was evaluated by immersing and equilibrating the 5 mg of freeze-dried hydrogel in 1 mL of PBS buffer with different pH levels (3, 5, 6, 7.4, and 8) (Fig. 2(b)) at room temperature (25 °C). From Fig. 2(b), it is observed that the swelling behaviour of the hydrogel is pH-dependent. For example, for pH 3, 5, 6, 7.4, and 8, the MSI values were calculated at different time intervals, and the values were obtained to be 2274%, 2458%, 2872%, 3676% and 3383%, respectively, for 45 min of incubation of the polymeric particles (Fig. 2(b)). For 72 h of incubation, the MSI

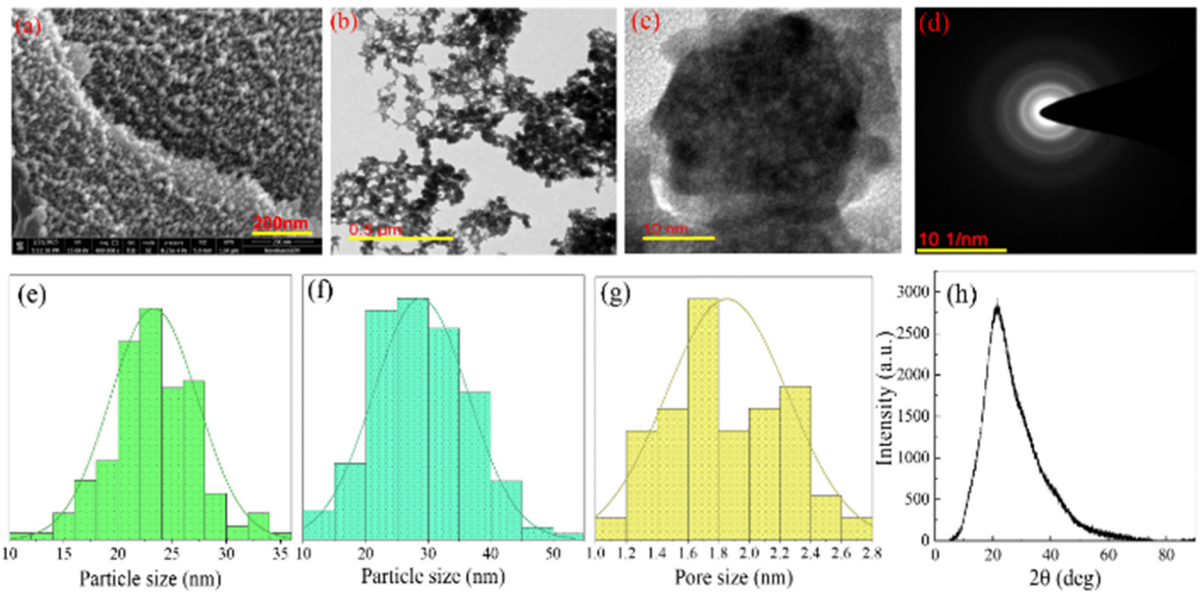

Fig. 1 Physical properties of the poly[(*N*-acryloyl-glycine)-*co*-(acrylamide)-*co*-(*N*-acryloyl glutamate)] (p(NAG-Ac-NAE)) hydrogel. (a) FESEM image and (b) and (c) HRTEM images at low and high magnifications. (d) SAED pattern of the particles. (e) and (f) are the average particle size distribution obtained from Fig. 1(a) and (b) respectively. (g) Pore size distribution of the particles obtained from 1c, and (h) XRD pattern of the hydrogel.

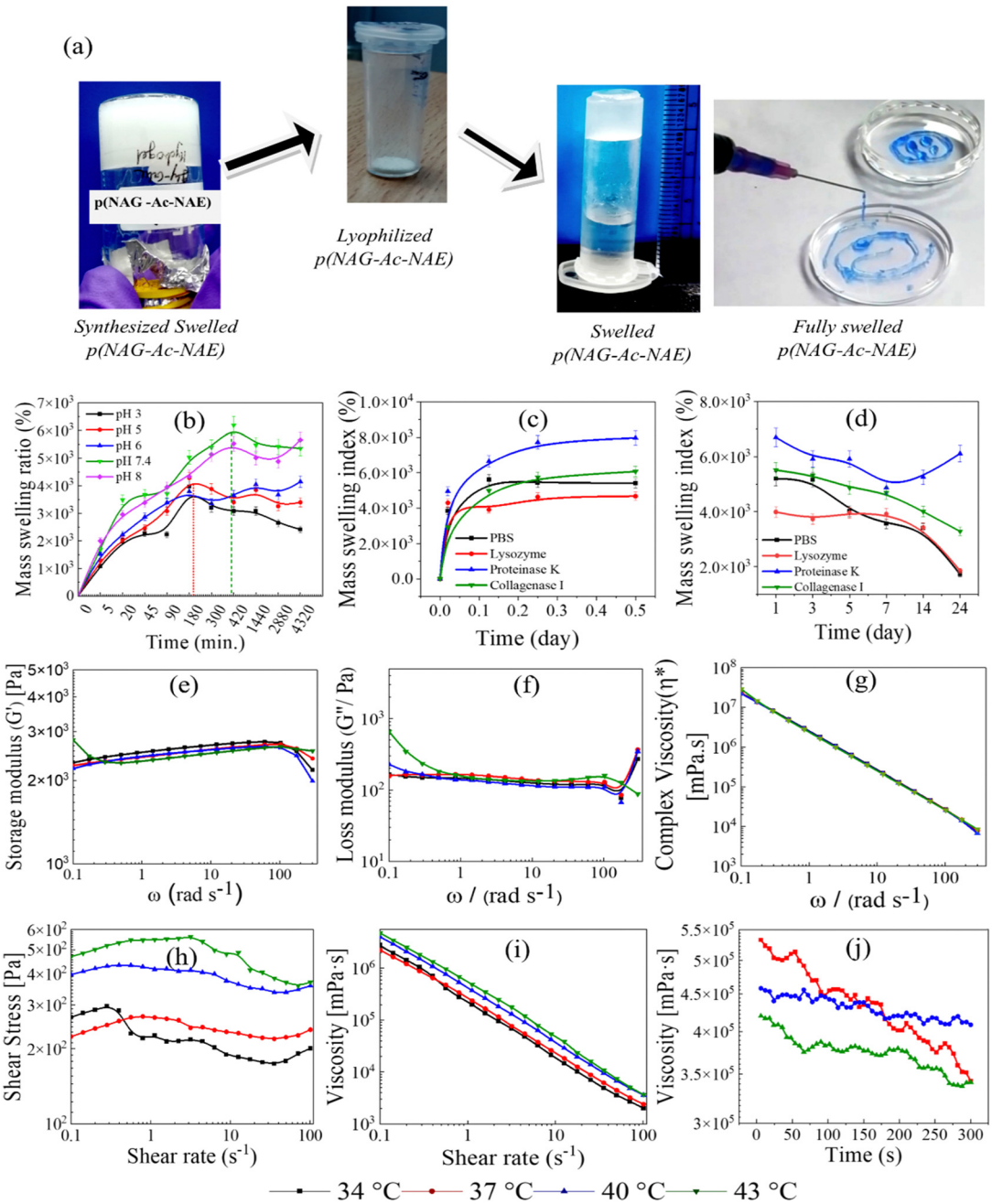

Fig. 2 Swelling and degradation behaviour: (a) pictorial representation of the swelled and lyophilized hydrogel along with flow of fully swelled hydrogel from 2 mL syringe gauze size 21G, (b) MSI of the hydrogel at different pH levels of PBS, (c) MSI of the hydrogel in different enzymes, (c) degradation of hydrogel in different pH levels, and (d) degradation of hydrogel in the presence of different enzymatic solutions: lysozyme, proteinase K and collagenase IV with 100 μg mL^{-1} concentration and PBS. (e)–(j) Rheological properties measured at different temperatures (34 °C, 37 °C, 40 °C and 43 °C). (e) Storage modulus *vs.* angular frequency, (f) loss modulus *vs.* angular frequency, and (g) complex viscosity (η^*) *vs.* angular frequency. (h) Change in shear stress *vs.* shear rate at different temperatures, (i) co-efficient of viscosity (η) as a function of shear rate (γ) and (j) co-efficient (η) as a function of time and temperature.

values were obtained to be 2645%, 4280%, 4144%, 6188% and 5660%, respectively (Fig. 2(b)). The change in MSI with a change in pH is observed due to the presence of a larger extent of –COOH groups. Protonation of –COOH makes the tighter and less hydrophilicity at lower pH, while at higher pH, the electrostatic Interactions of –COOH groups are responsible for more hydration and more swelling.[14,28] Further, polymeric particles were taken in water, and the size distribution, zeta potential and conductivity were measured using DLS (Fig. S8, ESI†). The average hydrodynamic diameter of the polymeric hydrogel nanoparticles was calculated to be 1250 ± 6.28 nm with a PDI of 0.695. This increase in particle size is observed

due to the swelling of the hydrogel particle. The average zeta potential value (ζ) is calculated to be -36.9 ($\pm$ 6.28) mV at 25 °C. The conductivity of the p(NAG-Ac-NAE) hydrogel was also measured to be 7.85×10^{-5} S cm^{-1}, which is in the semiconducting range and can correlate with the conductivity of the brain tissues. The hydrodynamic diameter obtained from DLS and the particle size results obtained from TEM (Fig. 1(c)) correlated and found that there was $\sim$40 times (6400%) increase in the swelling of the hydrogel particles.

Disassociation/degradation behaviours

The disassociation behaviours of the hydrogel are studied in terms of swelling behaviour at different pH levels (3, 5, 6, 7.4, and 8) and in the presence of different enzymes, *e.g.*, lysozyme, proteinase K and collagenase, to mimic biological mediums, in which the MSIs varied both with the medium as well as with time and pH. At different pH levels, the degradation was observed in the order of pH: 3 > 5 > 6 > 7.4 > 8 (Fig. 2(b)). The maximum MSI was observed within 12 h of incubation by 5402%, 4672%, 7966%, and 6067% when incubated in PBS, lysozyme, proteinase K, and collagenase, respectively. Subsequently, the swelling index values for hydrogel decreased continuously after 12 h due to the disassociation of the polymer side functional groups in the presence of enzymes (Fig. 2(c) and (d)). This biodegradation is observed for up to 24 days of incubation and then continuously degraded, as shown in Fig. 2(c) and (d) (enzyme solution was with 5 days of interval).

After 24 h of incubation, the highest degradation is observed in the presence of lysozyme and PBS. Similarly, when the hydrogel was incubated for 40 days in the same solution (without replacing) (Fig. S7, ESI†), the highest degradation was observed in the presence of lysozyme and PBS. The swelling ratio of the hydrogel increased after 7 days of incubation with proteinase K, which can be corroborated with the protease inhibitory activities of p(NAG-Ac-NAE). This increase in swelling is observed due to the agglomeration and formation of a new complex (Fig. S7, ESI†). Thus, under physiological conditions and in the presence of different biological components, this degradable hydrogel is advantageous for use in the living body for different therapeutic applications.

Viscoelastic and rheological flow behaviour

Viscoelastic and rheological flow behaviour of p(NAG-Ac-NAE) hydrogel were measured through frequency sweep measurements and steady shear measurements (Fig. 2(e)–(j)).

Storage modulus (G') values were calculated to vary from 2.3 kPa to 2.7 kPa at 0.1–100 rad s^{-1} (Fig. 2(e)) and loss modulus (G'') varied from 0.12 kPa to 0.16 kPa at 0.1–100 rad s^{-1} (Fig. 2(f)) at the physiological temperature (37 °C). At higher temperatures, such as 40 °C and 43 °C, the G' decreases and G'' increases due to the deformation of the hydrogel at a higher angular frequency. This poly(NAG-Ac-NAE) hydrogel exhibits viscoelastic behaviour with an increase in the storage modulus as the frequency increases up to 100 rad s^{-1}. A similar trend is observed for complex viscosity (Fig. 2(g)), with an increase in the frequency in all different temperature ranges, showing non-Newtonian behaviour and shear thinning properties of poly(NAG-Ac-NAE) hydrogel. An increase in temperature shows higher viscosity, and with shear rate (Fig. 2(i)) and time (Fig. 2(j)), it decreases due to the shear thinning property of the poly(NAG-Ac-NAE) hydrogel. Shear thinning behavior allows injectability and plays an advantageous role in drug delivery, cell encapsulation, granular hydrogel formation and tissue regeneration.[29] Further, shear stress *vs.* shear rate shows a complex viscoelastic behavior of the hydrogel (Fig. 2(h)), and at higher temperatures, it decreases, which may be due to the deformation of the network structure.

Biocompatibility and hemocompatibility of p(NAG-Ac-NAE)

After evaluation of physicochemical properties, the biocompatibility of p(NAG-Ac-NAE) hydrogel was assessed using healthy cell lines (Fig. 3(a)), HUVEC cells (human umbilical vein endothelial cells), and neural crest-originated catecholamine PC12 cell line, and using the different cancer cell lines, such as MDA-MB-231, MCF7 and LN229 cells, treated with different concentrations of hydrogel (*e.g.*, 10, 25, 50, 100, 250, 500 and 1000 μg mL^{-1}) for 24 h. At a dose of 200 μg mL^{-1} of p(NAG-Ac-NAE) hydrogel (Fig. 3(a)), HUVEC cells are 100% viable. When treated with a lower concentration of 5 μg mL^{-1}, an increase in cell proliferation is observed (114 $\pm$ 0.07%). In PC12 cells, a significant increase in cellular proliferation is observed at different concentrations of hydrogel, and the highest proliferation is observed at a concentration of 250 μg mL^{-1} (152.7 $\pm$ 13.7%) ($p \sim 0.0024$) (Fig. 3(a)). However, in aggressive-type cancer cell lines, substantial cell death and cell killing are observed in the following order: LN229 > MDA-MB-231 > MCF7 (Fig. 3(a)). The AO/PI stained macroscopic images of PC12 cells (on day 5th) revealed that in treatment with p(NAE-Ac-NAG) hydrogel, normal apoptotic cell death was observed (Fig. 3(b)). This occurred due to the prolonged effect of p(NAE-Ac-NAG) on the cell cycle stages. Furthermore, these results suggest that the cytotoxicity towards cancer cells revealed the non-tumorigenic activity of our hydrogel. It is worth mentioning that 20% cytotoxicity is observed against the cancer cells. Moreover, this hydrogel favours cellular proliferation in healthy PC12 cells.

Furthermore, hemolysis studies were performed for its biologically safe use considering five concentrations (62.5, 125, 250, 500, and 1000 μg mL^{-1}), and the hemolysis percentages observed for 8 h were 0.36 $\pm$ 0.13, 0.15 $\pm$ 0.05, 0.96 $\pm$ 0.7, 7.00 $\pm$ 1.04 and 4.33 $\pm$ 0.53, respectively. For 24 h treatment, the values obtained are 1.90 $\pm$ 0.21, 0.32 $\pm$ 0.17, 4.68 $\pm$ 0.14, 3.03 $\pm$ 0.64 and 8.17 $\pm$ 3.68 for five concentrations, respectively (Fig. 3(c)). Above the concentration of 250 μg mL^{-1}, this hydrogel acts as a hemolytic material, while below this concentration, it acts as a nonhemolytic material. Hence, for future biological application, p(NAG-Ac-NAE) hydrogel is limited to use at lower concentrations. However, the observation of the highest cell proliferation at 250 μg mL^{-1} revealed this material to be hemocompatible and safe to use for therapeutic applications at lower concentrations.

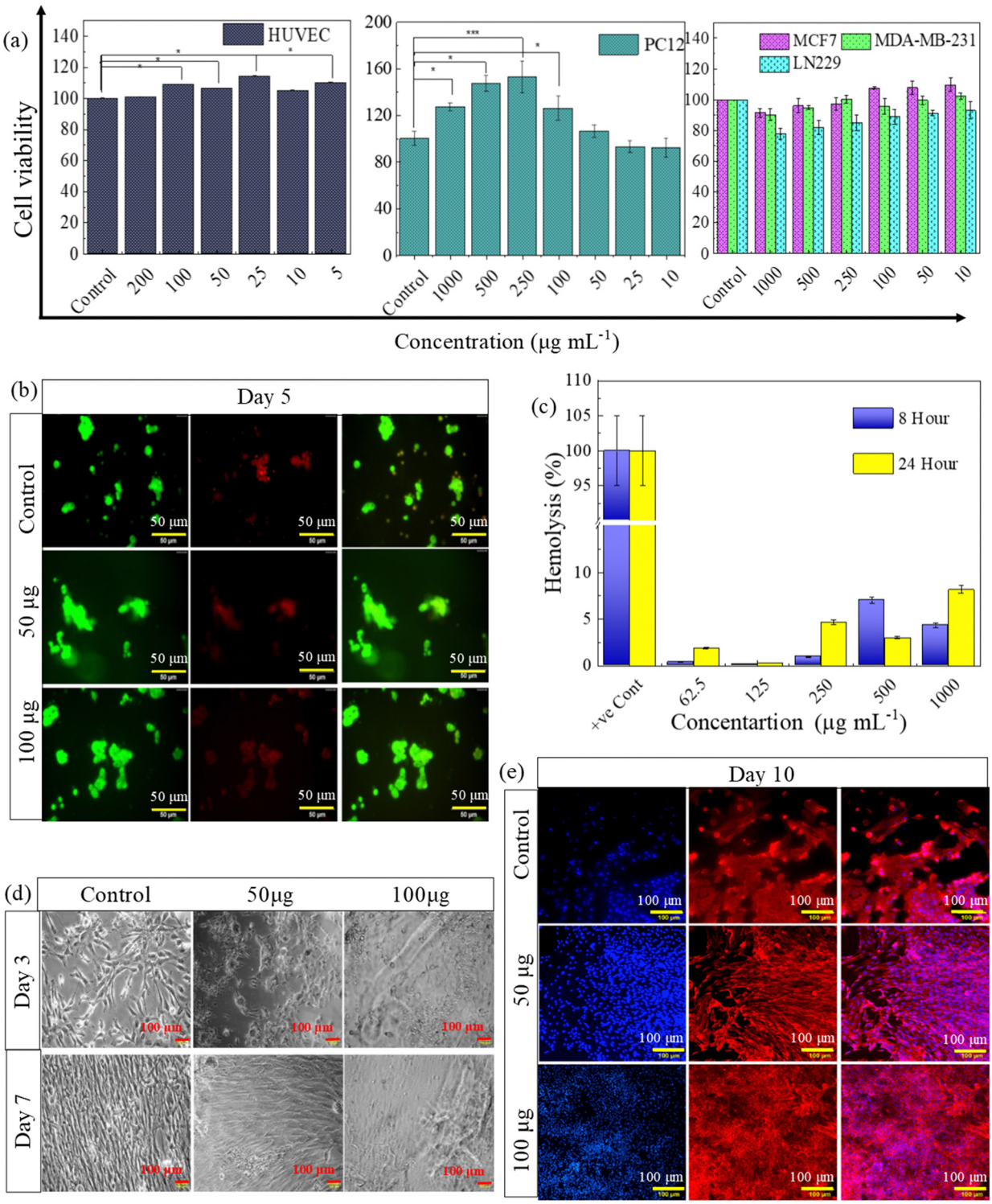

Fig. 3 Biocompatibility and hemocompatibility of the poly(NAG-Ac-NAE) hydrogel. (a) Cell viability in HUVEC, PC12 and cancer cell lines such as LN229, MDA-MB-231 and MCF7 in the presence of the p(NAG-Ac-NAE) hydrogel. (b) Live/dead (AO/PI stained) macroscopic images of PC12 cells in the treatment of the p(NAG-Ac-NAE) hydrogel at concentrations of 100 μg mL^{-1} and 250 μg mL^{-1} on day 5, (c) % hemolysis at different concentrations of the hydrogel (1000, 500, 250, 125 and 62.5 μg mL^{-1}). (d) Microscopy images of primary neuronal cells in the treatment of p(NAG-Ac-NAE) hydrogel (50 and 100 μg mL^{-1}) and (e) the cytoskeleton framework of primary neurons in the presence of the p(NAG-Ac-NAE) hydrogel at concentrations of 100 μg mL^{-1} and 250 μg mL^{-1}, (red = F-actin and blue = nucleus) only.

Then, to evaluate the neurogenic potential of the (NAE-Ac-NAG) hydrogel, primary neurons were cultured in the presence of p(NAE-Ac-NAG) and grew comparably healthy with a mature neuronal structure. It was scrutinized on the 3rd and 7th days,

which showed high biocompatibility of p(NAE-Ac-NAG) towards the primary neuronal cells (Fig. 3(d) and (e)). Furthermore, rhodamine phalloidin selectively labeled the F-actin of primary culture neurons, as shown in Fig. 3(e), and revealed that the p(NAG-Ac-NAE) hydrogel promotes the cellular proliferation with the healthy network formation of actin filament along with a very high stability of cytoskeleton network structure compared to the control group (on the 10th day).

p(NAG-Ac-NAE) hydrogel-induced primary neurite outgrowth

The neurite outgrowth, substantial stability of cytoskeleton, and microtubule dynamics *in vitro* study were performed on primary rat cortical neurons at different time intervals for 2, 7, 14, and 21 days (Fig. 4(a)–(g)). From the confocal microscopy study, it is evident that at the concentration of 250 μg mL^{-1} of hydrogel (Fig. 4(a), on day 2, β-tubulin panel), initial differentiation of neuronal cells started along with the adhesion, while in the control group, only the cell adhesion was achieved. It is also observed that there is a significant increase in the cell population on treatment with 250 μg mL^{-1} coated hydrogel within 2 days ($p \sim 0.00188$) compared to the control group (on 2nd and 7th days) and p(NAG-Ac-NAE) hydrogel slice group ($p \sim 0.00349$). The decrease in cell populations with an increase in differentiation and the extent of neurite outgrowth was confirmed through a gradual increase in green fluorescence (Fig. 4(e)). β-Tubulin III expression from day 2nd to 21st is found to be continuously increased for the p(NAG-Ac-NAE) hydrogel compared to the control group. These results further confirmed an increase in the axonal path length with an increase in the treatment period (Fig. 4(f)). It is also revealed that, among the three groups under study, the relative growth order of axonal path length is found to be p(NAG-Ac-NAE) hydrogel (250 μg coating) > p(NAG-Ac-NAE) hydrogel > control (Fig. 4(f)) within 21 days.

From Fig. 4(g), a significant difference in the number of junctions is observed between the 2nd and 14th days. In p(NAG-Ac-NAE) hydrogel (250 μg coating slide), maximum growth of neuron junction is calculated within the 7th day ($p \sim 0.00197$), and the results were compared with the control group and p(NAG-Ac-NAE) hydrogel. In the p(NAG-Ac-NAE) hydrogel slice, it is observed that the highest number of junctions formed on day 14 ($p \sim 0.0001$) and day 21 ($p \sim 0.04$) compared to the control (Fig. 4(g)). Thus, the increase in the number of junctions refers to the increase in the number of branches and synapses. Furthermore, a continuous increase in the signal of F-actin from day 2nd to 21st was observed, signifying a very high growth and a very high stability of the neuronal structure in the novel hydrogel (Fig. 4(a)–(d)). Interestingly, in a previous report, the highest neuronal growth was observed on day 14 of incubation using our hydrogels.[17] However, in the present study, an increased signal of axonal growth is observed within 7 days of treatment. This could occur due to the associated excitatory signal of glutamate moieties present in the p(NAG-Ac-NAE) hydrogel. Thus, this finding confirms that the novel hydrogel promotes greater efficiency in neuronal growth within a short time.

Neuroprotective role of p(NAG-Ac-NAE) hydrogel

Higher oxygen consumption in the brain and the presence of high polyunsaturated fatty acid content in neuronal membranes lead neuronal cells to become vulnerable to oxidative damage. Oxidative stress results in the accumulation of reactive oxygen species (ROS) that leads to lipid peroxidation, mitochondrial dysfunction, enhanced production, and migration of oxidized forms of α-synuclein as a consequence of neuronal cell death.[30,31] H_2O_2-induced oxidative stress shows a dose-dependent effect in various cells; for example, at 0.8–6 μM, concentration cells remain healthy.[31] At the intermediate concentration, such as 30 μM of H_2O_2, the membrane babbling occurred within 3 h of treatment,[32] and within 24 h of treatment, ~50% of treated cells could survive. However, at relatively higher concentrations of H_2O_2 (50 μM), almost all the cells become lethal.[33] Hence, to mimic and analyse the probable outcome of the p(NAG-Ac-NAE) hydrogel under pathological conditions, H_2O_2-induced stress was generated on PC12 cells using different concentrations in the range of 5–160 μM of H_2O_2. In a previous report, we already showed the neuroprotective role of p(NAG-*b*-A) hydrogel, which was only glycine-based hydrogel.[17] Herein, we modulated the p(NAG-*b*-A) hydrogel with glutamate and further investigated its neuroprotective activity. We studied the neuroprotective assay at a lower concentration of the p(NAG-Ac-NAE) hydrogel. Treatment with 250 μg mL^{-1} and 100 μg mL^{-1} of p(NAG-Ac-NAE) hydrogel under oxidative stress (H_2O_2) conditions shows an excellent protective role. Similarly, with primary exposure to oxidative stress for 12 h and removal of stress, followed by treatment with 250 μg mL^{-1} and 100 μg mL^{-1} of p(NAG-Ac-NAE) hydrogel, it exhibited excellent recovery potential. Further, it is observed that almost 80–90% of the cells become lethal at 80–160 μM concentration of H_2O_2, whereas 40–60% of the cells are viable at 40 μM concentration of H_2O_2 (Fig. 5(a) and (b)). Excitingly at 250 μg mL^{-1} concentration of p(NAG-Ac-NAE), it possesses a substantial protective role (Fig. 5(a)) of up to 40 μM concentration of H_2O_2-induced oxidative stress (OS), whereas under the lower stress conditions (40–20 μM H_2O_2 induced OS), the cell viability is enhanced. Furthermore, this finding can be corroborated with the acridine orange AO) and ethidium bromide (EtBr) staining of PC12 cells after 12 h of incubation in the control under (20 μM and 40 μM) H_2O_2-induced oxidative stress conditions and in the presence of 100 μg mL^{-1} of p(NAG-Ac-NAE) hydrogel (Fig. 5(c) and (d)). It is observed that the maximum number of cells undergo apoptotic cell death under H_2O_2-induced OS conditions in the order of 40 μM > 20 μM concentrations. Differentiated PC12 cells under OS conditions prevented neurite outgrowth, damage in axonal terminals, shortening of neurites, nuclear damage and a decrease in F-actin (Fig. 5(d)) compared to the standard control. Moreover, p(NAG-Ac-NAE) neutralizes the OS, promotes an intact neuronal structure with thicker neurite and prominent axonal terminal and increases the signal for F-actin along with an intact nucleus.

Effect of p(NAG-Ac-NAE) in the cell cycle

Stress mitigating effect analysis was performed through cell cycle analysis. The DNA content was detected by flow cytometry

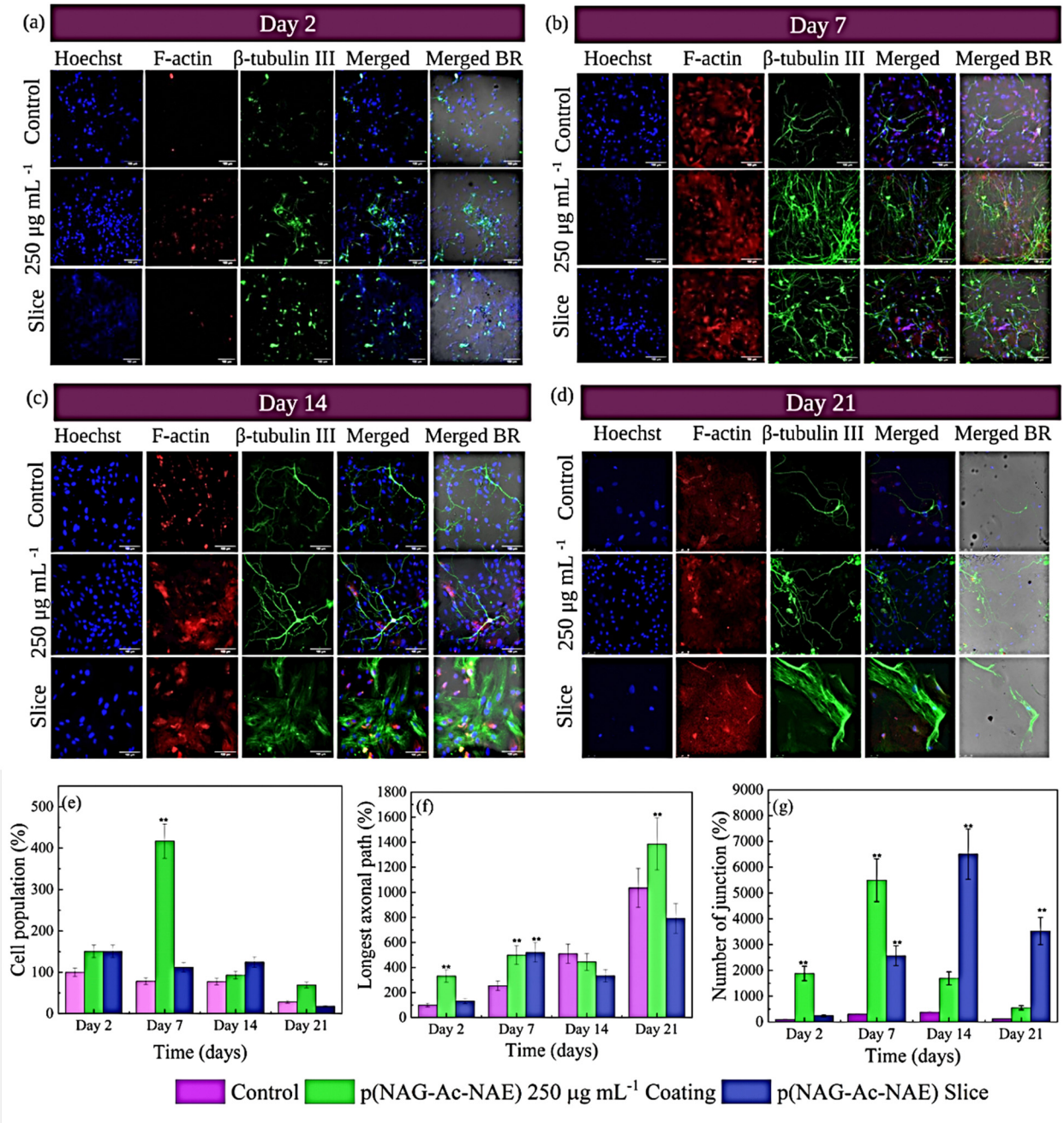

Fig. 4 Confocal microscopy results of neuron growth on 250 μg mL^{-1} nanohydrogel coated slide and a thin slice of the poly(NAG-Ac-NAE) co-polymeric hydrogel. (a) Images showing the nature of cellular adhesion and growth on day 2, (b) images showing cellular differentiation and neurite extension on day 7 and (c) and (d) are images of cellular differentiation and neurite extension on day 14 and 21,respectively. (e) Estimated values showing the increase in the cell population (%) at different intervals of culture, (f) percentage (%) increase in the longest axonal path varied at different time periods and (g) percentage (%) increase in the number of junctions (branching in neuron) changed at different time periods. In microscopy images, the Hoechst 33258 (blue) stain represents the nucleus, immune-labelled β-tubulin III (green) shows neurite extension, and immune labelled with phalloidin (red) shows F-actin. (scale bar 100 μm).

after the treatment of cells with p(NAG-*b*-A), p(NAG-Ac-NAE), H_2O_2, H_2O_2 along with p(NAG-*b*-A) and H_2O_2 along p(NAG-Ac-NAE) hydrogel, as discussed in the Experimental section. In the control, 55.01% of cells are in G0/G1 phase, 0.18% in the S phase and 10.59% in the G2/M phase; 22.80% are in the sub-G1 phase when cells are cultured for 24 h. The sub-G1 phase shows degraded DNA fragments as evidence of apoptosis[34] (Fig. 6).

In the previous study, we reported on neuroprotective activity.[17] Furthermore, in this work, we revealed that p(NAG-*b*-A) influences the increase in the G0/G1 and G2/M phases to a higher extent with a 50% decrease in the sub-G1 phase in contrast to the control (Fig. 6). However, the p(NAG-Ac-NAE) hydrogel helps to increase the G0/G1 and decrease the G2/M in the sub-G1 phase. Furthermore, 40 μM of H_2O_2 treatment

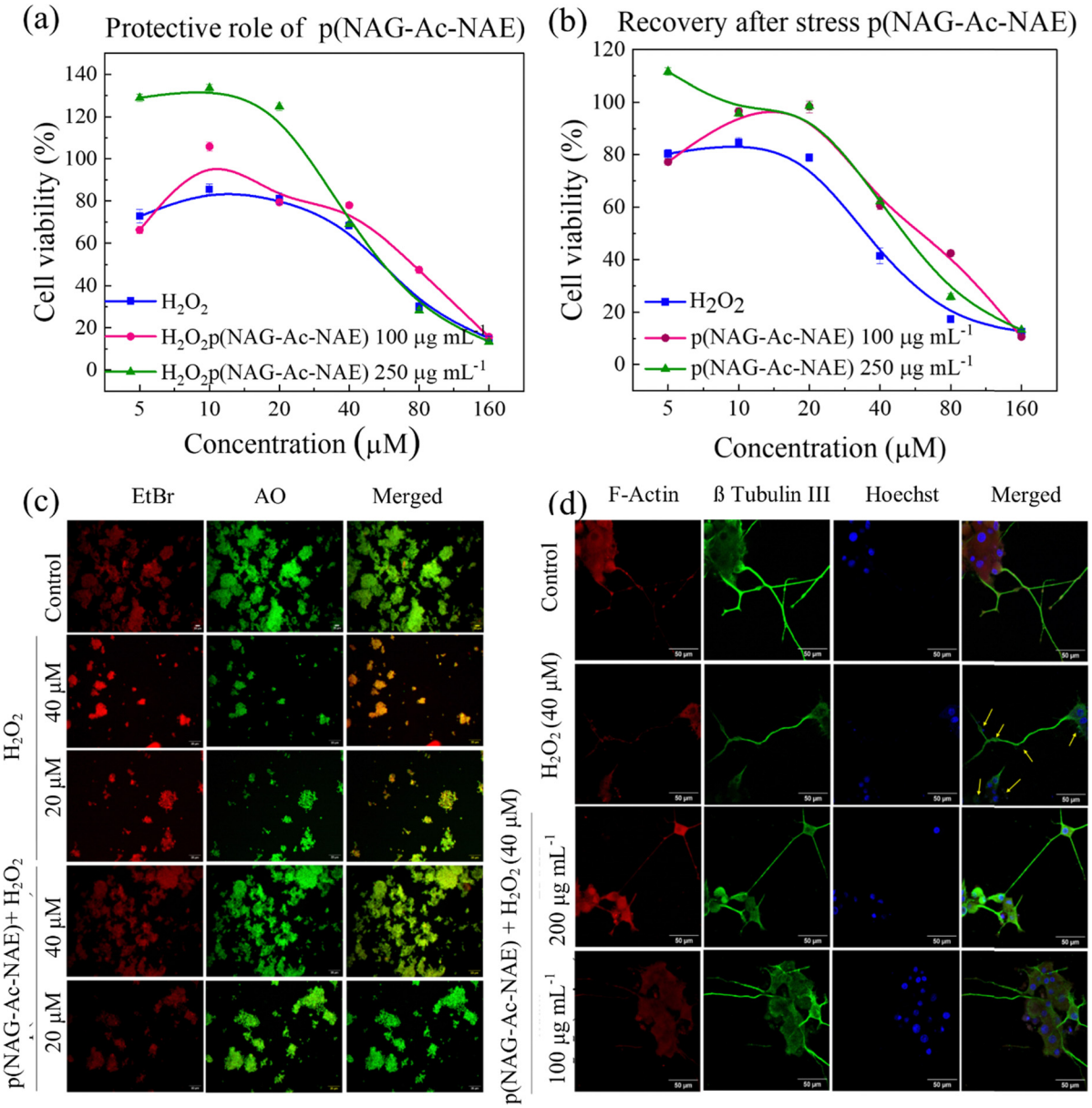

Fig. 5 Neuroprotective role of the p(NAG-Ac-NAE) hydrogel. (a) Protective role of the p(NAG-Ac-NAE) hydrogel in the presence of different concentrations of H_2O_2, (b) stress-induced recovery status of PC12 cells using the p(NAG-Ac-NAE) hydrogel after H_2O_2-induced stress. (c) Fluorescent microscopy images for AO/EtBr stained PC12 cells under different conditions: untreated control, treated with H_2O_2 40 μM and H_2O_2 20 μM in the p(NAG-Ac-NAE) hydrogel in H_2O_2 40 μM. p(NAG-Ac-NAE) hydrogel in H_2O_2 20 μM and (d) cytoskeleton network stabilization by the p(NAG-Ac-NAE) hydrogel and in the presence of 40 μM H_2O_2 induced OS at highest proliferative concentration of 250 μg mL^{-1} hydrogel, respectively which further confirmed by cell cycle analysis.

induces the sub-G1 phase (30.9%), and the reduction of the G0/G1 phase represents the induced apoptosis. Treatment with p(NAG-Ac-NAE) and p(NAG-*b*-A) reduced the cell population in the sub-G1 phase. Additionally, in the presence of H_2O_2 stress, cellular proliferation was revealed with an increase in cell numbers at the G0/G1 phase. These results are the pieces of evidence of the stress-mitigating effect of p(NAG-Ac-NAE) and p(NAG-*b*-A) hydrogels.

Comparative ROS mitigating effect of p(NAG-Ac-NAE) and p(NAG-*b*-A) hydrogels

A critical level of ROS is essential to meet the high demand for ATP for a normal physiological response. However, dysfunction in mitochondrial machinery, exaggerated ROS production, and alteration in mitochondrial metabolism leads to the neurological condition. Mitochondrial membrane potential ($\Delta\Psi_M$) is a central intermediate in oxidative energy metabolism.[35] The cationic dye rhodamine 123 accumulates in the mitochondrial inner membrane, and the decay in fluorescence is proportional to mitochondrial membrane potential depolarization.

Furthermore, to elucidate the exact mechanism in neurogenesis and neuroprotection effects of p(NAG-Ac-NAE), mitochondrial depolarization and ROS generation were evaluated. The treatment of PC 12 with p(NAG-Ac-NAE) does not show any effect on the mitochondrial polarization, while minimum

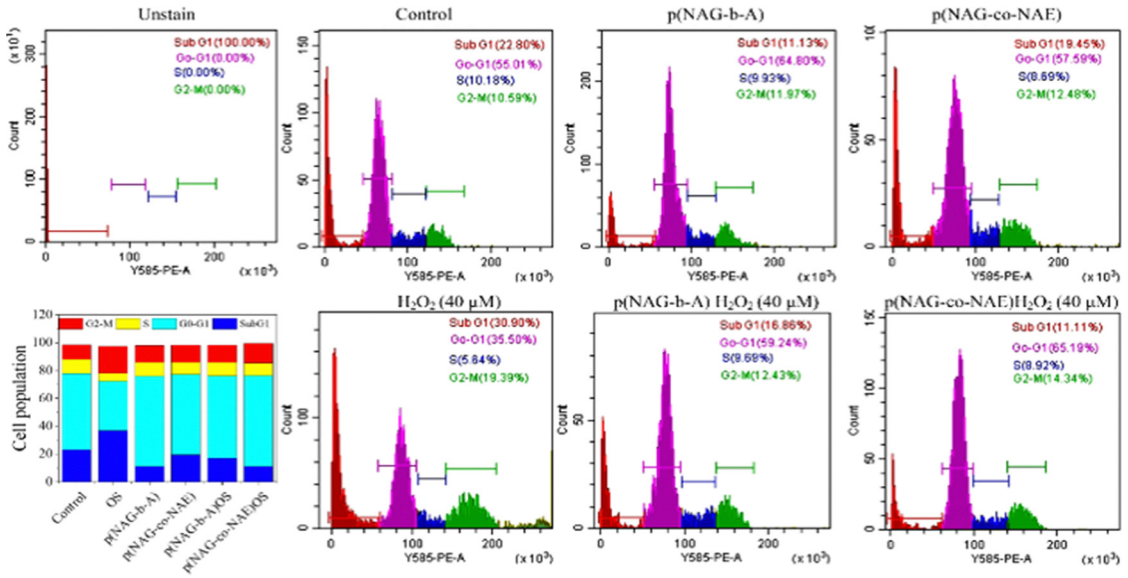

Fig. 6 Stress mitigating effect analysis through cell cycle analysis. DNA content detected by flow cytometry in the treatment of the p(NAG-*b*-A), p(NAG-Ac-NAE), H_2O_2, H_2O_2 along with p(NAG-*b*-A) and H_2O_2 along p(NAG-Ac-NAE) hydrogel.

depolarization is observed with p(NAG-*b*-A) hydrogel. As depicted in Fig. 7, H_2O_2-induced apoptosis is observed due to the depolarization of the mitochondria in a dose-dependent manner (reduces the fluorescence intensity; Fig. 7(a)). This increase in depolarization is reduced by treatment with p(NAG-Ac-NAE) and p(NAG-*b*-A) hydrogels. Interestingly, at the exposure of 20 μM H_2O_2 and treatment with p(NAG-*b*-A) hydrogel, MMP is almost equal to the control. With exposure of 20 μM and 40 μM H_2O_2 under treatment with p(NAG-Ac-NAE) hydrogel, an increase in fluorescence intensity ratios was observed similar to the 20 μM H_2O_2 treatment group. Earlier, it was reported that 20 μM H_2O_2 expresses a preconditioning effect and suppresses apoptosis.[36,37] This phenomenon is clearly shown in our results, where exposure to 20 μM and 40 μM H_2O_2, followed by treatment with p(NAG-Ac-NAE) hydrogel, increased the fluorescence intensity to an equivalent extent to 20 μM H_2O_2 treatment. These results are comparable with Fig. 6, where a reduction in the sub-G1 phase was observed, which corroborated the mitigating effect of p(NAG-Ac-NAE). The percentage of ROS-producing cells in normal control (untreated PC12 cell) is found to be less by 33.72% (Fig. 7(b)-1), while for treatment with 20 μM (Fig. 7(b)-2) and 40 μM H_2O_2 (Fig. 7(b)-3), it is found to be increased in ROS by up to 42.33% and 52.49%, respectively. After treatment with p(NAG-Ac-NAE) (Fig. 7(b)-4) and p(NAG-*b*-A) (Fig. 7(b)-7) hydrogels, intracellular ROS is found to be equivalent to the control. The PC12 cells were cultured in the presence of p(NAG-Ac-NAE) and p(NAG-*b*-A) hydrogels and exposed to 20 μM and 40 μM of H_2O_2 for 24 h separately. Intracellular ROS scavenging effects were observed more in the treatment groups compared to the OS group alone. ROS scavenging effect is observed more in p(NAG-*b*-A) hydrogel compared to the p(NAG-Ac-NAE) hydrogel with differences in values of 5.67% and 13.88% for p(NAG-*b*-A) hydrogel, and 3.49% and 13.38% for p(NAG-Ac-NAE) hydrogel to the respective concentrations of 20 μM and 40 μM of H_2O_2, respectively. These results revealed that the p(NAG-Ac-NAE) and p(NAG-*b*-A) hydrogels helped to reduce the depolarization state of PC12 cells under oxidative stress conditions and provided the preconditioning effect for survival, proliferation and differentiation of the PC12 cells. Furthermore, to elucidate the mechanism involved in the protective role of p(NAG-Ac-NAE) and p(NAG-*b*-A) hydrogels, we immersed the treated hydrogel into 40 μM of H_2O_2 for 24 h. The changes were identified through Raman spectroscopy and FTIR analyses (Fig. 7(c)). FTIR spectrum of H_2O_2-treated p(NAG-Ac-NAE) (Fig. 7(c)-1) and H_2O_2-treated p(NAG-*b*-A) (Fig. 7(c)-4) hydrogel revealed that the alkane (2923 cm^{-1}) disappeared in both groups. In H_2O_2-treated p(NAG-*b*-A) hydrogel, additional C=O (1734 cm^{-1}) bands disappeared. Furthermore, from the Raman spectroscopic analysis (Fig. 7(d)), the common bands in all H_2O_2 treated and untreated p(NAG-*b*-A) and p(NAG-Ac-NAE) hydrogels appeared at 2946 cm^{-1} for CH_2 stretching, and 3139 cm^{-1} of NH of p(NAG-*b*-A) shifted to 3224 cm^{-1} (NH) in p(NAG-Ac-NAE). However, in H_2O_2-treated p(NAG-*b*-A) hydrogel, an additional Raman band is observed at 1622 cm^{-1} due to the presence of amide bonds. In H_2O_2-treated p(NAG-Ac-NAE), a band at 2364 cm^{-1} is observed due to the formation of C≡C. This observation revealed that when hydrogel comes in contact with H_2O_2, it triggers the release of CO_2 and H_2O molecules as by-products, and degradation of polymeric chains occurs. The same was confirmed as a few bands disappeared and few of them shifted.

Angiogenesis stimulatory effect of p(NAG-Ac-NAE) hydrogel

Angiogenesis plays an important role in the functional recovery of neurovascular units under traumatic, ischemic and pathological conditions of the brain. Neuronal progenitor cells (NPCs) are present near blood vessels, which provide guidance to NPCs[38] for neurogenesis. To develop dual properties bearing angiogenesis/neurogenesis imprinted hydrogel, both previously

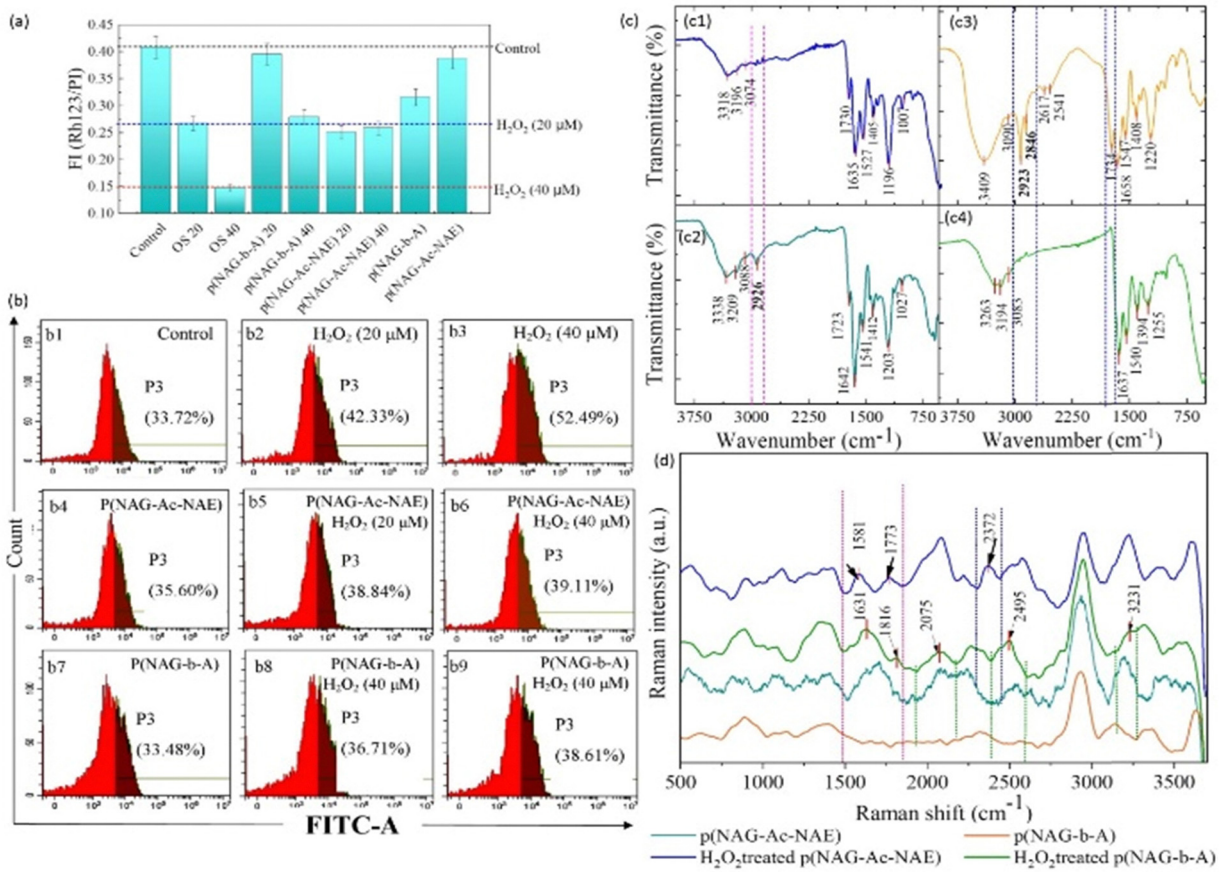

Fig. 7 Effect of p(NAG-Ac-NAE) and p(NAG-*b*-A) hydrogels on mitochondrial membrane potential and intracellular ROS production in PC12 cells. (a) Reduction in mitochondrial membrane potential depolarization observed in H_2O_2 oxidative stress by p(NAG-Ac-NAE) and p(NAG-*b*-A) hydrogels. (b) Flow cytometry detection of intracellular ROS in PC12 cells: (b1) untreated control, (b2) exposure of H_2O_2 20 μM, (b3) exposure of H_2O_2 40 μM, (b4) treatment with the p(NAG-Ac-NAE) hydrogel, (b5) exposure of H_2O_2 20 μM treatment with the p(NAG-Ac-NAE) hydrogel, (b6) exposure of H_2O_2 40 μM treatment with the p(NAG-Ac-NAE) hydrogel, (b7) treatment with the p(NAG-*b*-A) hydrogel, (b8) exposure of H_2O_2 20 μM and treatment with the p(NAG-*b*-A) hydrogel and (b9) exposure of H_2O_2 40 μM and treatment with the p(NAG-*b*-A) hydrogel. (c) FTIR spectrum of (c1) and (c2) H_2O_2 treated with and without the p(NAG-Ac-NAE) hydrogel, (b) H_2O_2 treated with and without the p(NAG-*b*-A) hydrogel, and (d) Raman spectrum under different treatment conditions.

reported p(NAG-*b*-A)[17] and presently synthesized p(NAG-Ac-NAE) hydrogels were examined for angiogenic potential. The p(NAG-Ac-NAE) hydrogel is composed of a combination of glycine (inhibitory) and glutamate (excitatory) units, while the p(NAG-*b*-A) hydrogel is the only inhibitory glycine-containing polymer. Both polymers are biocompatible and increase the cell proliferation of HUVEC cells at low concentrations (Fig. S9, ESI†).

Furthermore, a chick embryo assay was performed for p(NAG-Ac-NAE) and p(NAG-*b*-A) hydrogels to analyse vascular sprouting. The chick embryo was incubated with 1 μg mL^{-1}, 25 μg mL^{-1} and 100 μg mL^{-1} of p(NAG-Ac-NAE) hydrogel for 0 h and 8 h, which showed matured prominent blood vessel formation (Fig. 8(a), the mature blood vessels represented by arrow). Furthermore, the acquired images were analysed for vessel area, junction density, total number of junctions and total vessel length using the Angiotool software, and the results are shown in Fig. 8(b)–(e). The vessel area (Fig. 8(b)) significantly increased by 18% ($p \sim 0.03$) and 20% ($p \sim 0.047$) within 2 h for 25 μg mL^{-1} of dose and total vessel length (Fig. 8(d)) by 39% ($p \sim 0.006$) and 7.5% ($p \sim 0.044$) within 8 h in response to 1 μg mL^{-1} of the dose applied, respectively. The total number of junctions significantly increased from 10.2% ($p \sim 0.024$) to 46.2% ($p \sim 0.005$) within 2 h to 8 h when 1 μg mL^{-1}, 25 μg mL^{-1} and 100 μg mL^{-1} hydrogel doses were used, respectively. Thus, the total number of junctions (Fig. 8(e)) and junction density (Fig. 8(c)) significantly increased as the hydrogel dose was increased from 1 μg mL^{-1} ($p \sim 0.005$ and 0.01, respectively) to 25 μg mL^{-1} ($p \sim 0.02$ and 0.006, respectively). In conclusion, p(NAG-Ac-NAE) hydrogel shows pro-angiogenic behaviour at low doses, such as 1 μg mL^{-1} and 25 μg mL^{-1} of hydrogel.

Further, a similar CEA assay was performed using p(NAG-*b*-A) hydrogel at the lowest dose of 1 μg mL^{-1} for 0 h, 2 h, 4 h and 8 h. As per the quantitative assessment, a significant decrease in vessel area, total number of junctions, junction density and total vessel length was observed within 4 and 8 hours, as shown in Fig. S10(a)–(d) (ESI†). The vessel area (Fig. S10a, ESI†) is found to be significantly decreased by 36.74% ($p \sim 0.02$) and 38.61% ($p \sim 0.02$); total number of junctions (Fig. S10b, ESI†)

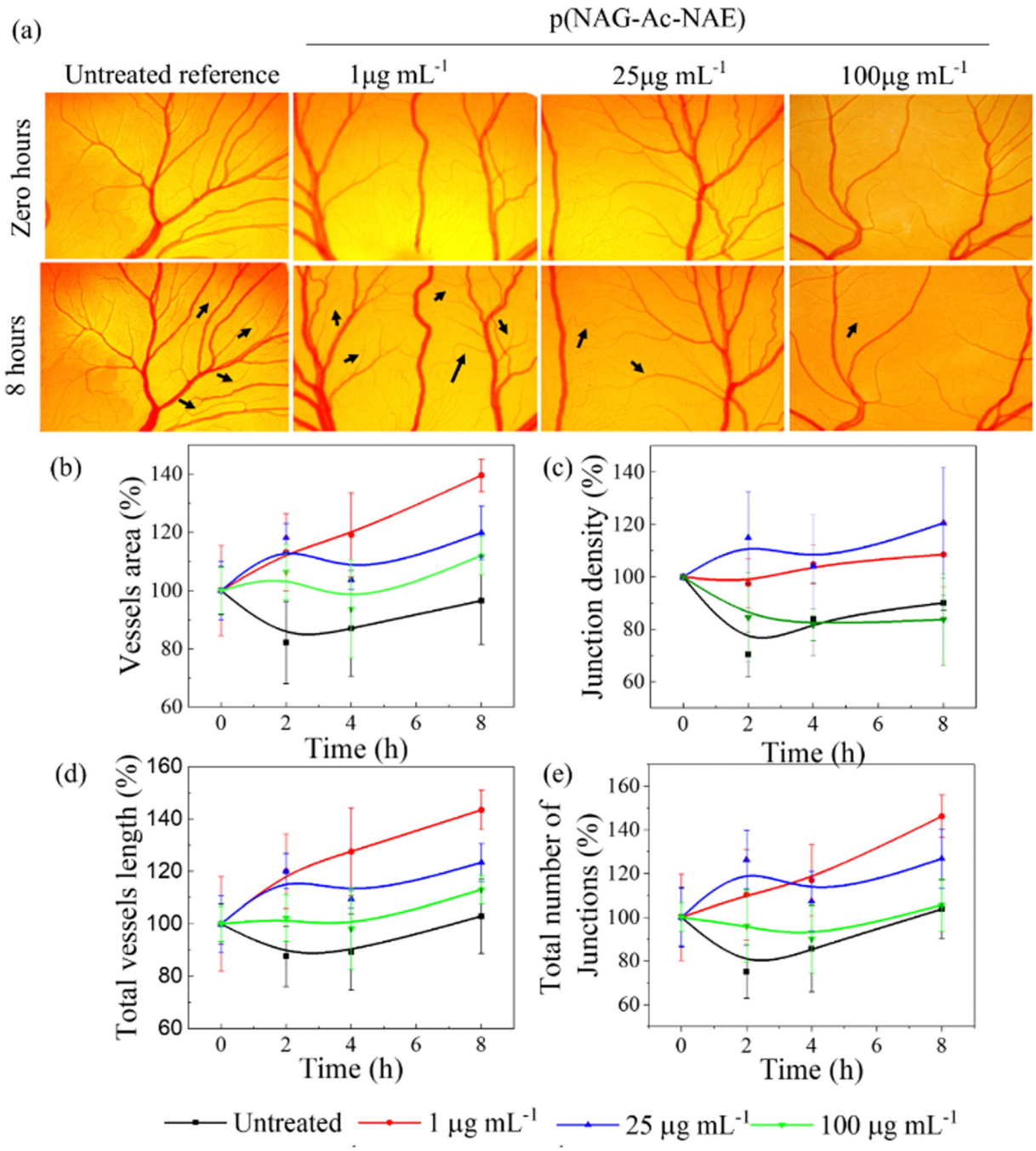

Fig. 8 Angiogenic stimulatory effect of the p(NAG-Ac-NAE) hydrogel. (a) *In ovo* CEA assay in the presence of p(NAG-Ac-NAE) enhanced vascular sprouting (marked as a black arrow) in a dose-dependent manner. (b)–(e) shows the change in several angiogenic parameters, such as blood vessel area, the total number of junctions, density of junctions and total vessel length obtained in time-dependent (statistical significance level of $*p < 0.05$).

decreased by 65.88% ($p \sim 0.004$) and 70.87% ($p \sim 0.006$), junction density (Fig. S10c, ESI†) decreased by 64.56% ($p \sim 0.003$) and 63.12% ($p \sim 0.005$), and total vessel length increased by 30.24% ($p \sim 0.01$) and 31.37% ($p \sim 0.02$) at 4 and 8 h, respectively (Fig. S10d, ESI†). These results are the clear shreds of evidence that the p(NAG-Ac-NAE) hydrogel is angiogenic, while the p(NAG-*b*-A) hydrogel is anti-angiogenic. These results further indicate that the angiogenic potential could arise due to the presence of excitatory neurotransmitter glutamate imprinting. Therefore, the biocompatibility and neurogenic potential were analysed only for the p(NAG-Ac-NAE) hydrogel.

Effect of hydrogel on gene expression analysis

In the current study, we leveraged the effects of p(NAG-Ac-NAE) hydrogel on the molecular events of neurogenesis and angiogenesis under oxidative conditions. The first finding in the discovery of the hypoxia-inducible factor indicates the

formation of new neurons. Hypoxia-induced factor-1α (HIF-1α) expression affects several downstream target genes, such as VEGF, nitric oxide synthase, and IGF. Moreover, HIF-1α possesses negative effects by triggering the expression of endothelin-1 (ET-1) and brain natriuretic peptide (BNP) in a controlled manner to exercise a preconditioning effect in ischemia.[39] Low dose of H_2O_2 10–20 μM concentration can up-regulate the HIF-1α expression, thereby mediating the preconditioning protection in ischemic brain[40] and also protecting PC12 cells against dopamine-induced apoptosis.[41] Our results corroborated with this finding as H_2O_2 treatment with 20 μM induced the expression of HIF-1α, while at 40 μM, the HIF-1α expression diminished. With treatment using both the p(NAG-Ac-NAE) and p(NAG-*b*-A) hydrogels, induced expression of HIF-1α is observed. Interestingly, with 40 μM H_2O_2, the complete diminished expression of HIF-1α is observed, while the induced expression is observed with treatment of p(NAG-Ac-NAE) and p(NAG-*b*-A) along with 40 μM H_2O_2, confirming the HIF-1α mediated preconditioning effects of both hydrogels even in higher oxidative stress (Fig. 9(a)). This could be due to the cell cycle in which we observed a decreased sub-G0 phase (Fig. 6). It is known that HIF1α cross talks with VEGF and induces the expression of VEGF by interacting with HIF1α to the HRE promoter region of the VEGF gene. Furthermore, VEGF guides neuronal migration in the embryonic brain and supports axonal and arterial co-patterning and the formation of micro vessels. In PC12 cells, we observed almost similar expression in the presence/absence of both hydrogels under oxidative stress or normal conditions. However, the increased expression for the VEGF isoform was observed in the treatment of p(NAG-Ac-NAE) hydrogel at concentrations of 25 and 250 μg mL^{-1}, even under oxidative stress conditions. However, p(NAG-*b*-A) hydrogel induces the expression of VEGF isoform at only 25 μg mL^{-1} concentration of hydrogel but not at the 250 μg mL^{-1} of hydrogel even under oxidative stress conditions (Fig. 9(a)), and KDR has high affinity towards the VEGF isoforms.

Increased KDR expression is related to recurrent depressive disorder.[42] We observed the increased expression of KDR with a concentration of H_2O_2 from 20 μM to 40 μM. Treatment with p(NAG-*b*-A) does not affect KDR expression. However, when treated with p(NAG-Ac-NAE), it slightly decreases the expression of KDR. However, the increased expression of hydrogel along with H_2O_2 treatment increases the expression of KDR equivalent to the expression induced by 20 μM of H_2O_2. The overexpressed KDR when treated with 40 μM of H_2O_2 revealed excessively stressed conditions of PC12 and requirements of external supplied growth factor to reduce the oxidative stress. With the decreased expression of KDR even under oxidative stress, the p(NAG-Ac-NAE) hydrogel could prevent neuronal cells from further damage and may prevent recurrent depressive disorder. Furthermore, to validate the VEGF stimulatory effect of p(NAG-Ac-NAE) and p(NAG-*b*-A) hydrogels, RAW264.7 cells were treated with both hydrogels. In treatment with p(NAG-*b*-A) hydrogel at 25 μg concentration, a 0.2-fold increase in expression is observed, while in treatment with 250 μg mL^{-1} concentration of hydrogen, a 0.4-fold decrease in expression is observed. However, in the treatment with p(NAG-Ac-NAE) hydrogel, 0.3- and 0.6-fold increases in the VEGF expression are observed at 25 and 250 μg mL^{-1} of hydrogel, respectively (Fig. 9(b)). The p(NAG-*b*-A) hydrogel induces the overexpression of TNFα, 7 folds at 25 and 3.5 folds at 250 μg mL^{-1}. Treatment with p(NAG-Ac-NAE) hydrogel shows a one-fold increase in TNFα expression at 25 μg mL^{-1}. However, a decrease in the expression of TNFα with the treatment of 250 μg mL^{-1} hydrogel is observed. TNFα is a pro-inflammatory cytokine that regulates the homeostatic function in neurogenesis, myelination and synaptic plasticity.[43] Thus, treatment with p(NAG-Ac-NAE) hydrogel reduces the inflammation. However, its expression can also be correlated with the initiation of degenerative cascades after peripheral nerve injury. In our previous study, we did not investigate the effect of p(NAG-*b*-A) hydrogel on neurogenesis. As per the present investigation, the p(NAG-*b*-A) hydrogel shows the induction of pro-inflammatory cascades, which raises the question of how p(NAG-*b*-A) hydrogel induces neurogenesis. With the current fold expression of TNFα, we can conclude that the p(NAG-*b*-A) hydrogel shows dose-dependent inflammatory activity; with an increase in hydrogel concentration, a one-fold decrease in expression is observed. In the previous study, we majorly used 500 μg mL^{-1} of p(NAG-*b*-A) hydrogel,[17] and this could be the reason neurogenesis and astrocyte-like morphology were observed. In the present study, we can consider that the p(NAG-Ac-NAE) hydrogel is more effective even at a lower concentration. Only one-fold TNFα expression is observed. With an increase in the concentration of p(NAG-Ac-NAE) hydrogel, a diminished TNFα expression is observed. Furthermore, the p(NAG-*b*-A) hydrogel induces the IL1β expression, while the present hydrogel p(NAG-Ac-NAE) does not show any effect on IL1β. From these results, we can conclude that the p(NAG-*b*-A) hydrogel is pro-inflammatory, while the p(NAG-Ac-NAE) hydrogel does not have any effect on the pro-inflammatory cascade. Further, the p(NAG-Ac-NAE) hydrogel used in this work induces the angiogenic, neurogenic and neuroprotective effects *via* HIF1α/VEGF/KDR cascade.

4. Discussion

Understanding the role of glutamic acid and glycine in neurogenesis reveals the development of CNS regenerative medicine. A wide distribution of excitatory glutamate and inhibitory glycine neurotransmitters was observed in nerve cells and astrocytes, as well as in glial cells, and disruptions of balance are responsible for the pathophysiology.[44,45] Glycine influences cellular events[46] and plays a ubiquitous role in neuronal stem cell survival and neuroprotection.[18,19,47,48] The most abundant excitatory glutamate neurotransmitter maintains neuronal homeostasis and is involved in synaptic plasticity, learning and memory.[49] The deregulation of glutamate, spreading depolarization and glutamatergic signalling can be related to neurological and psychiatric disorders, especially epilepsy.[50,51] Hence, targeting glutamatergic signalling is useful in promoting regeneration/repair and in pain management.[52] Existing

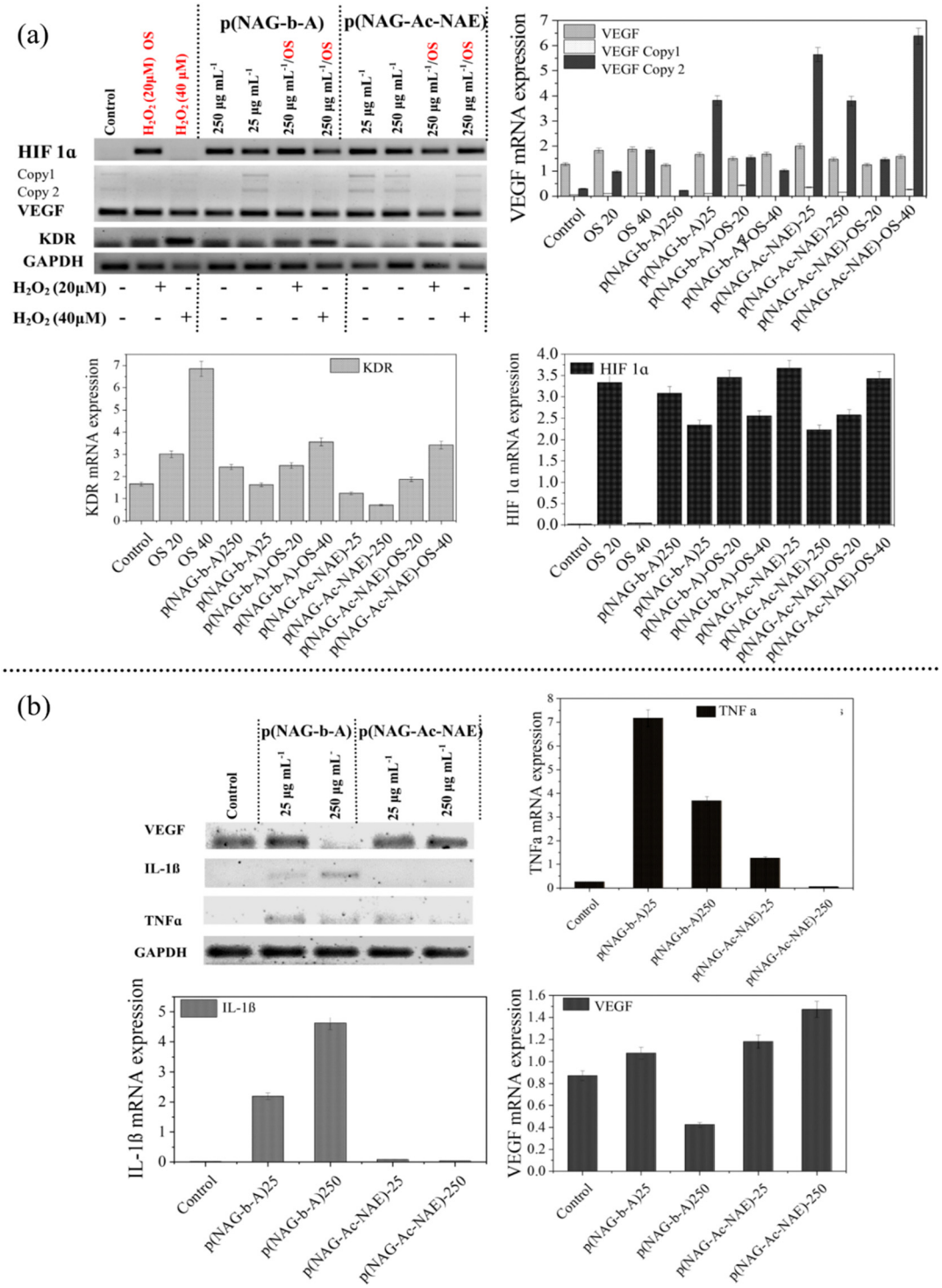

Fig. 9 (a) Change in HIF 1α, VEGF and KDR mRNA expressions with the treatment of p(NAG-*b*-A) and p(NAG-Ac-NAE) in the presence and absence of H_2O_2-induced oxidative stress at 20 μM and 40 μM concentrations against PC12 cells. After sqRT-PCR, the amplicon was separated on a 2% agarose gel. Densitometry analysis was performed using FIJI software and represented in a graph. (b). Change in VEGFa, IL1-β, and TNFα mRNA expressions with the treatment of p(NAG-*b*-A) and p(NAG-Ac-NAE) at 25 and 250 μg mL^{-1} in RAW264.7 cells. After sqRT-PCR, the amplicon was separated on a 2% agarose gel. Densitometry analysis was performed using FIJI software and represented in graphs.

antidepressant drugs work on the release of glutamate because they block the *N*-methyl-D-aspartate (NMDA) and burst the release of glutamate. Hence, glutamate neurotransmitter-based treatment reverses the stress-induced behaviour and molecular and structural discrepancies of MD. As per the mechanism, the burst release of glutamate induces depolarization of cells, and

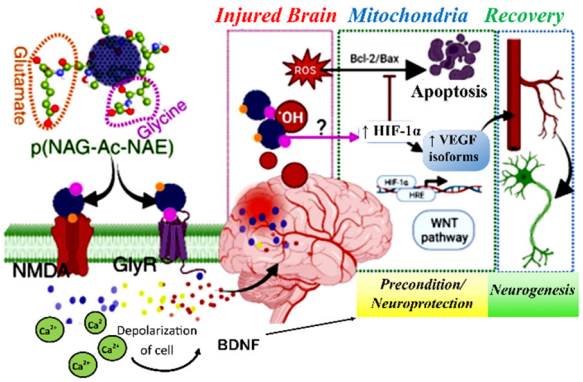

Fig. 10 Mechanism of p(NAG-Ac-NAE)-induced neuroprotection and neurogenesis. Side chains of p(NAG-Ac-NAE) interact with the NMDA and glycine receptor, which depolarize the cells, and induce BDNF secretion, leading to neuroprotection. This hydrogel interacts with the free radicals and in the neuronal cell increases the expression of HIF-1α which delayed the apoptosis. This increased HIF-1α promotes the VEGF expression and increases angiogenesis. Increased angiogenesis leads to neuronal stem cell migration and promotes neurogenesis.

depolarized cells release the brain-derived neurotrophic factor (BDNF).[53] This BDNF induces the synthesis of synaptic proteins, maintains the synaptic functions by activating the mTORC1 and influences the neuroprotective pathways and neurogenesis (Fig. 10).[54] To develop pro-angiogenic and neurogenic properties, the imprinted p(NAG-Ac-NAE) hydrogel was synthesized *via* the free radical mini-emulsion polymerization (Scheme 1 and Fig. 1) technique. An ultra-sonication process was applied to form mini-emulsion and to obtain nanosized particles. Polyalkene-functionalized monomers serve the role of the formation of stable polymer particles.[55] In the polymerization process, AIBN acts as an initiator, and DVB is used as a cross-linker that helps stabilize the polymer particles. The incorporation of amino acids inside the chains plays an important role in the formation of narrower molecular weight distributed polymer, which has several beneficial properties, such as hydrophilicity, biocompatibility, stimuli responsiveness and chiral recognition. This hydrogel is mechanically soft and stable (Fig. 2(e)–(j)), has high swelling properties (Fig. 2(a) and (c)), and is biodegradable (Fig. 2(b) and (d)) and biocompatible in nature (Fig. 3). High swelling capacities and higher branching are induced by incorporating the DVB, which creates micropores of size 2 ± 0.5 nm in diameter (Fig. 1(c) nad (g)). The high swelling behaviour of this hydrogel further provides the capability of this hydrogel to improve the microenvironment to favor the neuronal cells for cellular adhesion and viability. Further, the pH-responsive behaviour of p(NAG-Ac-NAE) hydrogel (Fig. 2(a)) can be an advantage for drug delivery and for the treatment of neurodegenerative diseases; because the pH is a biomarker of neurodegenerative diseases, the cerebral pH is significantly higher under a disease condition.[56] Conductive polymers, either with or without external electrical stimulation, direct the electrochemical stimulation to the cells, enhance the cellular functions and also activate the gene expression of nerve growth factor compared to the nonconductive materials.[57] Compared to the non-conducting collagen films, semiconducting ($7.00 \pm 1.10 \times 10^{-5}$ S cm^{-1}) (Fig. S8, ESI†) melanin thin film enhanced the Schwann cell growth and neurite extension.[58] The p(NAG-Ac-NAE) hydrogel used in this work shows semiconducting behaviour, such as melanin thin film (Fig. S8, ESI†), which shows one advantageous feature of this hydrogel over the existing hydrogel. The p(NAG-Ac-NAE) hydrogel used in this work has elastic modulus values ranging from 2.3 kPa to 2.7 kPa (Fig. 2(e)–(j)). Soft biomaterial having a modulus value below 1 kPa favours neuronal differentiation, 1–3 kPa favours astrocyte differentiation,[59] and a modulus of 2 kPa can increase the differentiation of immature to mature neurons.[60] The major focus of this work is to develop angiogenic potential possessing material because it is mentioned earlier. Moreover, p(NAG-Ac-NAE) hydrogel showed pro-angiogenic activity at a lower concentration of 2.5-25 μg mL^{-1} (Fig. 8) compared to the glycine-containing p(NAG-*b*-A) hydrogel only (Fig. S9, ESI†) and increased cellular proliferation of PC12 cells (Fig. 3(a)). These enhanced cellular proliferation and differentiation occurred due to the influence of chiral amino acid (L-glutamic acid). As reported by Dou *et al.*, cellular differentiation depends on chirality; for example, L-amino acid can influence cellular proliferation, spreading and differentiation, whereas D-amino acid suppresses this behavior.[61]

Intracellular ROS generation increases the Bcl-2/Bax ratio, which leads to apoptosis in a dose-dependent manner. A low concentration of H_2O_2, decreases the level of the Bcl-2/Bax ratio and provides the preconditioning effect to MSCs. These preconditioned MSCs upregulate phosphorylated Akt-1 expression and increase the HIF1α expression. This increase in HIF-1α upregulates the VEGF expression, followed by the angiogenesis (Fig. 10).[36] Furthermore, in the present study, stress generated using H_2O_2 (at 5 μM) does not show any cytoprotection, as shown in Fig. 5(d) and 6(a). The use of 10-20 μM H_2O_2 influences the ROS generation (Fig. 7(b)-2 and 3), and an increase in HIF 1α expression is observed (Fig. 9(a)). However, at the higher concentration of H_2O_2 (at 40 μM), it induces cytotoxicity in PC12 cells, and it is observed as completely diminished HIF-1α expression with a high level of ROS and induced apoptosis, which corroborates the increased sub-G0 phase of the cell cycle.[62] Similarly, in the presence of 5–20 μM H_2O_2 along with p(NAG-Ac-NAE) hydrogel, it shows a 45% increase in cell viability compared to the used H_2O_2 oxidative stress only, while at 40 μM H_2O_2 exposure, treatment with p(NAG-Ac-NAE) hydrogel results in significantly higher cell survival (Fig. 5(a)). This increase in cellular viability is observed due to the influence of both the hydrogel in the cell cycle, where a reduction in the sub-G1 phase and induction in G0/G1 (Fig. 6) occurred, followed by a reduction in apoptosis. This is one of the crucial points under diseased conditions, where most of the cells die. Thus, the p(NAG-Ac-NAE) hydrogel influences the apoptosis and induces G0/G1 phase, which is responsible for the recovery of PC12 H_2O_2 pre-treated cells. Therefore, we can accelerate the recovery status of PC12 cells assisted by the p(NAG-Ac-NAE) hydrogel even after sufficient oxidative stress was applied, as shown in Fig. 5(b). Similar conclusions can also

be drawn based on the results obtained by studying the change in the mitochondrial membrane potential (Fig. 7(a)). Primarily, with the exposure of 20 μM and 40 μM of H_2O_2, membrane depolarization increased more than with the untreated control, which could induce apoptosis and cellular death (Fig. 5(c)). However, at the exposure of 20 and 40 μM H_2O_2 and treatment with p(NAG-Ac-NAE) hydrogel, it exhibited an increase in the fluorescence activity in support of the protective/HIf1α induced preconditioning role of p(NAG-Ac-NAE) hydrogel towards the mitochondria. Intracellular ROS generation was higher in 20 μM and 40 μM H_2O_2 exposure. However, when it was treated with both p(NAG-Ac-NAE) and p(NAG-*b*-A) hydrogels in the presence of H_2O_2, a decrease in ROS production was observed (Fig. 7(b)). ROS production is more highly inhibited in the p(NAG-*b*-A) hydrogel than in the p(NAG-Ac-NAE) hydrogel. This could be due to the presence of a glycine moiety because glycine uptake can activate the AKT/NF-κβ65/Hif1α signalling pathway. In differentiated cells, the 40 μM H_2O_2 treatment restricts neurite extension, disturbs the terminals and dendrites and exhibits nuclear damage. The neuroprotective role of the p(NAG-Ac-NAE) hydrogel prevents the H_2O_2 oxidative stress-induced damage, promotes neurite extension with healthy dendrites, axon, and axonal terminal and also protects against nuclear damage (Fig. 5(c)). The mechanism behind the protection is the interaction between the NH and NH_2 groups of p(NAG-Ac-NAE) with $OH^{\bullet}$ free radicals identified from the Raman study (Fig. 7(d)), which downregulates the ROS level of intracellular concentration up to the physiological ROS condition and assists neurogenesis. It can also be noted that the physiological level of ROS supports the crucial cellular processes, acting as a second messenger that can regulate the intrinsic signalling pathways, contribute to the neurogenesis, polarization, and maturation of neurons and help in discriminating between oxidative distress and oxidative eustress.[63]

Under physiological conditions, glutamine is metabolized into glutamate by glutaminase-I, and inhibition of glutaminase-I or glutamine deprives endothelial cells, causing the vessel sprouting defect,[64] which shows the potential role of glutamate in angiogenesis. This phenomenon corroborated our CMA results, as shown in Fig. 8. It is evident that vessel sprouting is induced by p(NAG-Ac-NAE) hydrogel with an increase in vessel area, total vessel length, junction density and total number of junctions with increased expression of VEGF isoforms (Fig. 9(b)) even under stress conditions. However, the treatment with p(NAG-*b*-A) hydrogel at lower concentrations induces the expression of VEGF. From all these results, we can propose that the p(NAG-Ac-NAE) hydrogel can exhibit the VEGF stimulatory action *via* PI3K/Akt/mTOR signalling pathway because mTOR signalling regulates the gene expression of vascular endothelial growth factor (VEGF).[65] However, extensive studies need to be conducted in this direction to understand the biological mechanism of the pro-angiogenic activity, and *in vivo*-based study, which is beyond the scope of this work. Angiogenesis is a major issue in brain cancer, and glioma-derived neurotransmitter glutamate plays a crucial role in tumor angiogenesis.[66] Interestingly, our p(NAG-Ac-NAE) hydrogel shows pro-angiogenic activity (Fig. 8) and non-tumorigenic activity against the aggressive cancer cell lines, such as LN229 and MDA-MB-231 (Fig. 4(a)).

Overall, the p(NAG-Ac-NAE) hydrogel possesses key advantages over the existing hydrogel for neuroregeneration.

1. It was earlier reported that for the preconditioning activity and ROS elimination, the hydrogels were encapsulated with antioxidant drugs, such as curcumin,[67] gallic acid[68] and tannic acid.[69] However, interestingly, p(NAG-Ac-NAE) hydrogel gives the preconditioning effects and ROS eliminating activity by triggering the Hif1α expression; thus, there is no need to load with any drugs.

2. The use of neurotrophic factors plays a crucial role in enhancing neurogenesis. However, the delivery of neurotrophic factors is challenging due to the requirement of trophic factors at a specific concentration, as an excessive dose may create other consequences. Therefore, several nanoparticles and hydrogels required for the delivery of neurotrophic factors are very important for achieving effective therapeutic efficiency. However, our hydrogel is effective without any additional neurotrophic factors and gives a stimulatory effect for neurotrophic factors, such as VEGF.[70,71]

3. Excitingly, to the best of our knowledge, the novel hydrogel p(NAG-Ac-NAE) is the only one that possesses the dual characteristics of angiogenesis and neurogenesis.[72]

4. For the development of conductive hydrogel, there is a need for doping with conductive material; however, synthesized hydrogel falls into the category of semi-conductive material.

Thus, the p(NAG-Ac-NAE) hydrogel synthesized in this work has the potential for angiogenesis and neurogenesis and could be helpful in the management of neurodegenerative diseases, which increases the scope to study the role of p(NAG-Ac-NAE) hydrogel in mitochondrial impaired functioning for the prevention of the neurodegenerative diseases.

5. Conclusions

In this work, a p(NAG-Ac-NAE) hydrogel was synthesized. The free radical polymerization technique and the presence of acryloyl glutamate and acryloyl glycine yield the highest water-retaining, pH-responsive, and biodegradable polymeric hydrogel. The viscoelastic behaviour of this hydrogel, such as an elastic modulus of 2.3–2.7 kPa, provides a suitable macro-environment to the neuronal stem cell for outer growth. The presence of glycine derivatives moiety and glutamate derivative moiety provides the physical cue and vasculogenesis-assisted neurite outgrowth along with maintaining the microtubule integrity of the neuronal cells. The p(NAG-Ac-NAE) hydrogel has the free functional groups of glycine and glutamate that are involved in neuronal homeostasis and angiogenesis because it shows the HIF-1α induced and VEGF expression stimulatory effect. Furthermore, this hydrogel possesses protective roles and preconditioning effects by scavenging ROS generation and mitochondrial membrane depolarization under oxidative stress conditions along with increased expression of HIF-1α.

Thus, this hydrogel can treat neurodegenerative diseases for the delivery of neuronal stem cells and growth factors for regenerative applications because it does not exhibit a pro-inflammatory effect. Investigating the complete molecular level mechanisms and *in vivo* study can be considered the future scope of this work.

Author contributions

P. P is the main project investigator (PI). Ideation, experimental design, and experimental results analysis performed by K. W and P. P.: Characterization helped by P. S. G. Angiogenesis helped by G. S., rheology helped by R. P. NMR and cytotoxicity in HUVEC cell carried out by S. M. Zeta potential measured by S. M. Biodegradation study helped by S. P., D. P. and S. K. Y. M. helped to conduct and analysis of MALDI-ToF. Manuscript written and finalized by K. W. and P. P. All the authors checked and approved manuscript for publication.

Conflicts of interest

The authors declare no competing financial interest.

Acknowledgements

Paik acknowledges the project funds awarded to him by I-DAPT Foundation (Ref. I-DAPT/IT (BHU)/2023-24/Project Sanction/47), STARS-IISc Bangalore (Ref. MoE-STARS/STARS-2/2023-0318) and Institute start-up grant/plan-OH, Instrument facilities of IIT-BHU and ISLS-CIF. Acknowledge to Prof. S. K. Mahto, and Prof. Richa Arya for fluorescent microscopy facilities and Prof. Shantanu Das for Raman spectroscopy.

References

1 M. A. Grimaudo, G. S. Krishnakumar, E. Giusto, F. Furlani, G. Bassi, A. Rossi, F. Molinari, F. Lista, M. Montesi and S. Panseri, *Acta Biomater.*, 2022, **140**, 88–101.
2 Y. Chen, J. Lin and W. Yan, *Front. Neurol.*, 2022, **13**, 908468.
3 V. L. Feigin, T. Vos, E. Nichols, M. O. Owolabi, W. M. Carroll, M. Dichgans, G. Deuschl, P. Parmar, M. Brainin and C. Murray, *Lancet Neurol.*, 2020, **19**, 255–265.
4 GBD 2016 Neurology Collaborators, Global Burden of Disease Collaborators. Global, regional, and national burden of neurological disorders, 1990–2016: a systematic analysis for the Global Burden of Disease Study 2016, *Lancet Neurol.*, 2019, **18**, 459–480.
5 S. Ahmed, H. Venigalla, H. M. Mekala, S. Dar, M. Hassan and S. Ayub, *Indian J. Psychol. Med.*, 2017, **39**, 114–121.
6 G. Kim, J. Kim, S. Rhie and S. Yoon, *Neurobiology*, 2015, **24**, 325.
7 G. H. Kim, J. E. Kim, S. J. Rhie and S. Yoon, *Exp. Neurobiol.*, 2015, **24**, 325–340.
8 L. R. Nih, S. Gojgini, S. T. Carmichael and T. Segura, *Nat. Mater.*, 2018, **17**, 642–651.
9 R. Boni, A. Ali, A. Shavandi and A. N. Clarkson, *J. Biomed. Sci.*, 2018, **25**, 90.
10 X. Ma, M. Wang, Y. Ran, Y. Wu, J. Wang, F. Gao, Z. Liu, J. Xi, L. Ye and Z. Feng, *Polymers*, 2022, **14**(8), 1549.
11 A. Akhtar, V. Farzam Rad, A.-R. Moradi, M. Yar and M. Bazzar, *Smart Mater. Med.*, 2023, **4**, 337–355.
12 G. Li, W. Feng, N. Corrigan, C. Boyer, X. Wang and J. Xu, *Polym. Chem.*, 2018, **9**, 2733–2745.
13 S.-B. Park, M.-H. Sung, H. Uyama and D. K. Han, *Prog. Polym. Sci.*, 2021, **113**, 101341.
14 M. Wei, T. Inoue, Y. I. Hsu, M. H. Sung, T. Fukuoka, S. Kobayashi and H. Uyama, *ACS Biomater. Sci. Eng.*, 2022, **8**, 551–559.
15 M. H. Kim, J. N. Lee, J. Lee, H. Lee and W. H. Park, *ACS Biomater. Sci. Eng.*, 2020, **6**, 3103–3113.
16 W. Zhang, K. Zhang, S. Yan, J. Wu and J. Yin, *J. Mater. Chem. B*, 2018, **6**, 6865–6876.
17 K. Wasnik, P. S. Gupta, S. Mukherjee, A. Oviya, R. Prakash, D. Pareek, S. Patra, S. Maity, V. Rai, M. Singh and G. Singh, *ACS Appl. Bio Mater.*, 2023, **6**(12), 5644–5661.
18 E. Samarut, A. Bekri and P. Drapeau, *Front. Mol. Neurosci.*, 2016, **9**, 22, DOI: **10.3389/fnmol.2016.00022**.
19 E. Brustein, S. Côté, J. Ghislain and P. Drapeau, *Calcium Transients in Neurogenesis*, 2012, **73**(2), 168–175.
20 L. Wang, Y. Pang, Y. Tang, X. Wang, D. Zhang, X. Zhang, Y. Yu, X. Yang and Q. Cai, *Bioact. Mater.*, 2023, **25**, 399–414.
21 S. Yu, S. Yao, Y. Wen, Y. Wang, H. Wang and Q. Xu, *Sci. Rep.*, 2016, **6**, 33428.
22 F. González-Pérez, M. Alonso, I. González de Torre, M. Santos and J. C. Rodríguez-Cabello, *Adv. Healthcare Mater.*, 2022, **11**, e2201646.
23 S. Y. Park, S. Y. Kim, T. Kim, H. Ahn and I. Chung, *Polym. Adv. Technol.*, 2019, **30**, 872–878.
24 *MALDI mass spectrometry for synthetic polymer analysis*, ed. L. Li, John Wiley & Sons, 2009.
25 J. Schindelin, I. Arganda-Carreras, E. Frise, V. Kaynig, M. Longair, T. Pietzsch, S. Preibisch, C. Rueden, S. Saalfeld, B. Schmid, J. Y. Tinevez, D. J. White, V. Hartenstein, K. Eliceiri, P. Tomancak and A. Cardona, *Nat. Methods*, 2012, **9**, 676–682.
26 J. D. Van Dyke and K. L. Kasperski, *J. Polym. Sci., Part A: Polym. Chem.*, 1993, **31**, 1807–1823.
27 N. L. Dassanayake and R. W. Phillips, *Anal. Chem.*, 1984, **56**, 1753–1755.
28 L. B. Peres, R. S. dos Anjos, L. C. Tappertzhofen, P. E. Feuser, P. H. H. de Araújo, K. Landfester, C. Sayer and R. Muñoz-Espí, *Eur. Polym. J.*, 2018, **101**, 341–349.
29 S. Uman, A. Dhand and J. A. Burdick, *J. Appl. Polym. Sci.*, 2020, **137**, 48668.
30 R. E. Musgrove, M. Helwig, E.-J. Bae, H. Aboutalebi, S.-J. Lee, A. Ulusoy and D. A. Di Monte, *J. Clin. Invest.*, 2019, **129**, 3738–3753.
31 H. J. Forman, A. Bernardo and K. J. A. Davies, *Arch. Biochem. Biophys.*, 2016, **603**, 48–53.
32 E. R. Whittemore, D. T. Loo, J. A. Watt and C. W. Cotmans, *Neuroscience*, 1995, **67**, 921–932.

33 V. Zenin, J. Ivanova, N. Pugovkina, A. Shatrova, N. Aksenov, I. Tyuryaeva, K. Kirpichnikova, I. Kuneev, A. Zhuravlev, E. Osyaeva, E. Lyublinskaya, I. Gazizova, N. Guriev and O. Lyublinskaya, *Redox Biol.*, 2022, **50**, 102245.
34 P. W. Kämmerer, V. Engel, F. Plocksties, A. Jonitz-Heincke, D. Timmermann, N. Engel, B. Frerich, R. Bader, D. G. Thiem and A. Skorska, *Biomedicines*, 2020, **8**, 482.
35 A. A. Gerencser, C. Chinopoulos, M. J. Birket, M. Jastroch, C. Vitelli, D. G. Nicholls and M. D. Brand, *J. Physiol.*, 2012, **590**, 2845–2871.
36 F. Nouri, S. N. Nematollahi-Mahani and A. M. Sharifi, *Adv. Pharm. Bull.*, 2019, **9**, 76–83.
37 X.-Q. Tang, J.-Q. Feng, J. Chen, P.-X. Chen, J.-L. Zhi, Y. Cui, R.-X. Guo and H.-M. Yu, *Brain Res.*, 2005, **1057**, 57–64.
38 M. A. Font, A. Arboix and J. Krupinski, *Curr. Cardiol. Rev.*, 2010, **6**, 238–244.
39 H. Wang, F. Niu, W. Fan, J. Shi, J. Zhang and B. Li, *Metab. Brain Dis.*, 2019, **34**, 1299–1311.
40 S. Chang, X. Jiang, C. Zhao, C. Lee and D. M. Ferriero, *Neurosci. Lett.*, 2008, **441**, 134–138.
41 T. Xiao-qing, Z. Jun-li, C. Yu, F. Jian-Qiang and C. Pei-Xi, *Life Sci.*, 2005, **78**, 61–66.
42 P. Gałecki, A. Orzechowska, D. Berent, M. Talarowska, K. Bobińska, E. Gałecka, A. Lewiński, M. Maes and J. Szemraj, *J. Affective Disord.*, 2013, **147**, 144–149.
43 L. Leung and C. M. Cahill, *J. Neuroinflammation*, 2010, **7**, 27.
44 A. J. Patel and A. Hunt, *J. Neurochem.*, 1985, **44**, 1816–1821.
45 A. Bekri and P. Drapeau, *Front. Cell Dev. Biol.*, 2018, **6**, 68.
46 J. Y. Hansen, G. Shafiei, R. D. Markello, K. Smart, S. M. L. Cox, M. Nørgaard, V. Beliveau, Y. Wu, J.-D. Gallezot, É. Aumont, S. Servaes, S. G. Scala, J. M. DuBois, G. Wainstein, G. Bezgin, T. Funck, T. W. Schmitz, R. N. Spreng, M. Galovic, M. J. Koepp, J. S. Duncan, J. P. Coles, T. D. Fryer, F. I. Aigbirhio, C. J. McGinnity, A. Hammers, J.-P. Soucy, S. Baillet, S. Guimond, J. Hietala, M.-A. Bedard, M. Leyton, E. Kobayashi, P. Rosa-Neto, M. Ganz, G. M. Knudsen, N. Palomero-Gallagher, J. M. Shine, R. E. Carson, L. Tuominen, A. Dagher and B. Misic, *Nat. Neurosci.*, 2022, **25**, 1569–1581.
47 R. Liu, X. Y. Liao, M. X. Pan, J. C. Tang, S. F. Chen, Y. Zhang, P. X. Lu, L. J. Lu, Y. Y. Zou, X. P. Qin, L. H. Bu and Q. Wan, *J. Immunol.*, 2019, **202**, 1704–1714.
48 A. Bekri, M. Liao and P. Drapeau, *Front. Mol. Neurosci.*, 2019, **12**, 1–7.
49 V. Y. Brodsky, L. A. Malchenko, D. S. Lazarev, N. N. Butorina, T. K. Dubovaya and N. D. Zvezdina, *Biochemistry*, 2018, **83**, 294–298.
50 T. S. Chen, T. H. Huang, M. C. Lai and C. W. Huang, *Biomedicines*, 2023, **11**(3), 783.
51 N. Hubel, M. S. Hosseini-Zare, J. Ziburkus and G. Ullah, *PLoS Comput. Biol.*, 2017, **13**, e1005804.
52 T. J. Chen and M. Kukley, *Neural Regener. Res.*, 2020, **15**, 438–447.
53 D. M. Gerhard, E. S. Wohleb and R. S. Duman, *Drug Discovery Today*, 2016, **21**, 454–464.
54 T. Numakawa, H. Odaka and N. Adachi, *Int. J. Mol. Sci.*, 2018, **19**(11), 3650.
55 A. K. Yamala, V. Nadella, Y. Mastai, H. Prakash and P. Paik, *Nanoscale*, 2017, **9**, 14006–14014.
56 M. M. Chaumeil, J. Valette, C. Baligand, E. Brouillet, P. Hantraye, G. Bloch, V. Gaura, A. Rialland, P. Krystkowiak, C. Verny, P. Damier, P. Remy, A. C. Bachoud-Levi, P. Carlier and V. Lebon, *J. Cereb. Blood Flow Metab.*, 2012, **32**, 771–779.
57 A. Saberi, F. Jabbari, P. Zarrintaj, M. R. Saeb and M. Mozafari, *Biomolecules*, 2019, **9**(9), 448.
58 C. J. Bettinger, J. P. Bruggeman, A. Misra, J. T. Borenstein and R. Langer, *Biomaterials*, 2009, **30**, 3050–3057.
59 N. D. Leipzig and M. S. Shoichet, *Biomaterials*, 2009, **30**, 6867–6878.
60 S. Ali, I. B. Wall, C. Mason, A. E. Pelling and F. S. Veraitch, *Acta Biomater.*, 2015, **25**, 253–267.
61 X. Dou, B. Wu, J. Liu, C. Zhao, M. Qin, Z. Wang, H. Schonherr and C. Feng, *ACS Appl. Mater. Interfaces*, 2019, **11**, 38568–38577.
62 X.-Q. Tang, J.-Q. Feng, J. Chen, P.-X. Chen, J.-L. Zhi, Y. Cui, R.-X. Guo and H.-M. Yu, *Brain Res.*, 2005, **1057**, 57–64.
63 C. Wilson, E. Muñoz-Palma and C. González-Billault, *Semin. Cell Dev. Biol.*, 2018, **80**, 43–49.
64 H. Huang, S. Vandekeere, J. Kalucka, L. Bierhansl, A. Zecchin, U. Bruning, A. Visnagri, N. Yuldasheva, J. Goveia, B. Cruys, K. Brepoels, S. Wyns, S. Rayport, B. Ghesquiere, S. Vinckier, L. Schoonjans, R. Cubbon, M. Dewerchin, G. Eelen and P. Carmeliet, *EMBO J.*, 2017, **36**, 2334–2352.
65 K. Tsuji-Tamura, M. Sato, M. Fujita and M. Tamura, *Biochem. Biophys. Res. Commun.*, 2020, **529**, 596–602.
66 F. Zheng, B. Thomas, Y. Eduard, S. Tina, S. Sebastian, P. M. Eric, S. Nevenka Dudvarski, H. H. S. Mirko, S. Marco, A. C. Marcus, N. Robert, B. Michael, F. Oliver, Y. E. Ilker and E. S. Nicolai, bioRxiv, 2017, 134924. , DOI: **10.1101/134924**.
67 Q. Li, X. Shao, X. Dai, Q. Guo, B. Yuan, Y. Liu and W. Jiang, *NPG Asia Mater.*, 2022, **14**, 14.
68 D. Zhang, Y. Ren, Y. He, R. Chang, S. Guo, S. Ma, F. Guan and M. Yao, *Mater. Today Bio*, 2022, **15**, 100278.
69 J. Xu, T.-Y. Chen, C.-H. Tai and S.-H. Hsu, *Biomater. Res.*, 2023, **27**, 8.
70 P. Madhusudanan, G. Raju and S. Shankarappa, *J. R. Soc., Interface*, 2020, **17**, 20190505.
71 Y. El Ouaamari, J. Van den Bos, B. Willekens, N. Cools and I. Wens, *Int. J. Mol. Sci.*, 2023, **24**(4), 3866.
72 J. Lu, F. Guan, F. Cui, X. Sun, L. Zhao, Y. Wang and X. Wang, *Regener. Biomater.*, 2019, **6**, 325–334.

ACS APPLIED BIO MATERIALS

www.acsabm.org

Article

Poly(*N*-acryloylglycine-acrylamide) Hydrogel Mimics the Cellular Microenvironment and Promotes Neurite Growth with Protection from Oxidative Stress

Kirti Wasnik, Prem Shankar Gupta, Sudip Mukherjee, Alagu Oviya, Ravi Prakash, Divya Pareek, Sukanya Patra, Somedutta Maity, Vipin Rai, Monika Singh, Gurmeet Singh, Desh Deepak Yadav, Santanu Das, Pralay Maiti, and Pradip Paik*

Cite This: *ACS Appl. Bio Mater.* 2023, 6, 5644−5661

Read Online

ACCESS | Metrics & More | Article Recommendations | Supporting Information

ABSTRACT: In this work, the glycine-based acryloyl monomer is polymerized to obtain a neurogenic polymeric hydrogel for regenerative applications. The synthesized poly(*N*-acryloylglycine-acrylamide) [poly(NAG-*b*-A)] nanohydrogel exhibits high swelling (∼1500%) and is mechanically very stable, biocompatible, and proliferative in nature. The poly(NAG-*b*-A) nanohydrogel provides a stable 3D extracellular mimetic environment and promotes healthy neurite growth for primary cortical neurons by facilitating cellular adhesion, proliferation, actin filament stabilization, and neuronal differentiation. Furthermore, the protective role of the poly(NAG-*b*-A) hydrogel for the neurons in oxidative stress conditions is revealed and it is found that it is a clinically relevant material for neuronal regenerative applications, such as for promoting nerve regeneration via GSK3β inhibition. This hydrogel additionally plays an important role in modulating the biological microenvironment, either as an agonist and antagonist or as an antioxidant. Furthermore, it favors the physiological responses and eases the neurite growth efficiency. Additionally, we found out that the conversion of glycine-based acryloyl monomers into their corresponding polymer modulates the mechanical performance, mimics the cellular microenvironment, and accelerates the self-healing capability due to the responsive behavior towards reactive oxygen species (ROS). Thus, the p(NAG-*b*-A) hydrogel could be a potential candidate to induce neuronal regeneration since it provides a physical cue and significantly boosts neurite outgrowth and also maintains the microtubule integrity in neuronal cells.

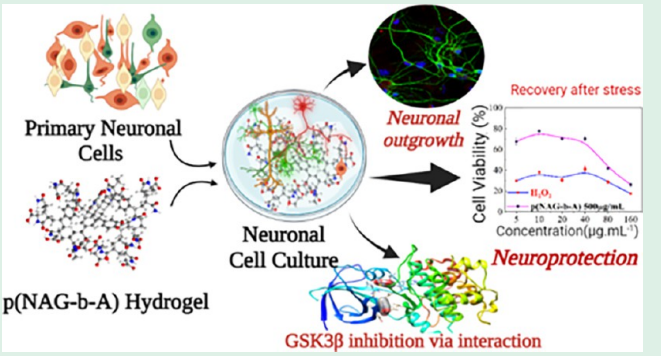

KEYWORDS: *glycine, N-acryloylglycine, poly(NAG-b-A) nanohydrogel, neuron regeneration, neurite extension, neuroprotection, oxidative stress*

1. INTRODUCTION

Neural regeneration is clinically challenging; progressive neuronal damage causes severe consequences like Alzheimer's disease (AD) and Parkinson's disease (PD), and there are limited options for the treatment.[1−3] However, neurotransmitters act as trophic factors in an immature nervous system, which influences the cellular proliferation and differentiation, migration of neurons, and axonal growth and development of neuronal circuits.[4,5] Disruption in neurotransmitters leads to excitatory/inhibitory imbalance, and it causes severe neurological disorders.[6] Glycine is a well-known inhibitory neurotransmitter in adult mature neurons, and it generates the first electrical signal in immature neurons during embryogenesis.[6] Glycine further promotes neurogenesis via promoting calcium transients in neuronal stem cells, which further helps to enhance the interneuron and neurogenic program.[7,8] On the other hand, insulin-like growth factor-1 (IGF-1) can induce the proliferation and differentiation, because it initiates activation of downstream substrates PI3K and AKT and phosphorylates the glycogen synthase kinase-3 (GSK3β) at SER9. This phosphorylated GSK3β leads to GSK3β inhibition.[9,10] The overexpression of GSK3β in adult neurons is one of the responsible components for the faster neuronal death in injury, AD, and PD.[11] Therefore, GSK3β could be a potential target for neuroregeneration. However, reports on glycine- and glycine-derivative-mediated GSK3β inhibition are limitedly available. It can also be noted that

Received: September 13, 2023
Revised: November 4, 2023
Accepted: November 8, 2023
Published: November 22, 2023

glycine is administered by intracerebral ventricular delivery of glycine−proline−glutamate, which prevents the loss of astrocytes and reduces the caspase-3-dependent/-independent apoptosis in the hippocampus.[12] The modulation and role of the glycine-based polymer in neurogenesis are still unknown. Therefore, there is a huge scope to overcome the clinical challenges prevailing with the existing polymers, and glycine-based polymers could help to develop the biological clue and to improve the therapeutic efficiency for neuroregeneration.

In the above line, in this work, glycine has been used as a small molecule and precast into polymeric hydrogels to mimic the cellular microenvironment for promotion of neurite growth. Small molecule-based polymers demonstrate increased molecular weight, modulating material properties such as mechanical strength and consequently regulating the biological behavior.[13] Functionalized self-assembled peptides and injectable hydrogels provide higher cytocompatibility with structural and mechanical similarities, stabilize the extracellular matrix components, and provide the biological cue mimicking the neural environment.[14] It is also important to note that neurite outgrowth is important for nerve regeneration,[3] and the effort has been intended in this direction through the present work using the synthesized *N*-acryloylglycine-based polymeric hydrogel.

It is observed that amino acid-based polymers are biologically active and helpful for the release of fibroblast growth factors (FGFs) and promote toxin binding activities and protein−protein inhibition activities.[15,16] Amino acid-derived acrylic polymers such as poly(acrylic acid), poly acrylamide, and poly(*N*-acryloyl glycinamide) have been studied for their upper critical solution temperature.[17] Poly(*N*-acryloyl glycinamide) possesses a gelling property and robust adhesion behavior, promotes wound healing efficacy,[18] and exhibits osteo-regeneration properties.[19] Similarly, poly(*N*-acryloyl glycine) (PNAG) shows the pH- and thermoresponsive drug-releasing behavior.[20] A number of natural and synthetic polymers such as chitosan, alginate, natural silk, and polymers of lactic and glycolic acids have been evaluated for neural regeneration.[2] Self-assembled peptides conjugated with nanoparticles have also been used for neurite/axonal outgrowth with improved myelination.[21] Similar to chemical properties, the mechanical stability of the material controls the neuronal regeneration and glial differentiation.[22] Despite continuous research, however, neuronal repair is still a challenging task, because the CNS follows the break system, which limits the regeneration property with maturity.[23] Hence, incorporation of controlled topography and biochemical cue can facilitate the redevelopment of the biological system.[24] Although development of materials with biochemical cue is challenging, there is a lot of scope to improve.

Herein, we reported the proof of concept of the use of the poly(*N*-acryloyl glycine-acrylamide) p(NAG-*b*-A) copolymeric hydrogel and studied the efficiency of neuronal growth and the hydrogel's neuroprotective role in oxidative stress conditions. First, we prepared a "mer" with glycine and *N*-acryloyl chloride and then we synthesized the copolymeric p(NAG-*b*-A) hydrogel using AIBN as an initiator and divinylbenzene (DVB) as a cross-linking agent and characterized it for structural, chemical, and mechanical properties. Then, we studied the response toward the primary neuronal cells and PC12-differentiated cells in oxidative stress conditions to check the neuroregenerative properties of the synthesized p(NAG-*b*-A) hydrogel. For the neurite growth, the swelling of the hydrogel and the pH at the local environment are two important factors, and therefore, the swelling behavior was studied at a physiological temperature (37 °C) and at different pH levels (3−8). The mechanical stability of the hydrogel is important to modulate and mimic the microenvironment for neuroregeneration, which was studied in the physiological temperature range using rheological measurements. The cell viability of the hydrogel was studied through various cell-based studies using PC12, HEK293, and HepG2 cell lines. The primary cortical neurons were isolated from Wistar rats, and their neuroregenerative properties were studied. The growth of the neurons was studied up to 21 days of post treatment with the hydrogel, and the morphology and the nature of the growth such as 3D reconstruction, morphology, and colocalization were studied using immunofluorescence staining. Additionally, extensive *in silico* molecular interaction studies were performed to analyze the behavior of glycine, the *N*-acryloylglycine (NAG) monomer, and the p(NAG-*b*-A) hydrogel in GSK3β inhibition for the neuronal growth. Furthermore, the neuronal cells are vulnerable to oxidative damage and imbalance between generation of free radicals and antioxidant defense often lead to oxidative stress followed by the neuropathological conditions.[25] In order to elucidate the applicability of the p(NAG-*b*-A) hydrogel in biomedical applications, PC12 cells were grown in the presence of oxidative stress generated by H_2O_2 and treated with the p(NAG-*b*-A) hydrogel. The interactions between neurons and hydrogel, macromolecule preparation, and energy minimization were conducted on UCSF Chimera 1.10.2 with 100 steepest descent steps by applying AMBER ff14SB and ligand structures, as well as through the energy minimization approach and with the MMff94 force field. Molecular docking was performed by using the AutoDock 4.2 tool to check the molecular interactions. Finally, the impact of the glycine moiety and its conversion into copolymer hydrogel to check whether it provides the physical cue or not as well as its significant role in boosting the neurite outgrowth and maintaining the microtubule integrity in neuronal cells was studied.

2. EXPERIMENTAL SECTION

2.1. Materials. Glycine (98%, Qualigens); Rhodamine 6G (Rh 6G, >97.8%); methyl thiazol tetrazolium (MTT, >99.9%, HiMedia); triethylamine (≥99.5%, Merck); hexadecane anhydrous (99%, Sigma-Aldrich); DVB (Alfa Aesar); acryloyl chloride stab. with 400 ppm phenothiazine (96%, Alfa Aesar); chloroform, ethyl acetate, and 1,4-dioxan (99%, Merck); 2,2-azo-bis-isobutyronitrile (AIBN, 98%, SRL); SDS (90%, Merck); Neurobasal Medium SFM (Thermo); neuronal growth factor (Thermo); B-27 supplement (Thermo); fetal bovine serum (Gibco); HBSS 1× (Thermo); and penicillin−streptomycin cocktail, gentamicin, and poly-L-lysine (Sigma-Aldrich) were the chemicals used for this study, without further purification.

2.2. Synthesis of *N*-Acryloyl Glycine. The NAG monomer was synthesized according to our previously reported method (*Patent No.: 419638, Granted on. 30−01−2023*), and the steps involved in the synthesis process are shown in Scheme 1. In brief, for solution A, 20 mmol of glycine was dissolved in 20 mL of 2 M KOH in an ice bath; for solution B, 20 mmol of acryloyl chloride was dissolved in 5 mL of 1,4-dioxan in an ice bath. Then, solution B was added dropwise into solution A under vigorous stirring (for 1 h in an ice bath) followed by overnight (12 h) at room temperature (25 °C) with continuous stirring. Next, the reaction mixture was washed with diethyl ether (three times, with 20 mL for each time) followed by acidification (∼pH 2 adjusted by adding 5 M HCl dropwise) and was saturated by adding excess NaCl. Afterward, the aqueous solution was extracted

https://doi.org/10.1021/acsabm.3c00807
ACS Appl. Bio Mater. 2023, 6, 5644−5661

Scheme 1. The Probable Mechanism Involved in the Synthesis of Poly(*N*-acryloylglycine-acrylamide) Hydrogel

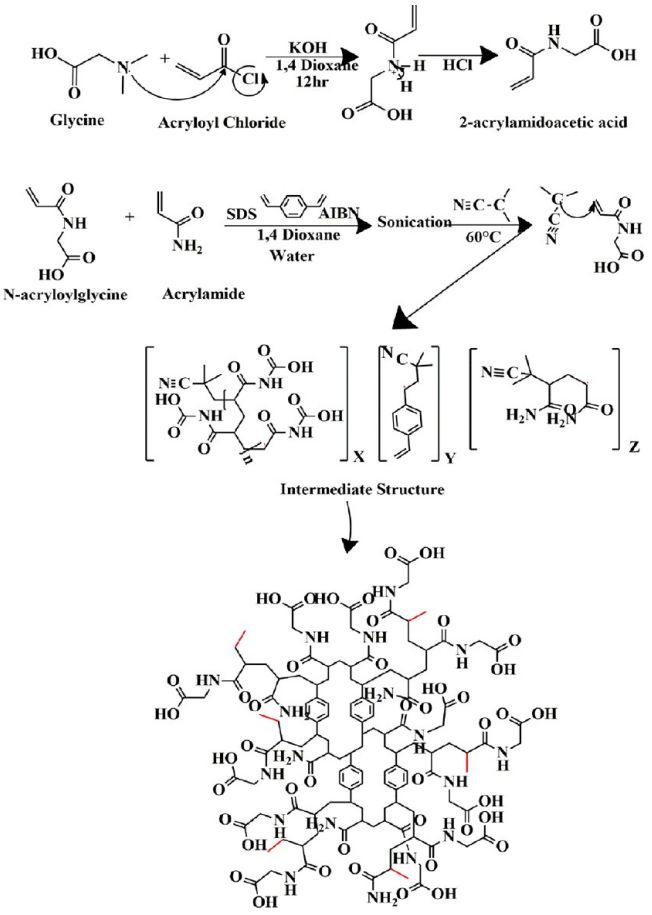

with ethyl acetate (five times, with 20 mL each time) and dried by adding anhydrous $MgSO_4$. Finally, the filtered reaction mixture containing the NAG monomer was concentrated under reduced pressure using rota evaporator followed by lyophilization.[26]

2.3. Preparation of the Poly(NAG-*b*-A) Hydrogel. The copolymer synthesis method is shown in Scheme 1. The poly(NAG-*b*-A) copolymeric hydrogel was prepared by a free radical mini-emulsion polymerization approach. 800 mg of NAG was dispersed in 8 mL of 1,4 dioxane for 30 min under bath sonication (bath temperature, 25 °C) with 5 min of pulse. Then, 40 mg of hexadecane (HD) was added followed by the addition of 40 mg of divinylbenzene (DVB) and addition of dissolved acrylamide (200 mg of acrylamide in 1000 μL of water) and then 20 mg of AIBN within continuous stirring. Furthermore, SDS (44 mg in 300 μL water) was added into the reaction mixture and stirred for 30 min at RT. Then, it was sonicated for another 7 min (ultraprobe sonicator, 750 W, 30% power, 45:15 cycles) at 25 °C. Afterward, the total reaction mixture was transferred into a 100 mL round-bottom flask and stirred for 12 h at 75 °C (in oil bath) for the conversion of the monomer into polymer. The prepared sample was washed with the (50:50) ethanol−water 8−10 times followed by washing with ethanol−water mixture (30:10) three times. Finally, the sample was lyophilized and kept for further study. The detailed method was reported in an Indian Patent (*Patent No.: 419638, Granted on 30−01−2023*).

2.4. Characterization of the NAG and p(NAG-*b*-A) Hydrogels. Functional groups and structural analysis were confirmed through FTIR, ^{1}H NMR spectroscopy, and ^{13}C NMR spectroscopy. FTIR spectra for NAG with the KBr pellet and for the copolymer nanohydrogel (poly(NAG-*b*-A)) with ATR were recorded (Thermo Electron Scientific Instruments LLC, model Nicolet iS5). ^{1}H NMR and ^{13}C NMR spectroscopic measurements were conducted by dissolving 10 mg of the NAG monomer in DMSO-d6 and p(NAG-*b*-A) in $CDCl_3$ (AVH D 500 AVANCE III HD 500 MHz spectrometer). The molecular weight of p(NAG-*b*-A) was calculated by MALDI-TOF (MS: Bruker AutoFlex Speed MALDI-ToF). Thermal stability was studied with TGA (a TGA-50 TGA instrument) (from 25 to 500 °C, at a heating rate of 10 °C min^{-1} in a N_2 gas environment, with a gas flow rate of 100 mL min^{-1}). The phase transition of the polymer was studied through DSC (DSC-60 Plus) (sample holder in an aluminum pan, reference indium, and heating rate 10.0 °C min^{-1}, in a N_2 gas environment, experimental range −140 to 550 °C). X-ray diffraction (XRD) patterns of the samples were recorded at 2θ = 5 to 90° using an HR-XRD (Rigaku SmartLab 9 kW powder type) equipped with a Cu Kα X-ray radiation source of λ = 1.54 Å).

2.5. Morphological Evaluation. Morphology and 3D structural analysis of the p(NAG-*b*-A) copolymeric hydrogel was characterized by a field-emission scanning electron microscope (FESEM) (model: Nova NanoSEM 450) with the accelerating voltage of 15 kV and by a high-resolution transmission electron microscope (HRTEM) (model: Tecnai G2 20 TWIN). Energy-dispersive X-ray spectroscopy (EDXS) analysis was performed, and chemical compositions were estimated using a TEM EDS SYSTEM with the Octane Plus SDD Detector, which is attached with the HRTEM. For the FESEM analysis, ∼0.1 mg of lyophilized sample (p(NAG-*b*-A)) was dispersed in 500 μL of isopropanol, drop casted on silicon wafers, and coated with Au−Pd for 30 s. Similarly, for HRTEM analysis, ∼0.1 mg of lyophilized p(NAG-*b*-A) was dispersed in 500 μL of isopropanol along with two drops of 2% uranyl acetate (UA) and the suspension was kept for 6 h. Then, a few drops of the dispersed sample were cast on the C-coated Cu grid (200 mesh) and HRTEM images were acquired after proper drying.

2.6. Swelling Behavior of the Poly(NAG-*b*-A) Hydrogel. To find out the dynamic swelling behavior of the prepared p(NAG-*b*-A) nanohydrogel, a defined amount of hydrogel was taken and then incubated in PBS buffer of different pH levels of 3, 5, 6, 7.4, and 8 at 25 °C. In the specified time interval, the weight and volume of the swelled hydrogel were recorded. The Mass Swelling Index (MSI) and Volume Swelling Index (VSI) were calculated using eq 1 and eq 2:

$$\mathrm{MSI} = \frac{W_s - W_i}{W_i} \times 100 \quad (1)$$

$$\mathrm{VSI} = \frac{V_s - V_i}{V_i} \times 100 \quad (2)$$

where W_s = weight of the swelled hydrogel, W_i = initial dry weight of the hydrogel, V_s = swelled volume of the hydrogel, and V_i = initial dry weight of the hydrogel. All of the experiments were performed in triplicates.

2.7. Rheological Behavior of the Hydrogel. Rheological characterization of the hydrogel was performed using an Anton Paar MCR 102 rheometer with a parallel plate (30 mm diameter). Each sample was handed out on the preheated/cooled rheometer plate while it was in the swelled (semisolid) state. The test geometry was lowered to the desired gap height of 0.5 mm, and the excess hydrogel was discarded. The samples were allowed to equilibrate at 25 °C for 2 min before each test. The continuous shear tests with a shear rate range of 10^{-6} to 10^{2} s^{-1} were performed to determine the relationship between the viscosity and the shear rate with the various concentrations of hydrogel samples at 34, 37, and 43 °C. Preliminary amplitude sweep tests were confirmed with 5% strain (within the linear viscoelastic region of all samples). The frequency sweep tests were conducted to evaluate the change in the viscoelastic modulus as a function of angular frequency (0.1−100 rad s^{-1}) with an oscillating strain of 5%. The temperature ramp test was carried out to determine the viscoelastic modulus, loss modulus (G''), storage modulus (G') and the complex viscosity as a function of angular frequency and temperature.

2.8. *In Vitro* Cytotoxicity Assay. The cytotoxicity and neurotoxicity of p(NAG-*b*-A) copolymers were assessed through the MTT

https://doi.org/10.1021/acsabm.3c00807
ACS Appl. Bio Mater. 2023, 6, 5644−5661

assay on PC12, HEK293, and HepG2 cell lines. All cell lines were acquired from NCCS, Pune Repository, India. For all the experiments, 1×10^4 cells were seeded in a 96-well plate in 100 μL of DMEM supplemented with 100 U of penicillin−streptomycin cocktail and 15% FBS and incubated for 24 h at 37 °C with 5% CO_2. After 24 h, the medium was replaced with different concentrations of hydrogels in complete DMEM (200 μL) and was incubated for another 24 h. Then, the medium was replaced with MTT reagent (5 μg mL^{-1}) and was incubated for 4 h to form the formazan crystals. Next, the formazan crystals were dissolved in 200 μL of DMSO. Then, after 30 min of incubation in the dark, the absorbance was measured at λ = 570 nm using a microplate reader (BioTek). Similarly, to evaluate the material response under stress conditions, PC12 cells were treated with different concentrations (10, 20, 40, 80, and 160 μM) of H_2O_2 and with 100 and 250 μg mL^{-1} concentrations of hydrogel (in the presence of stress and by removal of stress) and cell viability was measured using the MTT assay. Details of the method are presented in the subsequent sections.

2.9. Animal Ethics Permission. *In vivo* work was approved by the Institute Animal Ethical Committee of IIT (BHU), Varanasi, Uttar Pradesh, India (Regd. No. 2123/GO/Re/S/21/CPCSEA (IAEC Approval Number: IIT(BHU)/IAEC/2022/079). All the experimental procedures and handling of the animals were performed as per the ethical guidelines.

2.10. Cortical Neuron Isolation and Primary Culture. The primary cortical neuron was isolated from Wistar rats (day 1 pups). In brief, rat brains were separated and collected in 1× HBSS solution. By removal of the meninges, the cerebellum was collected. Then, the collected cerebellum was transferred to serum-free neurobasal media. The trituration process was conducted by aspirating and passing the brain tissue using a 20 mL syringe followed by a 10, 5, and 2 mL syringe. Furthermore, the rat brain cortex was enzymatically treated with 0.25% trypsin for 10 min with incubation at 37 °C. Then, 10 mL of complete medium was added to stop the trypsinization process. The cell containing the medium was passed through a 70 μM strainer. Then, the filtrate cells were centrifuged at 1600 rpm for 10 min at room temperature (25 °C). After removal of media, the cells were dispersed in complete neurobasal media and 1×10^6 cells were seeded in the p(NAG-*b*-A) hydrogel. Then, the cells were incubated and cultured in a CO_2 cabinet for 24 h at 37 °C with 5% CO_2. After 24 h, the media were changed with freshly prepared 1× B-27-supplemented and 50−100 ng of NGF-supplemented complete neurobasal media.

2.11. Immunofluorescence Staining. The 3×10^6 primary neuronal cells were loaded on the hydrogel as well as in a poly(L-lysine)-coated 12-well plate with neurobasal media supplemented with 10% FBS, 1× B-27, and 50 ng of NGF. After incubation of different time intervals, the cells were fixed with 4% paraformaldehyde in PBS for 20 min followed by incubation with chilled methanol and then permeabilization was conducted for 20 min with 0.1 wt % Triton X-100 in 1× PBS. Cells were blocked with 2% BSA for 1 h at room temperature. Furthermore, the blocked cells were incubated overnight at 4 °C with primary antibody β-tubulin III (1:500) in 0.1% BSA followed by 1 h incubation with a secondary antimouse antibody (1:1000), Rhodamine phalloidin, and Hoechst 33258. It can be noted that in each step of transition, the cells were washed with 1× PBS three times. Then, confocal microscopy images were acquired using an LSM780 Carl Zeiss confocal microscope (Germany) for 3D visualization and Z-stack images were then imported into Fiji software[27] for 3D reconstruction, morphological analysis, and colocalization.

2.12. *In Vitro* Recovery from Oxidative Stress. To evaluate the material's response in stress conditions, 1×10^4 PC12 cells per well were seeded on a 96-well plate with FBS-supplemented complete DMEM and incubated in a CO_2 incubator at 37 °C for 24 h. For the measurement of the protective role, the cells were treated with different concentrations of H_2O_2 (10, 20, 40, 80, and 160 μM) and treated with 500 μg mL^{-1} of hydrogel and the cell viability was estimated using the MTT assay. For the evaluation of recovery status, after 24 h of incubation, 1×10^4 cells per well were incubated for 24 h and they were treated with different concentrations of H_2O_2 (10, 20, 40, 80, and 160 μM) followed by incubation for another 12 h in a 5% CO_2-supplemented humidified environment. After 12 h, the complete H_2O_2-treated media were removed and then the cells were treated with 500 μg mL^{-1} of hydrogel; then, cell viability was estimated using the MTT assay. Furthermore, for macroscopic examination, 500 μg mL^{-1} (in 1× HBSS solution) of hydrogel was coated on a sterile coverslip and placed on a 12-well plate. 1×10^5 cells per well were seeded in a 12-well plate for 24 h and treated with 40 μM concentration of H_2O_2 for another 24 h followed by AO/EtBr staining. After staining, the cells were fixed with 4% paraformaldehyde and fluorescence macroscopy images were acquired. Similarly, to analyze the protective role of hydrogel on differentiated neurons, 1×10^5 cells per well were seeded on a 500 μg mL^{-1} hydrogel-coated slide and differentiated by providing 50 ng of NGF-supplemented complete DMEM for 3 days. Then, the differentiated neurons were treated with 40 μM concentration of H_2O_2 for 24 h and then immunolabeling was performed, as mentioned in the subsequent sections. After immunolabeling, confocal macroscopic images were acquired and evaluated for the morphology. To elucidate the protective role of the p(NAG-*b*-A) hydrogel, 500 μg mL^{-1} of the p(NAG-*b*-A) hydrogel was treated with a 40 μM concentration of H_2O_2 in a 1.5 mL centrifuge tube for 24 h at 37 °C. Then, the hydrogel was centrifuged and lyophilized. Next, Raman (WITec alpha300 access, WITec, Germany) and FTIR spectroscopic analyses were performed and the obtained results were compared with the untreated hydrogel. To avoid the effect of heating on the spectrum's red shift, Raman measurements were conducted under ambient conditions, with a significantly low laser power (1.5 ± 0.5 mW).

2.13. Protein Ligand Interaction Screening. The molecular docking approach was used to determine the nature of interactions between the NAG monomer and different polymeric units like dimers of *N*-acryloylglycine-*N*-acryloylglycine (G−G) and *N*-acryloylglycine-acrylamide (G−A), trimers of *N*-acryloylglycine-*N*-acryloylglycine-*N*-acryloylglycine (G−G−G) and *N*-acryloylglycine-*N*-acryloylglycine-acrylamide (G−G−A; G−A−G; G−A−A), and the GSK3β protein. The crystal structure of GSK3β was taken from the RCSB protein data bank with PDBID-1q5k (https://www.rcsb.org/structure/1Q5K) having a resolution of 1.94 Å. Furthermore, the reference molecules such as TMV (*N*-(4-methoxybenzyl)-*N*′-(5-nitro-1,3-thiazol-2-yl)urea), SB415286 (3-(3-chloro-4-hydroxyphenylamino)-4-(2-nitrophenyl)-1*H*-pyrrole-2,5-dione), and SB216763 (3-(2,4-dichlorophenyl)-4-(1-methyl-1*H*-indol-3-yl)-1*H*-pyrrole-2,5-dione), which are the potent inhibitors of GSK3β, were retrieved from PubChem. Macromolecule preparation and energy minimization were conducted using UCSF Chimera 1.10.2 with 100 steepest descent steps by applying AMBER ff14SB. Similarly, for the ligand structure, the energy was minimized using the PyrX interface by applying the MMff94 force field in the AutoDock 4.2 tool. The receptors were prepared by removing the heteroatoms and adding the polar hydrogen atoms and Kollman charges. Furthermore, the solvation parameter and 80 × 80 × 80 grid box were generated at the ATP pocket. Then, the computational rigid docking was performed by setting the genetic algorithms of 30 runs and the Lamarckian parameter. Finally, the analysis of data was performed by using AutoDock, Chimera software, and LigPlot software.

2.14. Statistical Analysis. All data presented were confirmed using at least three replicates for each of the experimental groups. The results are expressed as the mean of the values ± standard error of the mean. One-way ANOVA was performed to determine the statistical significance ($p < 0.05$), unless otherwise stated.

3. RESULTS

The NAG monomer was synthesized in the presence of potassium hydroxide. Acryloyl chloride reacts with glycine, by applying the basic principle of the Schotten−Baumann reaction mechanism.[28] Furthermore, acidification of the aqueous phase followed by saturation with NaCl and extraction with ethyl acetate improved the yield of the monomer (Scheme 1). Copolymerization of the NAG

https://doi.org/10.1021/acsabm.3c00807
ACS Appl. Bio Mater. 2023, 6, 5644−5661

Scheme 2. Synthesis of the Poly(*N*-acryloylglycine-acrylamide) Copolymeric Hydrogel and Various Processing Steps to Achieve Its Different Forms

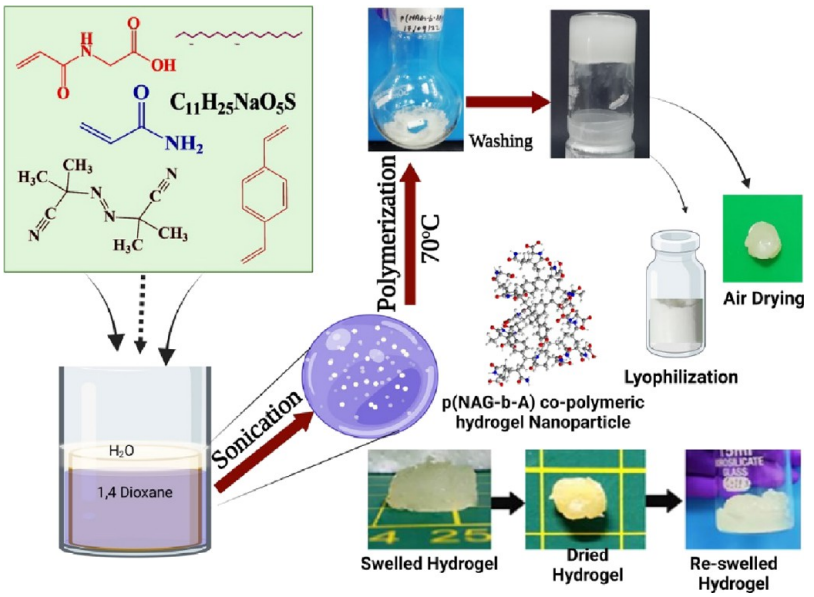

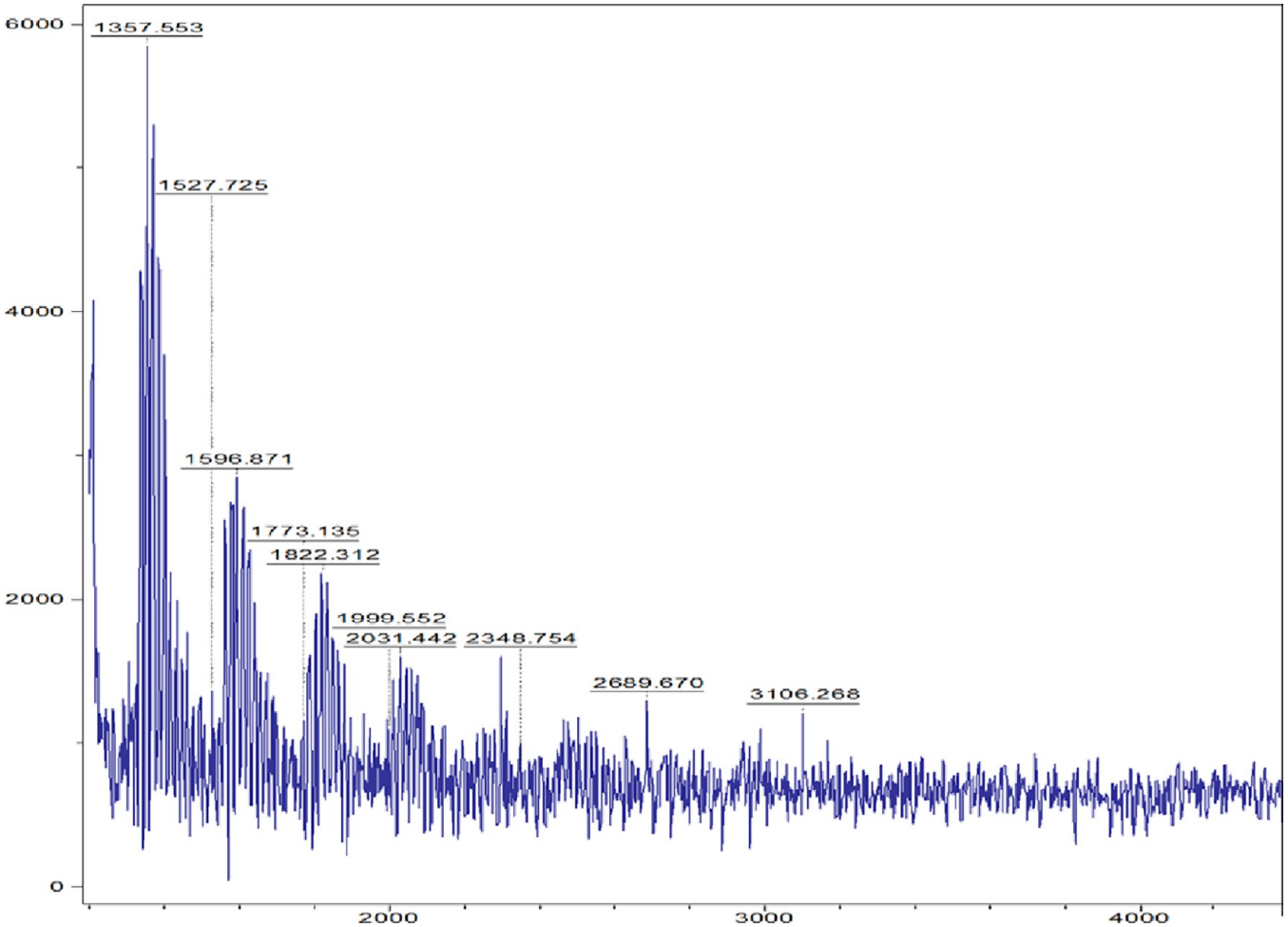

Figure 1. MALDI-ToF spectra of the p(NAG-*b*-A) hydrogel show the molecular weight (MW) distribution of the p(NAG-*b*-A) hydrogel.

monomer and acrylamide was accomplished by free radical polymerization by using radical initiator AIBN in 1,4 dioxane solution. In the presence of AIBN, vinyl groups of acryloyl glycine and acrylamide monomer were converted into a linear aliphatic chain containing polymer. The use of DVB in small amount and the presence of two vinyl groups yielded high

https://doi.org/10.1021/acsabm.3c00807
ACS Appl. Bio Mater. 2023, 6, 5644−5661

swelling capacity containing cross-linked polymers.[29] Generally, DVB yielded the highly branched polymer; however, the use of DVB in the mini-emulsion process produced the sphere-shaped cross-linked polymeric hydrogel (Scheme 1 and Scheme 2).

3.1. Physical and Physicochemical Properties of Hydrogel. Chemical functionalities of the synthesized NAG were confirmed through FTIR (Figure S1), ^{1}H NMR (Figure S2a), and ^{13}C NMR (Figure S2b). The p(NAG-*b*-A) copolymer was synthesized and characterized through FTIR, ^{1}H NMR, and ^{13}C NMR. The FTIR spectrum of p(NAG-*b*-A) (Figure S3) confirmed the presence of characteristic bands appearing at 3409 and 1725 cm^{-1} due to the presence of —NH (stretched)/−OH and for C═O (aliphatic ketone), respectively. An overtone band for —OH appeared at 1547 cm^{-1}. The sharp bands appearing at 2930, 1408, and 1220 cm^{-1} are due to the presence of aliphatic alkane (—CH_2), C═C, and −C−N (stretching of amine), respectively. The ^{1}H NMR ($CDCl_3$) spectrum (Figure S4a) of p(NAG-*b*-A) confirmed the formation of polymers with chemical shifts (δ in ppm) at 12.8 (O−H of carboxylic acid), 8.3 (N−H of 2° amine), 7.26 ($CDCl_3$), 6.8 (Aromatic-H), and 4.7 for —CH_2. Similarly, in the ^{13}C NMR spectra (Figure S4b), all the chemical shifts that were observed for the NAG monomer disappeared in the p(NAG-*b*-A) hydrogel and 44 ppm (45.36, 45.26, 45.09, 44.99, and 44.81 ppm) is the split peak of 2° alkane, which confirmed the synthesis of the p(NAG-*b*-A) hydrogel. To evaluate the solubility, 1 mg of the p(NAG-*b*-A) hydrogel immerged in 1 mL of the solvent or a mixture of solvents (e.g., water, tetrahydrofuran, toluene, chloroform, methanol, acetonitrile, acetone, dimethylformamide, and tetrachloromethane). Among these solvents, the p(NAG-*b*-A) hydrogel shows swelling behavior in water and partial solubility in toluene, chloroform, and tetrachloromethane. However, it is insoluble in other solvents (Figure S5) within 12 h of incubation with stirring. MALDI-ToF was performed by using a dithranol matrix and chloroform as a solvent (Figure 1 and Figure S5). Since the hydrogel nanoparticles are cross-linked polymers, the molecular weight obtained is therefore Mc, i.e., a molecular weight of the chain length between two adjacent cross-links. Figure 1 shows the heterogeneous fragments of the MALDI-ToF spectrum, which is evident of the maximum molecular weight (MW) of the p(NAG-*b*-A) hydrogel ranging between 1357 and 3106 Da (Figure 1). However, the maximum intensity for the MW is achieved to be 1357 Da. The repeated units vary from 200 to 120 and shows the heterogeneous population, which confirmed the formation of random and cross-linked polymers. The first highest fragment was observed at $\bar{M}_w$ = 1357 (m/z), $\bar{M}_n$ = 1327 (m/z), with PDI ≈ 1.02, the second highest fragment at $\bar{M}_w$ = 1538 (m/z), $\bar{M}_n$ = 1550 (m/z) with of PDI ≈ 1.00. Similarly, in the repeated intrapersonal variable batch, the first highest fragment was observed at $\bar{M}_w$ = 1357 (m/z), $\bar{M}_n$ = 1309 (m/z), with PDI ≈ 1.03, the second highest fragment at 1596 (m/z), 1527 (m/z), with PDI ≈ 1.04 (Figure S6). From these results, it can be concluded that the fragment sets are random; however, the synthesis method shows excellent repeatability.

The thermal stability of the p(NAG-*b*-A) copolymeric hydrogel was evaluated by TGA (Figure S7a,b). The hydrogel was stable at physiological temperatures (i.e., 37 °C). The weight loss (7.45 wt %) in TGA (Figure S7a) around 100 °C was observed due to the loss of moisture. However, the hydrogel was stable up to 220 °C, and weight loss above this temperature occurred due to thermal decomposition. Some residue of the hydrogel still remained beyond 500 °C. To identify the thermal phase transition of the p(NAG-*b*-A) hydrogel, DSC was performed at −140 to 550 °C (Figure S7b). The glass transition temperature of the hydrogel was observed to be at −20.11 °C. The broad endothermic transition observed at 69 °C (ΔH = 86.22 J g^{-1}) was due to the loss of moisture or some low molecular weight mass. A second endothermic transition was observed at 210 °C due to the melting of the block copolymer hydrogel. Exothermic heat flow was observed from 300 °C and above, due to the degradation (weight loss) of the polymer, which matched well with the TGA (Figure S7a) and was obtained due to the degradation of polyamide ketone and nitrile derivatives.[30] The acrylamide was cross-linked with DVB, and due to heating, the evolution of NH_3 gas was started at 210 °C, which can be correlated with the TGA results of p(NAG-*b*-A).[33] However, the DVB-associated cross-linking bonds in the copolymer hydrogel helped to enhance the thermal stability of the synthesized hydrogel.[31,32] The alkene evolution was started from 480 °C, and it was continued until 600 °C.[33] A similar phenomenon was observed when the (amylamide-sodium acrylate) copolymer was pyrolyzed at 492 °C, and the carboxylate residue remained.[34] Therefore, the observed 49% residue was obtained due to the presence of highly stable cross-linked parts generated due to the DVB (a cross-linker) and carboxylate functional parts of the hydrogel.

3.2. Morphology of the p(NAG-*b*-A) Copolymeric Hydrogel. The particle size and morphology of the p(NAG-*b*-A) hydrogel were confirmed through SEM and HRTEM (Figure 2). SEM images confirmed a particle size of 20−40 nm in diameter (Figure 2a,b). From HRTEM (Figure 2c,d), the particle size was calculated to be 25−30 nm in diameter (Figure 2e). It is also revealed that the hydrogel nanoparticles are connected with each other through the cross-linking and helped to create macropores inside them (HRTEM, Figure 2c). Furthermore, HRTEM (Figure 2d) reveals that the polymeric hydrogel particles are porous in nature and the pore sizes are calculated to be 1.8 to 2.5 nm in diameter (Figure 2f). It can also be noted that these pore sizes can expand during the swelling in a ratio similar to that of the hydrogel. In the HRTEM micrograph (Figure 2d), it is observed that the fringes of the semi-crystalline plains are formed due to the cross-linking of the polymeric chains and the distance between the two adjacent fringes is calculated to be 2 nm. Furthermore, the semi-crystalline nature of the polymer has been confirmed through XRD (Figure S8). The XRD pattern of NAG mers shows that the major crystalline peaks appeared at 2θ = 11.18, 16.3, 21.2, 22.32, and 27.16° in addition to a broad crystalline peak appearing at 2θ = 20° with 87% of crystallinity (Figure S8a). In contrast, the hydrogel nanoparticles were found to be semicrystalline in nature and exhibited a broad diffraction peak at 2θ = 20° (Figure S8b).

3.3. Swelling Behavior of p(NAG-*b*-A) for the Cellular Microenvironment. Hydrogels can provide an excellent microenvironment for differentiating the neuronal cells, and soft hydrogels could provide mechanical support and physical cue for regenerating the neurons.[35] Furthermore, the swelling of polymeric hydrogels could help in controlling the release of exogenous molecules such as neurotrophic factors, neuronal growth factors, and inhibitors.[36] The swelling behavior was evaluated by equilibrating the hydrogel at different pH levels (such as 3, 5, 6, 7.4, and 8) in PBS (Figure 3a). It is noticed

https://doi.org/10.1021/acsabm.3c00807
ACS Appl. Bio Mater. 2023, 6, 5644−5661

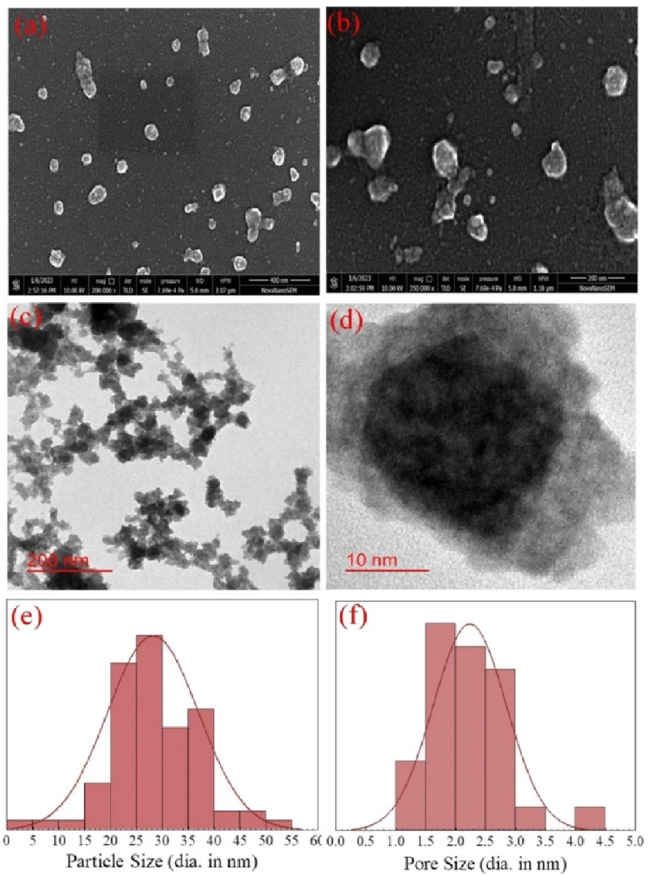

Figure 2. Morphology and particle size distribution analysis of the p(NAG-*b*-A) copolymeric hydrogel. (a, b) SEM micrographs, (c, d) HRTEM micrographs, (e) histogram for average particle size distribution obtained from (c) and (d), and (f) the pore size distribution obtained from HRTEM images (d).

that this hydrogel can expand to a higher extent and the swelling nature is pH dependent (Figure 3b,c). The synthesized hydrogel can be swelled up to 1700% (v%) within 90 min of incubation in PBS. Furthermore, it is noticed that with the increase in pH, the swelling ratio was also increased to a larger extent. However, the highest mass and volume swelling index were observed to be in the order of pH 8 > 7.4 > 6 ≥ 3 > 5, within 90 min of incubation in PBS (Figure 3b,c). The hydrogel was dispersed in water, and the size distribution and zeta potential were measured (Figure S9a,b). From DLS, it is found that the particle size increased with the increase in incubation time, such as at 120 s, $d \approx 141 \pm 10^{-6}$ nm; at 248 s, $d \approx 164.2 \pm 10^{-6}$ nm; and at 480 s, and $d \approx 725 \pm 77$ nm, due to the swelling of particles (Figure S9a). The minor hump of particle size distribution observed may be due to the smaller fragment or smaller sizes of parties. The average zeta potential value (ξ) was calculated to be −25 (±4) mV (Figure S9b). This increase in particle size (hydrodynamic diameter) is obtained from TEM and is due to swelling of the particles in water. The average particle size of the dried p(NAG-*b*-A) hydrogel (TEM results, Figure 2e) is compared with the DLS (hydrodynamic diameter of the hydrogel, Figure S9a), and it is exhibited to be ∼25−32 times (2566−3100%) increased in swelling ratio within 5 min of incubation in PBS (at pH 7.4); these results corroborated well with the swelling behavior of the hydrogel observed in PBS (Figure 3). However, the obtained zeta potential result (ξ −25 ± 4 mV) revealed that the hydrogel particles are colloidally stable.

3.4. Rheological Properties of the p(NAG-*b*-A) Hydrogel. The mechanical properties and viscoelastic behavior of polymeric material strongly influence the proliferation and differentiation of neuronal stem cells.[22] Therefore, the dynamic rheological behavior of the p(NAG-*b*-A) hydrogel was studied at different physiological temperatures through frequency sweep measurement. The storage modulus (G'), loss modulus (G''), and complex viscosity (η^*) were measured as a function of angular frequency (ω) for the p(NAG-*b*-A) hydrogel, and the results are shown in Figure 4a, b, and c, respectively. The steady shear measurements were used to elucidate the flow behavior and molecular network structure of the synthesized

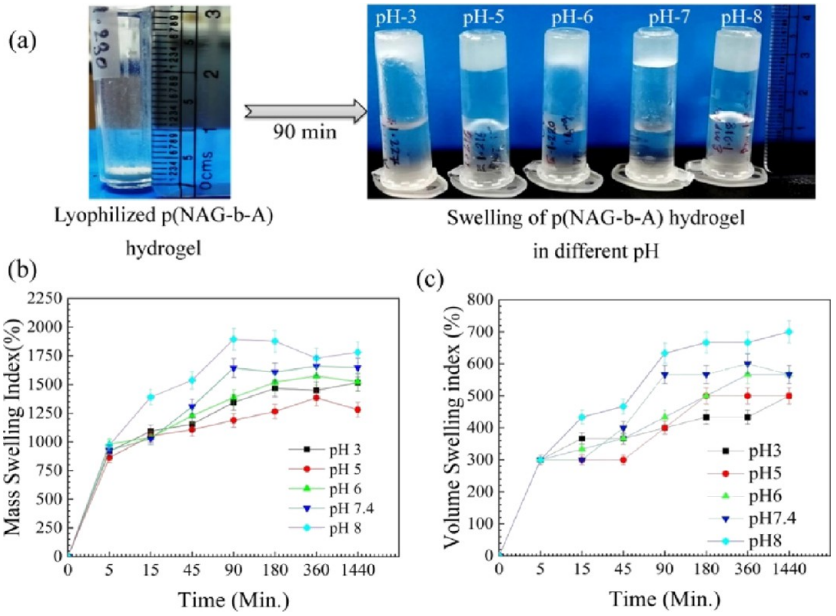

Figure 3. Swelling behavior of the p(NAG-*b*-A) copolymeric hydrogel. (a) Pictorial representation of the swelled hydrogel at different pH levels of PBS. (b) Percentage of mass swelling index at different pH levels. (c) Volume swelling index of the hydrogel at different pH levels.

https://doi.org/10.1021/acsabm.3c00807
ACS Appl. Bio Mater. 2023, 6, 5644−5661

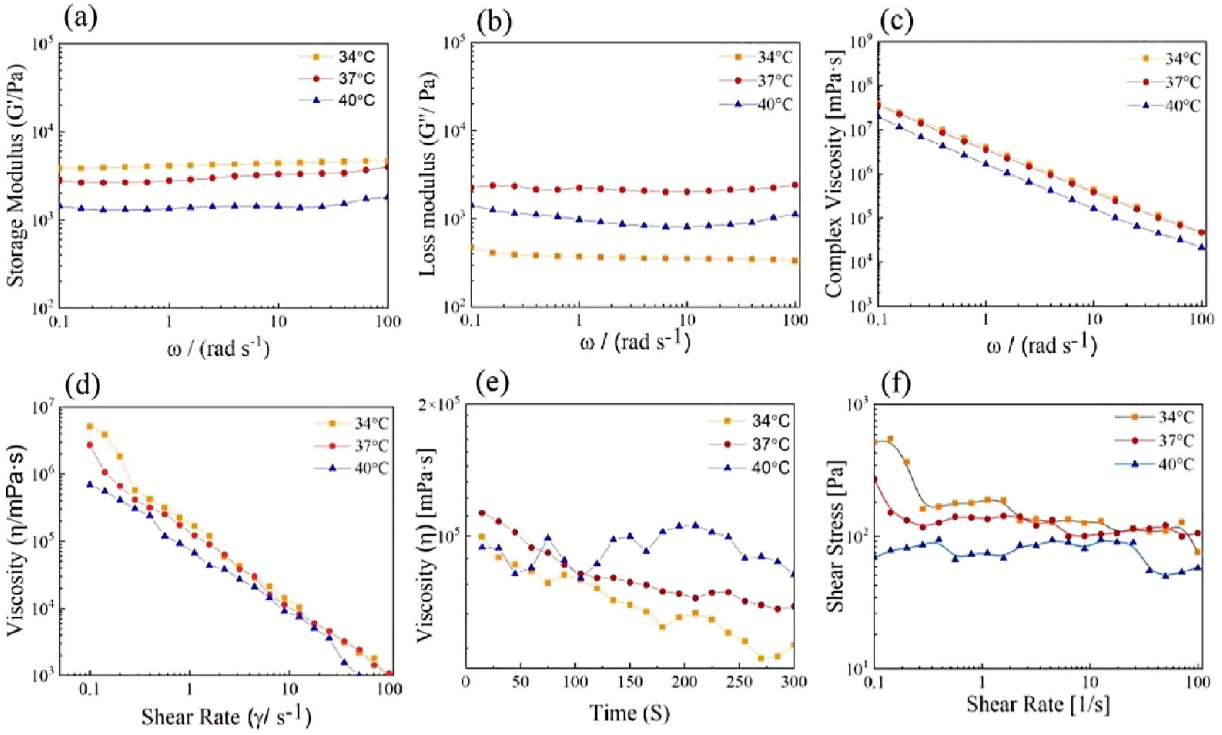

Figure 4. Rheological properties of the p(NAG-*b*-A) hydrogel studied at different conditions. Frequency sweep measurements of the p(NAG-*b*-A) hydrogel were performed at different temperatures (34, 37, 40, and 43 °C). (a) Storage modulus vs ω. (b) Loss modulus vs ω, at different temperatures. (c) Complex viscosity (η^*) vs ω at different temperatures. (d) Coefficient of viscosity (η) flow behavior of p(NAG-*b*-A) hydrogel as a function of shear rate (γ). (e) Coefficient of viscosity (η) as a function of time and temperature. (f) The change in shear stress with shear rate at different temperatures.

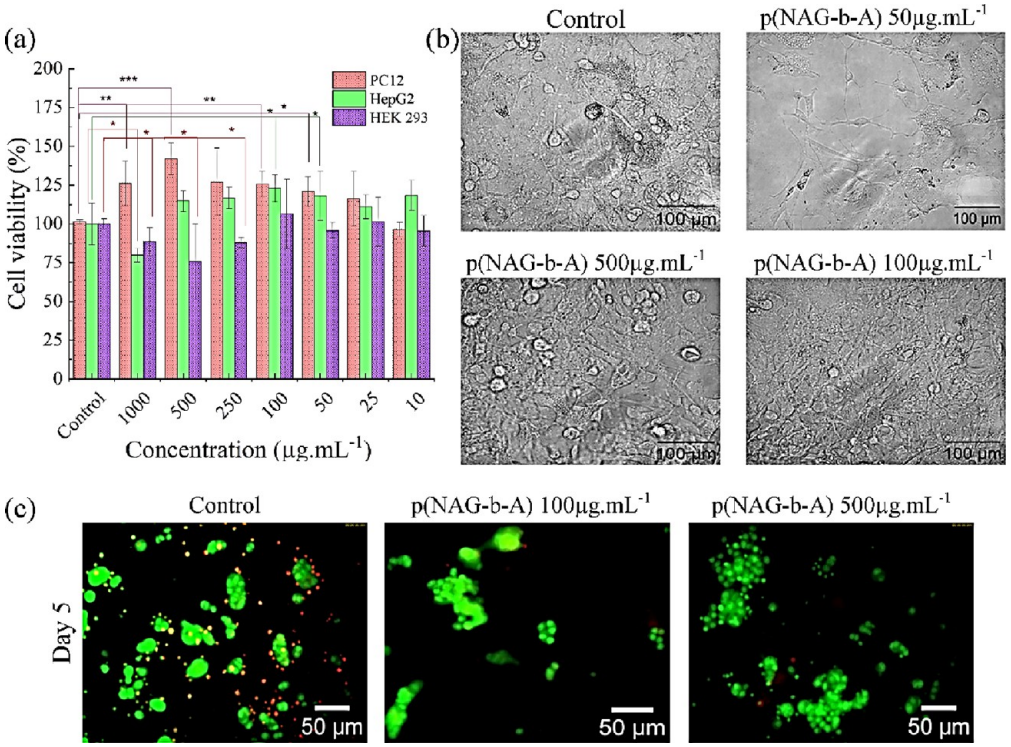

Figure 5. Cytocompatibility and neurotoxicity results of the p(NAG-*b*-A) copolymeric hydrogel. (a) The cell viability results on HEK293, HepG2, and PC12 cells at different concentrations of the p(NAG-*b*-A) hydrogel. (b) The primary neuron differentiation in control and with different concentrations of hydrogel (50, 100, and 500 μg mL^{-1}). (c) Acridine orange and PI staining of PC12 cells grown on the control and p(NAG-*b*-a) hydrogel at concentrations of 100 and 500 μg mL^{-1} on the fifth day.

https://doi.org/10.1021/acsabm.3c00807
ACS Appl. Bio Mater. 2023, 6, 5644−5661

hydrogel.[37] At the physiological temperature, the storage modulus was found to be varied from 2.9 to 3.7 kPa at 0.1 to 100 rad s^{-1} (Figure 4a) and the loss modulus was found to be varied from 2.4 to 2.3 kPa (Figure 4b). The G' value decreased with the increase in the temperature (34 to 40 °C). For similar reasons, the loss modulus (G'') for the hydrogel varied with change in the temperature and ω. Furthermore, it is noticed that at 37 °C, G' is nearly equal to G'' at 0.15 rad s^{-1}, which demonstrates the complex viscoelastic behavior of the synthesized hydrogel. Similarly, at 40 °C and at lower ω (i.e., ω = 0.1 rad s^{-1}), the crossover point is observed, which comprises the change in the viscoelastic behavior of the hydrogel due to the change in the swelling behavior and the interpolymer chain interactions/entanglement effects. The crossover point is related to the molecular architecture and cross-linking behavior of the polymeric hydrogel, and the crossover points at low frequency refer to the low molecular weight polymeric structure,[38] which has been confirmed from the MALDI-TOF results (Figure 1). The polymeric hydrogel retained the viscoelastic property as G'' was lower than that of G', and this is observed due to the complex behavior of the hydrogel. However, other than 40 °C, for all other temperatures, the G' and G'' values proportionally increased with the increase in ω. It is also observed that with the change in ω, the complex viscosity η^* changes and it is temperature dependent (Figure 4c).[39] Figure 4d shows that the viscosity changes with increase in the shear rate (γ). Figure 4e shows the decrease in viscosity in response to the shear rate and in response to time, which refers to the shear thinning behavior (at 34 and 37 °C) of the hydrogel. It is further noted that the shear stress vs shear rate properties of the polymeric hydrogel can also be correlated (Figure 4f). However, the shear rate decreases with increase in the temperature at all the ω ranges (in the entire experimental region). This phenomenon appeared due to the molecular motion, grafting, and cross-linking of the polymer chains present in the hydrogel.

3.5. Biocompatible p(NAG-*b*-A) Hydrogel Protects the Cytoskeletal Framework of Cortical Neurons. The cytocompatibility of p(NAG-*b*-A) was assessed at different concentrations of hydrogel on various cell lines such as HEK293 (a human embryonic kidney cell could be transformed in a human neuronal lineage cell), HepG2 cells (human hepatoma cells commonly used in drug metabolism and hepatotoxicity assessment studies),[38] and PC12 cells (a type of catecholamine cells, which exhibit a feature of mature dopaminergic neurons).[40] In brief, 1×10^4 cells were seeded in each well of a 96-well plate and incubated for 24 h, followed by treatment with different concentrations of hydrogel (e.g., 10, 25, 50, 100, 250, 500, and 1000 μg mL^{-1}) for another 24 h. The cell viability was calculated by taking absorbance at λ = 570 nm. Our results showed that the HEK293 cells are biocompatible up to the concentration of 100 μg mL^{-1} ($p < 0.05$) (Figure 5a). However, above the 250 μg mL^{-1} concentration, HEK293 exhibited ~80% viability. Similarly, HepG2 cells are biocompatible up to 500 μg mL^{-1} of hydrogel and significantly show cell proliferation at the concentration range from 50 to 100 μg mL^{-1} of p(NAG-*b*-A) ($p \sim 0.03$ and 0.02, respectively). However, at relatively higher concentrations such as 1000 μg mL^{-1}, the cell viability was obtained to be 79% ($p = 0.03$) (Figure 5a). Interestingly, in PC12 cells, we observed a significant increase in proliferation (up to 150%) at the concentration of 500 μg mL^{-1} ($p \sim 0.0024$) of hydrogel whereas at 1000 μg mL^{-1}, the proliferation was observed to be ~125% ($p \sim 0.007$). At a higher concentration, the reduction in cell proliferation occurred due to the contact inhibition and mechanically generated stress due to the swelling of the hydrogel (Figure 5a). The present finding for the cell viability of PC12 cells in the presence of the p(NAG-*b*-A) hydrogel supports our hypothesis for the application of the p(NAG-*b*-A) hydrogel in neuroregenerative applications. Furthermore, to assess the role of this hydrogel in neurogenesis, the primary neuronal cells (1×10^6 number) were cultured in the presence of different concentrations of hydrogel in the 12-well plate. Macroscopic images were obtained, and the results revealed the increase in cell count with increase in the concentration of the hydrogel (Figure 5b). Furthermore, a live/dead assay was performed using acridine orange (AO) and EtBr on the PC12 cell lines (Figure 5c) by culturing 1×10^5 cells on the slide coated with the p(NAG-*b*-A) hydrogel of different concentrations (100 and 500 μg) for 5 days. The microscopic images reveal that in the control group, the cell population was decreased due to the apoptotic cell death while in the hydrogel the dead cells observed are negligible. Thus, it can be concluded that, in the p(NAG-*b*-A) hydrogel, the cells remained healthy for a longer duration (Figure 5c). Furthermore, to evaluate the cytoskeletal framework, 3×10^6 primary neuron cells were seeded in each well of a 48-well plate containing 500 μg of p(NAG-*b*-A) hydrogel with neuronal media supplemented with B-27 and 50 ng of NGF for the differentiation of neurons until the 10th day. Then, the cells were fixed with 4% paraformaldehyde and stained with rhodamine phalloidin, which selectively labeled the F-actin and nucleus with Hoechst 33258 (Figure S10). Then, fluorescence microscopic images were acquired, which reveal that the p(NAG-*b*-A) hydrogel promotes cellular proliferation and the healthy network formation of actin filament and confirms very high stability of the cytoskeleton network (Figure S10) compared to the control sample.

3.6. p(NAG-*b*-A) Hydrogel-Assisted Neurogenesis. To establish the potential use of the p(NAG-*b*-A) hydrogel in neuronal applications and estimation of *in vitro* axonal regenerative properties, β-tubulin III expression was assessed by immunolabeling of cells cultured on the surface of the granular hydrogel (500 μg mL^{-1} granular nanohydrogel-coated slide) and on a 1 mm-thick film of the p(NAG-*b*-A) hydrogel. A 1 mm thin film was generated by following the polymerization step for a lesser time of 4 h compared to the steps mentioned in Section 2 followed by pouring onto the glass Petri plate. Then, the poured hydrogel was air-dried and washed repeatedly with water:ethanol (1:1) to remove impurities if any. To obtain the granular p(NAG-*b*-A) hydrogel, polymerization was continued until the end of the reaction as mentioned in Section 2 and subsequently washed with water:ethanol (1:1) followed by lyophilization. Furthermore, 500 μg mL^{-1} of granular nanohydrogel was suspended in 1× HBSS and smeared onto the coverslip followed by UV sterilization of film and coated with the granular hydrogel. Then, the isolated hippocampal neurons (1×10^6) were seeded on the 500 μg mL^{-1} granular nanohydrogel-coated slide p(NAG-*b*-A)(A-group), p(NAG-*b*-A) hydrogel film (B-group), and poly(L-lysine)-coated coverslip (control creates the hydrophilic surface, which further facilitates the kinetics of neuronal adhesion[41] with supplemented media (neurobasal media + 10% FBS + 50 ng NGF + antibiotic). Furthermore, cells were cultured for a specified time interval and proper immunolabeling was done, and the high-resolution confocal

https://doi.org/10.1021/acsabm.3c00807
ACS Appl. Bio Mater. 2023, 6, 5644−5661

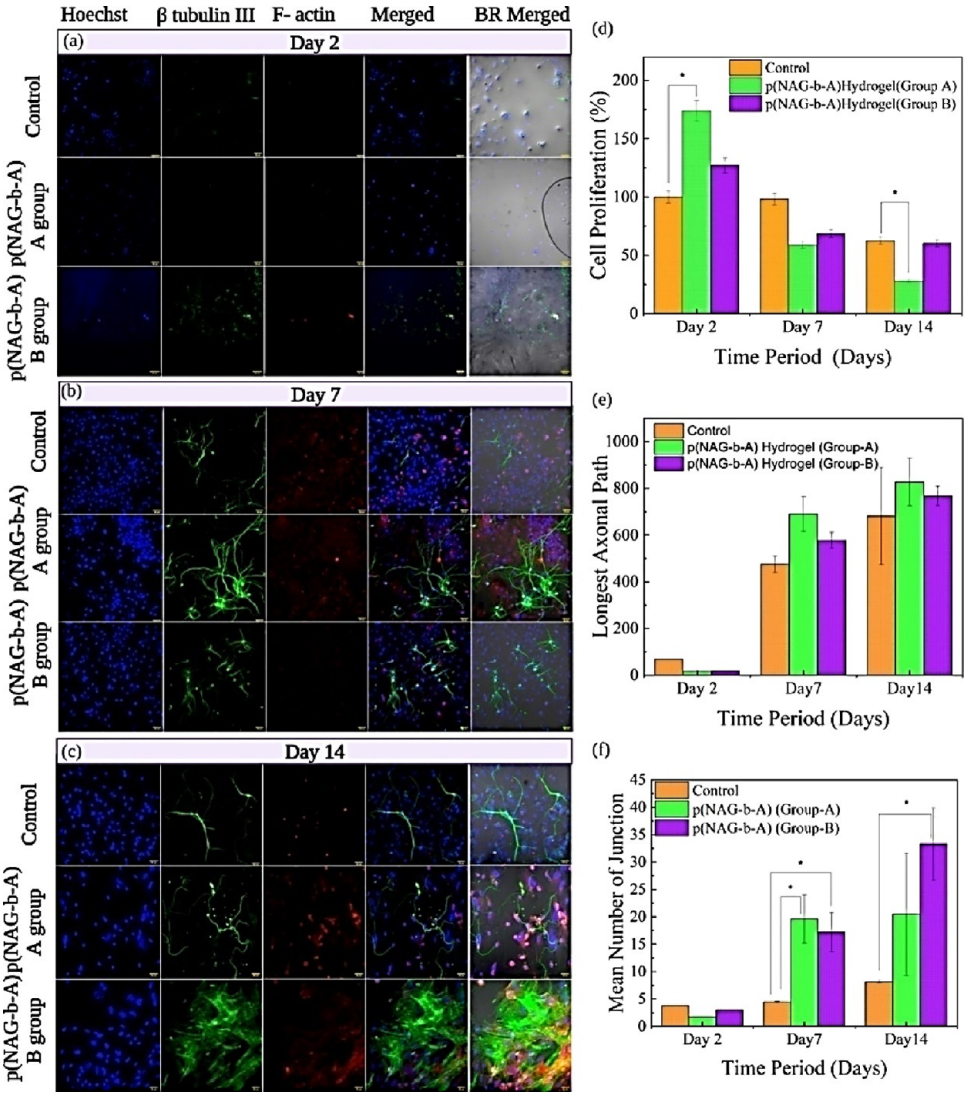

Figure 6. Confocal microscopy images represent the neuronal growth on the p(NAG-*b*-A) copolymeric hydrogel: 500 μg mL^{-1} granular nanohydrogel-coated slide (p(NAG-*b*-A), A-group), p(NAG-*b*-A) hydrogel film (p(NAG-*b*-A), B-group), and control (poly(L-lysine)-coated slide) until the 14th day. (a) Cellular adhesion and growth on the 2nd day, (b) cellular differentiation and neurite extension on the 7th day, and (c) cellular differentiation and neurite extension on the 14th day. (d) Cellular proliferation (%) obtained from images. (e) The longest axonal path, which varied at different time periods. (f) The increase in the number of junctions (branching in neurons) at different time periods. Hoechst 33258 (blue) stains represent the nucleus, immune-labeled β-Tubulin III (green) shows neurite extension, and immune-labeled phalloidin (red) shows the F-actin (all the confocal microscopy images were captured at 20×).

microscopy images were acquired on the 2nd (Figure 6a), 7th (Figure 6b), and 14th days (Figure 6c and Figure S11) and analyzed through Fiji software.[27] For this study, Matrigel and laminin can also be used; however, we limited our study to poly(L-lysine) coating for the control group and obtained comparatively exciting results. Furthermore, β-tubulin III expression was compared with the control and treated groups by acquiring confocal images. The β-tubulin III specially localized in neurons and its heterodimer assembly formed the microtubule network and decreased β-tubulin III expression, which correlated with impaired axonal elongation.[42] β-Tubulin III is required for the formation of nervous system; however, it has a specific role in peripheral axon regeneration.[43] Therefore, further analysis was conducted using microscopic images. The confocal microscopy results revealed that on the second day, primary neuronal cells have established the adhesion and the cell−cell association along with initial differentiation of neuronal cells in the control group, p(NAG-*b*-A) (A-group), and p(NAG-*b*-A) (B-group) samples (Figure 6 and Figure S11). It is clearly evident that the cell population increased significantly with a higher extent of p(NAG-*b*-A) (A-group) (p = 0.04) used, whereas in control and p(NAG-*b*-A) (B-group), the cell population differences were found to be negligible. On the seventh day, a substantial decrease in the cellular proliferation and an increase in neuronal differentiation were statistically significant with increase in the number of junction points. In the control group, p(NAG-*b*-A) (A-group), and p(NAG-*b*-A) (B-group) samples, the cellular proliferation and increased differentiation were statistically significant and differences in neurite length (green signal) are shown in Figure 6 and Figure S11. However, in the control group of samples, mostly unipolar neuronal growth was observed. Furthermore, in both the p(NAG-*b*-A) (A-group) and (B-group) hydrogel samples, most of the neurons were found bipolar and pyramidal in nature with thicker axons and their numbers of junctions were also significantly increased (p ∼

https://doi.org/10.1021/acsabm.3c00807
ACS Appl. Bio Mater. 2023, 6, 5644−5661

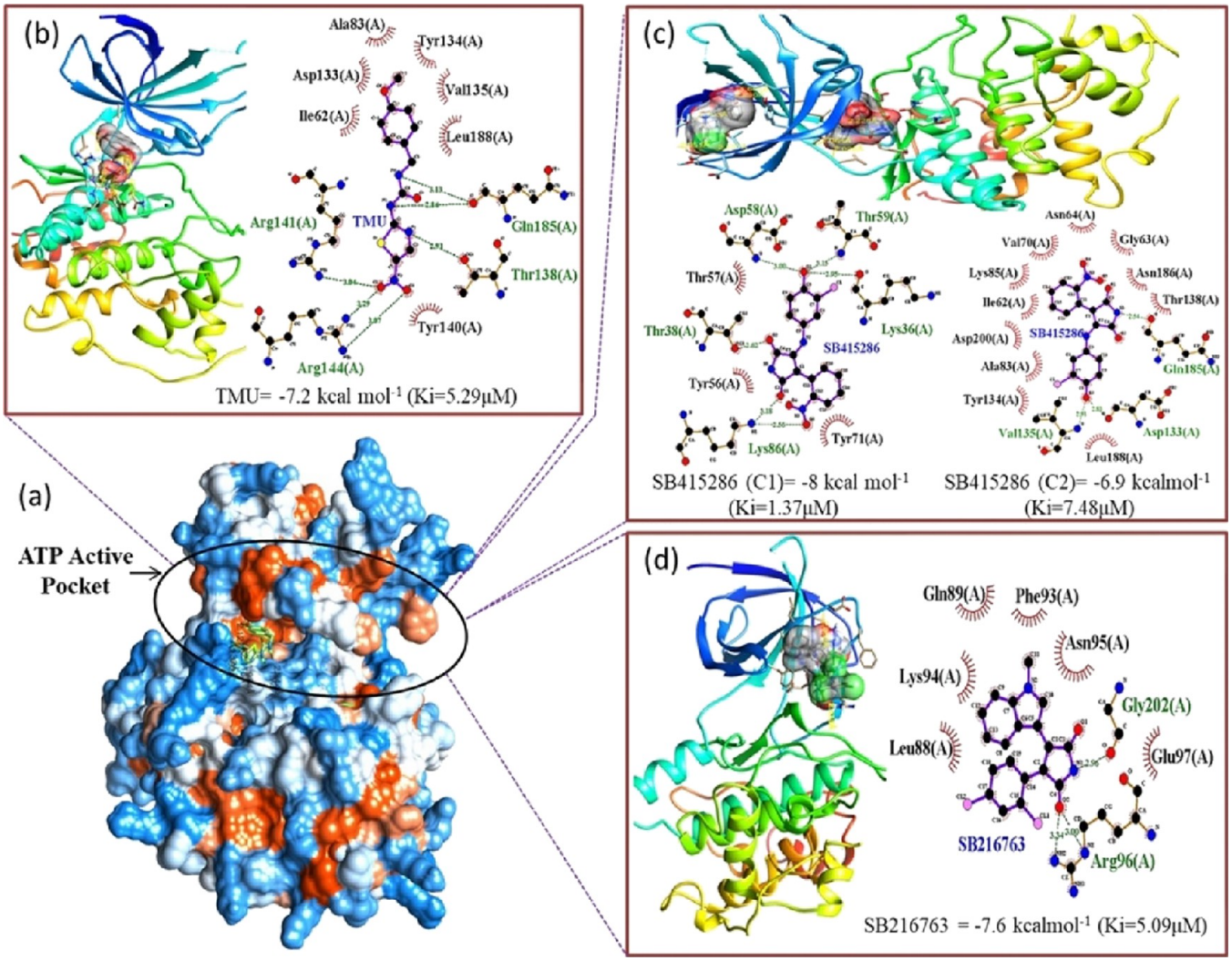

Figure 7. Molecular interactions between GSK3β (PDBID-1Q5K) with reference inhibitors. (a) Surface structure shows the ATP binding pockets with the TMU inhibitor. (b) Ribbon conformation of 1Q5K with *N*-(4-methoxybenzyl)-*N*′-(5-nitro-1,3-thiazol-2-yl) urea (TMU); LigPlot shows the interacted residues. (c) Ribbon conformation of 1Q5K-SB415286; LigPlot shows the interacted residues with two different pockets. (d) Ribbon conformation of 1Q5K-SB216763; LigPlot shows the interacted residues of amino acid with highest binding energy in kcal mol^{-1} and K_i (inhibition constant).

0.04 and $p \sim 0.03$, respectively) with low signal of F-actin, as shown in Figure 6. On the 14th day, the cell population decreased in all control samples and in both the A-group and B-group (Figure 6d). It is further noticed that the density of the network structure also substantially increased. The F-actin signal is increased with the healthy network structure of the neuron on the 14th day (Figure 6c) with respect to the seventh day (Figure 6b). Similarly, the longest axonal growth is observed in p(NAG-*b*-A) (A-group) compared to p(NAG-*b*-A) (B-group) and for the control samples (Figure 6e). The differences in axonal growth in all the samples are found to be statistically significant. Furthermore, it is observed that the number of junctions formed at 14 days are higher in the control group of samples as compared to 7 days (Figure 6f), whereas a negligible difference is observed in the p(NAG-*b*-A) (A-group) sample. However, the number of junctions was found to be increased in p(NAG-*b*-A) (B-group) ($p \sim 0.03$), which means that the deep penetration of axons in hydrogel occurred resulting in an increase in the number of branches. Similarly, after 14 days, a high-density neuronal network was identified, which looks like the structure of astrocytes (Figure S11a–f).[44] Furthermore, a higher signal for F-actin surrounding the nucleus is observed, which is evident for the formation of the dendrites (Figure S11c). Thus, the confocal microscopy results concluded that the p(NAG-*b*-A) hydrogel stimulates the stabilization of neuronal network formation with increase in the axonal regeneration property. The Z-stack-projected images of neurons on p(NAG-*b*-A) (A-group) shown in Figure S11a–f are found to be 8 μm in thickness, while for the p(NAG-*b*-A) (B-group), it is found to be 28 μm in thickness. All of these results supported that the neurons/axons penetrated more in the swelled hydrogel film (Figure S11g–l). Interestingly, on the 14th day, the treatment group neurons were observed to have Purkinje neuron-like projections,[45] as shown in Figure S11d. It is known that Purkinje neuron cells play critical roles for the proper cerebral functions and play a major role in the transmission of electrical signals with propagation of impulsive signals to the various ventricular muscles.[46,47,49]

3.7. Molecular Interaction between Polymer and GSK3β. Furthermore, to establish the mechanism on how the p(NAG-*b*-A) hydrogel is involved in neurogenesis, protein

https://doi.org/10.1021/acsabm.3c00807
ACS Appl. Bio Mater. 2023, 6, 5644−5661

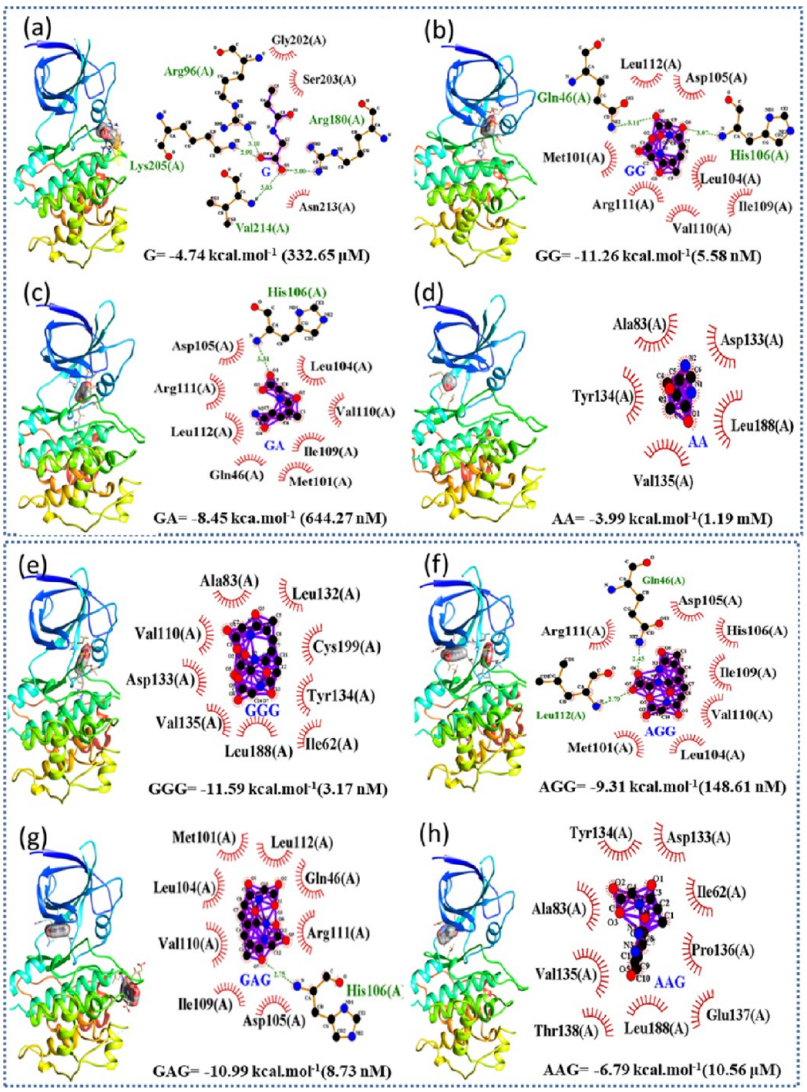

Figure 8. Molecular interactions between GSK3β (PDBID-1Q5K) with different monomeric units (a−d) and triunits (e−h) of poly(*N*-acryloylglycine-acrylamide). *N*-Acryloylglycine represented as (G) and *N*-acrylamide represented as (A). (a) 1Q5K-*N*-acryloylglycine, (b) 1Q5K-GG (*N*-acryloylglycine diunit), (c) 1Q5K-GA (*N*-acryloylglycine-acrylamide diunit), (d) 1Q5K-AA (acrylamide two units), (e) 1Q5K-GGG (homomeric triunit of *N*-acryloylglycine), (f) 1Q5K-AGG (triunit of *N*-acryloylglycine and *N*-acrylamide), (g) 1Q5K-GAG (triunit of *N*-acryloylglycine and *N*-acrylamide), and (h) 1Q5K-AAG (triunit of *N*-acryloylglycine and acrylamide). Ribbon structure shows the docking site between 1Q5K and ligplot, with each structure showing the interacted residue along with binding energy in kcal mol^{-1} and inhibition constants (K_i).

ligand interaction studies were performed through the *in silico* approach. Among several molecular circuits, GSK3β is considered as a potential target in neurodegenerative therapy due to its wide expression in adult neurons, regulated by PI3K−AKT, and it leads to the increase in the ratio of active/inactive GSK3β.[11] In adult neurons, mTOR signaling requires the outgrowth, which is regulated by the PI3K-AKT signal.[10] The inhibition of GSK3β leads to the activation of PI3K at the distal tip of the neuron, and it helps in neuronal regeneration.[10] Majority of the kinase inhibitors show affinity toward the ATP pocket of the GSK3β protein (PDBID-1Q5K). In the molecular structure of 1Q5K, the ATP pocket is present at the interface of the β-strand domain at N-terminal residues 25−138 and 139−343, which are broadened by the glycine-rich hinge regions.[11] Inhibitor TMU is a cocrystallized structure that is obtained with 1Q5K bound in the ATP pocket and shows interactions with LEU132 and ARG141. In the GSK3β structure, ASP133 and VAl135 are the predominant and important residues, where a diverse range of inhibitors gets bound. Similarly, ARG96, ARG180, and LYS205 are the crucial residues for the priming substrate.[48] As per our obtained results, the reference molecule TMU formed six hydrogen bonds. The selective inhibitor SB415286[49] interacted by forming five hydrogen bonds at one conformation, while in another conformation it formed three hydrogen bonds and potent inhibitor SB216763[50] formed two hydrogen bonds at the ATP pocket with almost similar binding energies from −6.9 to 8 kcal mol^{-1} at inhibitor constants of K_i = 7.48 to 1.37 μM along with hydrophobic interacting residues, as provided in Table S1 and Figure 7. Furthermore, we observed that NAG (G) and its polymeric units (dimer and trimer) established the protein−ligand interactions with ATP pockets of GSK3β with a higher binding energy at nanomolar (nM) concentrations compared to the available inhibitors at micromolar (μM) concentrations. With the modulation of glycine (Table S2) to *n*-acryloylglycine

https://doi.org/10.1021/acsabm.3c00807
ACS Appl. Bio Mater. 2023, 6, 5644−5661

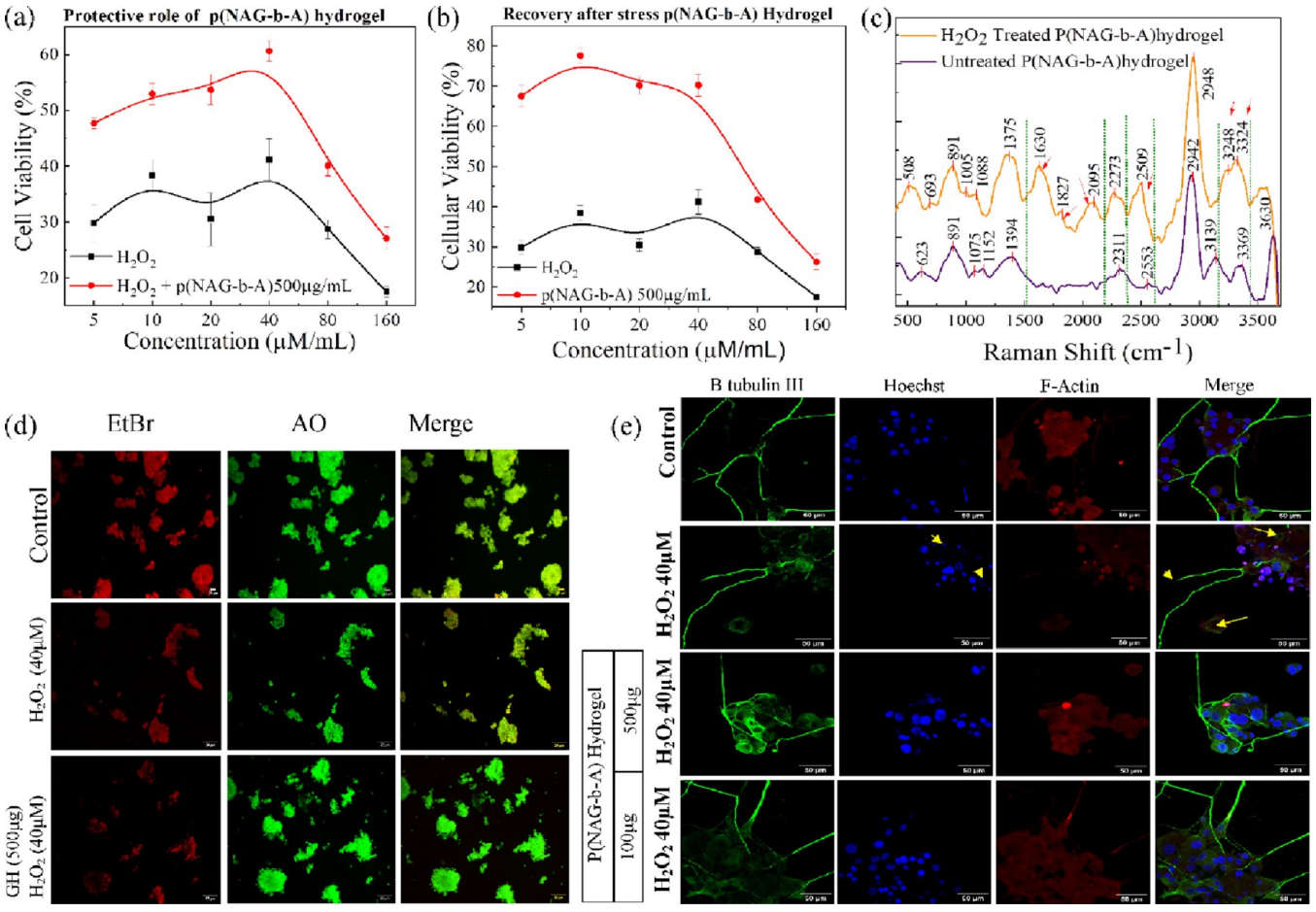

Figure 9. Protective role and recovery status after H_2O_2 induced oxidative stress-associated damage assisted by the p(NAG-*b*-A) hydrogel. (a) Protective role of the p(NAG-*b*-A) hydrogel obtained by the cell viability assay. (b) Stress-induced recovery status of PC12 cells using the p(NAG-Ac-A) hydrogel. (c) Raman shifting of the p(NAG-Ac-A) hydrogel. (d) AO/EtBr staining of PC12 cells untreated control, PC12 cells treated with H_2O_2 (40 μM), and PC12 cells treated with 40 μM H_2O_2 along with 500 μg mL^{-1} of p(NAG-*b*-A) hydrogel. (e) Cytoskeleton network stabilization by the p(NAG-*b*-A) hydrogel in the presence of 40 μM H_2O_2 induced oxidative stress at the highest proliferative concentration of 500 μg mL^{-1} hydrogel.

(Figure 8a), the binding energy is found to be increased from −3 kcal mol^{-1} (K_i = 6.33 mM) to −4.74 kcal mol^{-1} (K_i = 338.04 μM) while for the repetitive units of G, a significant increase in the binding affinity of GG (Figure 8b) is calculated to be −11.26 kcal mol^{-1} (K_i = 5.58 nM) forming two hydrogen bonds; for GGG (Figure 8e), it is calculated to be −12.62 kcal mol^{-1} (K_i = 512.32 pM), and mostly hydrophobic interactions occurred with the reference inhibitor. The GGG unit formed the strongest interaction with the LEU153HN and LEU250-O residues, while in another conformation, it interacted with the Val135 moiety. Furthermore, we checked the protein interactions with the acrylamide dimer (Figure 8d) and it shows only hydrophobic interactions with VAL135 (K_i = 1.19 mM) with a binding affinity of −3.99 kcal mol^{-1}. Heterodimers of NAG and *N*-acrylamide show interaction with one hydrogen bond at HIS106 along with increased binding affinity of −8.45 to −3.99 kcal mol^{-1} at a very low K_i of 644.27 nM (Figure 8c). Similarly, heteromers (three mer units, i.e., AAG) (Figure 8h) interacted with ASP95 with a binding affinity of −6.79 kcal mol^{-1} at K_i = 10.56 μM and with VAL135 at K_i = 11.83 μM. Interestingly, with increase in the G units, i.e., AGG (Figure 8f) and GAG (Figure 8g), an increase in the binding affinity of trimer is observed. For instance, AGG interacted with interacting residue LEU112 at K_i = 148.61 nM and binding energy of −9.31 kcal mol^{-1}. In another conformation, it interacted at K_i = 405.69 nM with Val135 residues with a binding affinity of −8.72 kcal mol^{-1}. The GAG trimer requires a higher value of K_i = 8.73 nM and a binding energy of −10.99 kcal mol^{-1} to bind with the LEU112 residues. As a conclusion, with increase in the *N*-acryloylglycine (G) units into a polymeric moiety, it increased the binding efficiency/affinity of the polymer hydrogel to GSK3β, which is further responsible for the neurite outer growth.

3.8. Protective Role of p(NAG-*b*-A) in Oxidative Stress. In order to elucidate the applicability of the p(NAG-*b*-A) hydrogel in clinical settings, PC12 cells were grown in the presence of oxidative stress that was generated by H_2O_2 and treated with the p(NAG-*b*-A) hydrogel. It is known that the neuronal cells are vulnerable to oxidative damage. Imbalance between generation of free radicals and antioxidant defense often leads to oxidative stress followed by neuropathological conditions.[25] For a proof of concept, PC12 cells were treated with different concentrations of H_2O_2 from 5 to 160 μM in the presence and absence of 500 μg mL^{-1} of the p(NAG-*b*-A) hydrogel (Figure 9a) and we observed almost 70, 61, 69, 62, 71, and 82% dead cells with respective concentrations of H_2O_2. However, in the presence of 500 μg mL^{-1} p(NAG-*b*-A) hydrogel, minimal 10% to maximum 30% cell viability was

https://doi.org/10.1021/acsabm.3c00807
ACS Appl. Bio Mater. 2023, 6, 5644−5661

increased in all different concentrations of H_2O_2-treated groups, which corroborates with the protective behavior of the p(NAG-*b*-A) hydrogel, as shown in Figure 9a. Furthermore, to check the recovery of damaged PC12 cells, they were initially treated with different concentrations of H_2O_2 for 24 h and then the H_2O_2-containing media were replaced with fresh complete media and then treated with 500 μg mL^{-1} p(NAG-*b*-A) hydrogel (treated group) and with only media (stress group). Interestingly, we did not observe any increase in cell viability (i.e., viability is almost 8 to 10%). However, in the 500 μg mL^{-1} p(NAG-*b*-A) hydrogel-treated group, the cell viability was increased from 8 to 39.28% as the treatment concentrations of H_2O_2 were maintained from 160 to 5 μM (Figure 9b). These findings are interesting evidence that our p(NAG-*b*-A) hydrogel promotes the recovery of damaged PC12 cells. Similarly, the status of the recovery for the AO/EtBr staining-untreated PC12 cells, PC12 cells treated with only H_2O_2 (40 μM), and PC12 cells treated with H_2O_2 (40 μM) with 500 μg mL^{-1} p(NAG-*b*-A) was investigated. It is observed that the treatment with 500 μg mL^{-1} p(NAG-*b*-A) prolongs the healthy cell viability and reduces the apoptotic death, as shown in Figure 9d. Furthermore, confocal microscopic images revealed that treatment with H_2O_2 (40 μM) causes nuclear damage along with destabilization of the cytoskeleton network (H_2O_2 treatment on PC12 shows a reduced red signal of F-actin) and axonal terminal damage (Figure 9e). These damages were prevented by using 500 μg mL^{-1} of p(NAG-*b*-A) hydrogel treatment, which shows the intact nuclear structure with an increased signal for F-actin and thicker axon growth (green signal for β-tubulin III). This protective behavior of the p(NAG-*b*-A) hydrogel could be obtained due to the neutralization of ȮH radicals by the —NH and —COOH groups of p(NAG-*b*-A) hydrogel. To establish this fact, the hydrogel was treated with H_2O_2 (40 μM) for 24 h, and subsequently, FTIR and Raman spectroscopy analyses were performed; the possible roles of these functional groups during the neuroprotection have been proven. FTIR spectra of the H_2O_2-treated p(NAG-*b*-A) hydrogel clearly revealed the diminished −C═O (1734 cm^{-1}) and alkane (2923 cm^{-1}) bands. Furthermore, from the Raman spectroscopic analysis (Figure 9c), the common bands in the untreated p(NAG-*b*-A) hydrogel and the H_2O_2-treated p(NAG-*b*-A) hydrogel appeared at 1078 and 1090 cm^{-1} (C−N of amide or protein or due to the bending vibration of CH), 1404 and 1398 cm^{-1} (CH_3 umbrella mode), 2937 and 2937 cm^{-1} (alkane), and 3142 and 3239 cm^{-1} (−NH). However, in the H_2O_2-treated hydrogel, an additional Raman band was observed at 1622 cm^{-1} due to the presence of amide bonds (—C═O mixed with —NH deformation). This observation shows that when a polymer comes in contact with H_2O_2, it triggers the release of CO_2 and H_2O molecules as byproducts. It is further noticed that few FTIR bands disappeared after the treatment with H_2O_2, which may have occurred due to degradation of the polymer. Detailed investigations are required to completely understand the mechanisms of action that are being planned for future studies. Thus, it can be concluded that the p(NAG-*b*-A) hydrogel possesses a strong protective role for the living cells in oxidative stress conditions.

4. DISCUSSION

In the recent era, the polymeric hydrogel is considered as the potential drug delivery platform for the management of neurological conditions due to its high drug loading capacity, good permeability, and high colloidal stability, which could bypass the physiological barrier (BBB). Glycine is an inhibitory neurotransmitter and takes part in early neurogenesis/neuroprotective activity. Therefore, a glycine-based polymeric hydrogel could boost the neurogenesis/neuroprotective activities. In the present work, glycine-based p(NAG-*b*-A) hydrogel particles were synthesized ($d \approx 25-40$ nm in diameter) (Figure 2). Void space of the hydrogel network structure limits the cell infiltration. However, it can be overcome by heterogeneous granular hydrogel formation as the pore sizes are proportional to the assembling into micron-sized particles that are useful for the cellular infiltration.[51] The synthesized p(NAG-*b*-A) hydrogel exhibits very high swelling behavior (∼1500%; Figure 3) within 12 h. However, the major limitation of the cross-linked polymer hydrogel is that it is not soluble in organic solvents and measuring the molecular weight accurately is very difficult.

In leading pathophysiological conditions, a change in the intracellular pH in neurons is correlated with neurodegenerative diseases; brain acidosis mediates neuronal death; AD, HD, PD, and cerebral alkalosis lead to ischemic stroke;[52,53] and *N*-acyloylation of amino acids could favor the development of pendant polymers and the charge distribution in a stereoselective configuration along with a higher gelling property.[15,16] Due to the presence of carboxylic acid groups (−COOH) and amide groups (−CO-NH) in *N*-acryloyl-based polymeric chains (Figures S1−S3), pH- and temperature-responsive behaviors in aqueous medium are exhibited. Hence, it could be a good candidate for the loading of various therapeutic molecules (Figure 2a) and useful in various brain physiopathological conditions and for neurite growth. The p(NAG-*b*-A) nanohydrogel is quite stable between 30 and 200 °C (Figure S7). In the biological system, the p(NAG-*b*-A) nanohydrogel could show biodegradable behavior due to the presence of *N*-acryloyl glycine as a monomeric unit. Glycine *N*-acyltransferase produces a minor metabolite of fatty acids, and the degradation of acyloylglycine through hydrolysis can produce the glycine.[54] The semi-crystallinity of p(NAG-*b*-A) (Figure 2d and Figure S8b) allows mechanical stability, and the high surface zeta potential of p(NAG-*b*-A) (−25 mV) establishes its colloidal stability in aqueous medium (Figure S9b). The shear thinning behavior of this hydrogel (Figure 4e) increases the injectability and contributes in enhancing the mixability, pumpability, and pourability.[55] Furthermore, it has been reported that in the soma (softest part) and neurite (stiffer part) microcompartments, different mechanical responses are shown, i.e., Young modulus values obtained to be 1.05 to 0.38 and 7 kPa, respectively, which are very important for neuroregeneration.[56] With different ranges of the elastic moduli, the neuronal cells behave differently; below the 1 kPa (softer surface) modulus value, it favors the neuronal differentiation, and above 7 kPa (stiffer surface), it favors oligodendrocyte differentiation. Again, between 1 and 3 kPa moduli, astrocyte differentiation is shown[57] and a modulus of 2 kPa can increase the differentiation of immature to mature neurons.[58] The p(NAG-*b*-A) hydrogel synthesized in this work shows the elastic modulus values of 2.9 to 3.7 kPa, which favors the differentiation of immature to mature neurons and promotes the astrocyte differentiation (Figure S11a−f). Along with biocompatibility, the p(NAG-*b*-A) nanohydrogel promotes proliferation of the HepG2 and PC12 cell lines to a higher extent (Figure 5a,b). Similarly, in primary neuron culture, it is observed that the p(NAG-*b*-A) hydrogel can

https://doi.org/10.1021/acsabm.3c00807
ACS Appl. Bio Mater. 2023, 6, 5644−5661

induce excellent neurite growth along with microtubule stabilization, which is possible due to the granular network formation capability of the hydrogel with 3D cellular infiltration (Figure 6a−c, p(NAG-*b*-A) group B). Deep penetration of cells (Figure 6e) into the hydrogel and the porous nature of the hydrogel film provided the highest nutrient to the cells and helped to mimic the neuronal microenvironment. A strong signal of Rhodamine phalloidin for F-actin exhibited that p(NAG-*b*-A) promotes neuronal integrity (Figure 6a,b) along with development of dendrites and spine penetration (in Figure 6a−c and Figure S11).[59] Additionally, the axonal elongation is confirmed through *β*-tubulin III (green) expression. Inactivation of GSK3*β* promotes the axon regeneration by increasing the microtubule growth speed in the growth cone.[60] As GSK3*β* mediates the phosphorylation of several proteins and is involved in various signaling pathways like the GSK3*β*-CRMP-2 axonal growth inhibitory pathway,[60] and PI3K-AKT pathway,[61] Akt/GSK3*β*/*β*-catenin and overexpression of GSK3*β* have a correlation with several neurological disorders.[62] *In silico* study suggests that the polymeric unit interacted with GSK3*β* at the ATP active pocket with higher binding efficiency comparable with the available inhibitors (Figures 7a and 8a−h). The obtained results further suggest that neurogenesis could occur due to GSK3*β* inhibition.

Accumulation of ROS followed lipid peroxidation and mitochondrial dysfunction. As a consequence, neuronal death and persistent oxidative stress lead to neurodegenerative diseases.[63,64] As per our observation, it can be concluded that the presence of free radicals in stress conditions may cause the oxidation of the p(NAG-*b*-A) hydrogel. These free radicals can attack the —C═O bond of the polymer and can oxidize p(NAG-*b*-A) and release CO_2 and water as byproducts. Furthermore, the conversion of secondary amine to primary amine occurs due to the attack of ȮH free radicals, which has been confirmed from the FTIR band shifting from 1658 cm^{-1} p(NAG-*b*-A) to 1637 cm^{-1} (H_2O_2-treated p(NAG-*b*-A)) (Figure S12). This interaction of ROS and the stimulatory effect on astrocytes assists in the neuroprotective role of p(NAG-*b*-A).[65] Furthermore, controlled synthesis and purification of the p(NAG-*b*-A) hydrogel with different molecular weights can provide clear insight about the neurogenesis and neuroprotection efficacy of the hydrogel.

5. CONCLUSIONS

In this work, we have successfully synthesized a porous, cross-linked p(NAG-*b*-A) hydrogel with high swelling behavior. The p(NAG-*b*-A) hydrogel shows shear thinning behavior and is injectable in nature. p(NAG-*b*-A) can promote the axon growth in primary neurons and can improve the microtubule integrity. However, its exact mechanism is yet to be found out. *In silico* study reveals that the p(NAG-*b*-A) hydrogel could be involved in the GSK3*β* inhibition and promote neuronal growth via modulation of the GSK pathway. Presence of various functional groups such as −COOH and amide groups in the p(NAG-*b*-A) hydrogel scavenges the free radicals via oxidation reaction and protects neuronal damage from oxidative stress conditions. It is found that the viscoelastic nature of the p(NAG-*b*-A) hydrogel favors the astrocyte differentiation and consequently neuroprotection. Finally, it can be concluded that the p(NAG-*b*-A) hydrogel is a potential candidate to induce neuronal regeneration and can be used in other regenerative purposes. Furthermore, the p(NAG-*b*-A) hydrogel can provide a huge scope to analyze the mechanistic activities for the various leading neurodegenerative diseases, which could be the future plan of this work.

■ ASSOCIATED CONTENT

Supporting Information

The Supporting Information is available free of charge at https://pubs.acs.org/doi/10.1021/acsabm.3c00807.

FTIR spectrum of the *N*-acryloylglycine (NAG) monomer; NMR spectra of *N*-acryloylglycine monomer; FTIR spectrum of the poly(*N*-acryloylglycine-acrylamide) co-polymeric hydrogel; ^{1}H-NMR of p(NAG-*b*-A) hydrogel and ^{13}C-NMR of p(NAG-*b*-A); solubility test of the p(NAG-*b*-A) hydrogel in different solvents at room temperature; molecular weight (MW) distribution of the p(NAG-*b*-A) hydrogel determined by MALDI-ToF spectra (for batch 1); thermal stability and heat flow; XRD patterns of NAG and p(NAG-*b*-A); dynamic light scattering (DLS) for the p(NAG-b-A) hydrogel NPs; actin filament stabilization in primary neurons; 3D orientation of the longer neurite growth on the 2D substrate; FTIR and Raman shift of untreated and H_2O_2-treated p(NAG-*b*-A) hydrogels; molecular interaction between GSK3*β* and reference inhibitor; molecular interaction of GSK3*β* (glycogen synthase kinase-3) with polymeric units; full list of abbreviations (PDF)

■ AUTHOR INFORMATION

Corresponding Author

Pradip Paik − *School of Biomedical Engineering, Indian Institute of Technology, Banaras Hindu University (BHU), Varanasi, Uttar Pradesh 221 005, India;* orcid.org/0000-0001-7033-0636; Email: paik.bme@iitbhu.ac.in, pradip.paik@gmail.com

Authors

Kirti Wasnik − *School of Biomedical Engineering, Indian Institute of Technology, Banaras Hindu University (BHU), Varanasi, Uttar Pradesh 221 005, India;* orcid.org/0000-0002-0794-9409

Prem Shankar Gupta − *School of Biomedical Engineering, Indian Institute of Technology, Banaras Hindu University (BHU), Varanasi, Uttar Pradesh 221 005, India*

Sudip Mukherjee − *School of Biomedical Engineering, Indian Institute of Technology, Banaras Hindu University (BHU), Varanasi, Uttar Pradesh 221 005, India;* orcid.org/0000-0002-3625-2272

Alagu Oviya − *School of Biomedical Engineering, Indian Institute of Technology, Banaras Hindu University (BHU), Varanasi, Uttar Pradesh 221 005, India;* orcid.org/0009-0000-0528-8777

Ravi Prakash − *School of Material Science, Indian Institute of Technology, Banaras Hindu University (BHU), Varanasi, Uttar Pradesh 221 005, India*

Divya Pareek − *School of Biomedical Engineering, Indian Institute of Technology, Banaras Hindu University (BHU), Varanasi, Uttar Pradesh 221 005, India*

Sukanya Patra − *School of Biomedical Engineering, Indian Institute of Technology, Banaras Hindu University (BHU), Varanasi, Uttar Pradesh 221 005, India*

Somedutta Maity − *School of Engineering Sciences and Technology, University of Hyderabad, Hyderabad, Telangana State 500 046, India*

Vipin Rai − *Department of Biochemistry, Institute of Sciences, Banaras Hindu University (BHU), Varanasi, Uttar Pradesh 221 005, India;* Present Address: Present address: Department of Anesthesiology, Rutgers New Jersey Medical School, Newark 7103, United States (V.R.)

Monika Singh − *School of Biomedical Engineering, Indian Institute of Technology, Banaras Hindu University (BHU), Varanasi, Uttar Pradesh 221 005, India*

Gurmeet Singh − *School of Biomedical Engineering, Indian Institute of Technology, Banaras Hindu University (BHU), Varanasi, Uttar Pradesh 221 005, India;* orcid.org/0000-0003-1106-5929

Desh Deepak Yadav − *School of Biomedical Engineering, Indian Institute of Technology, Banaras Hindu University (BHU), Varanasi, Uttar Pradesh 221 005, India;* orcid.org/0000-0002-2513-8853

Santanu Das − *Department of Ceramic Engineering, Indian Institute of Technology, Banaras Hindu University (BHU), Varanasi, Uttar Pradesh 221 005, India;* orcid.org/0000-0002-0147-449X

Pralay Maiti − *School of Material Science, Indian Institute of Technology, Banaras Hindu University (BHU), Varanasi, Uttar Pradesh 221 005, India;* orcid.org/0000-0002-6879-3591

Complete contact information is available at: https://pubs.acs.org/10.1021/acsabm.3c00807

Author Contributions

P.P. is the main project investigator (PI). Ideation, major experimental design, and experimental results analysis were performed by P.P. and K.W. *In silico* analysis was supported by A.O. Synthesis was supported by P.S.G., rheology by P.M. and R.P. Neuron isolation and culture were supported by V.R. Zeta potential was measured by So.M. Characterization was supported by D.P., S.P., M.S., G.S., and D.D.Y. Su.M. helped to design the experiments for oxidative stress and data analysis. The manuscript was written by K.W. and P.P. All the authors checked the final version of the manuscript and approved it for the submission.

Funding

P.P. acknowledges the projects awarded to him by DST-Nanomission, India (ref: SR/NM/NS-1005/2015), and the Science and Engineering Research Board (SERB) India (ref: EEQ/2016/000040), I-DAPT Foundation (ref. I-DAPT/IT (BHU)/2023−24/Project Sanction/47), STARS-IISc, Bangalore (ref. MoE-STARS/STARS-2/2023−0318), and Seed grants (OH-35) supported by the Indian Institute of Technology (BHU)

Notes

The authors declare no competing financial interest.

■ ACKNOWLEDGMENTS

The authors acknowledge the fellowships supported by MHRD and DST-Inspire Fellowship, Institute startup grant/plan OH. Instrument facilities of IIT (BHU) and ISLS-CIF have been used for acquiring data like TEM, SEM, FTIR, and confocal microscopic images. The authors acknowledge Dr. S. K. Mahto and Pooja Kumari, School of Biomedical Engineering, IIT(BHU), for helping us in acquiring fluorescent microscopic images. We acknowledge the MALDI-TOF facility of Rice University, USA ((MS: Bruker AutoFlex Speed MALDI-TOF, Shared Equipment Authority (SEA), Office of Research, Rice University).

■ ABBREVIATIONS

p(NAG-*b*-A), poly(*N*-acryloylglycine-acrylamide); CNS, central nervous system; PNS, peripheral nervous system; PLGA, poly(γ-glutamic acid); AIBN, azo-bis(isobutyronitrile; DVB, divinylbenzene; FTIR, Fourier transform infrared; NMR, nuclear magnetic resonance; HRTEM, high-resolution transmission electron microscopy; XRD, X-ray diffraction; TGA, thermogravimetric analysis; DSC, differential scanning calorimetry; SAED,, selected area (electron) diffraction; PBS, phosphate-buffered saline; PC12, adrenal phaeochromocytoma; IPSC,, induced pluripotent stem cells; AO, acrydin orange-; EtBr, ethidium bromide; NGF, nerve growth factor; HBSS, Hanks' Balanced Salt Solution; DMEM, Dulbecco's modified Eagle's medium-; FBS, fetal bovine serum; MTT, 3-(4,5-dimethylthiazol-2-yl)-2,5-diphenyltetrazolium bromide; BSA, bovine serum albumin; AD, Alzheimer's disease; PD, Parkinson disease; GSK3β, glycogen synthase kinase-3-beta; SER, serine; JNKs, c-Jun N-terminal kinase; p38MAPK, p38 mitogen-activated protein kinases; H_2O_2, hydrogen peroxide; AKT, three serine/threonine-specific protein kinases; NF-$\kappa\beta$65, nuclear factor kappa-light-chain-enhancer of activated B cells (p65); Hif1α, hypoxia-inducible factor-1-alpha; PI3K, phosphoinositide 3-kinases; mTOR, mammalian target of rapamycin; FESEM, field emission scanning electron microscopy; G'', loss modulus; G', storage modulus; η^*, complex viscosity; ω, angular frequency; ANOVA, analysis of variance

■ REFERENCES

(1) Serger, E.; Luengo-Gutierrez, L.; Chadwick, J. S.; Kong, G.; Zhou, L.; Crawford, G.; Danzi, M. C.; Myridakis, A.; Brandis, A.; Bello, A. T.; Müller, F.; Sanchez-Vassopoulos, A.; De Virgiliis, F.; Liddell, P.; Dumas, M. E.; Strid, J.; Mani, S.; Dodd, D.; Di Giovanni, S. The gut metabolite indole-3 propionate promotes nerve regeneration and repair. *Nature* **2022**, *607* (7919), 585−592.

(2) Liu, Y.; Hsu, S. H. Biomaterials and neural regeneration. *Neural Regen. Res.* **2020**, *15* (7), 1243−1244, DOI: 10.4103/1673-5374.272573.

(3) Scheib, J.; Höke, A. Advances in peripheral nerve regeneration. *Nature Reviews Neurology* **2013**, *9* (12), 668−676.

(4) Ruediger, T.; Bolz, J. Neurotransmitters and the development of neuronal circuits. *Axon growth and guidance* **2007**, *621*, 104−114.

(5) Hansen, J. Y.; Shafiei, G.; Markello, R. D.; Smart, K.; Cox, S. M. L.; Nørgaard, M.; Beliveau, V.; Wu, Y.; Gallezot, J. D.; Aumont, É.; Servaes, S.; Scala, S. G.; DuBois, J. M.; Wainstein, G.; Bezgin, G.; Funck, T.; Schmitz, T. W.; Spreng, R. N.; Galovic, M.; Koepp, M. J.; Duncan, J. S.; Coles, J. P.; Fryer, T. D.; Aigbirhio, F. I.; McGinnity, C. J.; Hammers, A.; Soucy, J. P.; Baillet, S.; Guimond, S.; Hietala, J.; Bedard, M. A.; Leyton, M.; Kobayashi, E.; Rosa-Neto, P.; Ganz, M.; Knudsen, G. M.; Palomero-Gallagher, N.; Shine, J. M.; Carson, R. E.; Tuominen, L.; Dagher, A.; Misic, B. Mapping neurotransmitter systems to the structural and functional organization of the human neocortex. *Nat. Neurosci.* **2022**, *25* (11), 1569−1581.

(6) Bekri, A.; Drapeau, P. Glycine promotes the survival of a subpopulation of neural stem cells. *Frontiers in Cell and Developmental Biology* **2018**, *6*, 68.

(7) Eric Samarut1, A. B. a. P. D. Transcriptomic Analysis of Purified Embryonic Neural Stem Cells from Zebrafish Embryos Reveals Signaling Pathways Involved in Glycine-Dependent Neurogenesis. *Front. Mol. Neurosci.* **2016**, *9*, 22 DOI: 10.3389/fnmol.2016.00022.

(8) Brustein, E.; Côt, S.; Ghislain, J.; Drapeau, P. Spontaneous Glycine-Induced Calcium Transients in Spinal Cord Progenitors Promote Neurogenesis. *Dev. Neurobiol.* **2012**, 165 DOI: 10.1002/dneu.22050.
(9) Yang, L.; Wang, H.; Liu, L.; Xie, A. The Role of Insulin/IGF-1/PI3K/Akt/GSK3beta Signaling in Parkinson's Disease Dementia. *Front Neurosci* **2018**, *12*, 73.
(10) van Niekerk, E. A.; Tuszynski, M. H.; Lu, P.; Dulin, J. N. Molecular and cellular mechanisms of axonal regeneration after spinal cord injury. *Molecular & Cellular Proteomics* **2016**, *15* (2), 394−408.
(11) Daggupati, T.; Pamanji, R.; Yeguvapalli, S. In silico screening and identification of potential GSK3beta inhibitors. *J. Recept Signal Transduct Res.* **2018**, *38* (4), 279−289.
(12) Guan, J.; Thomas, G. B.; Lin, H.; Mathai, S.; Bachelor, D. C.; George, S.; Gluckman, P. D. Neuroprotective effects of the N-terminal tripeptide of insulin-like growth factor-1, glycine-proline-glutamate (GPE) following intravenous infusion in hypoxic−ischemic adult rats. *Neuropharmacology* **2004**, *47*, 892−903.
(13) Zhang, Q.; Deng, Y.-X.; Luo, H.-X.; Shi, C.-Y.; Geise, G. M.; Feringa, B. L.; Tian, H.; Qu, D.-H. Assembling a Natural Small Molecule into a Supramolecular Network with High Structural Order and Dynamic Functions. *J. Am. Chem. Soc.* **2019**, *141* (32), 12804−12814.
(14) Peressotti, S.; Koehl, G. E.; Goding, J. A.; Green, R. A. Self-Assembling Hydrogel Structures for Neural Tissue Repair. *ACS Biomater Sci. Eng.* **2021**, *7* (9), 4136−4163.
(15) Cheng, Q.; Yu, X.; Xiong, Z.; Wan, Z.; Li, Y.; Ma, W.; Tan, W.; Liu, M.; Shea, K. J. Abiotic Synthetic Antibodies to Target a Specific Protein Domain and Inhibit Its Function. *ACS Appl. Mater. Interfaces* **2022**, *14* (17), 19178−19191.
(16) Bentolila, A.; Vlodavsky, I.; Ishai-Michaeli, R.; Kovalchuk, O.; Haloun, C.; Domb, A. J. Poly (N-acryl amino acids): a new class of biologically active polyanions. *Journal of medicinal chemistry* **2000**, *43* (13), 2591−2600.
(17) Seuring, J.; Agarwal, S. Polymers with Upper Critical Solution Temperature in Aqueous Solution: Unexpected Properties from Known Building Blocks. *ACS Macro Lett.* **2013**, *2* (7), 597−600.
(18) Cui, C.; Wu, T.; Gao, F.; Fan, C.; Xu, Z.; Wang, H.; Liu, B.; Liu, W. An Autolytic High Strength Instant Adhesive Hydrogel for Emergency Self-Rescue. *Adv. Funct. Mater.* **2018**, *28* (42), 1804925.
(19) Gao, F.; Xu, Z.; Liang, Q.; Li, H.; Peng, L.; Wu, M.; Zhao, X.; Cui, X.; Ruan, C.; Liu, W. Osteochondral regeneration with 3D-printed biodegradable high-strength supramolecular polymer reinforced-gelatin hydrogel scaffolds. *Advanced Science* **2019**, *6* (15), 1900867.
(20) Deepuppha, N.; Khadsai, S.; Rutnakornpituk, B.; Wichai, U.; Rutnakornpituk, M. Multiresponsive Poly(N-Acryloyl glycine)-Based Nanocomposite and Its Drug Release Characteristics. *J. Nanomater.* **2019**, *2019*, 1−12.
(21) He, L.; Xiao, Q.; Zhao, Y.; Li, J.; Reddy, S.; Shi, X.; Su, X.; Chiu, K.; Ramakrishna, S. Engineering an Injectable Electroactive Nanohybrid Hydrogel for Boosting Peripheral Nerve Growth and Myelination in Combination with Electrical Stimulation. *ACS Appl. Mater. Interfaces* **2020**, *12*, 53150−53163.
(22) Hsieh, F.-Y.; Tseng, T.-C.; Hsu, S.-h. Self-healing hydrogel for tissue repair in the central nervous system. *Neural regeneration research* **2015**, *10* (12), 1922.
(23) Nagappan, P. G.; Chen, H.; Wang, D.-Y. neuroregeneration and plasticity: a review of the physiological mechanisms for achieving functional recovery postinjury. *Military Medical Research* **2020**, *7* (1), 30−30. DOI: PubMed.
(24) Zamproni, L. N.; Mundim, M. T.; Porcionatto, M. A. Neurorepair and regeneration of the brain: a decade of bioscaffolds and engineered microtissue. *Frontiers in cell and developmental biology* **2021**, *9*, No. 649891.
(25) Liu, Z; Zhou, T.; Ziegler, A. C.; Dimitrion, P.; Zuo, L. Oxidative Stress in Neurodegenerative Diseases: From Molecular Mechanisms to Clinical Applications. *Oxid. Med. Cell. Longevity* **2017**, 11.
(26) Lv, Z.-F.; Xu, B.; Wang, J.-T. N-Acryloylglycine. *Acta Crystallographica Section E Structure Reports Online* **2006**, *62* (8), o3344−o3345.
(27) Schindelin, J.; Arganda-Carreras, I.; Frise, E.; Kaynig, V.; Longair, M.; Pietzsch, T.; Preibisch, S.; Rueden, C.; Saalfeld, S.; Schmid, B.; Tinevez, J.-Y.; White, D. J.; Hartenstein, V.; Eliceiri, K.; Tomancak, P.; Cardona, A. Fiji: an open-source platform for biological-image analysis. *Nat. Methods* **2012**, *9* (7), 676−682.
(28) Yamala, A. K.; Nadella, V.; Mastai, Y.; Prakash, H.; Paik, P. Poly-N-acryloyl-(L-phenylalanine methyl ester) hollow core nanocapsules facilitate sustained delivery of immunomodulatory drugs and exhibit adjuvant properties. *Nanoscale* **2017**, *9* (37), 14006−14014.
(29) Brady, J.; Dürig, T.; Lee, P.; Li, J.-X. Polymer properties and characterization. *Developing solid oral dosage forms* **2017**, 181−223.
(30) Ringeard, J. M.; Griesmar, P.; Caplain, E.; Michiel, M.; Serfaty, S.; Huerou, J. Y. L.; Marinkova, D.; Yotova, L. Design of poly (N-acryloylglycine) materials for incorporation of microorganisms. *J. Appl. Polym. Sci.* **2013**, *130* (2), 835−841.
(31) Shim, S. E.; Yang, S.; Jung, H.; Choe, S. Thermally robust highly crosslinked poly (methyl methacrylate-co-divinyl benzene) microspheres by precipitation polymerization. *Macromol. Res.* **2004**, *12* (2), 233−239.
(32) Vlad, C. D.; Dinu, M. V.; Dragan, S. Thermogravimetric analysis of some crosslinked acrylamide copolymers and ion exchangers. *Polymer degradation and stability* **2003**, *79* (1), 153−159.
(33) Van Dyke, J. D.; Kasperski, K. L. Thermogravimetric study of polyacrylamide with evolved gas analysis. *J. Polym. Sci., Part A: Polym. Chem.* **1993**, *31* (7), 1807−1823.
(34) Dassanayake, N. L.; Phillips, R. W. Determination of the composition of acrylamide/acrylate copolymers using thermogravimetric analysis. *Anal. Chem.* **1984**, *56* (9), 1753−1755.
(35) Kornev, V. A.; Grebenik, E. A.; Solovieva, A. B.; Dmitriev, R. I.; Timashev, P. S. Hydrogel-assisted neuroregeneration approaches towards brain injury therapy: A state-of-the-art review. *Comput. Struct Biotechnol J.* **2018**, *16*, 488−502.
(36) Madhusudanan, P.; Raju, G.; Shankarappa, S. Hydrogel systems and their role in neural tissue engineering. *J. R. Soc., Interface* **2020**, *17* (162), 20190505.
(37) Shah, R.; Saha, N.; Kitano, T.; Saha, P. Influence of Strain on Dynamic Viscoelastic Properties of Swelled (H2o) And Biomineralized (Caco3) Pvp-Cmc Hydrogels. *Appl. Rheol.* **2015**, *25* (3), 13−22.
(38) Donato, M. T.; Tolosa, L.; Gómez-Lechón, M. J. Culture and functional characterization of human hepatoma HepG2 cells. In *Protocols in In Vitro Hepatocyte Research*; Springer, 2015; pp 77−93.
(39) Lee, I. B.; Son, H. H.; Um, C. M. Rheologic properties of flowable, conventional hybrid, and condensable composite resins. *Dental materials: official publication of the Academy of Dental Materials* **2003**, *19* (4), 298−307.
(40) Wiatrak, B.; Kubis-Kubiak, A.; Piwowar, A.; Barg, E. PC12 cell line: cell types, coating of culture vessels, differentiation and other culture conditions. *Cells* **2020**, *9* (4), 958.
(41) Wang, J.; Tian, L.; Chen, N.; Ramakrishna, S.; Mo, X. The cellular response of nerve cells on poly-l-lysine coated PLGA-MWCNTs aligned nanofibers under electrical stimulation. *Materials Science and Engineering: C* **2018**, *91*, 715−726.
(42) Xu, G.; Pierson, C. R.; Murakawa, Y.; Sima, A. A. Altered tubulin and neurofilament expression and impaired axonal growth in diabetic nerve regeneration. *Journal of Neuropathology & Experimental Neurology* **2002**, *61* (2), 164−175.
(43) Latremoliere, A.; Cheng, L.; DeLisle, M.; Wu, C.; Chew, S.; Hutchinson, E. B.; Sheridan, A.; Alexandre, C.; Latremoliere, F.; Sheu, S. H.; Golidy, S.; Omura, T.; Huebner, E. A.; Fan, Y.; Whitman, M. C.; Nguyen, E.; Hermawan, C.; Pierpaoli, C.; Tischfield, M. A.; Woolf, C. J.; Engle, E. C. Neuronal-Specific TUBB3 Is Not Required for Normal Neuronal Function but Is Essential for Timely Axon Regeneration. *Cell Rep* **2018**, *24* (7), 1865−1879.
(44) Dráberová, E.; Del Valle, L.; Gordon, J.; Marková, V.; Šmejkalová, B.; Bertrand, L.; de Chadarévian, J. P.; Agamanolis, D. P.; Legido, A.; Khalili, K.; Dráber, P.; Katsetos, C. D. Class III *β*-

tubulin is constitutively coexpressed with glial fibrillary acidic protein and nestin in midgestational human fetal astrocytes: implications for phenotypic identity. *J. Neuropathol. Exp. Neurol.* **2008**, *67* (4), 341−354.
(45) Silva, T. P.; Bekman, E. P.; Fernandes, T. G.; Vaz, S. H.; Rodrigues, C. A. V.; Diogo, M. M.; Cabral, J. M. S.; Carmo-Fonseca, M. Maturation of Human Pluripotent Stem Cell-Derived Cerebellar Neurons in the Absence of Co-culture. *Front Bioeng Biotechnol* **2020**, *8*, 70.
(46) Clark, B. A.; Monsivais, P.; Branco, T.; London, M.; Häusser, M. The site of action potential initiation in cerebellar Purkinje neurons. *Nature neuroscience* **2005**, *8* (2), 137−139.
(47) Masoli, S.; Solinas, S.; D'Angelo, E. Action potential processing in a detailed Purkinje cell model reveals a critical role for axonal compartmentalization. *Frontiers in Cellular Neuroscience* **2015**, *9*, 47.
(48) Bhat, R.; Xue, Y.; Berg, S.; Hellberg, S.; Ormo, M.; Nilsson, Y.; Radesater, A. C.; Jerning, E.; Markgren, P. O.; Borgegard, T.; Nylof, M.; Gimenez-Cassina, A.; Hernandez, F.; Lucas, J. J.; Diaz-Nido, J.; Avila, J. Structural insights and biological effects of glycogen synthase kinase 3-specific inhibitor AR-A014418. *J. Biol. Chem.* **2003**, *278* (46), 45937−45945.
(49) de la Torre, A. V.; Junyent, F.; Folch, J.; Pelegrí, C.; Vilaplana, J.; Auladell, C.; Beas-Zarate, C.; Pallàs, M.; Verdaguer, E.; Camins, A. GSK3β inhibition is involved in the neuroprotective effects of cyclin-dependent kinase inhibitors in neurons. *Pharmacological research* **2012**, *65* (1), 66−73.
(50) Lee, Y.; Yoon, S. B.; Hong, H.; Kim, H. Y.; Jung, D.; Moon, B. S.; Park, W. K.; Lee, S.; Kwon, H.; Park, J.; Cho, H. Discovery of GSK3beta Inhibitors through In Silico Prediction-and-Experiment Cycling Strategy, and Biological Evaluation. *Molecules* **2022**, *27* (12). DOI: 3825.
(51) Riley, L.; Schirmer, L.; Segura, T. Granular hydrogels: emergent properties of jammed hydrogel microparticles and their applications in tissue repair and regeneration. *Curr. Opin Biotechnol* **2019**, *60*, 1−8.
(52) Clausen, T.; Khaldi, A.; Zauner, A.; Reinert, M.; Doppenberg, E.; Menzel, M.; Soukup, J.; Alves, O. L.; Bullock, M. R. Cerebral acid—base homeostasis after severe traumatic brain injury. *Journal of neurosurgery* **2005**, *103* (4), 597−607.
(53) Chaumeil, M. M.; Valette, J.; Baligand, C.; Brouillet, E.; Hantraye, P.; Bloch, G.; Gaura, V.; Rialland, A.; Krystkowiak, P.; Verny, C.; Damier, P.; Remy, P.; Bachoud-Levi, A. C.; Carlier, P.; Lebon, V. pH as a biomarker of neurodegeneration in Huntington's disease: a translational rodent-human MRS study. *Journal of cerebral blood flow and metabolism: official journal of the International Society of Cerebral Blood Flow and Metabolism* **2012**, *32* (5), 771−779. DOI: .
(54) Anderson, R. L.; Merkler, D. J. N-fatty acylglycines: underappreciated endocannabinoid-like fatty acid amides? *J. Biol. Nat.* **2017**, *8* (4), 156−165.
(55) Guvendiren, M.; Lu, H. D.; Burdick, J. A. Shear-thinning hydrogels for biomedical applications. *Soft Matter* **2012**, *8* (2), 260−272.
(56) Grevesse, T.; Dabiri, B. E.; Parker, K. K.; Gabriele, S. Opposite rheological properties of neuronal microcompartments predict axonal vulnerability in brain injury. *Sci. Rep* **2015**, *5*, 9475.
(57) Leipzig, N. D.; Shoichet, M. S. The effect of substrate stiffness on adult neural stem cell behavior. *Biomaterials* **2009**, *30* (36), 6867−6878.
(58) Ali, S.; Wall, I. B.; Mason, C.; Pelling, A. E.; Veraitch, F. S. The effect of Young's modulus on the neuronal differentiation of mouse embryonic stem cells. *Acta Biomater* **2015**, *25*, 253−267.
(59) Lamprecht, R. Actin Cytoskeleton Role in the Maintenance of Neuronal Morphology and Long-Term Memory. *Cells* **2021**, *10* (7). DOI: 1795.
(60) Liz, M. A.; Mar, F. M.; Santos, T. E.; Pimentel, H. I.; Marques, A. M.; Morgado, M. M.; Vieira, S.; Sousa, V. F.; Pemble, H.; Wittmann, T.; Sutherland, C.; Woodgett, J. R.; Sousa, M. M. Neuronal deletion of GSK3β increases microtubule speed in the growth cone and enhances axon regeneration via CRMP-2 and independently of MAP1B and CLASP2. *BMC Biology* **2014**, *12* (1), 47.
(61) Cuesto, G.; Jordan-Alvarez, S.; Enriquez-Barreto, L.; Ferrus, A.; Morales, M.; Acebes, A. GSK3beta inhibition promotes synaptogenesis in Drosophila and mammalian neurons. *PLoS One* **2015**, *10* (3), No. e0118475.
(62) Reddy, P. H. Amyloid beta-induced glycogen synthase kinase 3beta phosphorylated VDAC1 in Alzheimer's disease: implications for synaptic dysfunction and neuronal damage. *Biochim. Biophys. Acta* **2013**, *1832* (12), 1913−1921.
(63) Khatri, N.; Thakur, M.; Pareek, V.; Kumar, S.; Sharma, S.; Datusalia, A. K. Oxidative stress: major threat in traumatic brain injury. *CNS Neurol. Disord. Drug Targets* **2018**, *17* (9), 689−695.
(64) Musgrove, R. E.; Helwig, M.; Bae, E.-J.; Aboutalebi, H.; Lee, S.-J.; Ulusoy, A.; Di Monte, D. A. Oxidative stress in vagal neurons promotes parkinsonian pathology and intercellular α-synuclein transfer. *J. Clin. Invest.* **2019**, *129* (9), 3738−3753.
(65) Smethurst, P.; Risse, E.; Tyzack, G. E.; Mitchell, J. S.; Taha, D. M.; Chen, Y.-R.; Newcombe, J.; Collinge, J.; Sidle, K.; Patani, R. Distinct responses of neurons and astrocytes to TDP-43 proteinopathy in amyotrophic lateral sclerosis. *Brain* **2020**, *143* (2), 430−440.

https://doi.org/10.1021/acsabm.3c00807
ACS Appl. Bio Mater. 2023, 6, 5644−5661

Nanoscale

ROYAL SOCIETY OF CHEMISTRY

PAPER

View Article Online
View Journal | View Issue

Cite this: *Nanoscale*, 2024, **16**, 1770

Nitric oxide releasing novel amino acid-derived polymeric nanotherapeutic with anti-inflammatory properties for rapid wound tissue regeneration†

Prem Shankar Gupta, ‡[a] Kirti Wasnik, ‡[a] Sukanya Patra,[a] Divya Pareek,[a] Gurmeet Singh,[a] Desh Deepak Yadav,[a] Somedutta Maity[b] and Pradip Paik *[a]

Endogenous gasotransmitter nitric oxide (NO) is a central signalling molecule that modulates wound healing by maintaining homeostasis, collagen formation, wound contraction, anti-microbial action and accelerating tissue regeneration. The optimum delivery of NO using nanoparticles (NPs) is clinically challenging; hence, it is drawing significant attention in wound healing. Herein, a novel polymeric nanoplatform loaded with sodium nitroprusside (SP) NPs was prepared and used for wound healing to obtain the sustained release of NO in therapeutic quantities. SP NPs-induced excellent proliferation (~300%) of mouse fibroblast (L929) cells was observed. With an increase in the SP NPs dose at 200 μg mL^{-1} concentration, a 200% upsurge in proliferation was observed along with enhanced migration, and only 17.09 h were required to fill the 50% gap compared to 37.85 h required by the control group. Further, SP NPs showed an insignificant impact on the coagulation cascade, revealing safe wound-healing treatment when tested in isolated rat RBCs. Additionally, SP NPs exhibited excellent angiogenic activity at a 10 μg mL^{-1} dose. Moreover, the formulated SP nanoformulation is non-irritant, non-toxic, and does not produce any skin sensitivity reaction on the rat's skin. Further, an *in vivo* wound healing study revealed that within 11 days of treatment with SP nanoformulation, 99.2 ± 1.0% of the wound was closed, while in the control group, only 45.5 ± 3.8% was repaired. These results indicate that owing to sustained NO release, the SP NP and SP nanoformulations are paramount with enormous clinical potential for the regeneration of wound tissues.

Received 6th August 2023,
Accepted 14th December 2023

DOI: 10.1039/d3nr03923d

rsc.li/nanoscale

1. Introduction

Chronic wounds or hard-to-heal wounds negatively impact the quality of life, cause psychological stress and substantially increase the financial burden on patients.[1,2] According to epidemiology studies, in India, the prevalence rate of chronic wounds is estimated to be 4.5/1000 where major traumatic injuries are generally associated with diabetic cases. Various indigenous or exogenous factors impair wound healing mechanisms, leading to severe pathological sequelae and significant clinical challenges; therefore, it is considered a civilizational disease.[3]

Although many works on wound healing have been reported, a deeper understanding of the mechanism and implementation of more effective and cheaper treatment is an essential requirement. Further, wound healing in embryos and adults has some differences;[4] the significant differences observed are associated with the immune and inflammatory system and NO production, which is higher in the embryonic system than in an adult wound. It is reported that in the wound healing mechanism, endogenous gastro transmitter NO plays a crucial role in the regulation of overlapping phases of wound healing cascades.[5,6] Out of the many research reports available on different materials for therapeutic applications,[7] NO is mainly associated with inflammation, antibac-

[a]*School of Biomedical Engineering, Indian Institute of Technology (BHU), Varanasi, India. E-mail: paik.bme@iitbhu.ac.in*
[b]*School of Engineering Science and Technology, University of Hydrabad, Hydrabad, India*

†Electronic supplementary information (ESI) available: 1. Synthesis of NAG monomer, 2. fabrication of SP NPs, 3. characterization, 4. *in vivo* study, ethics and approval; Table S1: Formulation of SP nanoformulation, Table S2: Qualitative evaluation of SP nanoformulation, Table S3: Skin irritation evaluation; Scheme S1. Synthesis of NAG monomer; Fig. S1: Content uniformity test, Fig. S2: *In vitro* dissolution of SP nanoformulation, Fig. S3: ^{1}H NMR spectra of NAG monomer, Fig. S4: ^{13}C NMR spectra of NAG monomer, Fig. S5: FTIR spectra of NAG monomer, Fig. S6: PXRD pattern of NAG monomer, Fig. S7: Ninhydrin test, Fig. S8. Synthesis of PNAG NPs, Fig. S9. FTIR spectra of PNAG NPs, Fig. S10. Cytocompatibility PNAG NPs in L929 cells, Fig. S11. Histology of wound tissue. See DOI: https://doi.org/10.1039/d3nr03923d

‡These authors contributed equally.

terial activities, collagen production, cell proliferation, re-epithelialization, and angiogenesis, among others,[8] in adult wound healing. Therefore, if a controlled dose could be applied, NO-induced wound healing could be one of the most effective therapeutic options. Because NO can have several positive impacts on accelerated wound healing, its metabolites have been reported in correlation with the healing trajectory, suggesting the potential for recovery or aggravation.[9] It is reported that mice lacking inducible or endothelial NO synthase exhibit delayed wound repair and poor angiogenesis.[10–12] Impaired wound healing also results in blocking the knockdown of NOs or by the removal of NO by scavengers, and the emergence of chronic wounds is directly linked to turning down the supply of NO at the wounded sites.[13–15] However, the controlled release of NO content is crucial in wound healing. To increase the level of NO and consequently therapeutic efficiency, exogenous NO donors or stimulators can be used and administered either in the form of direct topical NO donor[16] or indirectly in the form of NO synthase (NOs) stimulator,[17] the transfer of the NOs gene, and the systemic delivery of the NOs substrate.[16] Earlier, silica NPs, gold NPs, liposomes, and dendrimers were used for the delivery of NO.[18,19] Polymeric nanoparticles can be used for NO delivery due to their advantages such as the precise and controlled release of NO, as discussed in our previous report.[20,21] Although several researches are focused on developing the stable and precise delivery of exogenous NO donors to increase the NO level at the wound site to accelerate the healing process,[22] the current challenges remain such as initial burst release poor biocompatibility and low loading capacity.[23] Therefore, developing the NO-releasing delivery system requires extreme care and expertise. Polymeric nanocarrier-based therapeutics of NO have proved promising as earlier from our proof of concept and it has been reported that NO delivery through these could enhance wound healing efficiency.[20] Further, due to fungi static, bacteriostatic, hemostatic, and collagen-forming properties of gelatin, chitosan, and antimicrobial peptides, they have some degree of wound-healing ability;[24,25] however, their therapeutic efficiency are unsatisfactory, and side effects including scar formation and infection, poor adhesive, hydrophobic nature, and uncontrolled polymerization were there in the long run, arising from the essential supply of new therapeutics, which will fulfil the current demand.[26] A rise in the toxicity with highly potent drugs always reduces their regular use in clinics, but with nanomedicine, there is always a hope that it will reduce the systemic damage and lower the toxicity by acting as nanoantidote and deliver compounds in a sustained and controlled manner with improved pharmaceutical stability.[27,28]

With the aim to overcome the above challenges and motivated with positive outcomes of nanomedicine, the present work is focused on the synthesis of an advanced biosafe material of poly-*N*-acryloyl glycine (PNAG) and formulated with a NO donor, sodium nitroprusside (SNP). Acryloyl glycine-based PNAG NPs are biocompatible, proven effective, and safe wound-healing materials with angiogenic and biodegradable capabilities and low cytotoxic effects. Due to the high NO content, quick metabolism, and ideal NO release property, SNP can be used as an NO-releasing drug. Clinically, SNP is frequently used to treat hypertensive emergencies and abrupt heart failure and is listed as one of the essential medicines by WHO.[29] NO-releasing polymeric nanoparticles could allow predictable and regulated NO delivery. The easiest and most efficient method to deliver NO to a cutaneous wound is the topical administration of NO-releasing or NO-generating biomaterials.[30] Therefore, to achieve optimum NO release, we designed an NO-releasing nanoformulation (SP nanoformulation) from NO-loaded PNAG NPs (SP NPs) and used it for wound healing. Herein, we have scrutinized the toleration of SP NPs against the mouse fibroblast (L929) cell lines and rat RBCs to show the effect on hemolysis. Further, we have studied the extent of proliferation and migration of L929 cells. The skin sensitization and irritation of SP nanoformulation have also been studied, and the levels of pro-inflammatory cytokines and chemokines during *in vivo* wound healing assessment have been investigated. Further, compared to previous NO-releasing therapeutics,[31] how these SP NPs and SP nanoformulation are advantageous such as stability, simplicity of application, and prolonged NO release have also been studied. Additionally, the cumulative impact of PNAG NPs and NO co-delivery has not yet been established; therefore, the synergistic effect on full-thickness skin wound healing has been investigated here.

2. Experimental

2.1 Materials and methods

2.1.1 Materials/chemicals. The following materials were used: acryloyl chloride (96%) stabilized with 400 ppm phenothiazines and divinylbenzene (Alfa-Aesar), glycine (98%), hexadecane (HD) anhydrous (Sigma Aldrich), chloroform, ethyl acetate, 1,4-dioxane (99%) extra pure, SDS (90%) (Merck), 2,2-azobisisobutyronitrile (AIBN, 98%), and sodium nitroprusside (SNP) (SRL). Standard cell culture reagents such as DMEM and foetal bovine serum (FBS), penicillin–streptomycin cocktail, and gentamicin from Gibco; and 3-(4,5-dimethylthiazol-2-yl)-2,5-diphenyltetrazolium bromide (MTT; >99.9%) were purchased from Himedia. Ultrapure water (18.2 M) was obtained from Pure Lab Ultra water system (ELGA, High Wycombe, United Kingdom) and used for all sample processing. All other analytical grade reagents, such as glycerol, petrolatum, wax, and mineral oil were obtained from Sisco Research Laboratories (SRL) Pvt. Ltd, Mumbai, India and were used without further purification. The detail of the formation of the nanomedicine has been filed for the Indian patent (patent application no.: 02311051276, date of filing: 31-07-2023).

2.2.1 Synthesis of NAG monomer. *N*-Acryloyl glycine monomer (NAG) was synthesized through a modified approach and converted into PNAG NPs.[20,32] The synthesis procedure is elaborated in the ESI.†

2.3.1 Preparation of sodium nitroprusside-loaded poly-(*N*-acryloyl glycine) nanoparticles. SNP-loaded poly(*N*-acryloyl glycine) nanoparticles (SP NPs) were fabricated in two steps: firstly, poly(*N*-acryloyl glycine) nanoparticles (PNAG NPs) were synthesized from *N*-acryloyl glycine (NAG) monomer, and then sodium nitroprusside (SNP) was loaded into these NPs. The elaborated fabrication method is discussed under the ESI (ESI, Fig. S8†). The details of the formation of the nanomedicine has been filed for the Indian patent (patent application no.: 02311051276, date of filing: 31-07-2023).

2.4.1 Entrapment efficiency (EE, %) and loading capacity (LC, %). The entrapment efficiency (EE, %) of SNP was measured through the UV-Vis spectra (550 nm) of the supernatant recovered after SNP loading using Griess Reagent using the following eqn (1).

$$\mathrm{EE}(\%) = \frac{\text{weight of SNP in NPs}}{\text{weight of SNP added to solution}} \times 100 \quad (1)$$

Loading capacity (LC, %) was measured by dispersing 1 mg lyophilized SP NPs in 5 mL DMSO and incubated for 30 min at 37 °C. After centrifugation at 18 000 rpm, the NO content was measured by a UV-Vis spectrometer, and the percentage of SNP loaded was determined using eqn (2).

$$\text{Drug loading}(\%) = \frac{\text{weight of SNP in NPs}}{\text{weight of SNP loaded NPs}} \times 100 \quad (2)$$

SEM analysis was conducted to confirm the morphology of the PNAG NPs and SP NPs. The EDS and elemental mapping for both the samples were conducted to confirm the loading of SNP in PNAG NPs (see ESI† for detailed methodology).

2.5.1 Characterization of NAG monomer, PNAG, and SP NPs. The NAG monomer, PNAG NPs, and SNP loaded PNAG NPs (SP NPs) were characterized for chemical functionality, crystallinity, particle size, zeta potential (ξ), and elemental mapping and analysis. The ESI† section explains the detailed methods for all characterization methods.

2.6.1 Determination of NO content and NO release profile. The NO content was determined for all the batches of SP NPs. Briefly, 1 mL DMSO and Griess reagent (1 : 1) was used to dissolve 5 mg SP NPs, which were then sonicated for 1 h. After centrifugation at 18 000 rpm, the supernatant was diluted, and the amount of NO was determined by measuring the absorbance at λ = 550 nm (UV-Vis spectrophotometer: Jasco; V-730, JASCO International Co., Ltd, Japan).

NO release was investigated using the dialysis method at a pH of 7.4. The release pattern of NO from the prepared SP NPs was studied for 24 h. Briefly, 5 mg SP NPs in 5 mL PBS (pH 7.4) was dispersed and poured into a dialysis bag and simultaneously immersed in 25 mL dissolution media (PBS pH 7.4, 37 ± 2 °C, 100 rpm), and release was conducted for 24 h. At a predetermined time interval, samples were withdrawn in sink condition, and the amount of NO released was measured by measuring the absorbance at λ = 550 nm, and cumulative drug release (%, CDR) was calculated.

2.7.1 Cytotoxicity study. The cytotoxicity of SP NPs was investigated using an adherent type cell line through the MTT assay.[20] Mouse fibroblast (L929) cells (1×10^4) were grown for 24 h in rich DMEM (DMEM + 10% v/v, FBS), penicillin (100 IU mL^{-1}), and streptomycin (100 μg mL^{-1}) at standard cell culture condition (5% CO_2 at 37 °C). Around 60% of confluence cells were treated with 100 μL SP NPs (0–250 μg mL^{-1}) dispersion and incubated for 24 h. Then, they were rinsed twice with PBS, and 20 μL MTT solution (5 mg mL^{-1} MTT) was added to cells and incubated again for 4 h. The MTT solution was then removed, and DMSO (200 μL) was further added to each well to dissolve formazan crystals and incubated for another 20 min. The absorbance was measured at 570 nm using a plate reader. The data were collected in three distinct biological replicates, each done on a different day, on a different cell passage, and with three repetitions. The cell viability was estimated using eqn (3),

$$\text{Cell viability}(\%) = \frac{\text{OD treatment}}{\text{OD control}} \times 100 \quad (3)$$

where OD is the optical density value recorded using a microplate reader.

2.8.1 Hemocompatibility. Venous blood samples were used to test the hemocompatibility of PNAG NPs. Sodium citrate was used as an anticoagulant in tubes holding whole venous blood.

2.8.1.1 Hemolysis study. Hemolysis was conducted on rat RBCs.[33] RBCs were isolated from whole blood, and a homogenous suspension was prepared by dispersing in PBS (5×10^{10} cells per mL). The hemolytic effects of SP NPs in the concentration range from 1 μg mL^{-1} to 1000 μg mL^{-1} were examined using a spectroscopic test, and the results of the hemolysis caused by 0.1% dispersion of SP NPs were compared with the positive control (0.1% Triton-X 100 in PBS) and the negative control (PBS, pH 7.4). In a 1.5 mL microcentrifuge tube, 500 μL SP NPs nanosuspension from each concentration and 500 μL RBC suspension were placed and incubated for 24 h at 37 °C and stirred at 100 rpm. Then, the samples were centrifuged (4000 rpm for 10 min at 25 °C). By comparing the sample's absorption at λ_{max} = 540 nm with the positive control (Triton X-100) and the negative control (PBS), the percent hemolysis was calculated using eqn (4).

$$\text{Hemolysis}(\%) = \frac{\text{OD treatment} - \text{OD}(-\text{ve})\text{control}}{\text{OD}(+\text{ve})\text{control} - \text{OD}(-\text{ve})\text{control}} \times 100 \quad (4)$$

2.8.2.1 Blood coagulation study. Two blood coagulation pathways were examined to gauge the effect of SP NPs on the blood coagulation cascade. The activated partial thromboplastin time (APTT) and prothrombin time (PT) were evaluated separately after incubating the plasma with SP NPs at 1, 5, 10, 25, 50, 100, and 200 μg mL^{-1} concentrations. The plasma fraction was separated from whole blood by centrifugation (2500 rpm for 10 min, at 25 °C). SP NPs were incubated with isolated plasma for 30 min at 37 °C with constant stirring. The incu-

bated samples were analysed using a coagulometer (Hemostar XF 2.0, Tulip Diagnostics Pvt. Ltd India). Each sample was examined thrice.

2.9.1 *In vitro* wound healing and live dead assay. The scratch wound healing assay is a well-established *in vitro* technique for investigating coordinated cell migration and proliferation in a two-dimensional context. It was employed to assess the regenerative potential of SP NPs within a controlled experimental setting. The detailed protocol adhered to established the methodologies, wherein 2×10^5 L929 cells were seeded per well in a 12-well plate and allowed to culture for 24 h, achieving 80% confluency. Subsequently, a precisely executed linear scratch wound was introduced on the surface of each well using a sterile 20 μL pipette tip. The cells were then subjected to culture conditions with SP NPs, both in the test (supplemented media) and untreated control (without SP NPs) groups, at concentrations ranging from 50 to 200 μg mL^{-1}. Then, imaging at 0 h, 24 h, and 48 h post-scratch was conducted, and the acquired images were analysed using the ImageJ software to calculate the percentage of wound closure area and closure rate, providing insights into the cellular healing dynamics influenced by SP NPs. By adopting the above protocol, further, the live/dead assay on the L929 cell line under *in vitro* condition was conducted using acridine orange (AO) and propidium iodide (PI) method[34] to verify the viability of cells in the presence of SP NPs. Live cells were incubated with acridine orange (1.5 μM) and dead cells with propidium iodide (31.5 μM). Following a 30-minute incubation period, specimens underwent a meticulous PBS washing procedure. Subsequently, cellular scrutiny and imaging were conducted utilizing a state-of-the-art fluorescent microscope (Nikon, A1, Tokyo, Japan), capturing high-resolution visuals.

2.10.1 *In vivo* angiogenesis. *In vivo* angiogenesis tests were performed to examine the vascular sprouting effect of SP NPs using egg yolk angiogenesis assay, as described in the previous report.[35] The fertilized eggs from a certified and trusted vendor (Ramana Hatchery, Varanasi) were purchased in Varanasi, Uttar Pradesh, India. Before the studies, the eggs were first incubated in an egg incubator for 4 days (96 h) in a controlled environment (38.0 ± 0.5 °C and 50–55% humidity). Using the light and shadow approach, the eggs were tested on the day of the experiment to see if successful embryogenesis had occurred. A little examination window was made on the top of the eggshell to determine the embryo development process. Carefully, while preserving the aseptic conditions, suspensions of various dosages of SP NPs (1, 10, and 100 μg) in PBS were added, compared to the reference (treated with PBS), which was examined for 8 h. Images were captured at various time intervals (0, 2, 4, and 8 h) during incubation using a stereo microscope-mounted Magnus camera (Magnus DC10, Magnus Opto Systems India Pvt. Ltd) at a resolution of 10 megapixels. Images were subsequently examined using the Angiotool and FijiJ image analysis tools.

2.11.1 Development of SP nanoformulation and macroscopical evaluation. SP NPs (5% w/w) were used to prepare a nanoformulation that could be applied smoothly to wounds. In an oleaginous ointment base that was made as described in ointment bases (ESI, Table S1†), SP NPs (5% w/w) were disseminated.[36] SP NPs were placed on an ointment slab and triturated with the base ointment using a long, broad-blade spatula. The ointment base had already been made using the melt fusion procedure. Glycerine (5% w/v) was added with the aid of trituration after proper trituration with an ointment base. Then, the formulation was stored in a wide-mouth bottle/ointment tube, placed in a refrigerator (2–8 °C), and filled into a syringe barrel to estimate the drug content further. The formulated SP nanoformulation was evaluated for macroscopic (observational) characterization (ESI, Table S2†).

2.12.1 Physicochemical evaluation of NO-PNAG nanoformulation

2.12.1.1 Nitric oxide content determination. The USP method (USP 40-NF35, 2017) was employed to evaluate the content homogeneity. Briefly, 100 mg SP nanoformulation was taken from the barrel's top (plunger end), centre, and bottom (needle end) parts of the SP nanoformulation filled syringes (ESI, Fig. S1†). They were combined with 5 mL PBS (pH 7.4) and Griess reagent (1 : 3). Then, the mixtures were homogenized at 25 °C for 15 min with 5000 rpm in shield condition. Then, it was filtered using a 0.45 nylon filter. The NO content was calculated using the Griess reagent method after diluting the samples for examination.

2.12.2.1 Nitric oxide release from the nanoformulation. A modified USP apparatus 2 (ESI, Fig. S2†) was employed to evaluate NO release from the SP nanoformulation. Excess SP nanoformulation was placed in a unique sample holder having a 3.14 cm^2 exposed surface area. After flattening, smoothing, and removing the extra material from the nanoformulation surface with a spatula, the precise loaded amount of nanoformulation was calculated by weight. The figure (ESI, Fig. S2†) shows that the sample holding cell was inverted on the static shaft connected to the burette stand. A pre-cut and pre-wetted 0.22 μm pore-size syringe filter membrane (Millipore, Billerica, MA) was placed on top of the nanoformulation and tightened with a rubber band. To reduce shearing stress induced during sample preparation and its potential impact on drug release, the mounted sample holding cell was left stationary inside the dissolution vessel for 30 min. The dissolution test was started by adding 200 mL pre-heated release medium (PBS, pH 6.8, 37 ± 2 °C) to the vessel and stirred with 200 rpm. Using the Griess reagent method, aliquots of the sample (0.5 mL) were obtained at predefined intervals (15 min, 30 min, 1, 2, 4, 8, 10, 12, and 24 h), and the amount of NO released from the SP nanoformulation was calculated.

2.13.1 Biological evaluation of SP nanoformulation

2.13.1.1 Ethical approval. Wistar rats (aged 6 to 8 weeks; obtained from Department of Pharmaceutical Engineering and Technology, IIT (BHU)) were shaved off their flank hair and treated with iodine solution before being put under anaesthesia with ketamine (10 mg kg^{-1}) and xylazine (10 mg kg^{-1}). This work has been performed as per the ethical guidelines. All the animal studies were examined and approved by the Institutional Animal Ethical Committee (IAEC: approval no.

IIT(BHU)/IAEC/2022/078, dated 03/05/2022, registration no. 2123/GO/Re/S/21/CPCSEA), and the use of animals in this work was carried out in compliance with the IEAC's recommendations. Details are mentioned in the ESI† (*in vivo* study, ethics, and approval).

2.13.2.1 Skin irritation and sensitization. The SP nanoformulation was applied to rat skin for a predetermined period to check for any irritation or erythematious reaction. About 4 cm^2 of the intact shaved skin of rats was treated with SP nanoformulation and formulation base of about 1 g, coupled with the positive control (1% formalin solution as a common irritant). The treated area was confined with bandages. 24 h post-treatment, the wrap was removed and washed with water. Then, the skin of the rats was examined visually for any indications of skin irritation and sensitization, and simultaneously, high-resolution camera images were acquired. Rats under experiments were observed for seven more days to check for indications of oedema and erythema. The Draize scoring system (ESI, Table S3†) was used to calculate the skin irritation score using the primary dermal irritation index (PDII), calculated using eqn (5).

$$\mathrm{PDII} = \frac{\mathrm{PDI}}{4} \tag{5}$$

2.13.3.1 In vivo wound healing. The efficiency of SP nanoformulation for wound healing was investigated using Wistar rats. A 10–12 mm, full-thickness cutaneous wound was developed on the back of rats using a 10 mm biopsy punch. The wound was then stitched together using sterile silicone rings. NO is a known inhibitor of platelet aggregation,[37] therefore; we started the treatment post-wounding of day 1 to provide adequate time for hemostasis and fibrin clot formation. The wounds were then topically treated with 100 mg SP nanoformulation. The formulation base and SP nanoformulation were then applied to the wounds of rats on alternate days (1^{st}, 3^{rd}, 5^{th}, 7^{th}, 9^{th}, and 11^{th}). Rats were kept carefully, and wounds were covered with a conventional gauze bandage dressing. The dressing was replaced with a fresh bandage after each application of treatment. A similar process was maintained for the control group.

2.13.4.1 Study of the histology. Deep granulation tissue and cross-sectional full-thickness skin specimens from cicatricial tissue were acquired on the 14^{th}-day post-treatment. Formalin-fixed paraffin-embedded blocks were sectioned in the transverse plane with a section thickness of 5 microns and stained with Mayer's hematoxylin and ethyl eosin and Mallory's Trichrome stain. Mounted sections were analysed with an optical microscope at different magnifications.

2.13.5.1 Immunochemical analysis. Blood serum was isolated from blood, collected at various time intervals (2, 7, and 12^{th} days of post-treatment), each representing the distinct phase of wound healing and kept at −80 °C until further processing. From these serum samples, the levels of IL-6, IL-1β, TNF-α, CRP, and IGF-1 were determined using commercially available enzyme-linked immunosorbent assay ELISA kits. The relative protein concentrations were estimated by recording the absorbance at 450 nm using a microplate reader, and the values of the inflammation markers were estimated and compared with the control sample.

2.13.6.1 Semi-quantitative reverse transcription and polymerase chain reaction (sqRT-PCR). From the excised wound of the control group and treatment groups of day 2, 7, and 14, nearly 1 mm of tissues were collected. RNA isolation was performed by homogenizing the tissue in 1 mL TRIZOL reagent, followed by chloroform extraction. Next, the aqueous layer was collected, and RNA was precipitated using 1 mL isopropyl alcohol and centrifuged at 12 000*g* and 4 °C temperature for 15 min. The RNA pellet was washed 2 times with 70% ice-cold ethanol and suspended in diethyl pyrocarbonate (DEPC)-treated water. After RNA quantification, 1 μg RNA was used for cDNA synthesis using oligo dT sequence and reverse transcriptase polymerase as per the manufacturer's protocol. Afterward, PCR was conducted using KiCqStart® (Sigma) primer for biomarker target gene PECAM-1 (forward primer sequence 5′-AAACCACAATTGAGTACCAG-3′ reverse primer 5′-ACTTAGCTTGACGTTCTTTG-3′), VEGFA (forward primer sequence 5′-GATAGAGTATATCTTCAAGCCG-3′ and reverse primer 5′-CTCATCTCTCCTATGTGCTG-3′), KDR (forward primer sequence 5′-AAACTGGATAAAATGGGCG-3′ and reverse primer 5′-AGCCTTTTAGGTAGAGTCAG-3′) and housekeeping gene GAPDH (forward primer sequence 5′-TCGGAGTCAACGGATTTG-3′ and reverse primer 5′-CAACAATATCCACTTTACCAGAG-3′) as the reference using Taq polymerase (TAKARA R001A) with 35 repetitive cycles of denaturation at 95 °C for 25 s, annealing at 59 °C for 30 s, and extension at 72 °C for 35 s, followed by final extension at 72 °C for 7 min. PCR products were run on 2% agarose gel, and dosimetry calculation was performed.

2.14.1 Statistical analysis. The independent Student's *t*-test and one-way ANOVA with the Tukey test were used to statistically analyse the *in vitro* and *in vivo* data using Origin software (OriginLab Corporations, Northampton, USA). Statistical significance was determined using a *p*-value of 0.05. The data are presented as mean ± SD.

3. Results

3.1 Characterization of SP NPs

NAG monomer was synthesized using a modified procedure (ESI, Scheme S1†) with 64.21% yield, the chemical functionality was confirmed through NMR [^{1}H NMR (ESI, Fig. S3†) and ^{13}C NMR (ESI, Fig. S4†)] spectroscopy and FTIR spectroscopy (ESI, Fig. S5†), and the crystalline nature of NAG monomer was confirmed through XRD (ESI, Fig. S6†). Unlike glycine, which reacts with ninhydrin to give a vibrant violet, it reveals the lack of a free amino group (ESI, Fig. S7†). The NAG monomer and PNAG NPs were tested for free amino groups using ninhydrin reagent that showed the lack of free primary amine groups and is free from glycine contamination.

Further, this monomer is used to synthesize PNAG NPs (ESI, Fig. S8†), formulated with raw SNP, which results in the

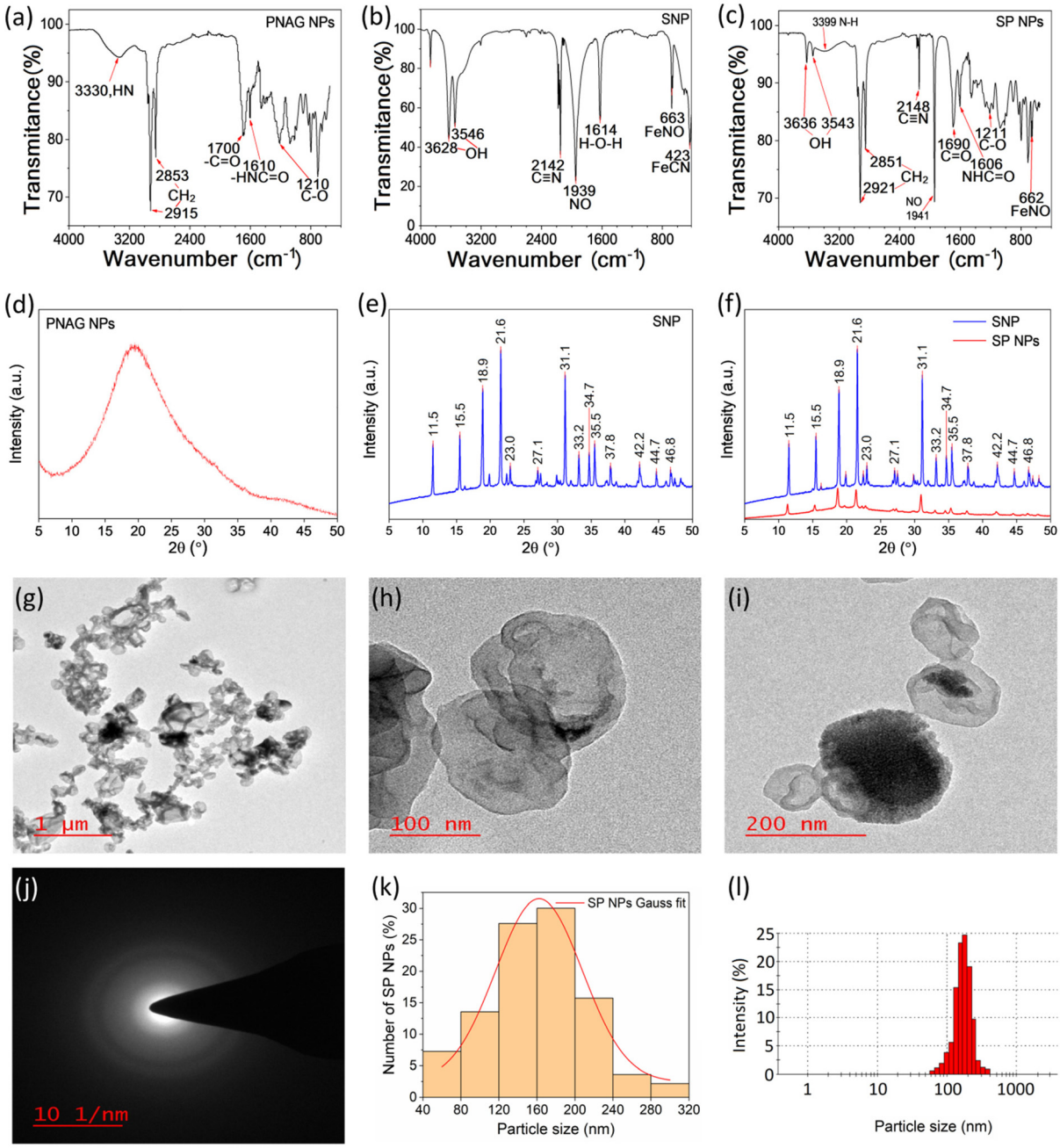

Fig. 1 Characterization of SP NPs. FTIR spectra of (a) PNAG NPs, (b) sodium nitroprusside (SNP) and (c) SP NPs. The XRD pattern of (d) PNAG NPs, (e) SNP and (f) SP NPs. TEM images of SP NPs (g–i), SAED pattern (j) and particle sizes (k) were calculated from the TEM images (number of particles >400) and DLS (l).

formation of SP NPs. The functional groups present in synthesized PNAG NPs (Fig. 1a and ESI, Fig. S9†), raw SNP (Fig. 1b), and fabricated SP NPs (Fig. 1c) were confirmed through FTIR and compared for the loading of SNP in the PNAG NPs FTIR spectrum of SP NPs, which reveals the characteristic distinct bands for the –C≡N and –NO appeared at 2148 cm^{-1} and 1941 cm^{-1} (Fig. 1c), respectively, which are characteristic of SNP (2142 cm^{-1} and 1939 cm^{-1}) loading, confirming the fabrication of SP NPs.[38,39] The bands that appeared at 3628–3546 cm^{-1} of (Fig. 1b) is attributed to the ν_s, OH of SNP, and the bands at 3636–3399 cm^{-1} (Fig. 1c) correspond to the ν_s –OH and $-NH_2$ of SP-NPs, which confirmed the loading of SNP in NPs. The XRD pattern of PNAG NPs, SNP, and SP NPs are shown in Fig. 1. The XRD pattern shows that PNAG NPs are semi-crystalline in nature (Fig. 1d), while raw SNP (Fig. 1e) shows fourteen major peaks at 2θ = 11.5°, 15.5°, 18.9°, 21.6°, 23.0°, 27.1°, 31.1°, 33.2°, 34.7°, 35.5°, 37.8°, 42.2°, 44.7°, and 46.8° in addition to a number of peaks that

correspond to the high degree of crystallinity. On the other hand, the primary diffraction peaks in SP NPs (Fig. 1f: SNP loaded PNAG NPs) appeared at 2θ = 11.5°, 15.5°, 18.9°, 21.6°, 31.1°, 35.5°, 37.8°, and 42.2°, confirming that the SNP are loaded in PNAG particles and the decreased intensity of peaks shows that the crystallinity of SNP reduced after loading into PNAG NPs (Fig. 1f). However, XRD also revealed that PNAG NPs are loaded with SNP. Further, the size and surface morphology of the SP NPs were confirmed through TEM (Fig. 1g–i). The TEM micrograph shows a co-connected (Fig. 1g) and balloon-like structure (Fig. 1h) of SNP-loaded nanoparticles, and the dense core (Fig. 1i) seen in particles supports that SNP is loaded inside the particles. Further, the diffused ring pattern (Fig. 1j) of the SAED confirmed that SP NPs are semi-crystalline in nature, which supports the results obtained from XRD (Fig. 1f). The particle size of SP NPs is found to be in the range of 120–200 nm (Fig. 1k). Particle size results were further confirmed through DLS (Fig. 1l), and the hydrodynamic diameter of particles was found to be *ca.* 167 nm. The stability of the SP NPs was confirmed through the zeta potential (ξ) measurement, and the value was obtained to be −32.8 mV, confirming the excellent colloidal stability of SP NPs. Further, elemental analysis/mapping was performed using EDS through the scanning and focusing of different areas of PNAG NPs and SP NPs, and their corresponding peaks are shown (Fig. 2). Both the elements, Fe and Na are present in SP NPs while the same are absent in PNAG NPs; this again confirms the loading of SNP into PNAG NPs and the successful formation of SP NPs. In the EDS spectrum, the quantitative estimation of Fe, Na, O, N, and C for PNAG NPs and SP NPs is shown. The SEM images and elemental mapping images of PNAG NPs (Fig. 2a1–g1) and SP NPs (Fig. 2a2–g2) are shown. The elements overlay for PNAG NPs found to be 92.9 (Fig. 2b1), 2.04 (Fig. 2c1), 4.84 (Fig. 2d1), 0.0 (Fig. 2e1), 0.21 (Fig. 2g1), and for SP NPs, 79.12 (Fig. 2b2), 1.38 (Fig. 2c2), 1.26 (Fig. 2d2), 7.66 (Fig. 2e2), and 10.59 (Fig. 2f2)%, respectively, of C, N, O, Na, and Fe. Mapping of C element Fig. 2(b1 and b2), N element (c1 and c2), O element (d1 and d2), Na element (e1 and e2), and Fe element (Fig. 2f1 and f2) and all elemental imaging merged (Fig. 2g1 and g2) are shown for f PNAG NPs and SP NPs, respectively. The elemental mapping of PNAG NPs and SP NPs shows the uniform presence of Na and Fe in SP NPs while the same elements are absent in PNAG NPs. The details of the EDX spectra of PNAG NPs and SP NPs measured in atomic and weight% are listed in the table inset in Fig. 2c and d. Further, elemental mapping results confirmed that the SNP molecules are properly loaded in PNAG NPs.

3.2 Drug content loading/entrapment efficiency and NO release efficiency from SP NPs

After accessing the cytotoxicity of PNAG NPs in mouse fibroblast (L929) cells (ESI, Fig. S10†), SNP was loaded in PNAG NPs following the method mentioned in the Experimental section. The EE (%) of SNP was evaluated by measuring the amount of SNP that remained in the supernatants and found that almost 40.97 ± 1.52% SNP was loaded in PNAG NPs, resulting in nearly 4.86% of absolute NO loading. SNP is a hydrophilic molecule and is entrapped in hydrophilic PNAG

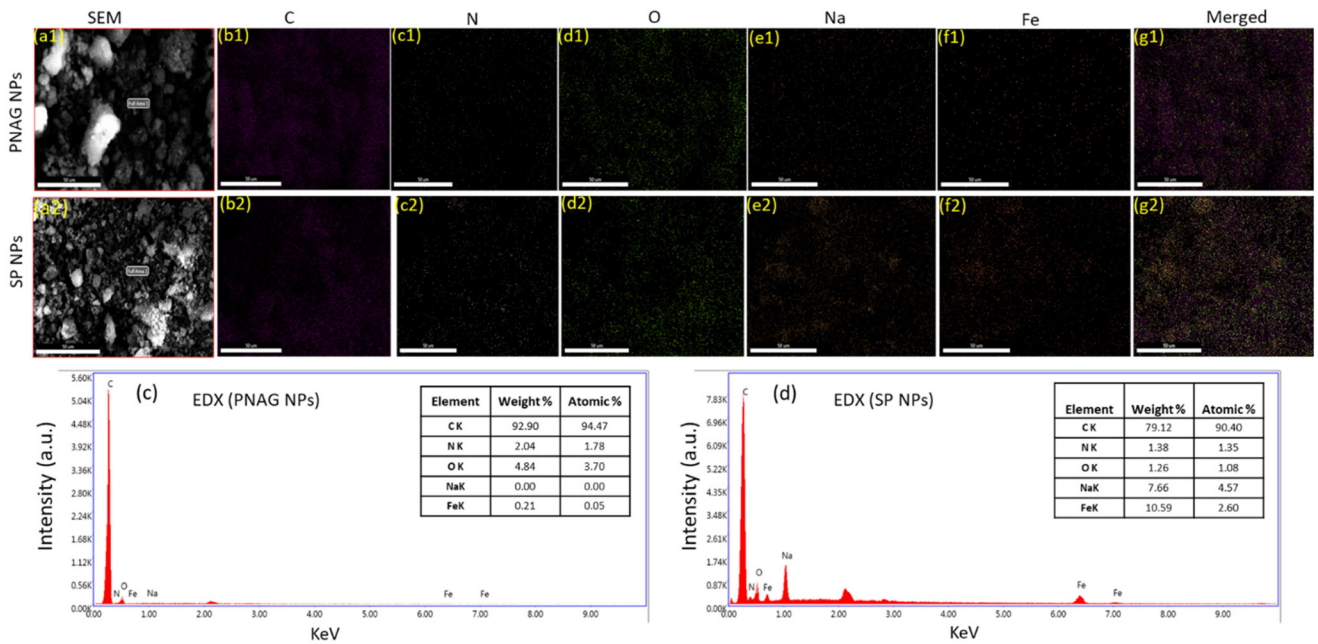

Fig. 2 SEM Images and elemental mapping images of PNAG NPs (a1–g1) and SP NPs (a2–g2). Elements overlay for PNAG NPs, 92.9 (b1), 2.04 (c1), 4.84 (d1), 0.0 (e1), 0.21 (g1), and for SP NPs, 79.12 (b2), 1.38 (c2), 1.26 (d2), 7.66 (e2), and 10.59 (f2)%, respectively, of C, N, O, Na, and Fe. Mapping of C elements (b1 and b2), mapping of N elements (c1 and c2), mapping of O elements (d1 and d2), mapping of Na elements (e1 and e2), and mapping of Fe element (f1 and f2), and all elemental imaging merged (g1 and g2), in the sample of PNAG NPs and SP NPs, respectively. (c) EDX for PNAG NPs and (d) EDX for SP NPs formulation. The inset of (c) and (d) represents the percentage of element presents for the corresponding sample.

NPs easily. Simultaneously, the LC (%) of PNAG NPs for SNP is found to be 48.23 ± 5.63%. The quantification of the NO content was done using UV-Vis spectroscopy using Griess reagent for the unit weight of SP NPs and found to be 98.29 ± 2.79%, which is equivalent to 1.59 ± 0.04 μmol mg^{-1} of SP NPs.

Further, SNP was loaded in PNAG NPs, enabling the release of NO sustainably. The rate of NO release in PBS (pH 7.4) was quantified using the Griess reagent method. The real-time NO release profile and plot of the total NO release in percentage are shown in Fig. 3. It is observed that NO flux was observed to be 19.58 ± 1.97 nmol mg^{-1} min^{-1} within the first 15 min of the start of the release. The total NO content released from the 5 mg of SP NPs within 24 h is 7.95 ± 0.23 μmol, or %CDR is 97.37 ± 8.19%. Further, SP NPs can release NO more in 24 h. It was observed that 47.64% NO is released within one hour from SP NPs. However, the NO release rate continuously decreases with time, as shown in Fig. 3, and follows a sustained release behaviour of 38% of NO over 22 h. Due to the PNAG NPs' hydrophilicity and the SNP's water-soluble characteristics, the release occurred in two stages. In the first stage, NO release was speedy due to the entrapment of SNP on the surface pores of the porous network structure of PNAG NPs. The second stage of NO release is relatively slow because the NO is released from the core part of PNAG NPs.

3.3 Cytocompatibility/cell proliferation and hemocompatibility of SP NPs

For any wound dressing material, it is essential to have cellular proliferative and migratory stimulatory activity along with hemocompatibility. Therefore, low cytotoxicity is one of the essential requirements for using SP NP's proliferative capacity in wound dressings. The cytotoxicity of the present materials was assessed using an MTT assay in mouse fibroblast cell (L929) lines, and PBS was used as the control group. It is noticed that the SP NPs-treated L929 cells survived more than 100% compared to the control, proving that the SP NPs are not cytotoxic. Additionally, with the increase in the concentration of SP NPs, the activity of the cells steadily increased, showing that SP NPs have a potent ability to promote cell growth. The impact of concentrations of SP NPs on the proliferation of L929 cells is shown in Fig. 4a. After the incubation of L929 cells with SP NPs at different concentrations of 2, 10, 20, 50, 100, 200, and 250 μg mL^{-1}, the cell viability (%) relative to the control group is found to be very high as 98.5 ± 11.7%, 101.4 ± 10.0%, 103.4 ± 10.2%, 117.0 ± 10.0%, 163.0 ± 13.0%, 193.3 ± 11.1%, 239.8 ± 10.8%, and 288.7 ± 12.0%, respectively, indicating that the SP NPs exhibits a significant growth-promoting effect on the proliferation of mouse fibroblasts are biocompatible. These studies show that the SP NPs are non-toxic over the concentration range of 2 to 250 μg mL^{-1} and ensure the potential use of SP NPs in *in vivo* wound healing. These results also revealed the cytoprotective effect of NO (Fig. 4a). Further, the hemocompatibility of SP NPs was evaluated by an *in vitro* blood coagulation test (Fig. 4b and c) and *in vitro* hemolysis, which are represented in the consecutive section (Fig. 4d and e).

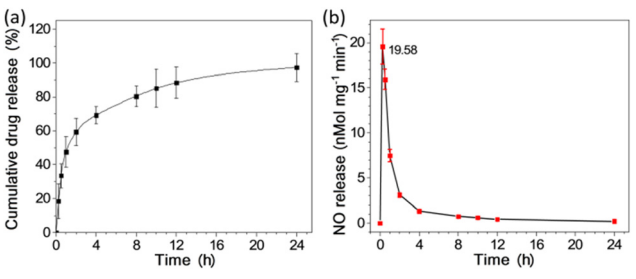

Fig. 3 *In vitro* NO release profile. (a) Cumulative NO release profile (%, CDR). (b) Real-time NO release determination. NO release study was conducted from SP NPs in PBS (pH 7.4) at 37 °C. Data is presented as mean ± SD (n = 3).

3.3.1 Blood coagulation cascade. The anticoagulant properties of the NO-releasing SP NPs to examine the potential biological interactions with the blood coagulation cascade have been studied, and the results are shown in Fig. 4b and c. Using APTT and PT, the *in vitro* anticoagulant activity of the synthesized SP NPs has been studied. The APTT values (Fig. 4b) for SP NPs were found to be 33.0 ± 2.1, 32.7 ± 2.6, 32.5 ± 3.2, 33.0 ± 2.6, 32.6 ± 3.7, 34.7 ± 2.9, and 35.5 ± 1.2 s, for the animals treated at 1, 5, 10, 25, 50, 100, and 200 μg mL^{-1} of SP NPs, respectively. These APTT values marginally deviated from the values reported for the control group of animals (33.0 ± 2.1 s); however, they do not significantly ($P > 0.05$) differ from the control group of animals. Similarly, the SP NPs could not substantially alter the PT values ($P > 0.05$). Therefore, it can be concluded that the coagulation cascade is unaffected by SP NPs in the concentration range of 1–200 μg mL^{-1}, even though the PT time is risen compared to the control. These results suggest that the anticoagulant potential of SP NPs and the enhanced concentrations have no appreciable impact on the PT.

3.3.2 Study of hemolysis. Death can result due to severe blood loss during surgery and trauma. As soon as tissue injury occurs, the wound has to cease bleeding immediately. Consequently, a dressing for wound healing should have high hemostatic[40] or low hemolytic activity. Due to the ease of separation of erythrocytes, the hemolysis assay is routinely considered in studies of novel xenobiotics and membrane-active biomaterials, and the hemolytic activity test provides a versatile approach for swift initial toxicity evaluation. Therefore, the hemolytic activity of SP NPs (Fig. 4d and e) was measured at different concentrations (0 to 1000 μg mL^{-1}) and compared with the results obtained for PBS. Fig. 4d shows the dose-dependent hemolysis caused by SP NPs. The hemolysis extent is found to be 0.06 ± 0.01, 0.08 ± 0.01, 0.29 ± 0.12, 0.39 ± 0.37, 0.49 ± 0.26, 0.53 ± 0.26, and 0.57 ± 0.42% for the SP NPs concentrations of 1, 10, 100, 250, 500, 750, and 1000 μg mL^{-1}, respectively, after 24 h of treatment. It is observed that hemolysis was below 2% at the maximum investigated dose (Fig. 4d), considered safe[41] for topical use or dermal application, and does not cause significant hemolytic activity compared to

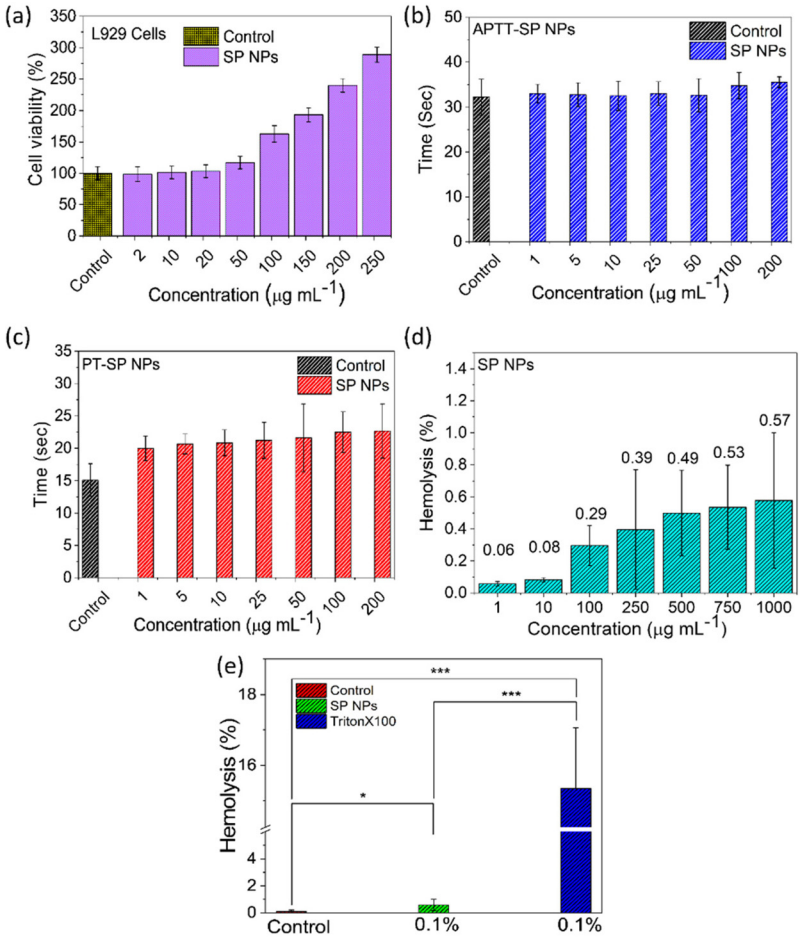

Fig. 4 Cytocompatibility and hemocompatibility of SP NPs. (a) Cytocompatibility assay: treatment of mouse fibroblast (L929) cells with SP NPs shows proliferation instead of cytotoxicity ($P < 0.05$). (b) Activated partial thromboplastin time (APTT) and (c) prothrombin time (PT) tested using different concentrations of SP NPs in the range of 1–200 μg mL^{-1} and compared to the control group (PBS-treated group) ($p > 0.05$). Data are presented as mean ± SD ($n = 3$). Hemolytic effect of SP NPs (4d and e) on rat RBCs. (d) Dose–response curves of hemolysis caused by SP NPs with concentrations ranging from 1 to 1000 μg mL^{-1} ($p > 0.05$). (e) SP NPs show less than 1% hemolytic activity, even at the highest tested concentration (1000 μg mL^{-1}), and hemolysis occurred in rat RBCs by SP NPs dispersion (0.1% w/v in PBS) compared with Triton-X 100 (0.1% v/v, positive control) against rat erythrocytes. Positive control shows ~15% hemolysis, while SP NPs show ~0.57% ($p < 0.05$).

Triton X-100, which causes 15.34 ± 1.71% hemolysis at 0.1% v/v concentration (Fig. 4e). The reason behind high hemolysis caused by adding a detergent like Triton X-100 at 0.1% (v/v) is that it completely hemolyzed the cells and haemoglobin was released, which consequently showed high hemolysis (Fig. 4e). It can be noted that positive control shows ~15% hemolysis, while SP NPs show ~0.57% hemolysis, which is relatively lower than the hemolysis caused by the positive control. Thus, it can be concluded that the SP NPs can be used effectively for wound healing.

3.4 *In vitro* wound healing and live dead assay

The ability of SP NPs to promote wound healing is thoroughly examined by establishing the fibroblasts' migration assay to the wounded area (Fig. 5). The outcomes of a scratch wound healing experiment are shown in Fig. 5(a)–(c), which demonstrates the migration of mouse fibroblast (L929) cells in the presence and absence of SP NPs. In comparison to untreated cells, SP NPs-treated L929 cells migrate more swiftly in the direction of the scratched area (Fig. 5a). Observations from the results conclude that even after 24 h of treatment, none of the group's scratch gap was filled, even though fibroblasts were present in each group in disproportionately huge numbers. However, the treatment group received SP NPs at a concentration of 200 μg mL^{-1}, which covered the scratch gap up to 70.0 ± 26.4%, compared to the control group (21.2 ± 6.2%), indicating that the filling rate is approximately 3.3 times higher. As the doses of SP NPs increased, the other treatment groups also exhibited dose-dependent impact, which showed a reduction in the scratch gap or increased coverage. For SP 50 μg mL^{-1} and SP 100 μg mL^{-1}, the scratch gap coverage for treatment groups was found to be 53.4 ± 28.9 and 60.2 ± 31.4%, respectively. The scratch gap of the control group (PBS) was only significantly narrow after 48 h incubation, and the

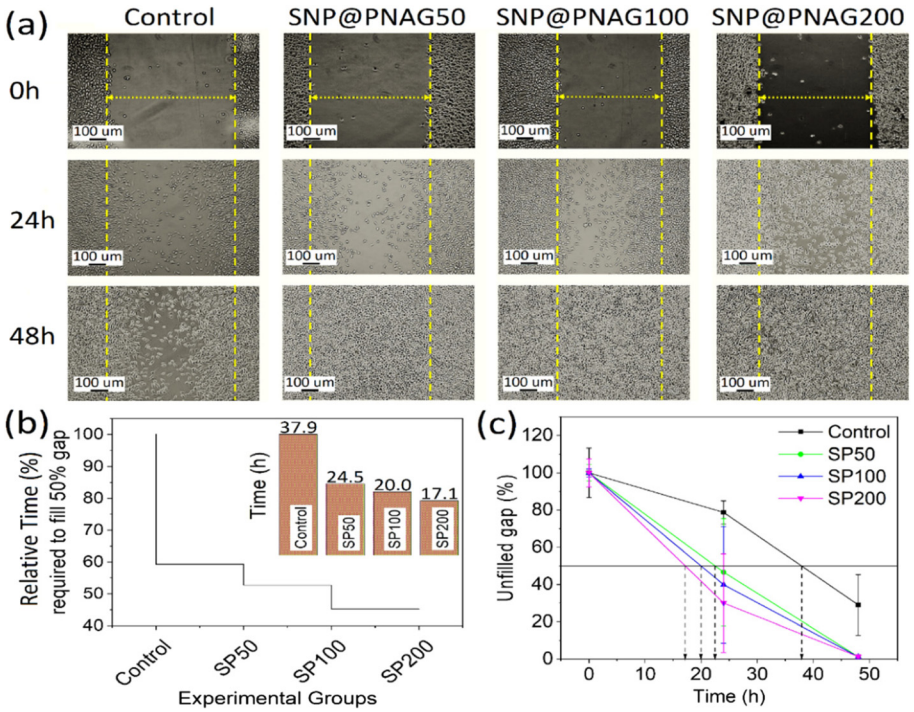

Fig. 5 Scratch wound assay. (a) Microscopic images of scratch wounds created in mouse fibroblast (L929) cells after being treated with SP NPs at concentrations of 50 μg mL^{-1}, 100 μg mL^{-1} and 200 μg mL^{-1} compared to the control at 0, 24 and 48 h. Images were taken at 10× magnification, and the scale bar shows 100 μm. (b) The time taken for cells to fill a 50% scratch gap determines how quickly cells migrated towards the scratch gap. (c) Remaining scratch area to be covered by cells.

gap covered (%) at this stage was found to be 71.0 ± 16.3%. Although the scratch gap of the untreated group showed wounds not wholly closed and some parts remained to fill, the scratch gap of all treatment groups at the concentrations of SP NPs of 50, 100, and 200 μg mL^{-1} were found to be filled (see Fig. 5).

Further, the live/dead assay of the L929 cell line was performed by treating the cells with 50, 100, and 200 μg mL^{-1} SP NPs, and the results were compared with the PNAG NPs (100 μg mL^{-1}). The fluorescent microscopy images after treatment were acquired and the results confirmed (Fig. 6) that the loading of NO in PNAG NPs enhances their viability with negligible sign of toxicity in the form of death of cells, as observed at day-1 (Fig. 6a) at all treatment concentrations. However, on day-3 (Fig. 6b), the PNAG NPs show some extent of apoptotic cell death, while all other concentrations of SP NPs are safe and do not induce the death of L929 cells.

3.5 Angiogenesis (chick embryo membrane assay: CEMA)

Angiogenesis can be precisely characterized as the process whereby new blood vessels emerge and proliferate from pre-existing vascular structures.[42] CEMA is one of the most used models for assessing *in vivo* angiogenic activity.[35] Chick embryos are incubated for 8 h with SP NPs (1–100 μg mL^{-1}) and without SP NPs (reference embryo) show the development of blood vessels. Developed blood vessels are observed at the 8^{th} h compared to the initial stage. The CEMA test in Fig. 7 depicts vascular sprouting or angiogenesis under the influence of NO released from SP NPs compared to the reference embryos. Fig. 7b–g shows the quantitative assessment of vascular development in the treatment embryos under the influence of SP NPs, and in the untreated reference, embryos were estimated using explant area, vessel length, vessel area, total number of junctions, total number of endpoints, and average vessel length. The quantitative data demonstrates that SP NPs treated at 1 and 10 μg mL^{-1} caused a significant rise in the development of blood vessels, while at 100 μg mL^{-1} exhibits adverse effects (seen as the development of distorted and damaged vasculature: Fig. 7a, SP 100) at higher concentrations. These findings assured that the SP NPs could have both pro-angiogenic or anti-angiogenic effects, depending on the dosage used, both *in vitro* and *in vivo*.

Experimental outcomes depict (Fig. 7a) that the chick embryos treated with SP NPs at 1 μg mL^{-1} have exhibited better development than the reference embryos. The embryos treated at 10 μg mL^{-1} showed flushing of blood vessels along with dilation for up to 4 h, while at 8 h, the flushing subsided, and vessels tended to reach their normal stage. On the other hand, embryos treated at a higher concentration (100 μg mL^{-1}) show no flushing, but after 2 h, damaged blood vasculature is observed, and after 4 h, the vasculature tends to revert to normalize anatomy and developmental stage; thus, it can be concluded that this distortion is temporary and may occur due to the access availability of NO (Fig. 7a).

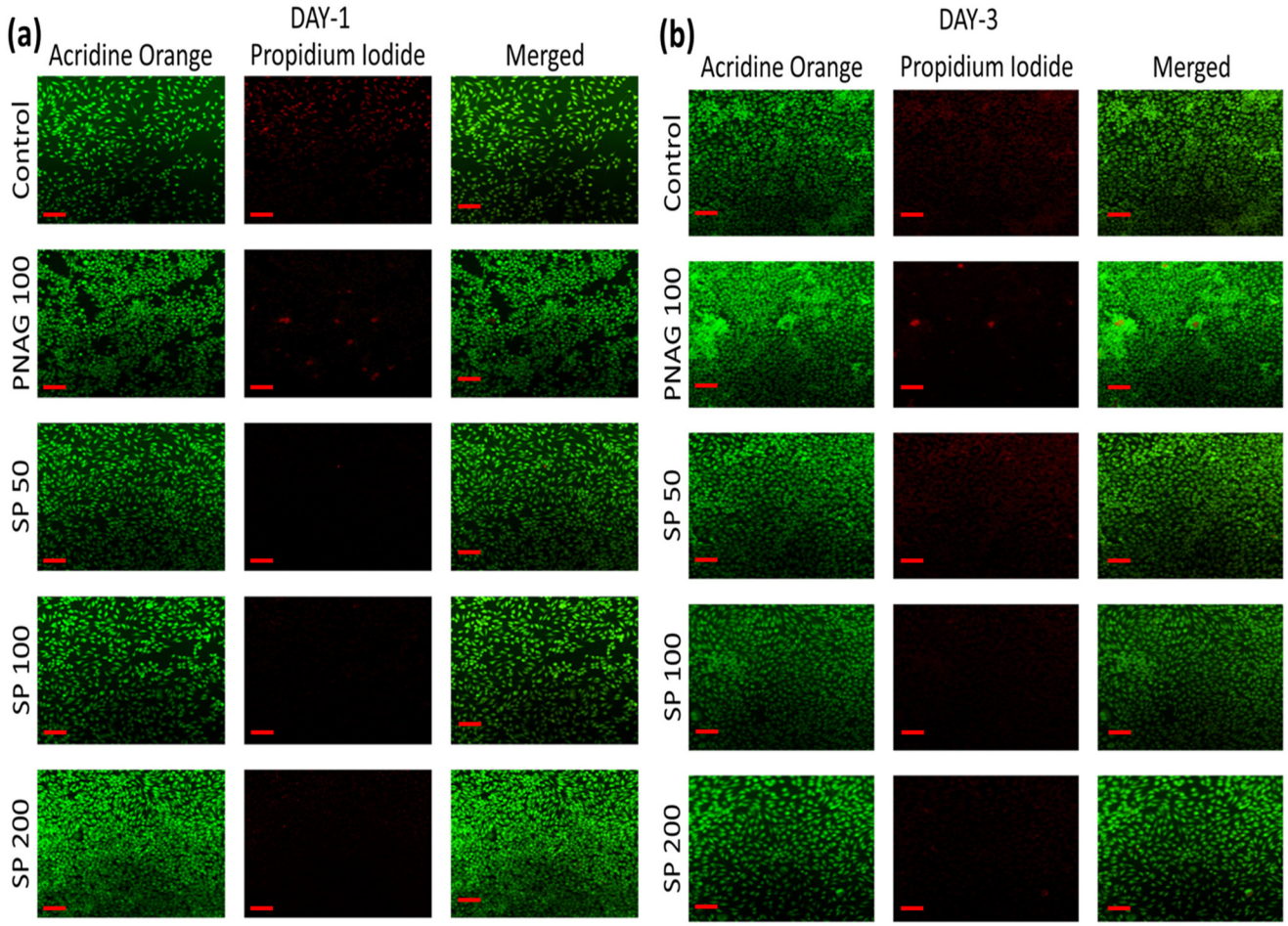

Fig. 6 Live/dead assay study: figures displaying illustrations of live and dead L929 cells, after day 1 (a) and day 3 (b) of treatment with the control, PNAG at 100 μg mL^{-1}, SP NPs at 50, 100, and 200 μg mL^{-1}. Scale bar = 100 μm. Cells were stained with acridine orange and propidium iodide.

The overall region in which blood vessels are developed is called the explant area (Fig. 7b). Embryos treated at lower concentrations of SP NPs (1 and 10 μg mL^{-1}) show a significant increase (158.6 ± 5.5% and 173.6 ± 7.9% of the initial area, respectively) compared to the reference (135.0 ± 8.7% of the initial area of reference). In contrast, the explant area of embryos treated with 100 μg mL^{-1} significantly decreased from 100% (initial explant area) to 95.7 ± 5.7% for the first 2 h. However, after 2 h, it maintained the normal anatomy of the explant area and continued to follow the trends of the reference embryo, and at the end of the 8^{th} h, it was found to be 114.0 ± 6.7% of the initial area.

Vessels area is the total surface area of blood vessels occupied in the explant area. The general trend increases the vessel area as the blood vessels develop and grow. In our experiment, each group's vessel area (Fig. 7c) increased by 113–173% of the initial vessel area. The vessels area measured at 8 h is found to be 121.8 ± 8.7, 166.9 ± 5.7, 173.7 ± 8.3, and 113.3 ± 6.1% of the initial vessels area of reference, and the treatment group treated with SP NPs at a concentration of 1, 10, and 100 μg mL^{-1}, respectively. Herein, the vessel area in embryos treated at high concentrations is lower than in the reference group. Therefore, these findings imply that the SP NPs have both pro-angiogenic and anti-angiogenic effects, depending on the dosage. Further, the junctions are the places from where a new blood capillary starts to arise. In our experiment, we observed an increase in the number of junctions. The highest junction density has been found in embryos treated at 10 μg mL^{-1}, followed by 1 μg mL^{-1}, reference, and 100 μg mL^{-1} (Fig. 7d). Total vessel length is the sum of lengths of blood vessels found in the explants area. The total vessel length (Fig. 7e) was measured. At the 8^{th} h of post-treatment, it has been found a significant increase in embryos treated with 10 μg mL^{-1} of SP NPs (187.9 ± 9.4). However, a non-significant increase (142.2 ± 5.7) is found at 1 μg mL^{-1}, while a significant decrease (123.8 ± 6.6) is found at higher concentrations (10 μg mL^{-1}) compared to the reference embryos (140.0 ± 8.6).

The average vessel length (Fig. 7f) is highest in embryos treated with 10 μg mL^{-1}, followed by a decreasing order at 1 μg mL^{-1}, reference, and 100 μg mL^{-1}. From the above results, it is clear that the embryos treated with 10 μg mL^{-1} show the formation of large blood vessels, while the embryos treated with 100 μg mL^{-1} formed smaller blood vessels.

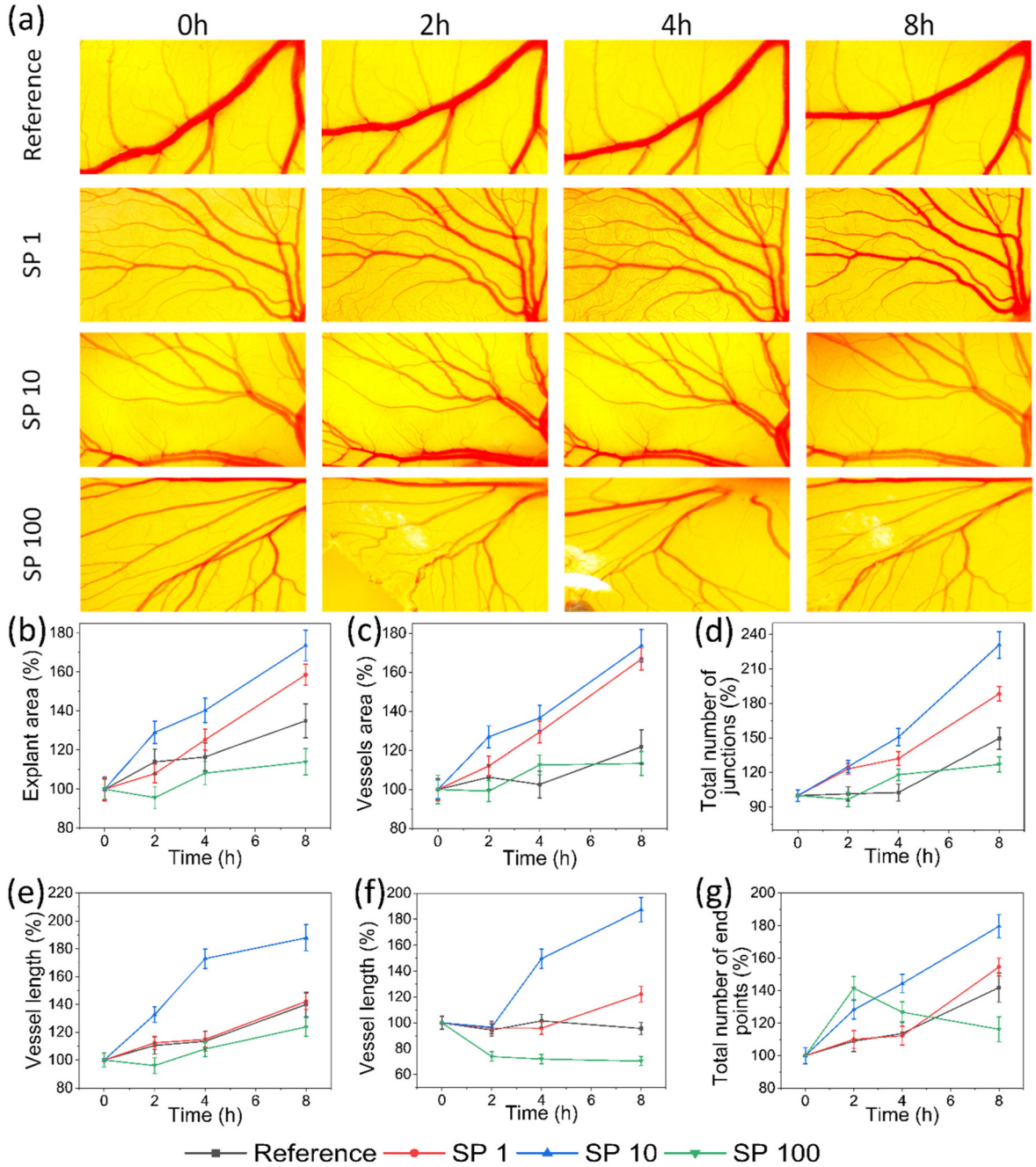

Fig. 7 *In vivo* chick embryo angiogenesis assay (CEMA): (a) determination of the effect of SP NPs on the formation and development of blood vessels in a chick embryo model. Corresponding quantitative assessment of vascular development: (b) explant area, (c) vessel area, (d) total number of junctions, (e) vessel length, (f) average vessel length, and (g) total number of endpoints (all images were taken at 10× magnification using a stereo zoom microscope).

Further, the highest blood vessel endpoints (Fig. 7g) are found in embryos treated with 10 μg mL^{-1}, whereas a decreasing order of blood vessel formation is observed once it was treated with 1 μg mL^{-1} SP NPs, reference, and 100 μg mL^{-1}. It can be noted that the embryos treated with 100 μg mL^{-1} SP NPs show a complex phenomenon within the first 2 h of treatment. At the same time, the highest endpoints were recorded after 2 h of treatment, such as the endpoints decreased and the blood vessels fused.

3.6 SP nanoformulation

To modify the SP NP's consistency and ease of application on the wounds, the SP NPs were mixed with the oleaginous base, one of the most often used ingredients in ointments. The

nanoformulation was examined to check for phase homogeneity, aggregation, and discolouration. It seemed uniform, white to off-white, smooth, and devoid of aggregation (ESI, Table S2†). Results further indicate that the SP nanoformulation had mean content uniformity of 97.29 ± 7.54% for the samples taken from the top, middle, and bottom of each nanoformulation-filled syringe. With a small amount of variance (SD 0.2), the pH of the nanoformulation was at the desired level (pH 7). Assessing the impact of pH variations is crucial because it affects the *in vitro* release of drugs[43] and, ultimately, bioavailability.

3.6.1 NO release from nanoformulation. SNP is a hydrophilic drug molecule entrapped within hydrophilic PNAG NPs. Oleaginous bases are used to prepare SP NPs nanoformulation to increase the control over NO release. *In vitro* drug release has been used to determine changes in the formulation's composition and process factors modulating the formulation's *in vitro* and *in vivo* performance (USFDA, 2016). The NO-release profile of SP nanoformulation (37 ± 2 °C, pH 6.8) was also established, and the outcomes are represented as micromoles per milligram (μmol mg^{-1}) of net SP NPs (Fig. 8). The figure (ESI, Fig. S2†) depicts the experimental setup of SP nanoformulation. In the current investigation, the cumulative NO released per unit area is also measured as a benchmark of the release profile for topical administration rather than cumulative percentage release. SP nanoformulation significantly sustains the rate of NO release than SP NPs. The observed percent cumulative NO release is 79.35 ± 4.43% and 97.37 ± 8.19%, respectively, for SP nanoformulations and SP NPs. Within the 1st h of release, around 2.73 ± 0.062 μmol NO was released, which is 43.75 ± 0.99% of total CDR (%) (34.72 ± 0.79% of the total loaded NO content per 5.0 mg of net SP NPs) from the SP nanoformulation, while the rest of ~56.25% of CDR (%) was released gradually in the subsequent 23 h (Fig. 8a and b). These results suggest that releasing all NO content from the SP nanoformulation required more than 24 h while maintaining the therapeutic level at the application site. The highest cumulative NO release rate (nmol mg^{-1} min^{-1} cm^{-2}) was found to be 5.146 ± 0.050 for the first 15 min, while the lowest release rate (0.064 ± 0.003) was observed in the last 12 h, while the SP nanoformulation releases NO at an average 0.276 ± 0.006 nmol mg^{-1} min^{-1} cm^{-2} for 24 h. This shows a controlled and sustained release of NO from the nanoformulation and is beneficial for wound healing.[44]

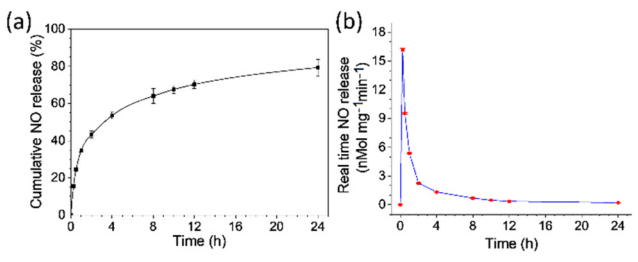

Fig. 8 NO release profile of SP nanoformulation (PBS, pH 6.8, 37 °C, *n* = 3). (a) Cumulative drug release, 79.35 ± 4.43% NO was released from the SP nanoformulation within 24 h, showing controlled and sustained release. (b) Real-time NO release profile.

3.7 Biological evaluation and effectiveness of treatment

3.7.1 Skin irritation. Skin irritation study was performed following the method discussed in the Experimental section. Here, during the study, no animal deaths occurred during the test. In all cases, skin colour is noted for up to 48 h following the dermal treatment (Fig. 9). Finally, aside from the positive group, which exhibits substantial irritation at the site of application of 1% formalin solution, no skin reaction is observed in the control and SP nanoformulation-treated animals at the site for 24 h to 72 h after administration. The PDII score for the positive control group was 2.5, whereas the PDII for the control and SP nanoformulation treatment groups was found to be 0.25.

3.7.2 *In vivo* wound healing. The *in vivo* wound healing studies were performed after describing the materials and the procedure, as discussed in the Experimental section. The findings revealed that the SP NPs exhibited strong cytocompatibility and enhanced cell proliferation, while the SP nanoformulation is non-irritant, both advantageous for the healing of injured skin. Based on the loading capacity of PNAG NPs (48.23 ± 5.63%) and maximum NO content found in SP nanoformulation (97.29 ± 7.54%), the cumulative NO release from SP nanoformulations has been calculated to be 79.35 ± 4.43%. The dose of SP nanoformulation was determined and applied to the wounds. 100 ± 10 mg SP nanoformulation (contains 5% w/w SP NPs) was applied to the cutaneous wounds since this

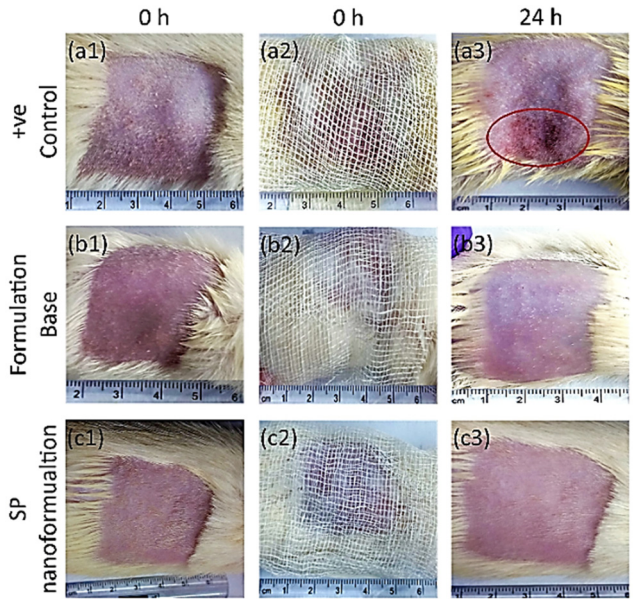

Fig. 9 Photographs of skin irritation study. Positive control (a1) before treatment, (a2) application of 1% formalin solution, (a3) erythema and oedema (shown in red circle) after 24 h of application of 1% standard solution, (b1–b3) control (formulation base) treatment group and (c1–c3) treatment (SP nanoformulation) group not showing any skin sensitivity and irritation after 24 h of treatment of the respective samples.

amount of nanoformulation can be released at a rate of 80.79 ± 0.78 nmol min^{-1} for the first 15 min, 47.67 ± 0.44 nmol min^{-1} for the next 15 min, and 45.57 ± 52 nmol min^{-1} for the next 30 min of nanoformulation treatment. These effective dosages cause nitrosative signalling (for nitrosative signalling, NO concentration must be more than 10 nmol) in the microbes, if any, present at the surface of a wound. After 2 h, these doses can maintain the concentration of NO release sufficiently and below 10 nmol for subsequent 22 h of application, which helps in effective wound healing.[45]

However, the impact of SP nanoformulation on Wistar rats' wound healing was investigated (Fig. 10). It is noted that under normal circumstances, wounds tend to heal with time, and it is a normal phenomenon of body homeostasis. However, we observed that the wound closure in the SP nanoformulation-treated rats moved along swiftly, while wound closure in the control group (formulation base treated group) was noticeably delayed (Fig. 10b). These results suggest that SP nanoformulation can accelerate the wound healing efficiency and can result in full wound closure within 12–13 days of treatment. In contrast to the control group, complete wound closure was not achieved even after 15 days of post-treatment. Consequently, the rate of gross wound closure in the treatment group increased at least 5 days earlier than in the control group. The percentage of wound area was determined to gauge the wound healing process (Fig. 10b). The corresponding percentages of wound closure in the treatment group were found to be 17.6 ± 1.1%, 81.7 ± 0.4%, and 98.3 ± 1.0%, and in the control group, it was found to be 3.6 ± 2.4%, 16.9 ± 4.3%, and 32.9 ± 7.2%, on the 3rd, 7th, and 11th day post-surgery/treatment, respectively. Rat wounds treated with SP nanoformulation heal at a much faster rate than the control for all time points (Fig. 9b). On day 7th, the extent of wound closure is found to be 16.85 ± 4.28% for the control group, whereas it is 81.74 ± 0.41% for the treatment group. These findings showed that the SP nanoformulation has superior healing capacity, which is attributable to NO release. Further, the histopathology studies have been verified and supported the positive

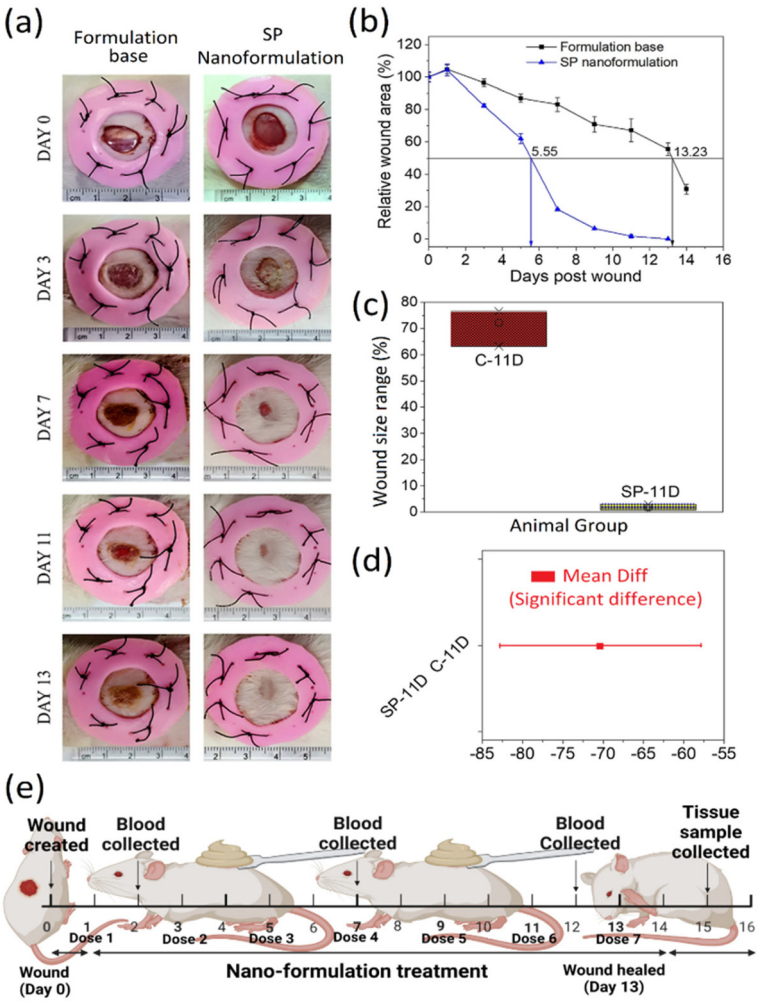

Fig. 10 *In vivo* wound healing assessment: (a) macroscopic images of wounds. (b) Measurement of relative wound area remaining to heal. (c) Range of wound size at 11th day that remained to heal. (d) Significant difference representation of mean wound size on the 11th day using the Tukey test to compare the mean. (e) Time-line of *in vivo* animal experimentation.

effects of SP nanoformulation on wound healing, which is covered in the next section. These findings revealed an apparent propensity for NO therapy to accelerate wound healing.[22,44] However, it can also be observed from the images (Fig. 10a) that after 3rd day post-treatment, both treatment and control groups developed dark red-coloured wound scabs, which prevented the passage of further blood and other fluids.[31] Compared to the control group, inflammatory cells in the treatment group were considerably less. This indicates that on the 3rd day, the early stages of the inflammatory healing process occurred in all the groups, although it progressed more efficiently in the treatment group. This could happen since NO produced by SP nanoformulation can limit the production of inflammatory mediators and stimulate growth factors like IGF-1 (Fig. 12e), which activate NF-κβ and treat the inflammatory phase while accelerating wound healing.[46]

From the images (Fig. 8a), developing layers of skin and wound surrounds are unclear, and these alignments are very loosely maintained because of the inflammatory phase, which promotes platelet clotting and macrophage generation rather than re-epithelialization and dermal remodelling.[31] As anticipated, the granulation tissue production in the treatment group was much higher than in the control groups within the 7th-day post-treatment. On the 13th day, the wound of the SP nanoformulation-treated group is surrounded and covered by fully developed skin layers, while for the control group, a significant wound area remains to be healed.

3.7.3 Histology study. Development of granulation tissue, collagen deposition, and angiogenesis are crucial processes in wound healing and must be carefully managed. An external infusion of NO can regulate these three aspects of wound healing.[44] Skin layer morphology was scrutinized during the healing process and are shown in this section (Fig. 11). The slices of the wounded skin were stained with H&E and Mallory's trichrome stain to show the formation of granulation tissue and re-epithelialization during wound healing. Healthy skin histological features are shown (Fig. 11A: N1, N2, and N3 and 11E: N). After 2nd, 7th, and 14th days post-surgery, the SP nanoformulation demonstrated granulation tissue generation, as shown in Fig. 11A–E.

Further, the morphology of the regenerated tissues can be explained through hematoxylin and eosin staining. From the images of healthy skin (Fig. 11A), a well defined and fully differentiated skin epidermis layer (N1, red arrows), dermis layer with some resting fibroblasts (N2, blue arrow) and active fibroblasts (N2, red arrow), collagen fibres connected with hypodermis, and smooth muscle fibres, skin hair follicle appendages (N2, blue bracket), fat cells and active fibroblasts (N3, red arrow) are identified.

On treatment with the formulation, it is clearly observed that for the 2nd day of wound healing, numerous inflammatory cells (panel C1 and C2 of Fig. 11A, black arrows) are present below the clot edge and the middle region of the wound. From the dermis, the infiltration of neutrophils and other immune cells in the control group indicate that a strong inflammatory reaction occurred (C3 of Fig. 11A, red arrow). Further, in the hypodermis region, it is observed that numerous inflammasomes are present (C3 of Fig. 11A, green arrow), while fewer inflammatory cells (T1 and T2 of Fig. 11A, black arrow) and fibroblast migration (T1 and T2 of Fig. 11A, blue arrow) in the hypodermal wound region occurred in the treatment group. Further, few fibroblasts (blue arrow), along with macrophages (black arrow) migrating to the dermal region and hypodermal region with active (blue arrow) and inactive fibroblasts (orange arrow) along with fewer inflammatory cells (red arrow) in the epidermal region of the wounded site, are observed. It is also noticed that the development of blood vessels started as the tube forming cells are clubbed together (green box) (T3 of Fig. 11A).

For the day 7th of wound healing (Fig. 11B), in the control group, the epidermis is observed to be full of inflammatory cells and messy tissue (C1). Fewer fibroblasts along with large immune cells are present in the dermal region (C2, red arrow). Also, few inactive fibroblasts in the extracellular matrix are present in the hypodermal layer with larger inflammasome (C3) compared to day 2, while a thick epidermis (T1) with numerous blood vessels (T2 and T3, green arrow), immune cells (blue arrow), and dense active fibroblasts (black arrow) are present in the treatment group. On the other hand, epithelial cells with a thicker layer are observed in the treatment group (T3).

On day 14th of wound healing (Fig. 11C), in the control group, the epidermis with diffused basement membrane and thin stratum corneum, stratum granulosum and thicker stratum spinosum (C1), inactive (C2, black arrow) and active fibroblasts (C2, blue arrow), and clumped collagen are observed. These results indicate excessive collagen deposition in the fibrotic tissue with clumped fibroblasts, whereas the treatment group shows the formation of well-defined layers of epidermis including stratum corneum, stratum granulosum, and stratum spinosum similar to normal skin, and the base membrane is also fully developed and differentiated properly (T1). Additionally, elastin-like fibres with active fibroblasts with more euchromatin and basophilic cytoplasm with larger nuclei in the treatment group are formed in the dermis layer (T2). T3 represents the formation of thick collagen bundles with close arrangement and, interestingly, the laying cellular components clearly represent the remodeling and repairing of the tissue.

Further, to investigate the collagen deposition on different days of treatment and the regeneration of tissues, Mallory's trichrome staining was performed. For healthy skin (Fig. 11D and E (N)), thin pink-coloured epidermis and thick blue-coloured collagen bundles having irregular arrangement (N1), irregular thick collagen fibres along with skin appendages (hair follicle) (N2), pinnacles muscle layer between hypodermis and dermis (N3) are observed. For the control group, immature and broken epidermis with diffused basement membrane with minimal collagen deposition are observed (see panels C1, C2, and C3 of Fig. 11D) and Fig. 11E (C-2, C-7, and C-14). Thin collagen bundles (C2 and C-14) with irregular arrangement and numerous immune cells (C-7) are also observed. Further,

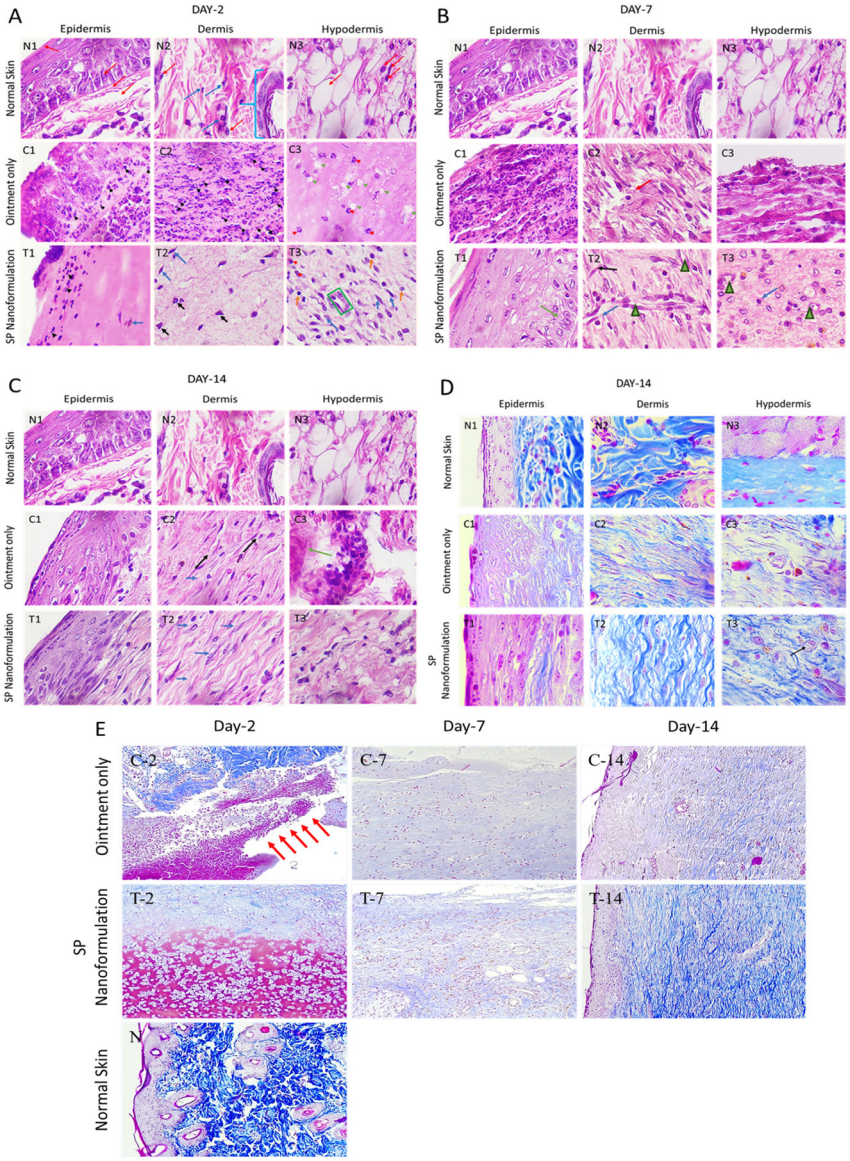

Fig. 11 Histological analysis of skin wound through staining with H & E stain and Mallory's trichrome stain. Histological assessment and comparative histological analysis of the wound on 14th day post-injury with the normal tissue stained with H & E (A, B, and C) on the 2nd, 7th, and 14th day and with Mallory's trichrome stain (D and E) on the 14th day (D) and comparative evaluation on the 2nd, 7th, and 14th day (E). Letters N, C, and T denote the images of healthy skin, control group (ointment base treated group), and treatment group (SP nanoformulation treated group), respectively. Wound healing on day 2 (A), 7, (B) and 14 in the control and treatment group compared to healthy skin. Wound healing comparison on the 14th day using Mallory's trichrome stain (D). (E) Wound healing comparison using Mallory's trichrome stain on day 2nd, 7th and 14th between the control and treatment with healthy skin. Fig. A–D with 100× and E with 20×.

regions with less collagen deposition and with thin irregular collagen fibres are also generated in the control group (C-7 and C-14). On the other hand, for the treatment group (Fig. 11D and E), the well-defined basement membrane with some extent of collagen fibre and well defined layers of epidermis are formed (T1 and T-14). Additionally, thicker collagen bundles with elastin fibre-like arrangement with other cells (T2) are observed. Further, the formation of blood capillaries along with the formation of thicker and more collagen bundles (T-14) with arrangement represents the remodelling of the regenerated tissue (T3). Thus, the SP nanoformulation works well for the treatment of the wounded tissue. The onset of the proliferative phase of wound healing, as well as the proliferation of keratinocytes, endothelial cells, and fibroblasts, can be demonstrated for the use of NO.[31] The exogenous administration of NO in the form of SP nanoformulation thus has better stimulating effects on wound healing. The processes, such as re-epithelialization and collagen deposition, are carried out after the diffusion of NO to the wound tissue region; hence, NO plays a vital role in the wound healing process. Therefore, the present formulation can successfully enhance wound healing. Additionally, angiogenesis promotes

the development of new blood vessels that carry oxygen and nutrients for tissue repair and rebuilding during the healing of wounds.[44]

3.7.4 Wound healing markers and inflammation study. On the inflammatory phase (2nd day), proliferative phase (7th day), and remodelling phase (12th day) of wounding, the levels of cytokines in the blood serum of the treatment and control groups were determined by ELISA to assess the effects of SP nanoformulation. During these phases, the level of cytokines changed significantly, demonstrating the impact of the SP nanoformulation. It is also observed that on the 2nd, 7th, and 12th day of post-treatment, the relative levels of TNF-α, IL-1β, and IL-6 were considerably lower for the treatment group than the control group (Fig. 12). The C-reactive protein (CRP) is a blood protein that is seen in the acute phase and activates the complement. In reaction to inflammatory cytokines, the liver releases CRP into the bloodstream. Herein, after tissue injury, the CRP level quickly rises in response to inflammation and infection, then drops as the wound heals, and the relative CRP levels are significantly lowered in the treatment group com-

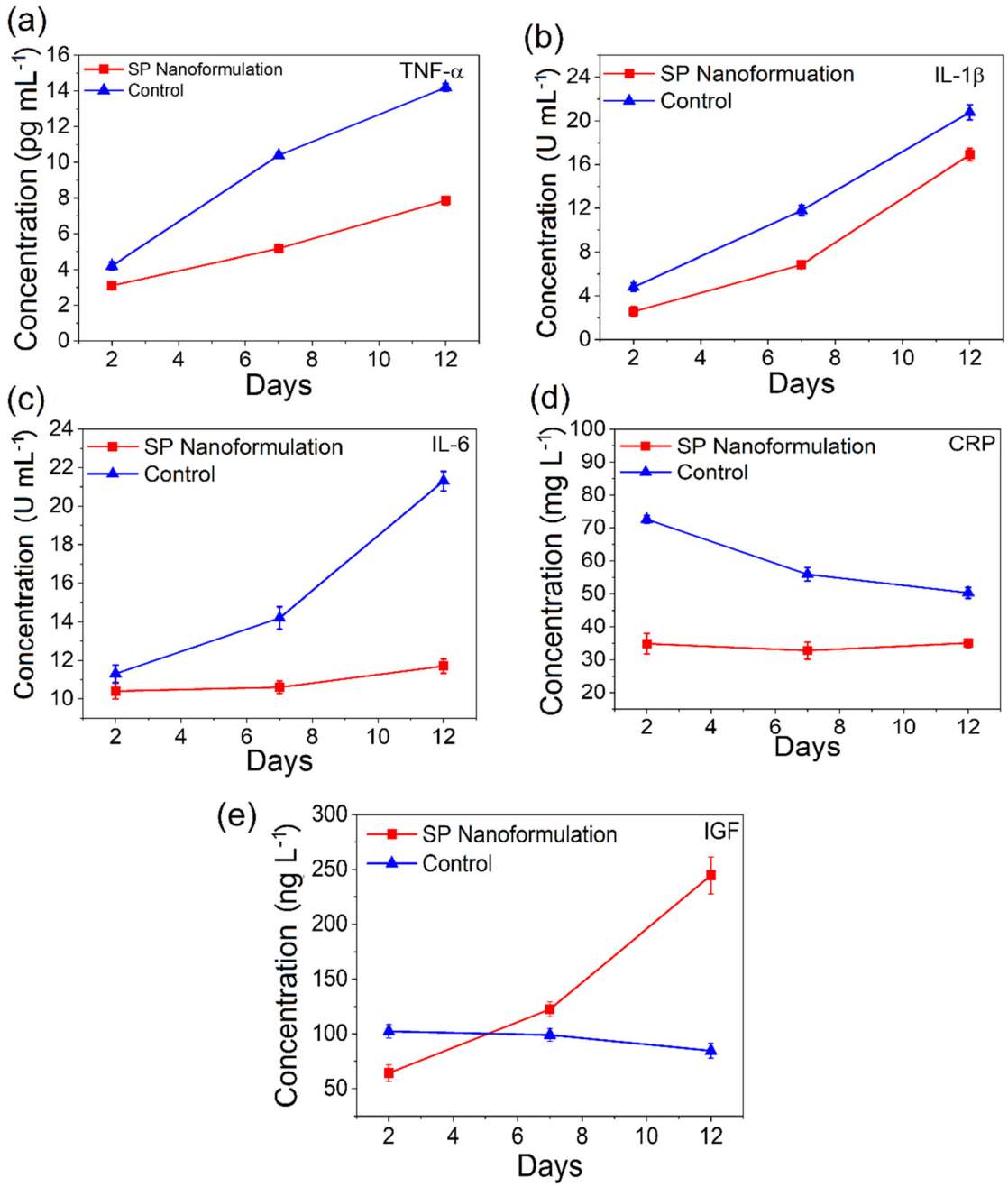

Fig. 12 Wound healing markers analysis by ELISA on the 2nd, 7th and 12th day of post-wounding. (a) TNF-α, (b) IL-1β, (c) IL-6, (d) CRP and (e) IGF-1 levels. Each data point represents the average ± SD of 3 independent determinations ($p < 0.05$).

pared to the control group. On the 7th and 12th day, the IGF-1 levels in the treatment group are considerably higher (Fig. 12e), suggesting a higher likelihood of keratinocyte migration to the injured areas during the proliferation and remodelling phase.[47] In contrast, the control groups have lower levels of IGF-1 while having high levels of pro-inflammatory cytokines (TNF-α, IL-1β, and IL-6). These deterrent effects on the levels of pro-inflammatory cytokines are found due to the regulated NO release from the SP nanoformulation. Thus, it can be concluded that NO functioned as an anti-inflammatory agent, and the SP nanoformulation successfully protects the cells from inflammation *via* controlled-release profiles.[48]

3.7.5 Semi-quantitative reverse transcription and polymerase chain reaction (sqRT-PCR). To study the gene expression during wound healing, an sqRT-PCR study was performed, as mentioned in the Experimental section, and the results have been shown in Fig. 13a–c. Fig. 13a shows the band of gene expression for day 2 (C-2), day 7 (C-7), and day 14 (C-14) for the control group and for day 2 (T-2), day 7 (T-7), and day 14 (T-14) for the treatment group. It can be noted that GAPDH is a housekeeping gene and is used as a reference control in gene expression analysis. Furthermore, in our study, the gene expression analysis by sqRT-PCR revealed that the expression level for the KDR gene is found to be higher in the control group with respect to the treatment group for all the treatment days (see Fig. 13b and c); however, the gene expression difference is non-significant. In wound healing, VEGFA plays a direct and indirect role in the migration of inflammatory cells and keratinocytes by inducing proliferation and collagen deposition in the remodelling phase.[49] VEGFA also interacts with the receptor KDR and mediates the internalization of KDR to the nucleus; finally, the activation of PI3-kinase/AKT occured.[50] The expression of VEGFA is higher on day 2nd and downregulated at day 7th and 14th in the control group at day 2 (see Fig. 13b and c). This high expression could have occurred due to the increased migration of inflammatory cells to the wounded region in the control group. On the other hand, in the treatment group, the VEGFA expression was downregulated on day 2nd of treatment. The expression of VEGFA was observed at the base line on day 7th and increased on day 14th of treatment. These results suggested that the SP NPs formulation have a major role in enhancing scarless wound healing. Similarly, PECAM-1 (CD31) plays a central regulatory role in wound healing as a representative of angiogenesis. However, the increased expression of PECAM-1 is occurred with day of treatment in the control group. In the treatment group, on day 2, the PECAM-1 expression was downregulated, whereas for day 7 and 14 of post treatment, the same increased compared to the control group (Fig. 13). Thus, SP nanoformulation has a regulatory effect on KDR, VEGFA, and PECAM-1 expression for the regeneration of the wounded tissue.

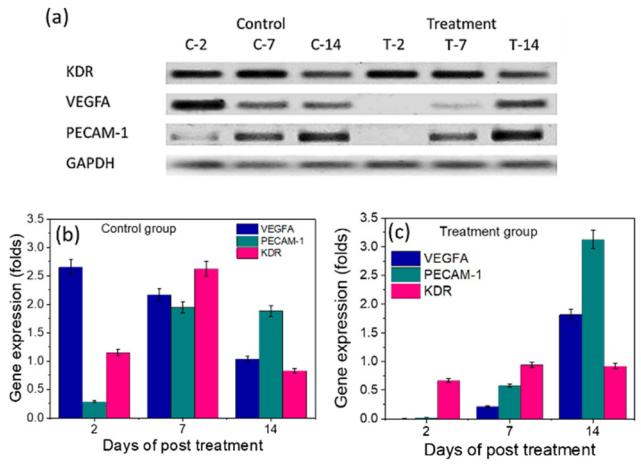

Fig. 13 (a) Relative expression of various genes during wound healing. (b) and (c) represent the gene expression level relative to GAPDH (in folds) for the control and treatment group, respectively, for VEGFA, PECAM-1, and KDR. In the figure, the band of gene expression for day 2 (C-2), day 7 (C-7) and day 14 (C-14) for the control group and for day 2 (T-2), day 7 (T-7) and day 14 (T-14) for the treatment group.

4. Discussion

This study has formulated water-dispersible NO-releasing biosafe advanced polymeric nanoparticles (SP NPs) by free radical polymerization and subsequently loading with SNP. FTIR shows characteristic bands of cyano, NO, and Fe-NO groups at 2148 cm^{-1}, 1941 cm^{-1}, and 662 cm^{-1}, which confirmed the formation of NO-releasing NPs (SP NPs) (Fig. 1c). Many parameters, such as formulation components, manufacturing processes, or process factors including time, temperature, pressure, instrument type, lyophilization, packaging, and storage conditions, have an impact on the average particle diameter of NPs. The particle size requirement and distribution of well-designed nanosystems should be in the submicron range[51] because the interactions between biochemical and cellular components of cells and nanocarriers take place only when particles are typically smaller than 200 nm; these interactions are distinct from those arising from relatively larger particles or implants made of biomaterials.[52] Therefore, using TEM and DLS, the morphology, size, and distribution were examined, and due to an average size of 162 nm (dia), these SP NPs potentially exhibited bioactivity. Herein, zeta potential (ξ),[51] found to be ~−32.8 mV, represents the colloidal stability of the SP NPs. Due to the abundance of anionic carboxylate groups, SP NPs are stabilized by electrostatic repulsion and steric stabilization. Drug loading is crucial when fabricating an NP-based delivery system since low loading requires significantly more formulation for an optimum therapeutic effect.[53,54] Therefore, low drug loading is an obstacle for using nanotherapeutics, necessitating high LC and EE. Herein, high LC (48.23 ± 5.63%) and high EE (40.97 ± 1.52%) were found for SP NPs. The loading of SNP was also confirmed by the elemental analysis of SP NPs, which shows the availability of Fe and Na as metallic components of SNP (Fig. 2). This proves that in fewer doses, SP NPs can deliver more NO. The reason for this high LC and EE are the cross-linking of PNAG NPs

with DVB, which also helps to retain their good water dispersibility. Thus, these SP NPs also have good NO content measured as 98.29 ± 2.79%, equivalent to 1.59 ± 0.04 μmol mg^{-1} of SP NPs.

In vitro release plays several crucial functions during a drug product life cycle from the viewpoint of product quality. Thus, the quality control strategy at the early and late stages of product development guarantees batch-to-batch consistency and uniformity.[55] According to the literature, SNP's mean plasma elimination half-life in aqueous solution is about 2 minutes.[56] In the study of NO delivering and releasing biomaterials, the release time is one of the essential performance parameters. Numerous studies were done to modulate the release of NO.[57–60] The *in vitro* release of NO entrapped on the SP NPs was investigated in PBS at pH 7.4 and temperature 37 ± 2 °C to simulate the intestinal environment and the CDR (%) was found to be 97.37 ± 8.19% within 24 h. Fig. 3 demonstrates that SP NPs successfully regulate and lower the release rate of NO. The requirement for frequent dosages may decrease with persistent NO administration. A regulated NO release is crucial for the actual clinical application of NO-releasing biomaterials.[61] For rapid and long-term pharmacological actions from NO-releasing biomaterials, sustained NO release for at least 24 h is necessary since once-daily dosing for chronic disorders can be manageable.

A successful demonstration of NPs biocompatibility through a series of *in vitro* and *in vivo* tests may evaluate the cytotoxic or immunological impact triggered after their administration is required for the regulatory approval of innovative nanocarriers. An ideal material for a wound dressing should be biocompatible, reduce inflammatory receptivity, manage inflammation, and accelerate wound healing.[46] The clinical availability of nanocarriers for delivering medicines to target diseased tissues more successfully depends on an accurate biocompatibility assessment. It is well known that interactions between cells and biomaterials can lead to protein adsorption and cell contacts, activating host defence mechanisms such as thrombogenicity and inflammation. These reactions may result from the body directly detecting nano-biomaterials or an unintentional release of pro-inflammatory cytokines, which results in cytotoxicity and, subsequently, loss of cell integrity in response to nano-biomaterials.[62] In this work, we found that SP NPs are well tolerated by mouse fibroblasts (L929) cells, exhibiting proliferation (Fig. 4a) and do not cause cytotoxicity while exhibiting acceptable hemolysis (Fig. 4d and e) at the highest concentration (1 mg mL^{-1}) tested for therapeutic purpose and having no adverse effects on the coagulation cascade (Fig. 4b and c). Therefore, the absence of cytotoxicity assures that the potential of SP NPs can be used for *in vivo* application. The experiments showed that SP NPs are biocompatible and have the potential to stimulate cell growth when loaded with SNP, and these findings also pointed to NO's cytoprotective properties. Therefore, our studies demonstrate both the biocompatibility of SP NPs and its ability to promote cell proliferation when loaded with SNP.

Conventional bioequivalence techniques based on plasma pharmacokinetic data sometimes may not be feasible and may not produce relevant results; in such a case, demonstrating the therapeutic equivalence of topical semi-solid therapeutic might be difficult. Suppose two formulations (test and reference) release medication at different rates when compared under the same circumstances and when the case reference data are unavailable. In that case, an *in vitro* release test can reveal the most significant information changes in the microstructure of the two formulations.[43] As a result, the *in vitro* release test is crucial in determining how well a medication product performs.

The role of NO in wound healing is extensively explored.[14] It has been challenging to identify which of NO's functions could modulate wound healing, although the different effects of NO depend on the location and concentration because several elements and modulators affect wound healing. To mimic the cutaneous wound healing processes more closely, sterile silicone rings are stitched around the wound in our investigation, which avoids tissue contraction. This mechanism was utilized to focus on the re-epithelialization process as a crucial stage in wound healing since skin contraction is more evident in murine models of wound healing than in human wounds. We observed that NO treatment promotes tissue repair after damage by direct re-epithelialization (Fig. 10).

Our findings also demonstrated that the topically applying SP nanoformulation to skin wounds in rats supplemented with NO levels slightly above physiological levels and markedly speed up the wound healing process.[47] Notably, by entering the cell and assaulting microbes DNA and cellular machinery, NO is anti-microbial, successfully boosting the host immune system and helping eliminate the microbial burden.[22,58,63,64]

SP nanoformulation enhances wound healing by fostering fibroblast migration and collagen depositions at the site of the injured area. By enhancing fibroblasts' proliferative capability and motility, increased granulation tissue development hastens wound healing.[65] SP NPs significantly increased the number of fibroblasts in the scratched region of a plate, indicating that particles upregulate fibroblasts' mobility and proliferation (Fig. 5), simultaneously not inducing any adverse effect, which may cause toxicity to cells and may result in the death of fibroblasts (Fig. 6). Fibroblasts are crucial in the regeneration of new tissue in wounded regions as they create the groundwork for the keratinocyte's migration and finally the wound healing. When considered as a whole, these findings demonstrated that NO seems to be involved in controlling fibroblast migration and proliferation through interlinked processes, eventually improving wound healing.

Earlier findings concerning the function of NO are encouraging to angiogenesis.[35,66] In comparison to the untreated CEMA, the SP NPs-treated CEMA showed much more significant vascular sprouting (Fig. 7). The quantitative data demonstrates that SP NPs treated with 1 and 10 μg cause a significant rise in the development and maturation of blood vessels, but at a higher dose (100 μg), it exhibits adverse actions during the starting hours of dosing (development of distorted and damaged vasculature). These findings imply that SP NPs have

both pro-angiogenic and anti-angiogenic effects, depending on the dosage. The mechanism of the angiogenic effect can be given in the context that enhancing and recruiting angiogenesis-supporting elements like TGF-β and vascular endothelial growth factor (VEGF) provide enough blood flow toward a healing wound, and NO can support improved wound healing.[65] For instance, TGF-β helps to increase the tissue debridement at the wound site brought on by macrophages and results in encouraging the recruitment of more and more inflammatory cells. Herein, we postulated that by controlling and regulating the interactions among the fibroblasts, inflammatory cells, cytokines, and remodelling proteins, the topical administration of NO-releasing nanoformulation could reduce the time and accelerate the rate of wound healing.[65]

Additionally, the favourable effects of NO on fibroblast migration and proliferation enhanced the effectiveness and accelerated wound healing. The SP nanoformulation with huge potency undoubtedly caused by nanoparticles changes the biodistribution and release of NO (Fig. 8).[67] With the topical administration of the SP NPs nanoformulation, we did not see any adverse effects in the form of skin irritation and sensitivity (Fig. 9), which is in line with another study[65] that showed that topically administered NO-releasing nanoparticles might cause local immunological modulation (Fig. 12) with minor inflammation (Fig. 12). When nitric oxide is released, it can trigger a cascade of events that polarizes macrophages toward a particular type of immune response.[20] The application of polymer nanoparticles in the delivery of NO can make it possible to administer a precise dosage, which would adequately heal the wound in a regulated manner without producing undesirable outcomes such as tissue damage or severe scarring confirmed through the expression of various gene during the wound healing treatment. An important protein expressed during wound healing is VEGFA, which have both direct and indirect effect on wound healing.[49] The relatively higher expression of VEGFA in the control group on day 2 is responsible for the attraction of inflammatory cells, while the level of the same is decreasing in the control group with time, which shows improper healing as VEGFA is responsible for angiogenesis, inflammation, cell proliferation and migration, granulation tissue formation, collagen synthesis and, finally, wound contraction,[49] which is accordingly expressed higher in the treatment group and accelerates the healing process through the abovementioned mechanisms (Fig. 13). The dynamic regulation of KDR gene expression is crucial for orchestrating the angiogenic response during wound healing. The proper control of KDR activation ensures the formation of a functional vascular network that supports the delivery of oxygen, nutrients, and immune cells to the healing tissue, ultimately promoting effective wound repair.[68] Another important aspect of accelerated wound healing is the expression of PECAM-1 molecules, which is involved in the regulation of endothelial cell function and leukocyte recruitment; during the initial stages of wound healing, it is involved in leukocyte recruitment and migration to the site of injury and regulates a critical step in the inflammatory response.[69] The availability of PECAM-1 during the later stage of wound healing is necessary because it also promotes the tissue that undergoes remodeling, and maturation contributes to the maintenance of vascular integrity during tissue repair.[70] Thus, our early outcomes are promising and encouraging to apply these polymeric nanoformulations as regenerative nanomedicines. Additionally, it would be appropriate to carefully examine the suitability of SP NPs and their nanoformulation for long-term, non-healing wounds and for enhancing difficult wound healing. However, long-term investigations are necessary to evaluate the potential consequences of administering SP NPs and its topical nanoformulation on the skin and other tissues.[65,67]

5. Conclusions

The synthesized novel PNAG NPs are loaded with NO donor (SNP) and transformed into NO-releasing PNAG NPs (SP NPs) with high loading efficiency. SP NPs can be used to deliver NO *in vitro* and *in vivo*. The prepared system can release NO in PBS (pH 7.4 and 6.8) for more than 24 h when tested *in vitro*. Cytotoxicity analysis indicated that SP NPs exhibited good biocompatibility in mouse fibroblast (L929) cell line and displayed negligible hemolytic behaviour on rat RBCs. To evaluate the effect of SP NPs on wound healing promotion, we prepared SP NPs-impregnated nanoformulation using an oleaginous ointment base for enhancing the residence time and smooth application. The nanoformulation is non-irritating for rat's skin. Both NO and PNAG NPs show synergistic effects on cutaneous wound healing by enhancing granulation tissue formation, collagen depositions, angiogenesis, and regulating cytokines, chemokines, and other genes responsible in wound healing and may prove superior compared to the available treatment methods. Therefore, SP NPs and SP nanoformulation is a versatile NO-releasing formulation with a promising future in regenerative medicine and is paramount for therapeutic technology.

Author contributions

Prem Shankar Gupta and Kirti Wasnik (conceptualization, investigations, formal analysis, cell based analysis, gene expression, data curation, visualization, software, writing – original draft and writing – review and editing), Sukanya Patra (methodology), Divya Pareek (methodology), Gurmeet Singh (angiogenesis, *in vivo*, histology study), Desh Deepak Yadav (review and editing), Somedutta Maiti (methodology) and Pradip Paik (project administration, supervision, resources, fund acquisition, writing – review and editing).

Conflicts of interest

The authors have no conflicts of interest to declare.

Acknowledgements

The authors acknowledge the fellowships supported by IIT (BHU) MHRD. Instrument facilities of IIT (BHU) and ISLS-CIF have been used for acquiring data like TEM, SEM and FTIR etc. Authors acknowledge the financial supports awarded to Prof. Pradip Paik by DST-Nanomission, India, (ref: SR/NM/NS-1005/2015), Science and Engineering Research Board (SERB), India, (ref: EEQ/2016/000040), I-DAPT Foundation (ref. I-DAPT/IT (BHU)/2023-24/Project Sanction/47), STARS-IISc. Bangalore (ref. MoE-STARS/STARS-2/2023-0318) and IIT (BHU) Seed Grant (Plan-OH 35). Authors also acknowledge the guidance and support provided by Dr Sudip Mukherjee, Assiatnt Professor, School of Biomedical Engineering, Indian Institute of Technology (BHU), Varanasi, India.

References

1 S. Wang, W.-Y. Wu, J. C. C. Yeo, X. Y. D. Soo, W. Thitsartarn, S. Liu, B. H. Tan, A. Suwardi, Z. Li, Q. Zhu and X. J. Loh, *BMEMat*, 2023, **1**, e12021.
2 C. K. Sen, *Adv. Wound Care*, 2021, **10**, 281–292.
3 V. K. Shukla, M. A. Ansari and S. K. Gupta, *Int. J. Lower Extremity Wounds*, 2005, **4**, 7–8.
4 P. Abaffy, S. Tomankova, R. Naraine, M. Kubista and R. Sindelka, *BMC Genomics*, 2019, **20**, 815.
5 J.-D. Luo and A. F. Chen, *Acta Pharmacol. Sin.*, 2005, **26**, 259–264.
6 A. Friebe, P. Sandner and A. Schmidtko, *Naunyn-Schmiedeberg's Arch. Pharmacol.*, 2020, **393**, 287–302.
7 X. Wang, M. Zhang, T. Zhu, Q. Wei, G. Liu and J. Ding, *Adv. Sci.*, 2023, **10**, 2206154.
8 Y. Yang, P. K. Qi, Z. L. Yang and N. Huang, *Biosurface Biotribology*, 2015, **1**, 177–201.
9 S. F. Bernatchez, V. Menon, J. Stoffel, S.-A. H. Walters, W. E. Lindroos, M. C. Crossland, L. G. Shawler, S. P. Crossland and J. V. Boykin Jr., *Wound Repair Regeneration*, 2013, **21**, 410–417.
10 P. C. Lee, A. N. Salyapongse, G. A. Bragdon, L. L. Shears 2nd, S. C. Watkins, H. D. Edington and T. R. Billiar, *Am. J. Physiol.*, 1999, **277**, H1600–H1608.
11 T. R. Lizarbe, C. García-Rama, C. Tarín, M. Saura, E. Calvo, J. A. López, C. López-Otín, A. R. Folgueras, S. Lamas and C. Zaragoza, *FASEB J.*, 2008, **22**, 3207–3215.
12 K. Yamasaki, H. D. Edington, C. McClosky, E. Tzeng, A. Lizonova, I. Kovesdi, D. L. Steed and T. R. Billiar, *J. Clin. Invest.*, 1998, **101**, 967–971.
13 M. J. Malone-Povolny, S. E. Maloney and M. H. Schoenfisch, *Adv. Healthcare Mater.*, 2019, **8**, e1801210.
14 M. Wu, Z. Lu, K. Wu, C. Nam, L. Zhang and J. Guo, *J. Mater. Chem. B*, 2021, **9**, 7063–7075.
15 T. P. Amadeu and A. M. A. Costa, *J. Cutaneous Pathol.*, 2006, **33**, 465–473.
16 A. B. Shekhter, V. A. Serezhenkov, T. G. Rudenko, A. V. Pekshev and A. F. Vanin, *Nitric Oxide*, 2005, **12**, 210–219.
17 G. Badr, W. N. Hozzein, B. M. Badr, A. Al Ghamdi, H. M. Saad Eldien and O. Garraud, *J. Cell. Physiol.*, 2016, **231**, 2159–2171.
18 M. A. Shalaby, M. M. Anwar and H. Saeed, *J. Polym. Res.*, 2022, **29**, 91.
19 D. A. Riccio and M. H. Schoenfisch, *Chem. Soc. Rev.*, 2012, **41**, 3731–3741.
20 A. K. Yamala, V. Nadella, Y. Mastai, H. Prakash and P. Paik, *Nanoscale*, 2017, **9**, 14006–14014.
21 J. F. Quinn, M. R. Whittaker and T. P. Davis, *J. Controlled Release*, 2015, **205**, 190–205.
22 J. Cao, M. Su, N. Hasan, J. Lee, D. Kwak, D. Y. Kim, K. Kim, E. H. Lee, J. H. Jung and J.-W. Yoo, *Pharmaceutics*, 2020, **12**, 926.
23 M. Li, J. Aveyard, K. G. Doherty, R. C. Deller, R. L. Williams, K. N. Kolegraff, S. B. Kaye and R. A. D'Sa, *ACS Mater. Au*, 2022, **2**, 190–203.
24 T. H. Bindu, M. Vidyavathi, K. Kavitha, Tp. Sastry and S. Rv, *Int. J. Drug Delivery*, 2010, **2**, 173–182.
25 D. Wei and X. Zhang, *Biosaf. Health*, 2022, **4**, 118–134.
26 Y. Zhang, Y. Xu, H. Kong, J. Zhang, H. F. Chan, J. Wang, D. Shao, Y. Tao and M. Li, *Exploration*, 2023, **3**, 20210170.
27 J. Yang and J. Ding, *BME Front.*, 2023, **4**, 0020.
28 U. Shimanovich, A. Lipovsky, D. Eliaz, S. Zigdon, T. P. J. Knowles, Y. Nitzan, S. Michaeli and A. Gedanken, *Adv. Healthcare Mater.*, 2015, **4**, 723–728.
29 WHO, WHO model list of essential medicines, 20th list (March 2017, amended August 2017), **https://apps.who.int/iris/bitstream/handle/10665/273826/EML-20-eng.pdf**, (accessed 12-05-2023, 2023).
30 R. Ahmed, R. Augustine, M. Chaudhry, U. A. Akhtar, A. A. Zahid, M. Tariq, M. Falahati, I. S. Ahmad and A. Hasan, *Biomed. Pharmacother.*, 2022, **149**, 112707.
31 Y. Kang, J. Kim, Y. M. Lee, S. Im, H. Park and W. J. Kim, *J. Controlled Release*, 2015, **220**, 624–630.
32 A. K. Yamala, V. Nadella, Y. Mastai, H. Prakash and P. Paik, *J. Appl. Polym. Sci.*, 2020, **137**, 48363.
33 I. Greco, N. Molchanova, E. Holmedal, H. Jenssen, B. D. Hummel, J. L. Watts, J. Håkansson, P. R. Hansen and J. Svenson, *Sci. Rep.*, 2020, **10**, 13206.
34 H. Hussain, R. L. Santhana, S. Ahmad, M. F. Abd Razak, W. N. Wan Mohamud, J. Bakar and H. M. Ghazali, *Cogent Food Agric.*, 2019, **5**, 1582398.
35 S. Mukherjee, P. Sriram, A. K. Barui, S. K. Nethi, V. Veeriah, S. Chatterjee, K. I. Suresh and C. R. Patra, *Adv. Healthcare Mater.*, 2015, **4**, 1722–1732.
36 M. M. D. Villiers, in *Ointment bases*, ed. J. E. Thompson, Lippincott Williams & Wilkins, 2009, pp. 277–290.
37 R. Weller, *Clin. Exp. Dermatol.*, 2003, **28**, 511–514.
38 H. Razmi and H. Heidari, *Anal. Biochem.*, 2009, **388**, 15–22.
39 Z. Xun, C. Cai and T. Lu, *Electroanalysis*, 2004, **16**, 674–683.
40 A. Chakraborty, S. Pacelli, S. Alexander, S. Huayamares, Z. Rosenkrans, F. E. Vergel, Y. Wu, A. Chakravorty and A. Paul, *Mol. Pharm.*, 2023, **20**, 767–774.

41 T. Goyal and C. L. Schmotzer, *Am. J. Clin. Pathol.*, 2015, **143**, 579–583.
42 R. Li, K. Liu, X. Huang, D. Li, J. Ding, B. Liu and X. Chen, *Adv. Sci.*, 2022, **9**, 2105152.
43 N. S. Kamal, Y. S. R. Krishnaiah, X. Xu, A. S. Zidan, S. Raney, C. N. Cruz and M. Ashraf, *Int. J. Pharm.*, 2020, **590**, 119914.
44 Y. Zhang, K. Tang, B. Chen, S. Zhou, N. Li, C. Liu, J. Yang, R. Lin, T. Zhang and W. He, *Biomater. Sci.*, 2019, **7**, 1607–1616.
45 R. González, F. J. Molina-Ruiz, J. A. Bárcena, C. A. Padilla and J. Muntané, *Antioxid. Redox Signaling*, 2017, **29**, 1312–1332.
46 P. Deng, L. Yao, J. Chen, Z. Tang and J. Zhou, *Carbohydr. Polym.*, 2022, **276**, 118718.
47 V. C. O. Póvoa, G. J. V. P. dos Santos, G. F. Picheth, C. P. Jara, L. C. E. da Silva, E. P. de Araújo and M. G. de Oliveira, *J. Tissue Eng. Regen. Med.*, 2020, **14**, 807–818.
48 Y. Oh, H. Jeong, S. Lim and J. Hong, *Biomacromolecules*, 2020, **21**, 4972–4979.
49 T. A. Wilgus, *Adv. Wound Care*, 2019, **8**, 671–678.
50 S. C. R. Santos, C. Miguel, I. Domingues, A. Calado, Z. Zhu, Y. Wu and S. Dias, *Exp. Cell Res.*, 2007, **313**, 1561–1574.
51 M. Moreno-Sastre, M. Pastor, A. Esquisabel, E. Sans, M. Viñas, D. Bachiller and J. L. Pedraz, *J. Microencapsulation*, 2016, **33**, 636–645.
52 L. M. Ernst, E. Casals, P. Italiani, D. Boraschi and V. Puntes, *Nanomaterials*, 2021, **11**, 2991.
53 J. Tan, T. J. Cho, D. H. Tsai, J. Liu, J. M. Pettibone, R. You, V. A. Hackley and M. R. Zachariah, *Langmuir*, 2018, **34**, 154–163.
54 C. Thauvin, B. Schwarz, F. Delie and E. Allémann, *Int. J. Pharm.*, 2018, **548**, 771–777.
55 X. Xu, M. Al-Ghabeish, Y. S. R. Krishnaiah, Z. Rahman and M. A. Khan, *Int. J. Pharm.*, 2015, **494**, 31–39.
56 M. R. Holme and T. Sharman, Sodium nitroprusside, **https://www.ncbi.nlm.nih.gov/books/NBK557487/**, (accessed 07-05-2023, 2023).
57 S. Liu, X. Cai, W. Xue, D. Ma and W. Zhang, *Carbohydr. Polym.*, 2020, **234**, 115928.
58 J. Lee, S. P. Hlaing, J. Cao, N. Hasan and J.-W. Yoo, *J. Pharm. Invest.*, 2020, **50**, 505–512.
59 H. T. T. Duong, Z. M. Kamarudin, R. B. Erlich, Y. Li, M. W. Jones, M. Kavallaris, C. Boyer and T. P. Davis, *Chem. Commun.*, 2013, **49**, 4190–4192.
60 M. Huang, J. Zhang, X. Ke, S. Gao, D. Wu, J. Chen and Y. Weng, *RSC Adv.*, 2022, **12**, 2383–2390.
61 S. Ghalei, M. Douglass and H. Handa, *ACS Biomater. Sci. Eng.*, 2022, **8**, 273–283.
62 G. K. Rout, H.-S. Shin, S. Gouda, S. Sahoo, G. Das, L. F. Fraceto and J. K. Patra, *Artif. Cells, Nanomed., Biotechnol.*, 2018, **46**, 1053–1062.
63 J. Lee, D. Kwak, H. Kim, J. Kim, S. P. Hlaing, N. Hasan, J. Cao and J.-W. Yoo, *Pharmaceutics*, 2020, **12**, 618.
64 H. Nurhasni, J. Cao, M. Choi, I. Kim, B. L. Lee, Y. Jung and J. W. Yoo, *Int. J. Nanomed.*, 2015, **10**, 3065–3080.
65 G. Han, L. N. Nguyen, C. Macherla, Y. Chi, J. M. Friedman, J. D. Nosanchuk and L. R. Martinez, *Am. J. Pathol.*, 2012, **180**, 1465–1473.
66 N. Yamamoto, T. Oyaizu, M. Enomoto, M. Horie, M. Yuasa, A. Okawa and K. Yagishita, *Sci. Rep.*, 2020, **10**, 2744.
67 E. Pereverzeva, I. Treschalin, M. Treschalin, D. Arantseva, Y. Ermolenko, N. Kumskova, O. Maksimenko, V. Balabanyan, J. Kreuter and S. Gelperina, *Int. J. Pharm.*, 2019, **554**, 161–178.
68 P. Bao, A. Kodra, M. Tomic-Canic, M. S. Golinko, H. P. Ehrlich and H. Brem, *J. Surg. Res.*, 2009, **153**, 347–358.
69 P. Martin and S. J. Leibovich, *Trends Cell Biol.*, 2005, **15**, 599–607.
70 A. Woodfin, M.-B. Voisin and S. Nourshargh, *Arterioscler., Thromb., Vasc. Biol.*, 2007, **27**, 2514–2523.